IntechOpen

# Plasmonics

*Edited by Tatjana Gric*

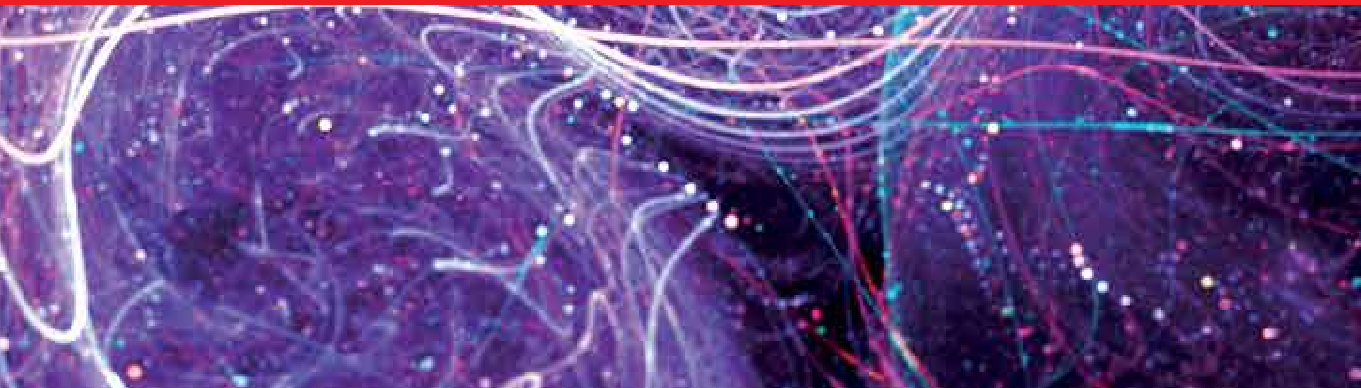

# PLASMONICS

Edited by **Tatjana Gric**

**Plasmonics**
http://dx.doi.org/10.5772/intechopen.73373
Edited by Tatjana Gric

**Contributors**

Nilesh Kumar Pathak, Partha Sarathi, Gyanendra Krishna Pandey, R P Sharma, Marinna Madrid, Christian Kuttner, Weiping Cai, Haoming Bao, Hongwen Zhang, Guangqiang Liu, Ina Schubert, Maria Eugenia Toimil-Molares, Xianguang Yang, Baojun Li, Tatjana Gric, Witold Jacak, Janusz Jacak, Bin Hu, Hyuntai Kim, Abdul Kariem Arof, Mh Buraidah, Ngoc Diep Lai, Fei Mao, Quang Cong Tong, Mai Hoang Luong, Rasta Ghasemi, Duc Tho Nguyen, Minh Thanh Do, Quoc Tien Tran

**© The Editor(s) and the Author(s) 2018**
The rights of the editor(s) and the author(s) have been asserted in accordance with the Copyright, Designs and Patents Act 1988. All rights to the book as a whole are reserved by INTECHOPEN LIMITED. The book as a whole (compilation) cannot be reproduced, distributed or used for commercial or non-commercial purposes without INTECHOPEN LIMITED's written permission. Enquiries concerning the use of the book should be directed to INTECHOPEN LIMITED rights and permissions department (permissions@intechopen.com).
Violations are liable to prosecution under the governing Copyright Law.

Individual chapters of this publication are distributed under the terms of the Creative Commons Attribution 3.0 Unported License which permits commercial use, distribution and reproduction of the individual chapters, provided the original author(s) and source publication are appropriately acknowledged. If so indicated, certain images may not be included under the Creative Commons license. In such cases users will need to obtain permission from the license holder to reproduce the material. More details and guidelines concerning content reuse and adaptation can be foundat http://www.intechopen.com/copyright-policy.html.

**Notice**

Statements and opinions expressed in the chapters are these of the individual contributors and not necessarily those of the editors or publisher. No responsibility is accepted for the accuracy of information contained in the published chapters. The publisher assumes no responsibility for any damage or injury to persons or property arising out of the use of any materials, instructions, methods or ideas contained in the book.

First published in London, United Kingdom, 2018 by IntechOpen
eBook (PDF) Published by IntechOpen, 2019
IntechOpen is the global imprint of INTECHOPEN LIMITED, registered in England and Wales, registration number: 11086078, The Shard, 25th floor, 32 London Bridge Street
London, SE19SG – United Kingdom
Printed in Croatia

British Library Cataloguing-in-Publication Data
A catalogue record for this book is available from the British Library

Additional hard and PDF copies can be obtained from orders@intechopen.com

Plasmonics
Edited by Tatjana Gric

p. cm.

Print ISBN 978-1-78984-434-4

Online ISBN 978-1-78984-435-1

eBook (PDF) ISBN 978-1-83881-738-1

We are IntechOpen,
the world's leading publisher of
Open Access books
Built by scientists, for scientists

3,800+
Open access books available

116,000+
International authors and editors

120M+
Downloads

151
Countries delivered to

Our authors are among the
Top 1%
most cited scientists

12.2%
Contributors from top 500 universities

CLARIVATE ANALYTICS
BOOK CITATION INDEX
INDEXED

WEB OF SCIENCE™

Selection of our books indexed in the Book Citation Index
in Web of Science™ Core Collection (BKCI)

Interested in publishing with us?
Contact book.department@intechopen.com

Numbers displayed above are based on latest data collected.
For more information visit www.intechopen.com

# Meet the editor

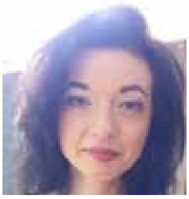

Dr. Gric's research career has been focused on the investigation of waveguide devices (waveguide modulators, filters, etc.), namely on proposing their electrodynamic analysis. Another major goal of her studies is plasmonics, the examination of the interaction between electromagnetic field and free electrons in a metal. Moreover, the broad scope of research carried out by Dr. Gric has included investigations into the new fascinating properties of novel materials. Dr. Gric also has a record of effective teaching in the rank of associate professor. She has published extensively in her field of investigation with more than 35 peer-reviewed papers in top journals in physics, electrodynamics, and optics.

# Contents

# Preface

*Plasmonics* gives researchers in universities and industries and designers an overview of phenomena enabled by artificially designed metamaterials and their application for plasmonic devices.

Optical interaction with nanostructures is studied by the field of plasmonics. Recently, the potential of subwavelength confinement and enhancement of optical fields close to appropriately designed nanoscale objects has opened a gateway to extensive investigations into plasmonic optical phenomena. The purpose of this book is to provide a detailed introduction to the basic modeling approaches and an overview of enabled innovative phenomena.

Surface waves open a gateway to a wide spectrum of physical phenomena providing a fertile ground for a number of applications. Discovery of metamaterials with tunable electric and magnetic features has allowed for a rich phenomenon, i.e. expansion of the wide spectrum of structures capable of supporting surface waves. Surface plasmon polaritons (SPPs) are electromagnetic excitations occurring at the interface between a conductor and a dielectric. These are evanescently confined in the perpendicular direction. It is possible to imitate the properties of confined SPPs by using geometrically induced SPPs, called spoof SPPs. The proposed phenomenon may take place at lower frequencies. It might be concluded that the surface structure could open a gateway to spoof surface plasmons. The former serves as a perfect prototype for structured surfaces. The main research agenda of this book is aimed at the study of the modeling techniques and novel functionalities such as plasmonic enhancement of solar cell efficiency, plasmonics in sensing, etc.

The topics addressed in this book cover the major strands: theory, modeling and design, applications in practical devices, fabrication, characterization, and measurement. It is worthwhile mentioning that the strategic objectives of developing new artificial functional materials require close cooperation of the research in each subarea.

**Tatjana Gric**
Vilnius Gediminas Technical University, Lithuania

## Section 1

# Introduction

# Introductory Chapter: Plasmonics

Tatjana Gric

Additional information is available at the end of the chapter

http://dx.doi.org/10.5772/intechopen.78036

## 1. Introduction

The optical interaction with nanostructures is studied by the field of plasmonics. Recently, the potential of subwavelength confinement and the enhancement of optical fields close to the appropriately designed nanoscale objects have opened a gateway to extensive investigations of plasmonic optical phenomena.

Consequently, the outstanding field of plasmonics has spread over different disciplines, providing the wide avenues for the promising applications in material science, biology, and engineering. Furthermore, the field of metamaterials has been enriched and enhanced by the plasmonic optics, for example, metasurfaces. The former concept is based on the collective electromagnetic behavior of many subwavelength inclusions and building blocks as "meta-atoms." Doing so, novel tunable composite materials, i.e., near-zero material parameters, and extreme-value material parameters, characterized by unconventional bulk and surface properties, have been proposed and applied.

Surface waves open a gateway to a wide spectrum of physical phenomena providing a fertile ground for a number of applications [1–3]. The discovery of metamaterials with tunable electric and magnetic features [4] has allowed for a rich phenomenon, i.e., expansion of the wide spectrum of structures capable of supporting surface waves. Surface plasmon polaritons (SPPs) are electromagnetic excitations occurring at the interface between a conductor and dielectric. These are evanescently confined in the perpendicular direction [5–8]. It is possible to imitate the properties of confined SPPs by geometrical-induced SPPs, named as spoof SPPs. The proposed phenomenon may take place at lower frequencies. It might be concluded that surface structure may open a gateway to spoof surface plasmons. The former serves as a perfect prototype for structured surfaces [9].

Thus, metasurfaces, a class of planar metamaterials possessing the outstanding functionality, i.e., capabilities to mold light flow, have recently attracted intensive attention. The main goal of the metasurfaces is to achieve the anticipated phase profile by designing subwavelength

IntechOpen

© 2018 The Author(s). Licensee IntechOpen. This chapter is distributed under the terms of the Creative Commons Attribution License (http://creativecommons.org/licenses/by/3.0), which permits unrestricted use, distribution, and reproduction in any medium, provided the original work is properly cited. (cc) BY

structures at the interface between two ordinary materials. Abilities to fully engineer the properties of the propagating waves are gained thanks to the rationally designed phase. It should be mentioned that anomalous reflection and refraction have been verified in the infrared range.

Metasurface-based optical devices, such as vortex plates, wave plates, and ultra-thin focusing lenses have also been proposed for various types of incident light, i.e., linearly polarized light or vertex beams. Now is the time that the fundamental research in the field is giving rise to the first promising applications for industry.

For centuries, the control of optical properties has been limited to altering material compositions, relying on light propagation through naturally occurring materials to impart phase shifts and tailor the desired wavefronts. The introduction of metamaterials allows control over optical wavefronts to deviate from the usual propagation methods and rely instead on its carefully engineered internal structure. This was first theorized 20 years ago by Pendry et al. [10], and since then, the development in the field of artificially designed materials has only accelerated. Metamaterials offer an extensive range of novel electromagnetic phenomena, which do not occur in natural materials, but whose existence is not restricted by physical laws. These artificially created "materials" are made up of a series of composite unit elements, which although are a few orders of magnitude larger than the molecular unit cells of regular materials. This allows the metamaterials to provide descriptions of its interactions with electromagnetic waves in terms of its effective "material" parameters. Metamaterials can, therefore, still be viewed as a homogenous material at their desired operational wavelengths, typically within the optical regime. With careful structuring of the elements within the metamaterial, unusual material properties such as a negative refractive index can be achieved. The refractive index $\eta$ of a material is governed by its macroscopic electromagnetic permittivity $e$ and permeability $\mu$, where $\eta = \pm\sqrt{e\mu}$.

The development of such negative index material could lead to novel applications especially within the optical regime, such as creating the perfect lens, which images beyond the diffraction limit, or an optical cloaking device. The initial realization of a negative refractive index metamaterial uses a pattern of metallic wires and split-ring resonators to form its unit cells, which have been experimentally demonstrated in the microwave regime and later at optical wavelengths as the elemental array is reduced into the nanoscale. Bulk metamaterials, however, are usually susceptible to high losses and strong dispersive effects due to the resonant responses of metallic structures used. Additionally, the complex structures required in a 3D metamaterial is challenging to build using the existing micro- and nanofabrication methods. Thus, recent studies have been focusing on the development of 2D metamaterials, or metasurfaces. These planar materials allow for the combined advantages of the ability to engineer electromagnetic responses with low losses associated with thin layer structures. The introduction of surfaces with subwavelength thicknesses results in minimal propagation phase; this shifts the focus from developing materials with negative permittivity and permeability to engineering surface structures to adjust surface reflection and transmissions. This is made possible by exploiting abrupt phase jumps and polarization changes from scattering effects, which can be realized and subsequently fine-tuned through designing spatially varying phase responses over the metasurface, through using either metallic or dielectric surface structures. In solid state physics, materials can be classified according to their electronic band structure. While metals have overlapping conduction and valence bands, which allows the free movement of electrons through the material, dielectric insulators have a large band gap between the two. Both types of materials are still able to interact with incident electromagnetic fields, although through different physical methods and result in light scattering effects. Thus, both materials have, therefore, been employed in the realization of the vast potential of metasurfaces.

## Author details

Tatjana Gric

Address all correspondence to: tatjana.gric@vgtu.lt

Department of Electronic Systems, Vilnius Gediminas Technical University, Vilnius, Lithuania

## References

[1] Yan H, Li X, Chandra B, Tulevski G, Wu Y, Freitag M, Zhu W, Avouris P, Xia F. Tunable infrared plasmonic devices using graphene/insulator stacks. Nature Nanotechnology. 2012;**7**:330

[2] Viti L, Coquillat D, Politano A, Kokh KA, Aliev ZS, Babanly MB, Tereshchenko OE, Knap W, Chulkov EV, Vitiello MS. Plasma-wave terahertz detection mediated by topological insulators surface states. Nano Letters. 2016;**16**:80

[3] Politano A, Chiarello G. Unravelling suitable graphene-metal contacts for graphene-based plasmonic devices. Nanoscale. 2013;**5**:8215

[4] Radkovskaya A, Tatartschuk E, Sydoruk O, Shamonina E, Stevens CJ, Edwards DJ, Solymar L. Surface waves at an interface of two metamaterial structures with interelement coupling. Physical Review B. 2010;**82**:045430

[5] Echtermeyer TJ, Milana S, Sassi U, Eiden A, Wu M, Lidorikis E, Ferrari AC. Surface plasmon polariton graphene photodetectors. Nano Letters. 2015;**16**:8

[6] Politano A, Chiarello G. The influence of electron confinement, quantum size effects, and film morphology on the dispersion and the damping of plasmonic modes in Ag and au thin films. Progress in Surface Science. 2015;**90**:144

[7] Nechaev IA, Aguilera I, Renzi VD, Bona A d, Lodi Rizzini A, Mio AM, Nicotra G, Politano A, Scalese S, Aliev ZS, Babanly MB, Friedrich C, Blügel S, Chulkov EV. Quasiparticle spectrum and plasmonic excitations in the topological insulator Sb2Te3. Physical Review B. 2015;**91**: 245123

[8] Politano A. Interplay of structural and temperature effects on plasmonic excitations at noble-metal interfaces. Philosophical Magazine. 2012;**92**:768

[9] Pendry JB, Martin-Moreno L, Garcia-Vidal FJ. Mimicking surface plasmons with structured surfaces. Science. 2004;**305**:847

[10] Pendry JB, Holden AJ, Robbins DJ, Stewart WJ. Magnetism from conductors and enhanced nonlinear phenomena. IEEE Transactions on Microwave Theory and Techniques. 1999; **47**(11):2075-2084

## Section 2

# Experimental Design and Modelling

# A Perspective on Plasmonics within and beyond the Electrostatic Approximation

Nilesh Kumar Pathak, Parthasarathi,
Gyanendra Krishna Pandey and R.P. Sharma

Additional information is available at the end of the chapter

http://dx.doi.org/10.5772/intechopen.81038

## Abstract

Plasmonic is an emerging branch of nanophotonics wherein the electromagnetic properties of nanoparticles are studied for variety of applications. The optics of nanoparticles is studied in terms of surface plasmon resonances and optical cross section. Initially the first principle approach has been used to study the plasmonic fundamentals known as electrostatic approach. Under this approach, various parameters are taken into account to observe the electromagnetic properties of plasmonic nanogeometries. This electrostatic model is only used to analyze the optical signature of smaller size plasmonic geometries. Therefore, for the estimation of optical properties of larger size nanoparticle numerical model (Discrete Dipole Approximation) has been used. The observed surface plasmon resonances could be useful in sensing field, SERS signal detection and thin film solar cell application.

**Keywords:** plasmonics, nanoparticle, surface plasmon resonance, optical cross section

## 1. Introduction

Plasmonics is the emerging branch of nanophotonics which deals the coupling of light to the collective oscillation of electrons inside the metal nanoparticles. The coupling of light to the metal nanoparticles produces resonances under specific condition known as surface plasmon resonance (SPR) that has tremendous applications [1–5]. The resonant interaction between them will localize the electromagnetic field near the meal surface and drastically enhances the optical scattering phenomenon. When the light interacts with the metallic nanostructures two fundamental excitations are observed. These two fundamental excitations are surface plasmon polaritons (SPP) and localized surface plasmon resonance (LSPR). The surface plasmon

IntechOpen

© 2018 The Author(s). Licensee IntechOpen. This chapter is distributed under the terms of the Creative Commons Attribution License (http://creativecommons.org/licenses/by/3.0), which permits unrestricted use, distribution, and reproduction in any medium, provided the original work is properly cited.

polaritons is propagating, dispersive electromagnetic waves coupled to the electron plasma of a metal at a dielectric interface. The other excitation is localized surface plasmons which are non-propagating excitations of the conduction electrons of metallic nanostructures coupled to the electromagnetic field. Such modes arise due to the scattering of a sub-wavelength conductive nanoparticle in an oscillating electromagnetic field. An effective restoring force on the driven electrons is induced by the curved surface of the particle leading to resonance and field amplification both inside and in the near-field zone outside the particle. This resonance is called the localized surface plasmon or short localized plasmon resonance [6–11]. Plasmon resonances can be excited by direct light illumination which do not require any phase-matching. In addition to solid particles, other nanostructures that support localized plasmons are dielectric inclusions in metal bodies or surfaces, and nanoshells [6, 12–15]. For gold and silver nanoparticles, the resonance lies in the visible region of the electromagnetic spectrum leading to bright colors exhibited by particles both in transmitted and reflected light. This is direct consequence of resonantly enhanced absorption and scattering of light from these particles. From the viewpoint of electromagnetic and optics, a major consequence of the resonantly enhanced polarization is associated enhancement in the efficiency with which a metal nanoparticle scatters and absorbs light [6, 8, 16–19].

An important properties exhibit by plasmonic elements like silver, gold, copper and aluminum is surface plasmons which concentrate the optical energy in nanoscale [20–24]. The existence plasmonic properties (like surface plasmon mode) in materials is entirely depends on their dielectric constants. Surface plasmon mode is an important property by which one can concentrate the optical energy in nanoscale domain [15, 25–28]. As the dielectric constants are the complex quantities in which real part is the reflection and imaginary part represent the absorption or loss. Therefore, on the basis of dielectric constant value one can define the definition good and bad plasmonic materials and also decides the weather the material having plasmonic properties or not. Those materials are the plasmonic materials for which dielectric constant $\varepsilon_m$ has a negative real part, Re $\varepsilon_m < 0$ and imaginary part of dielectric constant is much less than the real part of dielectric constant (Im $\varepsilon_m <<$ Re $\varepsilon_m$). Under these two conditions surface plasmon resonances are most effective due to minimum losses in metals. Silver and gold shows plasmon properties in visible range because it satisfies above two properties in visible range [11, 29–31]. The real and imaginary part of dielectric constant of gold metal shows their variation with wavelength in **Figure 1a** and **b**.

The work furnishes the study of plasmonic properties of metal nanostructures within and beyond the electrostatic approximation. In the electrostatic approximation we have analyze the interaction of electromagnetic field to metal nanoparticle whose size is much smaller than the wavelength of incident light. In such situation particle experienced only constant or static field throughout the particle volume. Since this model is restricted to smaller size nanoparticles in which only dipolar analysis is taken into account. The dipolar analysis means, we have truncated the potential series upto two terms and apply Laplace equation to obtain the field, polarizability expression and resonance condition. As the size of nanoparticle increases it starts to experience the oscillation behavior of field and electrostatic approximation completely fails. Therefore we need to require techniques which describe the full wave analysis.

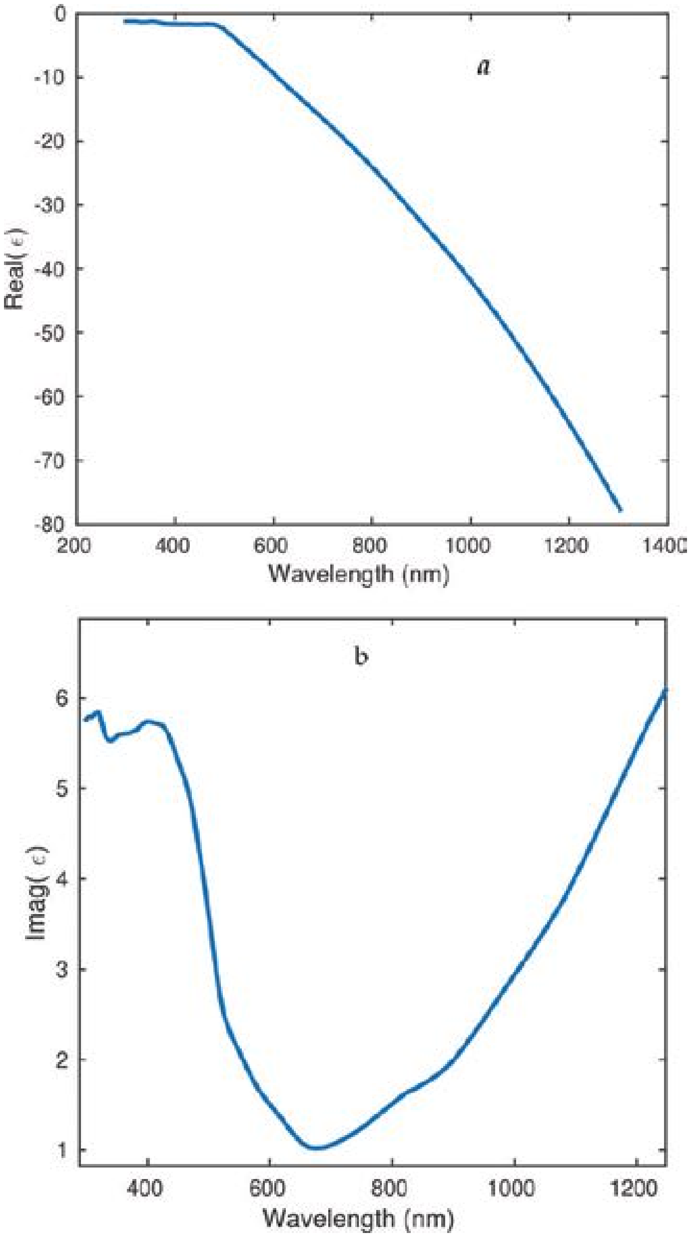

**Figure 1.** Wavelength dependent (a) real and (b) part of dielectric constant of gold.

Discrete Dipole Approximation (DDA) technique is one of them which is based on the dipole discretization concept and frequently used to simulate the plasmonic properties of arbitrary size, shape nanostructure. We have used this simulation technique to study the plasmonic properties of larger size metal nanostructure.

## 2. Theoretical model: scattering by small size metal nanosphere

Theoretical model discuss the plasmonic properties of metal nanoparticle within electrostatic approximation wherein particle size is smaller than the wavelength of light. Under such assumption Laplace equation has been solved with suitable boundary condition to find out the optical parameters [13, 32]. The Laplace equation is expressed as

$$\nabla^2 V = 0 \tag{1}$$

and its solution in spherical polar coordinate is

$$\mathrm{V(r)} = \sum_{l,\mathrm{m}} \mathrm{A}_{l,\mathrm{m}}\, r^{-l-1}\, Y_l^m(\theta,\varphi) + \sum_{l,\mathrm{m}} B_{l,\mathrm{m}}\, r^l\, Y_l^m(\theta,\varphi) \tag{2}$$

Truncating the potential series only for dipolar term which correspond to $l = 1$ one can find the value of potential inside and outside the spherical surface as

$$V_{in} = -\frac{3\,\varepsilon_m}{\varepsilon + 2\,\varepsilon_m} E_0\, r\cos\theta, \tag{2a}$$

$$V_{out} = -E_o\, r\cos\theta + \frac{r\cos\theta}{r^3} a^3 E_0 \left(\frac{\varepsilon - \varepsilon_m}{\varepsilon + 2\,\varepsilon_m}\right) \tag{2b}$$

Once we have potential profile, the calculation of field and polarizability can be easily obtained by $E = -\nabla V$ expression.

The applied field polarizes the metal nanostructure and its polarization is in the same direction of applied electric field. If the size of nanoparticle is small enough then polarization is in the direction of applied field while for larger size nanoparticle the oscillation of electron is no longer symmetric and the polarization mechanism is split into component form such as transverse and longitudinal. Here the study reveals the optical properties of smaller size nanoparticle therefore, polarization of particle is in the same direction of applied field. The polarization is simply the dipole moment per unit volume which is expressed as

$$p = \varepsilon_m \alpha E_0 \tag{2c}$$

where $E_0$ is the applied electric field and $\alpha$ is the polarizability of nanosphere expressed as

$$\alpha = 4\pi a^3 \left(\frac{\varepsilon - \varepsilon_m}{\varepsilon + 2\,\varepsilon_m}\right) \tag{3}$$

The symbol $a$ is the radius of metal nanosphere, $\varepsilon, \varepsilon_m$ are the dielectric constant of metal sphere and surrounding environment. The expression of polarizability is an important parameter in the discussion of resonance physics. The concept of resonance brought into the picture from the denominator part of polarizability expression. The polarizability gets resonantly enhanced when $|\varepsilon + 2\,\varepsilon_m| = 0$ which is known as Fröhlich condition.

As we know when the incident electromagnetic field interacts with metallic nanostructure, some fraction of light gets absorbed and some of them gets scattered. The magnitude of the these absorbed and scattered light can be expressed in terms of scattering and absorption cross section as

$$\langle C_{scat} \rangle = \frac{8\pi}{3} k^4 a^6 \left| \frac{\varepsilon - \varepsilon_m}{\varepsilon + 2\,\varepsilon_m} \right|^2 \tag{4}$$

$$Q_{scat} = \frac{\langle C_{scat} \rangle}{\pi a^2} \tag{5}$$

where symbol $k$ is the incident light wave vector, $\varepsilon, \varepsilon_m$ are the dielectric constant of metal and surrounding medium.

A spherical shape metal nanoparticle is taken into account to observe the optical properties like scattering cross section and surface plasmon resonances. **Figure 2** represent the wavelength dependent normalized cross section of three different radii of spherical shape silver metal nanoparticle. We observed that as the size of nanoparticle increases corresponding magnitude of scattering cross section increases. But the position of SPR peak position is same for all radii which is at 364 nm.

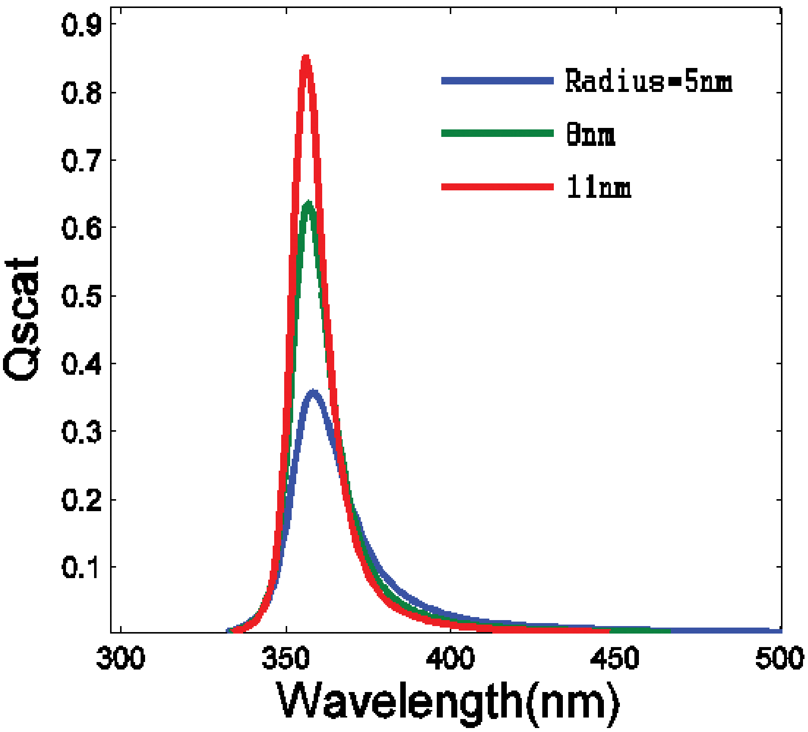

**Figure 2.** Wavelength dependent scattering cross section of silver metal nanoparticle of three different radii.

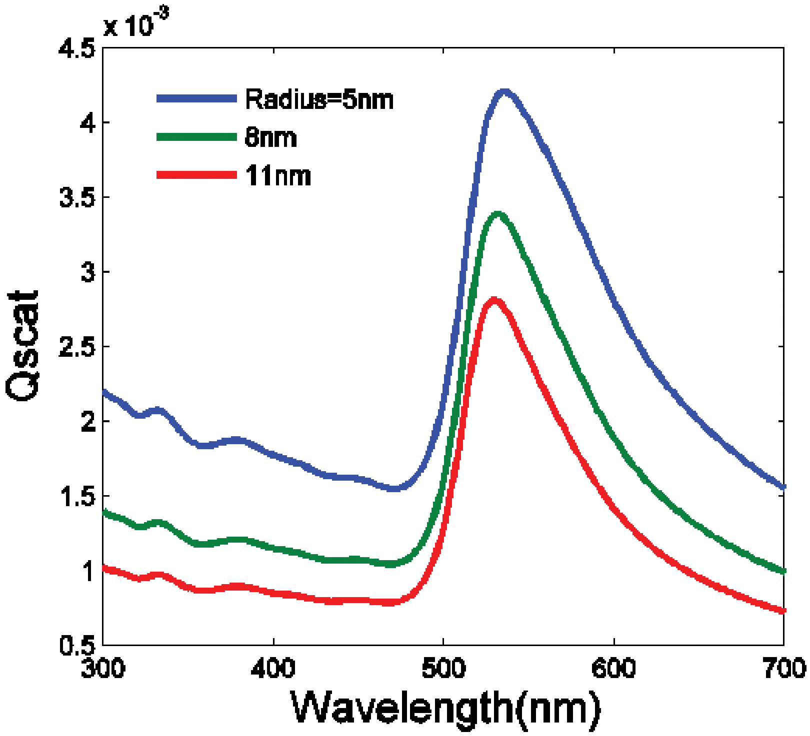

**Figure 3.** Wavelength dependent scattering cross section of gold metal nanoparticle of three different radii.

In **Figure 3**, we have discussed the wavelength dependent scattering cross section of gold metal nanoparticle for three different radii. Here we observed that, as the radii of gold nanoparticle increases corresponding cross section magnitude increases with red shifted SPR resonance. In case of silver the SPR peak position is fixed at one wavelength while for gold the peak positions are red shifted with the radii. The SPR peak position for gold nanosphere surrounded by air (N = 1) is at 554 nm for radius 5 nm. The additional advantages of gold nanoparticle over the silver are analyzed in terms of SPR peak positions and corresponding spectral width known as full width at half maxima (FWHM).

These two different types of metal nanoparticle are described within the electrostatic approximation which is only valid for smaller size. Therefore, for the description of lager size nanoparticle we have used the numerical method discrete dipole approximation (DDA) which is valid within and beyond the electrostatic approximation.

## 3. Numerical approach: scattering by large size metal nanosphere

The numerical technique that we have used to simulate the optical properties of large size nanoparticle is discrete dipole approximation method. In this method, target is discretized into large number of polarizable dipoles [33]. Each dipole situated at the corner of a cubic lattice and the relation between them i.e., separation or distance of one dipole to other are managed by the lattice parameter. The chosen target in this technique is expressed in terms of volume as $V = Nd^3$, where N is the number of discretized dipole and d is the lattice spacing and the size of target is also expressed in term of effective radius as $a_{eff} = (3V/4\pi)^{1/3}$. The technique is applicable only when the following criteria is satisfied

$$|m|kd < 1,$$

where k is wave vector, lattice parameter and m is the complex refractive index of chosen target material. The main input parameter in DDA technique is the dielectric constant of target and surrounding media in which target is embedded. The complex dielectric function of composite system is provided by input file which can be expressed as

$$\varepsilon_{relative} = \frac{\varepsilon_{target}}{\varepsilon_{medium}} \tag{6}$$

Here, the target is assumed as a point dipole situated at the each corner of cube. Further, placement position $\vec{r}_i$ and polarizability $\vec{\alpha}_i$ of the point dipoles need to be flexible for DDA calculation. Each entity is represented by a dipole moment as

$$\vec{p}_i = \alpha_i.\vec{E}_{i,loc} \tag{7}$$

$$\vec{E}_{i,loc} = \vec{E}_{i,app} + \vec{E}_{i,ind} \tag{8}$$

where $\vec{E}_{i,app}$ and $\vec{E}_{i,ind}$ is the applied and induced field respectively acting on the i^th^ individual because of the radiation of all the others (N – 1) dipoles that set up the NPs. The field $\vec{E}_{i,app}$ and $\vec{E}_{i,ind}$ is given by the following relation

$$\vec{E}_{i,app} = E_0 e^{i(\vec{k}.\vec{r}-\omega t)} \tag{9}$$

$$\vec{E}_{i,ind} = -\sum_{j=1}^{N} \vec{A}_{ij}.p_j \tag{10}$$

$$\vec{A}_{ij}.\vec{p}_j = \frac{e^{ikr_{ij}}}{r_{ij}^3}\left\{k^2\vec{r}_{ij}\left(\vec{r}_{ij}\times\vec{p}_j\right) + \frac{\left(1-ikr_{ij}\right)}{r_{ij}^2}\left[r_{ij}^2\vec{p}_j - 3\vec{r}_{ij}\left(\vec{r}_{ij}.\vec{p}_j\right)\right]\right\} \tag{11}$$

$$\vec{p}_i = \alpha_i.\left(\vec{\mathrm{E}}_{i,app} - \sum_{j=1}^{N}\vec{A}_{ij}.p_j\right) \tag{12}$$

where k = $|k|$ represents the incident wave vector.

Dipole moment symbolizes the optical behavior of the target geometry. Therefore, the extinction and absorption cross section can be achieved after calculating the set of dipole moments as given by

$$C_{ext} = \frac{4\pi k}{\left|\vec{E}_0\right|^2} \sum_{i=1}^{N} \operatorname{Im}\left\{ \vec{E}^{\,*}_{i,inc} . \vec{p}_i \right\} \tag{13}$$

$$C_{abs} = \frac{4\pi k}{\left|\vec{E}_0\right|^2} \sum_{i=1}^{N} \left\{ \operatorname{Im}\left[ \vec{p}_i . (\alpha_i^{-1})^* \vec{p}_i^{\,*} \right] - \frac{2}{3} k^3 \left|\vec{p}_i\right|^2 \right\} \tag{14}$$

$$\begin{aligned} C_{sca} &= C_{ext} - C_{abs} \\ Q_i &= \frac{C_i}{\pi a_{eff}^2} \end{aligned} \tag{15}$$

where $C_i$ signifies the optical cross section, $i$ represents the running index includes extinction, absorption and scattering, $Q_i$ represents the normalized optical cross section and $a_{eff}$ effective radius of target.

The simulation effects could be visualized in terms of scattering cross section as shown in **Figure 4**. A 50 nm radius gold metal sphere is discretized into 4224 number of dipole to see the plasmonic properties like scattering cross section and surface plasmon resonance. The SRP wavelength of 50 nm gold nanosphere was observed at wavelength 560 nm.

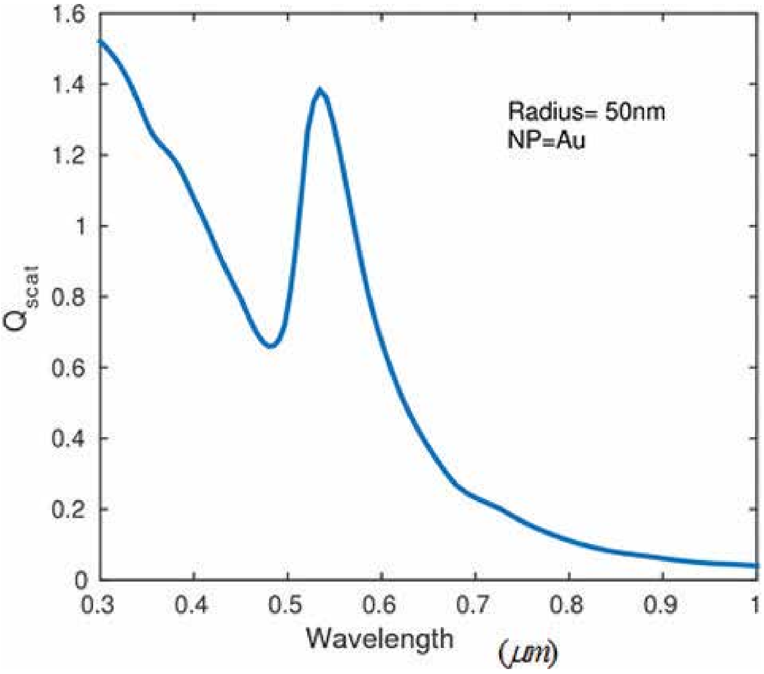

**Figure 4.** Wavelength dependent scattering cross section of 50 nm gold nanosphere surrounded by air.

## 4. Conclusion

The work described the optical properties of plasmonic nanogeometries in terms of optical cross section and surface plasmon resonance. Two different types of metals like silver and gold are taken into account to see the optical properties. The surface plasmon resonance corresponding to these metals lies in visible range of electromagnetic spectrum wherein most of the applications exist. Therefore, the work guides to plamonic community to simulate various types of metal nanostructure which exhibit SPR in different part of electromagnetic spectrum. These tunable nature of surface plasmon resonances can be used in many purposes such as sensing, photovoltaic and Raman spectroscopy.

## Acknowledgements

The authors would like to thanks to Maharaja Agrasen College, University of Delhi, Delhi 110096, India.

## Conflict of interest

The authors do not have any conflict of interest.

## Author details

Nilesh Kumar Pathak[1,2]*, Parthasarathi[1], Gyanendra Krishna Pandey[1] and R.P. Sharma[1]

*Address all correspondence to: nileshpiitd@gmail.com

1 Plasma and Plasmonic Simulation Laboratory, Centre for Energy Studies, Indian Institute of Technology, Delhi, India

2 Maharaja Agrasen College, University of Delhi, Delhi, India

## References

[1] Catchpole KR, Polman A. plasmonic solar cell. Optics Express. 2008;**6**:21793-21800

[2] Pathak NK, Alok J, Sharma RP. Tunable properties of surface plasmon resonances: The influence of core–shell thickness and dielectric environment. Plasmonics. 2014;**9**:651-657

[3] Atwater HA, Polman A. Plasmonics for improved photovoltaic devices. Nature Mater. 2010;**9**:205-213

[4] Pathak NK, Chander N, Komarala VK, Sharma RP. Plasmonic perovskite solar cells utilizing Au@$SiO_2$ core-shell nanoparticles. Plasmonics. 2017;**12**:237-244

[5] Runsheng W, Bingchu Y, Chujun Z, Yulan H, Yanxia C, Peng L, et al. Prominent efficiency enhancement in perovskite solar cells employing silica-coated gold nanorods. Journal of Physical Chemistry C. 2016;**120**:6996-7004

[6] Pandey GK, Pathak NK, Uma R, Sharma RP. Electromagnetic study of surface enhanced Raman scattering of plasmonicbiomolecule: An interaction between nanodimer and single biomolecule. Solid State Communications. 2017;**255**:47-53

[7] Verma M, Kedia A, Boazbou Newmaia M, Senthil Kumar P. Differential role of PVP on the synthesis of plasmonic gold nanostructures and their catalytic and SERS properties. RSC Advances. 2016;**6**:80342-80353

[8] Prodan E, Radloff C, Halas NJ, Nordlander P. A hybridization model for the plasmon response of complex nanostructures. Science. 2003;**302**:419-422

[9] Noguez C. Surface plasmons on metal nanoparticles: The influence of shape and physical environment. Journal of Physical Chemistry C. 2007;**111**:3806

[10] Zhang Y, Zhen YR, Neumann O, Day JK, Nordlander P, Halas NJ. Coherent anti-stokes raman scattering with single-molecule sensitivity using a plasmonic fano resonance. Nature Communications. 2014;**5**:4424

[11] Pathak NK, Sharma RP. Study of broadband tunable properties of surface plasmon resonances of noble metal nanoparticles using mie scattering theory: Plasmonic perovskite interaction. Plasmonics. 2016;**11**:713-719

[12] Wustholz KL, Brosseau CL, Casadio F, Van Duyne RP. Surface-enhanced Raman spectroscopy of dyes: from single molecules to the artists' canvas. Physical Chemistry Chemical Physics. 2009;**11**:7350

[13] Maier S. Plasmonics: Fundamentals and Applications. Berlin: Springer; 2007

[14] Hagfeldt A, Boschloo G, Sun L, Kloo L, Pettersson H. Dye-sensitized solar cells. Chemical Reviews. 2010;**110**:6595-6663

[15] Pathak NK, Ji A, Sharma RP. Study of efficiency enhancement in layered geometry of excitonic-plasmonic solar cell. Applied Physics A: Materials Science & Processing. 2014; **115**:1445-1450

[16] Kreibig U, Vollmer M. Optical Properties of Metal Clusters. Berlin: Springer; 1995

[17] Palik ED. Handbook of Optical Constants of Solids. Orlando: Academic; 1985

[18] Pandey GK, Pathak NK, Ji A, Pathak H, Sharma RP. Plasmonics. 2016;**11**:1343

[19] Wang H, Wang X, Yan C, Zhao H, Zhang J, Santschi C, et al. Full color generation using silver tandem nanodisks. ACS Nano. 2017;**11**:4419-4427

[20] Chandrasekhar PS, Chander N, Anjaneyulu O, Komaral VK. Plasmonic effect of Ag@ $TiO_2$ core–shell nanocubes on dye-sensitized solar cell performance based on reduced grapheme oxide–$TiO_2$ nanotube composite. Thin Solid Films. 2015;**594**:45-55

[21] Thyagarajan K, Ch S, Langlet P, OJF M. Highly improved fabrication of Ag and Al nanostructures for UV and nonlinear plasmonics. Advanced Optical Materials. 2016;**4**:871-876

[22] Dong L, Yang X, Zhang C, Cerjan B, Zhou L, Tseng ML, et al. Nanogapped Au antennas for ultrasensitive surface-enhanced infrared absorption spectroscopy. Nano Letters. 2017;**17**:5768-5774

[23] Ji A, Sharma R, Pathak H, Pathak NK, Sharma RP. Numerical simulation of plasmonic light trapping in thin-film Si solar cells: Surface coverage effect. Journal of Physics D: Applied Physics. 2015;**48**:275101-275107

[24] Bellido EP, Zhang Y, Manjavacas A, Nordlander P, Botton GA. Plasmonic coupling of multipolar edge modes and the formation of gap modes. ACS Photonics. 2017;**4**:1558-1565

[25] Zhang D, Martin OJF. A universal law for plasmon resonance shift in biosensing. ACS Photonics. 2015;**2**:144-150

[26] Ye T, Ma S, Xi J, Wei L, Vijila C. Seeram Ramakrishna performance enhancement of tri-cation and dual-anion mixed perovskite solar cells by Au@$SiO_2$ nanoparticles. Advanced Functional Materials. 2017;**27**(13):1606545

[27] Robatjazi H, Zhao H, Swearer DF, Hogan NJ, Zhou L, Alabastri A, et al. Plasmon-induced selective carbon dioxide conversion on earth-abundant aluminum-cuprous oxide antenna-reactor nanoparticles. Nature Communications. 2017;**8**:27

[28] Butet J, OJF M. Surface-enhanced hyper-Raman scattering: A new road to the observation of low energy molecular vibrations. Physical Chemistry C. 2015;**119**:15547-15556

[29] Mali SS, Chang SS, Hyungjin K, Pramod SP, Chang KH. In situ processed gold nanoparticle-embedded $TiO_2$ nanofibers enabling plasmonic perovskite solar cells to exceed 14% conversion efficiency. Nanoscale. 2016;**8**:2664-2677

[30] Parashar PK, Sharma RP, Komarala VK. Double-layer antireflection from silver nanoparticle integrated $SiO_2$ layer on silicon wafer: Effect of nanoparticle morphology and $SiO_2$ film thickness. Journal of Physics D: Applied Physics. 2017;**50**:035105

[31] Rundong F, Ligang W, Yihua C, Guanhaojie Z, Li L, Lia Z, et al. Tailored Au@$TiO_2$ nanostructures for the plasmonic effect in planar perovskite solar cells. Journal of Materials Chemistry A. 2017;**5**:12034-12042

[32] Bohren CF, Huffman DR. Absorption and Scattering of Light by Small Particles. New York: Willey; 1983

[33] Draine BT, Flatau PJ. Discrete-dipole approximation for periodic targets: Theory and tests. Journal of the Optical Society of America. 2008;**25**:2693-2703

Chapter 3

# Localized and Propagated Surface Plasmons in Metal Nanoparticles and Nanowires

Xianguang Yang and Baojun Li

Additional information is available at the end of the chapter

http://dx.doi.org/10.5772/intechopen.78284

## Abstract

Surface plasmons are coherent electron oscillations behaving as localized and propagated modes in metal nanoparticles and nanowires, respectively. In this chapter, we first review some of the applications made in plasmonics with gold nanorods/nanospheres and silver nanowires. For gold nanoparticles with a size of 1–100 nm, the surface plasmons are confined around the particle surface as localized modes to enhance the near-field. For diameter of around 200–300 nm silver nanowires with a length up to 10 μm, the surface plasmons can propagate along the nanowires as waveguide modes to guide the plasmons. We then describe some novel results with regarding to gold nanorod enhanced light emission, silver nanowire supported plasmonic waveguide, gold nanosphere mediated whispering-gallery-mode emission, and energy conversion in silver-polymer plasmonic nanostructures. The work of this chapter highlights the applications of metal nanoparticles and nanowires in plasmonic waveguides to achieve optical energy generation, propagation, and conversion.

**Keywords:** surface plasmon waveguides, metal nanoparticles, nanowires, nanostructures, absorption

## 1. Introduction

Plasmonics has the fascinating ability to localize and guide light wave at the deep subwavelength scale, becomes an inter-discipline merging photonics with electronics [1–6]. Surface plasmons are free electron oscillations induced by optical methods at the metal surfaces. Both localized and propagated surface plasmons excited in metal nanoparticles and nanowires are of great interest. They not only break the diffraction limit but also allow

IntechOpen

© 2018 The Author(s). Licensee IntechOpen. This chapter is distributed under the terms of the Creative Commons Attribution License (http://creativecommons.org/licenses/by/3.0), which permits unrestricted use, distribution, and reproduction in any medium, provided the original work is properly cited.

to guide light in various geometries such as 90° bending [1]. This promises the scaling of optical devices down to the diffraction limit for miniaturized photonic circuits. The localized surface plasmons have the functionality to scatter, absorb and squeeze light into nanometer scale, providing large enhancements of local near-fields [7]. It holds the potential applications in data storage, light energy generation, sub-wavelength optics, nano-optical tweezers, biophotonics and nanoscopy [8–11]. Gold nanoparticles with sphere/rod shapes and size below 100 nm are highly investigated for many useful applications, such as non/radiative enhancement of nano-crystals [12], inter-particle coupling effect [13], single particle plasmon spectroscopy [14–16], plasmonic sensing [17–19], plasmonic photocatalysis [20–22], and so on. Different from the localized surface plasmons of individual nanoparticles, the propagated surface plasmons existing at flat/curved surfaces in metallic planes, films, and wires also exhibit intriguing plasmonic phenomena [23]. The propagation length of surface plasmon modes is inevitably limited by metallic absorption, could also be strongly confined in the lateral section normal to propagation direction. This implies that plasmonic waveguides could transport larger bandwidth of information than that of conventional photonic waveguides. However, there is a trade-off between propagation loss and mode confinement in plasmonic waveguides [24]. To balance this trade off, an alternative method by seamlessly integrating photonic waveguides into plasmonic waveguides can be used [25]. Silver nanowires usually act as plasmonic waveguides with lateral size of 200−300 nm and axial length up to 10 μm, exhibiting many interesting applications. For example, plasmonic interference [26], wave-particle duality [27], remote excitation of Raman scattering [28–30], long-distance plasmonic gain [31–33], broadside nano-antennas [34], etc. It is impossible to introduce every result on plasmonics in this short chapter. In the following sections, we will specifically describe some novel results with gold nanorods/nanospheres and silver nanowires for achieving optical energy generation, propagation, and conversion.

## 2. Localized surface plasmon in gold nanorods

Metal-enhanced fluorescence can be realized via the resonant coupling with localized surface plasmon in metallic nanoparticles, nanorods, and nanostructures [35–40]. Different form two-dimensional films and/or three-dimensional solutions, metal-enhanced fluorescence in one-dimensional waveguides could provide a lower power consumption and higher density integration for plasmonic circuits. Herein, we describe a novel result of gold nanorod enhanced light emission, which is realized by embedding gold nanorods into polymer photonic waveguide doped with quantum dots at low concentration.

To study plasmonic properties, a single plasmonic waveguide was placed on $MgF_2$ substrate with refractive index ($n$) of 1.39. A blue light at 473-nm wavelength was coupled into the plasmonic waveguide via evanescent field. **Figure 1a** shows the dark-field optical microscope image with red emission excited by the incident light at an optical power ($P_{in}$) of 0.1 μW, where positions A to E manifesting gold nanorod enhanced light emission from embedded quantum dots for representative measurements. To make a comparison, a single photonic waveguide has a similar diameter as that of the plasmonic waveguide, was also excited by the incident light at an optical power ($P_{in}$) of 0.1 μW (**Figure 1b**).

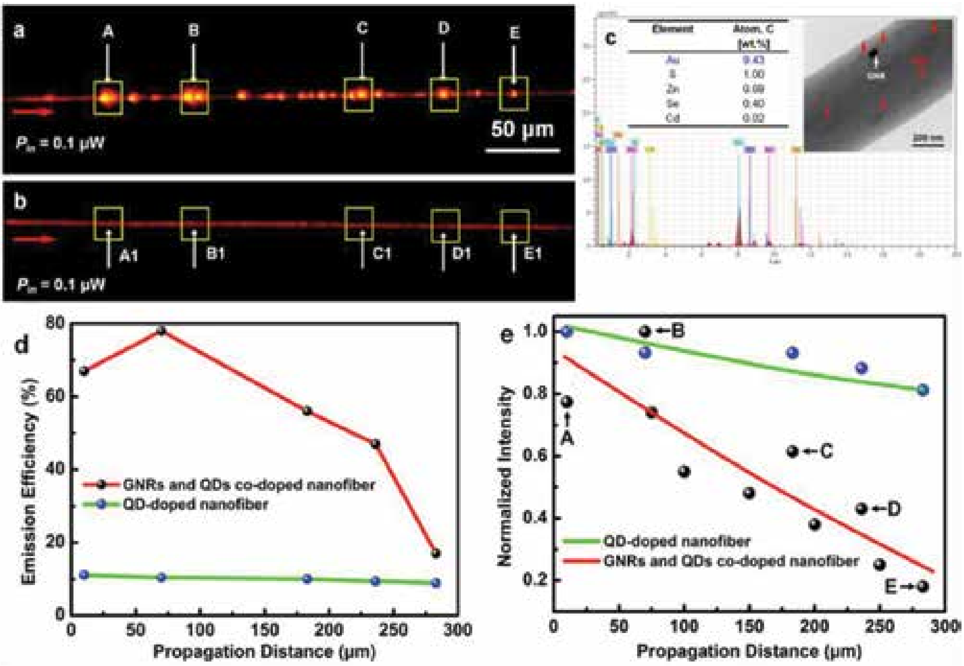

**Figure 1.** Plasmonic waveguides in polymer embedded with gold nanorods. Dark-field optical microscope images are corresponding to (a) plasmonic waveguide with gold nanorods and (b) photonic waveguide without gold nanorods. (c) TEM and EDS analysis of a plasmonic waveguide. (d) The relationship between emission efficiency and propagation distance. (e) Dependence of normalized intensity on the propagation distance. Red curve is for plasmonic waveguide, while blue curve is for photonic waveguide. GNRs mean gold nanorods, and QDs mean quantum dots. Reprinted with permission [41].

To clearly examine the distributions of gold nanorods and quantum dots embedded in the plasmonic waveguide, both a bright-field transmission electron microscope (TEM) and an energy dispersive X-ray spectroscopy (EDS) were simultaneously performed. **Figure 1c** shows EDS spectrum of a plasmonic waveguide while the inset shows the corresponding TEM image. The EDS spectrum verifies the existence of Au (9.43 wt%), Cd (0.02 wt%), Se (0.40 wt%), Zn (0.69 wt%), and S (1.00 wt%) elements. They came from gold nanorods and CdSe-ZnS core-shell quantum dots. The embedded concentrations for gold nanorods and quantum dots are estimated to be of 4 $\mu m^{-3}$ and $3.2 \times 10^3$ $\mu m^{-3}$, respectively.

**Figure 1d** shows the light emission efficiency at positions A to E (with gold nanorods) and positions A1 to E1 (without gold nanorods). At position B, the emission enhancement is maximized, where plasmonic wavelength overlapped with emission wavelength of quantum dots [42]. The mechanism for emission enhancement can be interpreted as follows: (1) by coupling a 473-nm blue light into plasmonic waveguide, the embedded quantum dots are photo-excited and then emit 600-nm red light. (2) The emitted 600-nm red light excites the localized surface plasmon of gold nanorods, which leads to an enhancement of local near-field. (3) The enhanced local near-field increases the stimulated radiative decay rate of quantum dots, thus leading to the increasing of quantum yields and the decreasing of fluorescence lifetime [43].

In fact, emission quenching could happen because free electrons can transfer from quantum dots to gold nanorods once they are closely contacted. For instance, emission quenching of quantum dots by gold nanoparticles has been previously reported [44, 45]. As shown in **Figure 1a**, the locally enhanced inhomogenously distributed emission spots can be explained by the unevenly-increased in the local density of plasmonic sates around gold nanorods. This inhomogeneous can be improved by linking quantum dots and gold nanorods via chemical/biological coupling to ensure their efficient interactions. In any case, the total emission efficiency depends on the quantum yield, self-absorption of quantum dots, resonance properties of localized surface plasmon in gold nanorods, and propagation loss of the plasmonic waveguide.

For the measurements of emission intensity, the dark-field optical microscope images with RGB modes were transformed into gray levels employing software (Adobe Photoshop), and the gray values were summed up to acquire the normalized intensity, this method was previously reported [46]. The yellow rectangular in **Figure 1a** and **b** is taken as the sum-up region with an area of 21 × 18 $\mu m^2$. **Figure 1e** shows the normalized intensity of red emission along the plasmonic waveguide (red line) and photonic waveguide (green line) as a function of propagation distance. It indicates that the existence of gold nanorods seriously affects the propagation distance of plasmonic waveguide, which is due to the larger scattering loss. In addition, some local regions with non-uniform particle density, refractive index, and crystalline would give rise to bulk scattering in the plasmonic waveguide.

## 3. Propagated surface plasmon in silver nanowires

Silver nanowires possess sub-wavelength mode confinement and low propagation loss, but the couple of light into such small nanowires are extremely challengeable. For this challenge, several methods to light coupling have been proposed, including: (1) total internal reflection method utilizing an optical prism to compensate for momentum mismatch between photon and surface plasmon [47]; (2) localized excitation method via focusing laser beam directly on a scattering center of silver nanowires [48, 49]; and (3) near-field coupling method using optical dipole with large momentum components to match that of surface plasmon, where quantum emitters usually located in the near-field of silver nanowire [50, 51]. However, above three coupling methods cannot easily interconnect silver nanowires with photonic waveguides for nanophotonic circuits. Herein, we describe a novel result of silver nanowire supported plasmonic waveguide by coupling photons from quantum-dot-doped nanowire.

A scanning electron microscope (SEM) micrograph of one silver nanowire with a diameter of 300 nm was interconnected with a quantum-dot-doped nanowire with a diameter of 800 nm at an angle of 60° is presented in **Figure 2a**. To inspect this crossing angle in better detail, an enlarged view is given in **Figure 2b**. For more practical device applications, the interconnection of more than one silver nanowire with a same quantum-dot-doped polymer nanowire is extremely desirable. For example, **Figure 2c** presents an SEM micrograph of silver nanowires 1 and 2 with the same diameters of 300 nm were interconnected with a quantum-dot-doped nanowire (800-nm in diameter) at angles of 60 and 65°, respectively. The mutual distance between silver nanowires 1 and 2 is about 6.4 μm. To realize hybrid interconnection with high-density of plasmonic and photonic nanowires, more than three silver plasmonic nanowires

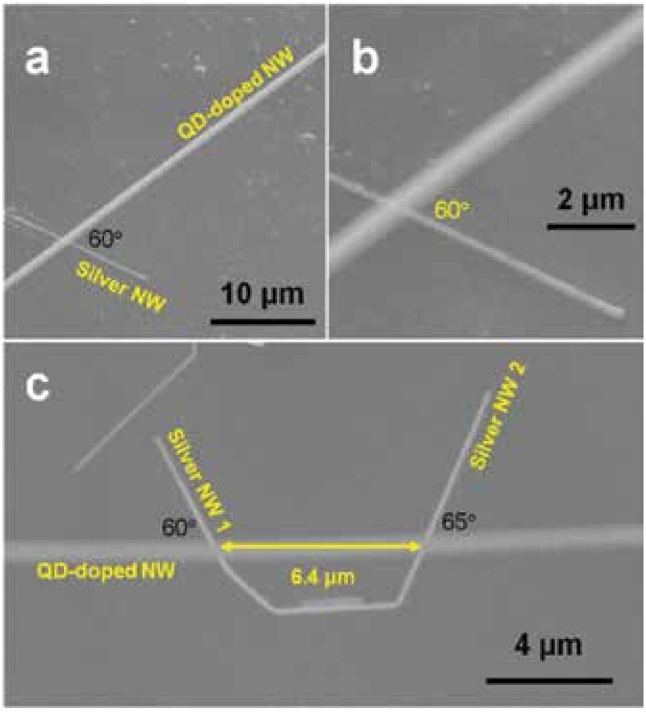

**Figure 2.** SEM characterization of silver nanowires. (a) One silver nanowire was interconnected with a quantum-dot-doped nanowire at an angle of 60°. (b) Enlarged view of the crossing angle in (a). (c) Silver nanowires 1 and 2 were interconnected with the same quantum-dot-doped nanowire at crossing angles of 60 and 65°, respectively. Note: NW means nanowire, and QD means quantum dot. Reprinted with permission [54].

with distinct lengths and diameters would be interconnected with the same quantum-dot-doped photonic nanowire at distinct angles and intervals, which could provide versatile multi-functionalities in nanoscale circuits [52, 53].

Optical characterization of the silver nanowires was performed under an optical microscopy using a micro-spectrophotometer (CRAIC, 20/20 PV, USA). **Figure 3a** shows a reflection-type optical microscope image of silver nanowires 1 and 2 with the same diameters of 300 nm was interconnected with an 800-nm diameter quantum-dot-doped nanowire at angles of 57 and 80°, respectively. The lengths of silver nanowires 1 and 2 are about 5 and 4 μm, respectively, and the mutual distance between them is of 10 μm. **Figure 3b** gives a scattering-type micrograph under dark-field for the crossing structure in **Figure 3a** illuminated by a beam of 532-nm laser at an optical power of 10 mW. The scattering position J0 comes from individual defects in the quantum-dot-doped nanowire. The larger scattering positions J1 and J2 come from the photonic-plasmonic junctions formed with the silver and quantum-dot-doped nanowires [55]. In the photonic-plasmonic junctions, when the surface plasmon of silver nanowires were launched by photoluminescence from quantum-dot-doped nanowire. Among the launched plasmonic modes, the dominant mode is longitudinal mode and the produced resonance could have Fabry-Perot characteristics [56]. The smaller scattering positions S1 and S2 come from the end tips of the silver nanowires, where the propagated surface plasmons were converted into free space photons.

The two silver nanowires with same diameters of 300 nm can strongly confine the 580-nm photoluminescence into sub-wavelength scale dimensions, giving rise to their relatively compact interconnection with the quantum-dot-doped nanowire. For briefness, the photoluminescence spectra collected at positions J0, J1, J2, S1, and S2 were plotted in a single graph as **Figure 3c**. The peak wavelengths for positions J0, J1, J2, S1, and S2 are 580, 585, 590, 595, and 605 nm, respectively. The inset image of **Figure 3c** shows surface plasmon propagation in the silver nanowires and emitted photon propagation in the quantum-dot-doped polymer nanowire. The quantum-dot-doped nanowire produced distinct colors of yellow, yellow-orange, and orange from positions J0, J1, and J2, respectively. This phenomenon is called "wavelength-converted waveguiding", which also previously observed in dye-doped polymer nanofiber [57]. The color difference between yellow-orange (J1) and red-orange (S1) in silver nanowire 1 comes from the metallic loss induced energy dissipation, and the resulted peak wavelength changed from 585 to 595 nm. Similarly, the colors are different between orange (J2) and red (S2) in silver nanowire 2, and the peak wavelength changed from 590 to 605 nm. This is a frequency-dependent dispersion effect in these two silver nanowires [58].

Another novel result is optical routing in single silver nanowires [59]. Semiconductor microribbon and silver nanowires were assembled to realize routing structure, as shown in SEM micrograph of **Figure 4a**. One silver nanowire was sitting on top of a semiconductor $SnO_2$ ribbon, and a second silver nanowire just cling to it with a 12 μm overlapping. The three color arrows show the end tips of the silver nanowires, and the Inset shows the enlarged view of the overlapping region. The surfactants on the silver nanowires have already been cleared so that the two silver nanowires were contact directly. **Figure 4b** and **c** show the intensity mapping and real-color micrograph of the optical routing from semiconductor $SnO_2$ ribbon

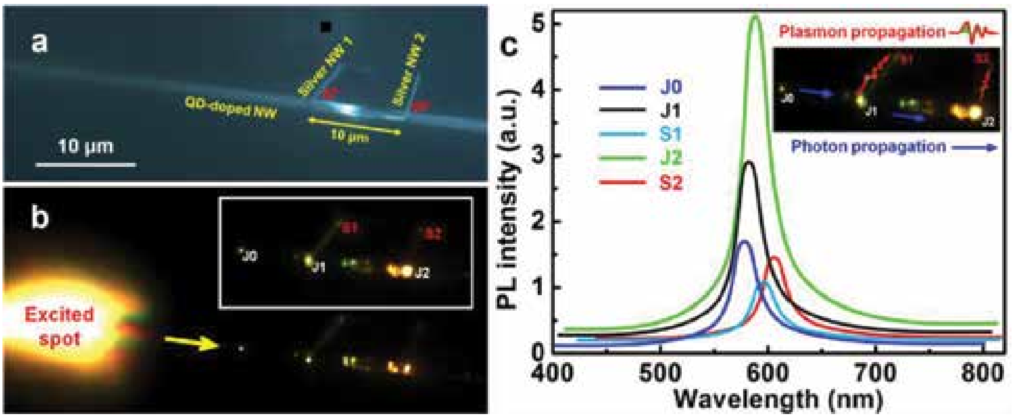

**Figure 3.** Optical characterization of silver nanowires. (a) Reflection-type optical microscope image of silver nanowires 1 and 2 were interconnected with the same quantum-dot-doped nanowire at crossing angles of 57 and 80°, respectively. Note that the black box (area: 1 $\mu m^2$) near silver nanowire 1 is the sampling spot to spectrum measuring. (b) Scattering-type optical microscope image of the crossing structure in (a) was illuminated by a 532-nm excitation laser with a spot diameter of 15 μm at an optical power of 10 mW. The yellow arrow gives the propagation direction of excited 580-nm photoluminescence. Inset was captured by focalizing to the two silver nanowires and measures the photoluminescence spectra on positions J0, J1, J2, S1, and S2. The scale bar in (a) is applicable to (b). (c) Photoluminescence spectra measured at positions J0, J1, J2, S1, and S2. Inset shows the propagation of photons and plasmons. NW means nanowire, and QD means quantum dot. PL means photoluminescence. Reprinted with permission [54].

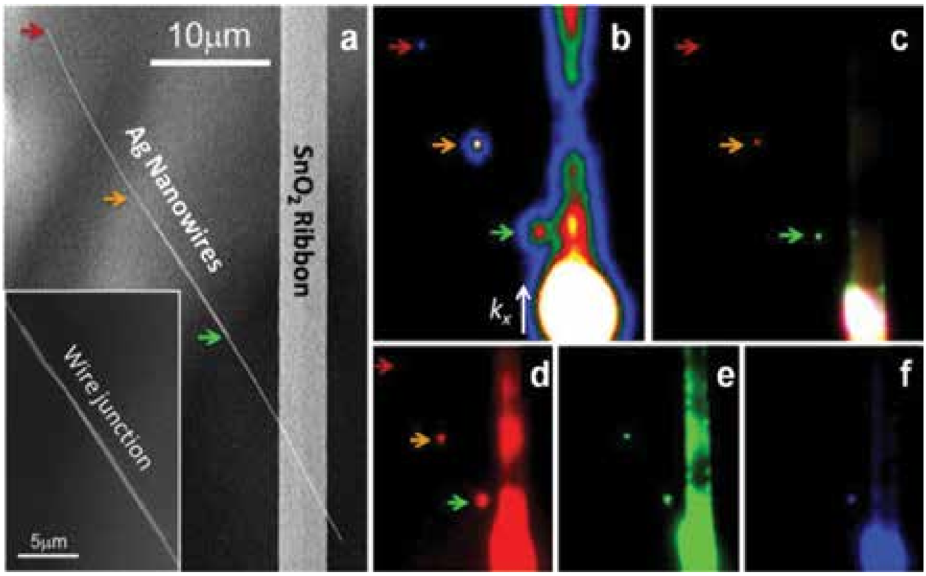

**Figure 4.** Optical routing of silver nanowires. (a) SEM micrograph of two overlapped silver nanowires coupling to a $SnO_2$ ribbon. The length of overlapped region is 12 μm. (inset) overlapped region of the two silver nanowires. (b) Intensity mapping of the routing structure when the photoluminescence of the $SnO_2$ ribbon was launched and coupled into silver nanowires with three different emission spots at distal ends. (c) the real-color micrograph of the same view as in (b). (d–f) individual red (R), green (G), and blue (B) color channels from (c), giving a gradual decrease in propagation loss from short (f) to long (d) wavelengths. The colors are obtained with the Bayer filter from the CoolSnap. Reprinted with permission [59].

photoluminescence. Surface plasmons were launched into the first silver nanowire in the silver-$SnO_2$ overlapped region, and evanescently coupled into the second silver nanowire with low scattering loss in the silver-silver overlapped region. This efficient coupling in the silver-silver region is benefited from the large surface plasmon mode overlaps due to the closely contact between the nanowires. Interestingly, the relationship of the end tip emission color with propagation distance on the case of single silver nanowire was also investigated. **Figure 4d–4f** individually display the red, green, and blue color panel of the real-color micrograph in **Figure 4c**. The closer the propagation distance, the emission composes more short-wavelength components. The blue-wavelength components just exist at the first silver nanowire tip with a propagation distance of 8 μm, while the green-wavelength components survived 20 μm of propagation and the red-wavelength components were the only visible one with propagation distance up to 40 μm.

## 4. Plasmonic nano-cavity in gold nanospheres

Different from dielectric micro-cavities, plasmonic nano-cavities could confine light into the nanometer scale mode volume [60, 61]. Optical investigations based on circular nano-cavities are extremely interesting due to the whispering-gallery-modes, which are attributed to the total internal reflection of light at the plasmonic interface along the equator. Herein, we describe a novel result of whispering-gallery-mode emission in plasmonic nano-cavity, which combines gold nanosphere and quantum dots by using electrostatic attraction. **Figure 5a** shows polarization-dependent photoluminescence intensity of the emitted light. The dependence can be described by a sinusoidal function. The minimum (−90°) and the maximum (10°) photoluminescence intensities are corresponding to perpendicular and parallel to the extinction direction of the gold nanosphere, respectively. The period of 180° is similar to that reported in quantum dots on gold nanodiscs [62].

**Figure 5b** shows the emission spectrum containing five narrow bands, which indicates the characteristic of the whispering-gallery-modes. The maximum peak of whispering-gallery-mode is well coincidence with that of solution photoluminescence. Meanwhile, the optical feedback is strong enough to resist the plasmonic loss. **Figure 5c** shows the photoluminescence spectra of 800 and 550 nm diameter quantum-dot-coated gold nanosphere producing the several narrow bands, while the maximum peaks towards to short wavelength range as diameter increasing. This phenomenon is governed by changing in whispering-gallery-mode

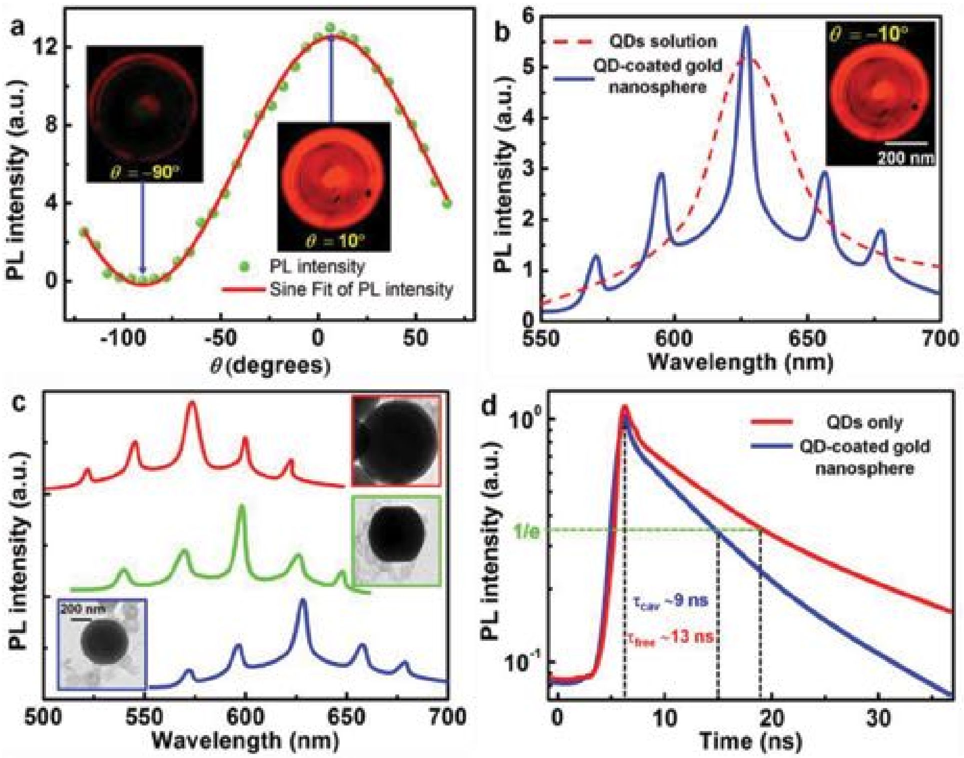

**Figure 5.** Whispering-gallery-mode emission. (a) Photoluminescence intensity as a function of polarization angle. Insets show optical micrographs of quantum-dot-coated gold nanosphere with polarization angles of 90 and 10°. (b) Whispering-gallery-mode emission spectrum from a quantum-dot-coated gold nanosphere (solid blue line) and the quantum dots solution emission spectrum (dashed red line). (c) Whispering-gallery-mode emission spectra of quantum-dot-coated gold nanosphere with diameters of 490 nm (blue), 550 nm (green), and 800 nm (red). Insets: Corresponding TEM micrographs. (d) Photoluminescence decay spectra of quantum-dot-coated gold nanosphere (blue line) and the quantum dots solution (red line) with lifetime at 9 and 13 ns, respectively. Reprinted with permission [63].

states density and the near-field coupling strengths. **Figure 5d** shows the photoluminescence decay spectra of quantum-dot-coated gold nanosphere (blue) and the quantum dots solution (red). They are multiple-exponential process, including intrinsic decay, plasmonic quenching, and plasmonic enhancement. The lifetimes were calculated from 1/*e* values to be of 9 and 13 ns, respectively. The decrease in lifetime verifies the near-field coupling between the localized surface plasmon of gold nanosphere and the radiative decay of quantum dots. As the light waves were confined along the equator of gold nanosphere by localized surface plasmon, the propagation medium of the light waves are the coated layers with quantum dots.

Molecular emitters located in a plasmonic nano-cavity experience an intriguing process to be coupled into the surrounding optical field [64]. Cucurbit(7)uril is hydro-soluble and can encapsulate only one molecule of methylene-blue inside it. Encapsulation of methylene-blue inside cucurbit(7)uril is verified by absorption spectroscopy analysis (**Figure 6a**): methylene-blue dimmers (with characteristic 'shoulder' of small peak at 625 nm on the red solid curve) disappear when mixing low concentrations of methylene-blue into cucurbit(7)uril (**Figure 6a**, blue solid curve). Contrast experiments use the smaller molecule of cucurbit(5)uril also have this shoulder peak (red dashed curve), eliminating the possibility of parasitic binding. Encapsulating single molecules of methylene-blue into cucurbit(7)uril can be used to avoid molecular aggregation. Carboxide portals at either end of the 0.9-nm in height cucurbit(*n*)uril molecules with rims were binding flatly onto the gold surface (**Figure 6b**). The formed nano-cavity volume can be down to less than 40 nm$^3$. This decorating of molecules via light opens up the venue to manipulate chemical bonds [65].

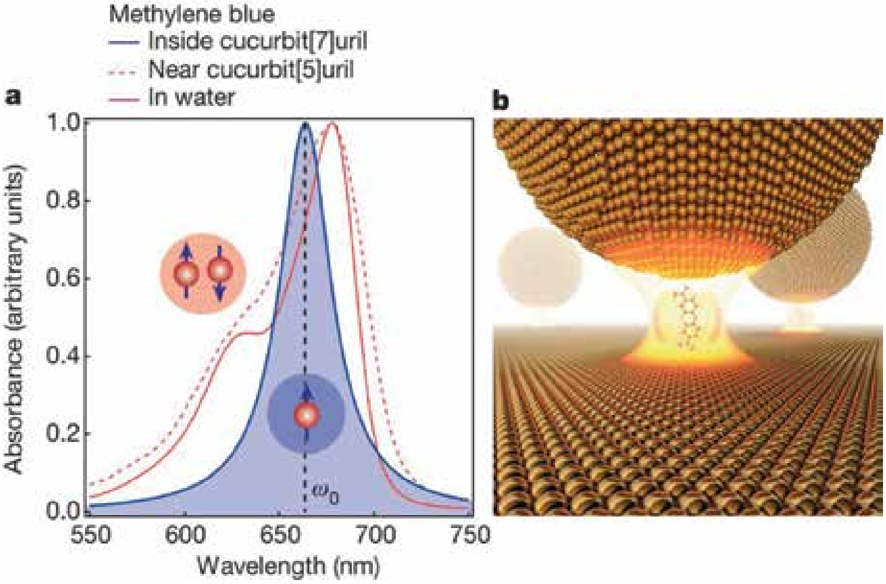

**Figure 6.** Plasmonic nano-cavity with a single dye molecule. (a) Absorption spectra for methylene-blue in water, with (blue solid line) and without (red solid line) encapsulation in cucurbit(*n*)urils. Blue and red icons show individual molecules (centred at $\omega_0$) and paired molecular dimmers, respectively. (b) Schematic illustration of a methylene-blue molecule in cucurbit(*n*)uril, located within the gold nanosphere-on-mirror geometry configuration. Reprinted with permission [64].

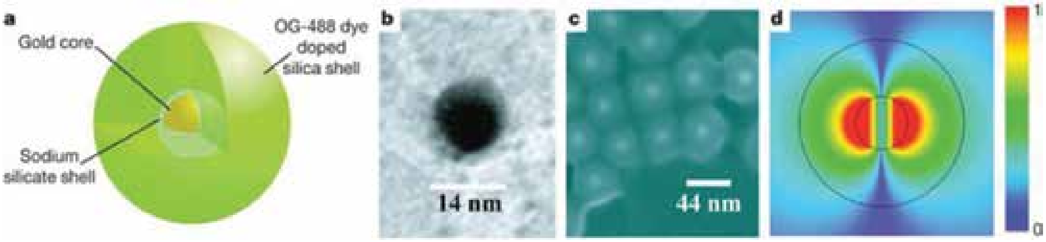

**Figure 7.** Plasmonic nano-cavity design. (a) Schematic of the hybrid nanosphere, indicating silica shell doped with dye molecules. (b) TEM micrograph of gold core. (c) SEM micrograph of gold-silica-dye core-shell nanospheres. (d) Localized surface plasmon laser mode with $\lambda$ of 525 nm and $Q$ factor of 14.8. The outer and inner circles stand for the 44-nm shell and 14-nm core, respectively. Strength color bar is on the right. Reprinted with permission [66].

Another novel result shows that 44-nm in diameter nanospheres with a gold core and dye-doped silica shell can be used to overcome the plasmonic loss with optical gain and realize a stimulated emission of surface plasmons [66]. **Figure 7a** shows a nanosphere with a gold core, supporting for localized surface plasmon modes, and coated by a silica shell doped with organic dye OG-488 (Oregon Green 488), supporting for optical gain. TEM and SEM measurements show the diameter of gold core and the thickness of silica shell are about 14 and 15 nm, respectively (**Figure 7b** and **c**). The molecule number of dye per nanosphere was estimated to be about $2.7 \times 10^3$, and the nanosphere concentration in suspension was about $3 \times 10^{11}$ cm$^{-3}$. The calculation of plasmonic laser mode (**Figure 7d**) obtains the stimulated emission wavelength ($\lambda$) to be of 525 nm and the quality ($Q$)-factor to be of 14.8. Although this $Q$-factor is governed by optical absorption, the produced gain is large enough to overcome the plasmonic loss.

## 5. Plasmonic conversion in silver-polymer nanostructures

Organic polymers with extraordinary properties to incorporate with laser dyes for providing optical gain over broadband visible spectrum, which makes them potential for tunable full-color lasers [67, 68]. Meanwhile, the mechanical flexibility of polymers allows to integrate them with metallic nanostructures, confining light into a small mode volume by surface plasmon [69]. In addition, flexible polymers have an outstanding function to self-assemble into optical micro-cavities with high-quality, where propagated light beam will be continuously confined via total internal reflection. Consequently, the large evanescent field around the air-cavity interface results in efficient conversion between photon and surface plasmon [70]. Herein, we describe a plasmonic conversion to obtain sub-wavelength output of full-color lasers in a silver-polymer heterostructure [71]. **Figure 8a** shows the assemble process of PS and dye molecules via dropping a defined amount of water into the PS-dye blend solution. During the nucleus formation of PS, the powerful π-π interaction makes the dye molecules slowly diffuse into the PS matrix. Once the solvent was evaporated, the silver-polymer microdisks with dyes can be successfully fabricated. Four organic dyes, trans-DPDSB, C153, CNDPASDB, and HMDMAC, with emission colors across the full visible spectrum, were intentionally selected for optical gain media. Under ultraviolet (330–380 nm) excitation, the silver-polymer microdisks emitted homogenous blue (b), cyan (c), green-yellow (d), and red (e) colors, respectively

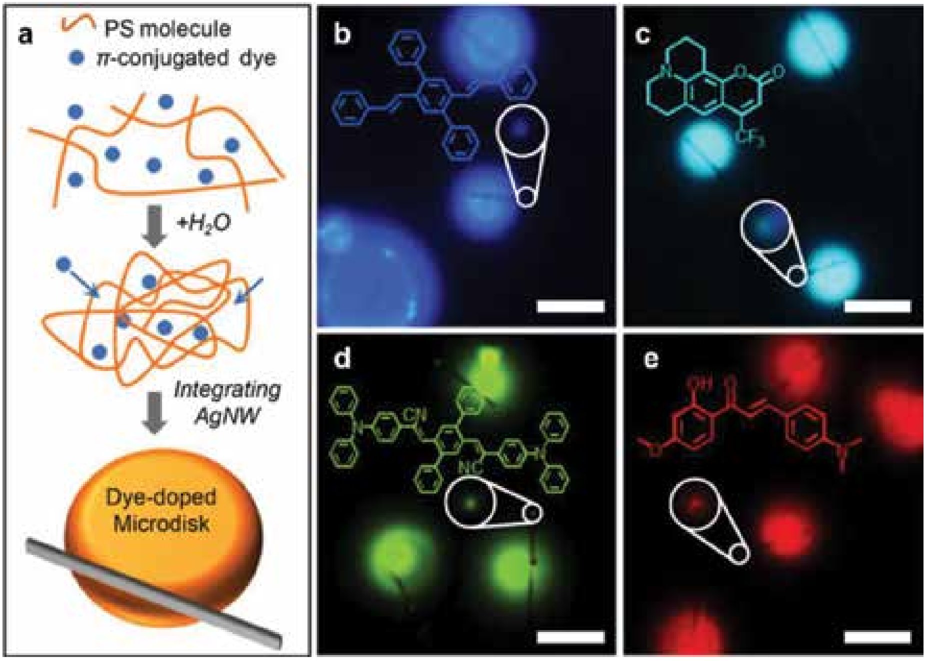

**Figure 8.** Sub-wavelength output of micro-lasers. (a) Diagram of the strategy to dope π-conjugated dye into microdisk for silver-polymer nanostructures. (b–e) Dark-field photoluminescence micrographs of the silver-polymer microdisks doped with organic dyes of (b) trans-DPDSB, (c) C153, (d) CNDPASDB, and (e) HMDMAC, respectively, under ultraviolet excitation. Photoluminescence spots enlarged in the white circles come from surface plasmon scattering in silver nanowire tips. Scale bar, 10 μm. Reprinted with permission [71].

(**Figure 8b–8e**). Importantly, the full colors were outputted with the sub-wavelength silver nanowire at end tips (white circles). This demonstrates the typical feature of surface plasmon waveguide, and the plasmonic conversion at the silver-polymer connections.

Another novel result of energy conversion between photonic nanowire and plasmonic nanowire will be described [72]. The photonic nanowire is CdSe-ZnS core-shell quantum dots doped polymer nanowire, and the silver nanowire served as plasmonic nanowire. The conversion efficiency is about 32%, which is realized by the Förster resonance energy transfer. **Figure 9a** shows SEM micrograph of quantum-dot-doped photonic nanowire were interconnected with silver plasmonic nanowire at a crossed angle of 45°. Once the plasmonic and photonic nanowires are directly contact, the surface plasmon field and evanescent field around photonic nanowire would overlap, leading to efficient conversion from photon to plasmon at the coupling area [73]. **Figure 9b** gives the dark-field optical micrograph of the silver-polymer crossed structure with red emission. The silver nanowire is about 55 μm in total length, and the lengths of the long (white arrow) and short (yellow arrow) regions on the two side of the photonic nanowire (refer as 'limbs') are 40 and 10 μm, respectively. The plasmonic conversion can be understood by the energy transition: photon-exciton-plasmon, and not need to match momentum, because the dipolar near-field of quantum dots has momentum components matching that of surface plasmon. Hence, the crossed angle cannot influence the plasmonic conversion efficiency [74]. The exponential decay curves of **Figure 9c** and **d** indicate surface

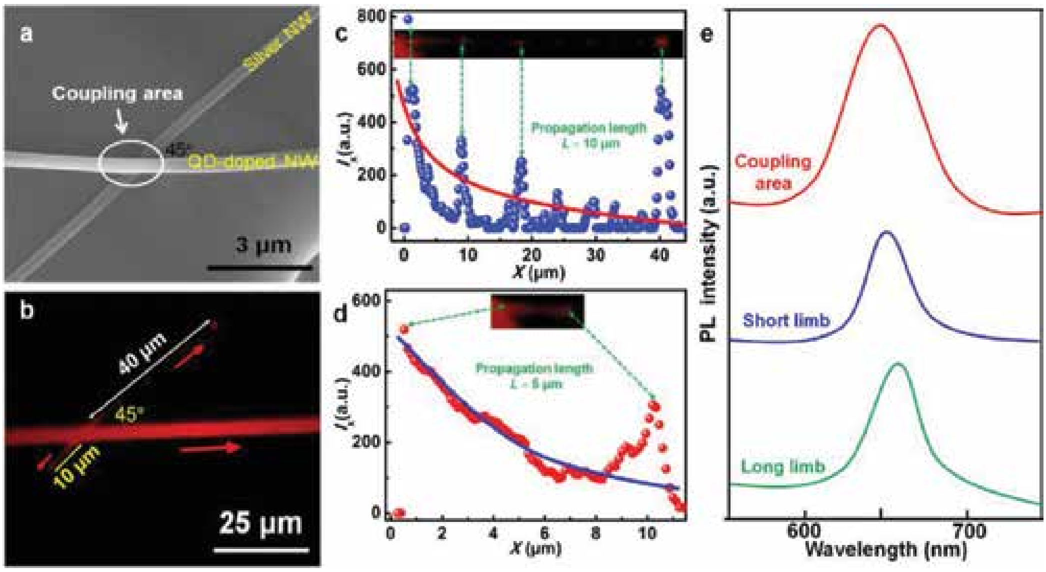

**Figure 9.** Energy conversion from photonic to plasmonic nanowires. (a) SEM micrograph of a 300-nm-diameter silver nanowire and a 400-nm-diameter quantum-dot-doped nanowire interconnected at a crossed angle of 45°. (b) Dark-field optical micrograph of the crossed silver-polymer structure excited by a 532-nm-wavelength laser at an optical power of 5 mW. (c, d) intensities of red emission along the long (c) and short (d) limbs of the silver plasmonic nanowire. Solid lines are plotted with an exponential decay. Insets and green dashed arrows give a visual guide. (e) Emission spectra collected at coupling area, two distal ends at long and short limbs. Reprinted with permission [72].

plasmon propagation lengths of 10 and 5 μm for long and short limbs, respectively. In addition, **Figure 9e** gives the emission spectra collected at coupling area, two distal ends of long and short limbs with wavelength centered at 650, 660, and 654 nm, respectively.

## 6. Conclusion

In this chapter, we have briefly introduced some important applications with localized and propagated surface plasmons in gold nanospheres/nanorods and silver nanowires. Specifically, we have described some novel results on gold nanorods enhanced light emission, surface plasmon propagation in silver nanowires, gold nanosphere as a plasmonic nano-cavity, energy conversion in silver-polymer nanostructures. Due to the limited space, many important progress in quantum plasmonics, nonlinear plasmonics, and photovoltaic plasmonics cannot be described altogether. The work in this chapter presents the applications of gold/silver nanoparticles/nanowires in nanophotonics to realize light generation, propagation, manipulation and conversion. It is an ultimate dream for plasmonics to combine photonics and electronics on practical devices and circuits. This huge challenge continued to motivate the research interests all around the world.

## Acknowledgements

We thank the supports provided by National Natural Science Foundation of China (Grant 21703083), the Natural Science Foundation of Guangdong Province (Grants 2017A030313026 and 2017A030310463), the Science Research Project of Guangzhou (Grant 201804010468) and the Fundamental Research Funds for the Central Universities (Grant 21617334).

## Conflict of interest

The authors declare no conflict of interest.

## Author details

Xianguang Yang and Baojun Li*

*Address all correspondence to: baojunli@jnu.edu.cn

Institute of Nanophotonics, Jinan University, Guangzhou, China

## References

[1] Maier SA, Brongersma ML, Kik PG, Meltzer S, Requicha AA, Atwater HA. Plasmonics—A route to nanoscale optical devices. Advanced Materials. 2001;**13**(19):1501-1505

[2] Polman A. Plasmonics applied. Science. 2008;**322**(5903):868-869

[3] Brongersma ML, Shalaev VM. The case for plasmonics. Science. 2010;**328**(5977):440-441

[4] Kauranen M, Zayats AV. Nonlinear plasmonics. Nature Photonics. 2012;**6**:737-748

[5] Marinica DC, Zapata M, Nordlander P, Kazansky AK, Echenique PM, Aizpurua J, Borisov AG. Active quantum plasmonics. Science Advances. 2015;**1**(11):e1501095

[6] Naldoni A, Shalaev VM, Brongersma ML. Applying plasmonics to a sustainable future. Science. 2017;**356**(6341):908-909

[7] Durach M, Rusina A, Stockman MI, Nelson K. Toward full spatiotemporal control on the nanoscale. Nano Letters. 2007;**7**(10):3145-3149

[8] Anker JN, Hall WP, Lyandres O, Shah NC, Zhao J, Van Duyne RP. Biosensing with plasmonic nanosensors. Nature Materials. 2008;**7**(6):442-453

[9] Schuller JA, Barnard ES, Cai W, Jun YC, White JS, Brongersma ML. Plasmonics for extreme light concentration and manipulation. Nature Materials. 2010;**9**(3):193-204

[10] Nicoletti O, de La Peña F, Leary RK, Holland DJ, Ducati C, Midgley PA. Three-dimensional imaging of localized surface plasmon resonances of metal nanoparticles. Nature. 2013; **502**(7469):80-84

[11] Juan ML, Righini M, Quidant R. Plasmon nano-optical tweezers. Nature Photonics. 2011; **5**(6):349-356

[12] Eustis S, El-Sayed MA. Why gold nanoparticles are more precious than pretty gold: Noble metal surface plasmon resonance and its enhancement of the radiative and nonradiative properties of nanocrystals of different shapes. Chemical Society Reviews. 2006;**35**(3):209-217

[13] Ghosh SK, Pal T. Interparticle coupling effect on the surface plasmon resonance of gold nanoparticles: From theory to applications. Chemical Reviews. 2007;**107**(11):4797-4862

[14] Tokareva I, Minko S, Fendler JH, Hutter E. Nanosensors based on responsive polymer brushes and gold nanoparticle enhanced transmission surface plasmon resonance spectroscopy. Journal of the American Chemical Society. 2004;**126**(49):15950-15951

[15] Novo C, Funston AM, Mulvaney P. Direct observation of chemical reactions on single gold nanocrystals using surface plasmon spectroscopy. Nature Nanotechnology. 2008; **3**(10):598-602

[16] Zijlstra P, Paulo PM, Orrit M. Optical detection of single non-absorbing molecules using the surface plasmon resonance of a gold nanorod. Nature Nanotechnology. 2012;**7**(6): 379-382

[17] Homola J. Surface plasmon resonance sensors for detection of chemical and biological species. Chemical Reviews. 2008;**108**(2):462-493

[18] Mayer KM, Hafner JH. Localized surface plasmon resonance sensors. Chemical Reviews. 2011;**111**(6):3828-3857

[19] Zeng S, Baillargeat D, Ho H-P, Yong K-T. Nanomaterials enhanced surface plasmon resonance for biological and chemical sensing applications. Chemical Society Reviews. 2014;**43**(10):3426-3452

[20] Murdoch M, Waterhouse G, Nadeem M, Metson J, Keane M, Howe R, Llorca J, Idriss H. The effect of gold loading and particle size on photocatalytic hydrogen production from ethanol over Au/$TiO_2$ nanoparticles. Nature Chemistry. 2011;**3**(6):489-492

[21] Hou W, Cronin SB. A review of surface plasmon resonance-enhanced photocatalysis. Advanced Functional Materials. 2013;**23**(13):1612-1619

[22] Lou Z, Kim S, Fujitsuka M, Yang X, Li B, Majima T. Anisotropic $Ag_2S$–Au triangular nanoprisms with desired configuration for plasmonic photocatalytic hydrogen generation in visible/near-infrared region. Advanced Functional Materials. 2018;**28**(13):1706969

[23] Han Z, Bozhevolnyi SI. Radiation guiding with surface plasmon polaritons. Reports on Progress in Physics. 2012;**76**(1):016402

[24] Gramotnev DK, Bozhevolnyi SI. Plasmonics beyond the diffraction limit. Nature Photonics. 2010;**4**(2):83-91

[25] Briggs RM, Grandidier J, Burgos SP, Feigenbaum E, Atwater HA. Efficient coupling between dielectric-loaded plasmonic and silicon photonic waveguides. Nano Letters. 2010;**10**(12):4851-4857

[26] Allione M, Temnov VV, Fedutik Y, Woggon U, Artemyev MV. Surface plasmon mediated interference phenomena in low-Q silver nanowire cavities. Nano Letters. 2008;**8**(1):31-35

[27] Kolesov R, Grotz B, Balasubramanian G, Stöhr RJ, Nicolet AA, Hemmer PR, Jelezko F, Wrachtrup J. Wave–particle duality of single surface plasmon polaritons. Nature Physics. 2009;**5**(7):470-474

[28] Fang Y, Wei H, Hao F, Nordlander P, Xu H. Remote-excitation surface-enhanced Raman scattering using propagating Ag nanowire plasmons. Nano Letters. 2009;**9**(5):2049-2053

[29] Sun M, Zhang Z, Wang P, Li Q, Ma F, Xu H. Remotely excited Raman optical activity using chiral plasmon propagation in Ag nanowires. Light: Science & Applications. 2013;**2**(11): e112

[30] Huang Y, Fang Y, Zhang Z, Zhu L, Sun M. Nanowire-supported plasmonic waveguide for remote excitation of surface-enhanced Raman scattering. Light: Science & Applications. 2014;**3**(8):e199

[31] Paul A, Zhen Y-R, Wang Y, Chang W-S, Xia Y, Nordlander P, Link S. Dye-assisted gain of strongly confined surface plasmon polaritons in silver nanowires. Nano Letters. 2014;**14**(6):3628-3633

[32] Evans CI, Zolotavin P, Alabastri A, Yang J, Nordlander P, Natelson D. Quantifying remote heating from propagating surface plasmon polaritons. Nano Letters. 2017;**17**(9):5646-5652

[33] Zhang D, Xiang Y, Chen J, Cheng J, Zhu L, Wang R, Zou G, Wang P, Ming H, Rosenfeld M, Badugu R, Lakowicz JR. Extending the propagation distance of a silver nanowire plasmonic waveguide with a dielectric multilayer substrate. Nano Letters. 2018;**18**(2):1152-1158

[34] Zhuo X, Yip HK, Ruan Q, Zhang T, Zhu X, Wang J, Lin H-Q, Xu J-B, Yang Z. Broadside nanoantennas made of single silver nanorods. ACS Nano. 2018;**12**(2):1720-1731

[35] Shimizu K, Woo W, Fisher B, Eisler H, Bawendi MG. Surface-enhanced emission from single semiconductor nanocrystals. Physical Review Letters. 2002;**89**(11):117401

[36] Pompa P, Martiradonna L, Della Torre A, Della Sala F, Manna L, De Vittorio M, Calabi F, Cingolani R, Rinaldi R. Metal-enhanced fluorescence of colloidal nanocrystals with nanoscale control. Nature Nanotechnology. 2006;**1**(2):126

[37] Hong G, Tabakman SM, Welsher K, Wang H, Wang X, Dai H. Metal-enhanced fluorescence of carbon nanotubes. Journal of the American Chemical Society. 2010;**132**(45):15920-15923

[38] Geddes CD. Metal-enhanced fluorescence. Physical Chemistry Chemical Physics. 2013; **15**(45):19537-19537

[39] Sorokin AV, Zabolotskii AA, Pereverzev NV, Bespalova II, Yefimova SL, Malyukin YV, Plekhanov AI. Metal-enhanced fluorescence of pseudoisocyanine J-aggregates formed

in layer-by-layer assembled films. The Journal of Physical Chemistry C. 2015;**119**(5): 2743-2751

[40] Kim JK, Jang D-J. Metal-enhanced fluorescence of gold nanoclusters adsorbed onto Ag@ $SiO_2$ core-shell nanoparticles. Journal of Materials Chemistry C. 2017;**5**(24):6037-6046

[41] Yang X, Xu R, Bao D, Li B. Gold nanorod-enhanced light emission in quantum-dot-doped polymer nanofibers. ACS Applied Materials & Interfaces. 2014;**6**(15):11846-11850

[42] Bardhan R, Grady NK, Cole JR, Joshi A, Halas NJ. Fluorescence enhancement by Au nanostructures: Nanoshells and nanorods. ACS Nano. 2009;**3**(3):744-752

[43] Cohen-Hoshen E, Bryant GW, Pinkas I, Sperling J, Bar-Joseph I. Exciton-plasmon interactions in quantum dot-gold nanoparticle structures. Nano Letters. 2012;**12**(8):4260-4264

[44] Gueroui Z, Libchaber A. Single-molecule measurements of gold-quenched quantum dots. Physical Review Letters. 2004;**93**(16):166108

[45] Pons T, Medintz IL, Sapsford KE, Higashiya S, Grimes AF, English DS, Mattoussi H. On the quenching of semiconductor quantum dot photoluminescence by proximal gold nanoparticles. Nano Letters. 2007;**7**(10):3157-3164

[46] Pyayt AL, Wiley B, Xia Y, Chen A, Dalton L. Integration of photonic and silver nanowire plasmonic waveguides. Nature Nanotechnology. 2008;**3**(11):660-665

[47] Ditlbacher H, Hohenau A, Wagner D, Kreibig U, Rogers M, Hofer F, Aussenegg FR, Krenn JR. Silver nanowires as surface plasmon resonators. Physical Review Letters. 2005;**95**(25):257403

[48] Sanders AW, Routenberg DA, Wiley BJ, Xia Y, Dufresne ER, Reed MA. Observation of plasmon propagation, redirection, and fan-out in silver nanowires. Nano Letters. 2006; **6**(8):1822-1826

[49] Knight MW, Grady NK, Bardhan R, Hao F, Nordlander P, Halas NJ. Nanoparticle-mediated coupling of light into a nanowire. Nano Letters. 2007;**7**(8):2346-2350

[50] Akimov AV, Mukherjee A, Yu CL, Chang DE, Zibrov AS, Hemmer PR, Park H, Lukin MD. Generation of single optical plasmons in metallic nanowires coupled to quantum dots. Nature. 2007;**450**:402

[51] Fedutik Y, Temnov V, Woggon U, Ustinovich E, Artemyev M. Exciton-plasmon interaction in a composite metal-insulator-semiconductor nanowire system. Journal of the American Chemical Society. 2007;**129**(48):14939-14945

[52] Huang Y, Duan X, Wei Q, Lieber CM. Directed assembly of one-dimensional nanostructures into functional networks. Science. 2001;**291**(5504):630-633

[53] Yan R, Gargas D, Yang P. Nanowire photonics. Nature Photonics. 2009;**3**(10):569-576

[54] Yang X, Bao D, Li B. Light transfer from quantum-dot-doped polymer nanowires to silver nanowires. RSC Advances. 2015;**5**(75):60770-60774

[55] Lee S-Y, Park J, Kang M, Lee B. Highly efficient plasmonic interconnector based on the asymmetric junction between metal-dielectric-metal and dielectric slab waveguides. Optics Express. 2011;**19**(10):9562-9574

[56] Shegai T, Miljkovic VD, Bao K, Xu H, Nordlander P, Johansson P, Käll M. Unidirectional broadband light emission from supported plasmonic nanowires. Nano Letters. 2011;**11**(2):706-711

[57] Yu H, Li B. Wavelength-converted wave-guiding in dye-doped polymer nanofibers. Scientific Reports. 2013;**3**:1674

[58] Dionne J, Sweatlock L, Atwater H, Polman A. Planar metal plasmon waveguides: Frequency-dependent dispersion, propagation, localization, and loss beyond the free electron model. Physical Review B. 2005;**72**(7):075-405

[59] Yan R, Pausauskie P, Huang J, Yang P. Direct photonic–plasmonic coupling and routing in single nanowires. Proceedings of the National Academy of Sciences. 2009;**106**(50):21045-21050

[60] Seo M-K, Kwon S-H, Ee H-S, Park H-G. Full three-dimensional subwavelength high-Q surface-plasmon-polariton cavity. Nano Letters. 2009;**9**(12):4078-4082

[61] Kang J-H, No Y-S, Kwon S-H, Park H-G. Ultrasmall subwavelength nanorod plasmonic cavity. Optics Letters. 2011;**36**(11):2011-2013

[62] Zhu QZ, Zheng SP, Lin SJ, Liu TR, Jin CJ. Polarization-dependent enhanced photoluminescence and polarization-independent emission rate of quantum dots on gold elliptical nanodisc arrays. Nanoscale. 2014;**6**(13):7237-7242

[63] Yang X, Bao D, Li B. Plasmon-mediated whispering-gallery-mode emission from quantum-dot-coated gold nanosphere. The Journal of Physical Chemistry C. 2015;**119**(45):25476-25481

[64] Chikkaraddy R, de Nijs B, Benz F, Barrow SJ, Scherman OA, Rosta E, Demetriadou A, Fox P, Hess O, Baumberg JJ. Single-molecule strong coupling at room temperature in plasmonic nanocavities. Nature. 2016;**535**:127

[65] Shalabney A, George J, Hutchison J, Pupillo G, Genet C, Ebbesen TW. Coherent coupling of molecular resonators with a microcavity mode. Nature Communications. 2015;**6**:5981

[66] Noginov MA, Zhu G, Belgrave AM, Bakker R, Shalaev VM, Narimanov EE, Stout S, Herz E, Suteewong T, Wiesner U. Demonstration of a spaser-based nanolaser. Nature. 2009;**460**:1110

[67] Cerdán L, Enciso E, Martín V, Banuelos J, López-Arbeloa I, Costela A, García-Moreno I. FRET-assisted laser emission in colloidal suspensions of dye-doped latex nanoparticles. Nature Photonics. 2012;**6**(9):621626

[68] Yu J, Cui Y, Xu H, Yang Y, Wang Z, Chen B, Qian G. Confinement of pyridinium hemicyanine dye within an anionic metal-organic framework for two-photon-pumped lasing. Nature Communications. 2013;**4**:2719

[69] Huang KC, Seo M-K, Sarmiento T, Huo Y, Harris JS, Brongersma ML. Electrically driven subwavelength optical nanocircuits. Nature Photonics. 2014;**8**(3):244-249

[70] Shi C, Soltani S, Armani AM. Gold nanorod plasmonic upconversion microlaser. Nano Letters. 2013;**13**(12):5827-5831

[71] Lv Y, Li Y, Li J, Yan Y, Yao J, Zhao Y. All-color subwavelength output of organic flexible microlasers. Journal of the American Chemical Society. 2017;**139**:11329-11332

[72] Yang X, Li Y, Lou Z, Chen Q, Li B. Optical energy transfer from photonic nanowire to plasmonic nanowire. ACS Applied Energy Materials. 2018;**1**(2):278-283

[73] Wu X, Xiao Y, Meng C, Zhang X, Yu S, Wang Y, Yang C, Guo X, Ning C, Tong L. Hybrid photon-plasmon nanowire lasers. Nano Letters. 2013;**13**(11):5654-5659

[74] Miyata M, Takahara J. Colloidal quantum dot-based plasmon emitters with planar integration and long-range guiding. Optics Express. 2013;**21**(7):7882-7890

# Plasmonic Modes in Au and AuAg Nanowires and Nanowire Dimers Studied by Electron Energy Loss Spectroscopy

Ina Schubert and Maria Eugenia Toimil-Molares

Additional information is available at the end of the chapter

http://dx.doi.org/10.5772/intechopen.79189

### Abstract

In this chapter, we review our recent work on the investigation of surface plasmon modes in metallic nanowires and nanowire dimers by means of electron energy loss spectroscopy combined with scanning transmission electron microscopy (STEM-EELS). Due to the very high spatial resolution, STEM-EELS is a powerful technique to visualize multipole order surface plasmon modes in nanowires and study the dependency of their resonance energies on different parameters such as nanowire dimensions or nanowire porosity. In addition, we investigate surface plasmon hybridization in nanowires separated by gaps of less than 10 nm or connected by small metallic bridges. In such structures new modes arise, which depend strongly on gap or bridge sizes. Experimental results are supported by finite element simulations. The investigated nanowires and dimers are fabricated by electrodeposition in etched ion-track templates, combined with a selective dissolution processes. The synthesis techniques and their advantages for the fabrication of plasmonic nanostructures are also discussed.

**Keywords:** gold, nanowires, nanogaps, nanowire dimers, surface plasmons, plasmon hybridization, electron energy loss spectroscopy, scanning transmission electron microscopy, electrodeposition, ion-track technology, etched ion-track membranes

## 1. Introduction

Over the past 20 years surface plasmons in metallic nanoparticles have attracted great attention due to their potential for many applications in the fields of sensing [1], light guiding [2] and

IntechOpen

© 2018 The Author(s). Licensee IntechOpen. This chapter is distributed under the terms of the Creative Commons Attribution License (http://creativecommons.org/licenses/by/3.0), which permits unrestricted use, distribution, and reproduction in any medium, provided the original work is properly cited.

energy conversion [3]. Surface plasmons are collective electronic oscillations that can be excited by an external electric field. At the surface plasmon resonance wavelength of the nanoparticle, the excitation of the electronic oscillation results in high electric near-fields. In the far-field the resonance frequency is strongly scattered and absorbed, but less transmitted. The resonance frequency of a given nanoparticle depends strongly on parameters such as, for example, the shape, dimension, and composition [4, 5]. Therefore, besides the continuous progress on the study of plasmonic properties, also the development of suitable methods to synthesize plasmonic nanostructures with very well-controlled characteristics is of great importance both for basic research as well as for technological applications.

### 1.1. Surface plasmons in nanowires

Surface plasmons in nanowires can be excited in two different directions [6]. Longitudinal surface plasmons are oscillations that occur in the direction of the long nanowire axis, whereas transversal modes oscillate in the direction of the nanowire diameter. This makes nanowires especially interesting for both plasmonic basic research as well as applications. In particular, longitudinal modes attract great attention since by varying the length of the nanowires, the resonance frequency can be tuned accurately within a wide range; for Au and Ag wires from the visible to infrared frequencies [7–10]. In this frequency range, the specific spectroscopic finger print of many molecules is located. This can be used for molecular sensing by surface enhanced infrared spectroscopy (SEIRA) [1]. When the molecules are located close to a Au or Ag nanowire, the high electric fields generated by surface plasmons can strongly increase the molecular absorption signals, thus enhancing the sensitivity of the method. For Au nanowires, enhancement factors up to a factor of $10^5$ were reported [1].

Surface plasmons in nanowires have been investigated for different kind of metals, as well as for alloy and segmented wires [11]. Compared to other metals, Au nanowires offer the advantages of being chemically stable and nontoxic. This is important because, since infrared light is less energetic that other radiation types, also in vivo applications of surface plasmons in these structures such as, for example, photothermal therapy are envisaged [12].

Another advantage of Au nanowires is the possibility of exciting multipolar modes in addition to the dipolar one (in analogy to standing waves in a resonator). Whereas in spherical particles these modes usually overlap, the geometry of the nanowires results in a clear energetic separation for several multipole orders [8, 13, 14].

Single Au nanowires are thus very interesting objects to obtain fundamental knowledge on the basics of surface plasmons. However, not only single nanowires but also complex systems consisting of more than one wire separated by small gaps of few nanometers or small metallic connections are attracting great interest [15–18]. In these kinds of structures coupling of the surface plasmons of the individual structures is possible, which results in many new modes and further enhanced electromagnetic fields [15, 19].

### 1.2. Electron energy loss spectroscopy

Electron energy loss spectroscopy (EELS) is a powerful technique to visualize surface plasmon modes in nanostructures. It benefits from the very high spatial resolution of the transmission electron microscope (TEM) that allows to analyze surface plasmons at specific positions of the nanostructure, for example, by the tip or in a gap [14, 20–22], together with the very broad energy range from ~0.3 eV to several eV. Different from other high spatial resolution techniques such as cathodoluminescence in the TEM [23] or scanning near-field optical microscopy (SNOM) [8], EELS not only allows investigating bright modes that couple efficiently to light, but also dark modes [20, 24].

Surface plasmon measurements with EELS are based on the interaction of the traveling electrons in the TEM with the electric field corresponding to the surface plasmons (excited by the electron itself) [25, 26]. The energy loss of the electrons is equivalent to the energy that is necessary to excite a given surface plasmon mode. For measuring this energy loss a magnetic prism in the TEM is used, deflecting electrons dependent on their energy loss [27]. Two different measurement modes exist:

For scanning transmission electron microscopy combined with electron energy loss spectroscopy (STEM-EELS), the electron beam is scanned along a defined path. At each position, a spectrum is created at the dispersive plane. The energy resolution of this technique is given by the natural energy width of the primary electrons that is decreased by a monochromator in the TEM to typically 0.1 eV. It is measured via the full width half maximum of the dominating zero loss peak of the spectrum. The high spatial resolution of the technique allows visualizing two dimensional EEL probability maps in the surrounding of the nanostructure.

For energy filtered transmission electron microscopy (EFTEM), a moveable slit is inserted at the position of the dispersive plane. Only electrons with a specific energy loss can pass the slit (typical slit width 0.2 eV) and deliver at the image plane a 2D image of the nanostructure. This image is created only by electrons with energy loss in the given range. In contrast to STEM-EELS, the energy resolution is worse but the measurement technique is faster.

For a more detailed introduction into the technique, the reader is referred to the following review articles [26, 28–30].

In this chapter, we review our recent activities on the investigation of surface plasmon modes in metallic nanowires and nanowire dimers by STEM-EELS. In Section 2, the synthesis of various Au-based nanowires by electrodeposition in etched ion-track membranes is presented, including Au and $Au_{1-x}Ag_x$ wires, as well as the fabrication of porous Au wires by subsequent dealloying of $Au_{0.4}Ag_{0.6}$ nanowires [31]. Following, the visualization of multipole order surface plasmon modes in these nanowires by STEM-EELS and the study of their resonance energies as a function of, for example, nanowire dimensions and nanowire porosity, is discussed [14, 32]. Section 3 describes the synthesis of nanowire dimers by electrodeposition of segmented Au-rich/Ag-rich/Au-rich nanowires and the subsequent dissolution of Ag [33]. It continues presenting STEM-EELS measurements on these nanostructures, which allowed the investigation of surface plasmon hybridization in nanowires separated by gaps of less than 10 nm [14] as well as connected by small metallic bridges [34]. In such structures, new modes arise that depend strongly on gap or bridge sizes, respectively. Section 3 finishes with discussing mode coupling of heterodimers consisting of two wires with different length [35]. All experimental results are supported by representative finite element calculations. The chapter concludes with a summary and final conclusions, both presented in Section 4.

## 2. Single nanowires

Recently, EELS analysis of metallic nanowires and rods consisting of Au [14, 20, 32, 36–38], Ag [13, 39, 40] and Al [41] demonstrated that it is an excellent technique to study their surface plasmon modes. Au nanorods with length up to 400 nm have been investigated by several authors using STEM-EELS and EFTEM visualizing their first- and second-order multipolar modes [20, 36–38]. In this chapter, we focus on our recent EELS investigations of the multipole order surface plasmon modes up to the seventh order in individual Au nanowires with 1–2 μm length and 60–100 nm diameter. The resonance energies were analyzed with respect to specific tailored wire parameters, such as length and diameter [14], composition and porosity [32] by STEM-EELS at Stuttgart Center for Electron Microscopy using a Zeiss SESAM transmission electron microscope operated at 200 keV. In this section, we first describe the fabrication of both smooth and porous Au nanowires by ion-track technology and electrodeposition and then summarize our results on the investigation of their plasmonic properties.

### 2.1. Synthesis of Au nanowires by ion-track technology and electrodeposition

The Au nanowires discussed in this chapter are fabricated by electrodeposition in etched ion-track membranes. The synthesis method is schematically displayed in **Figure 1** and involves the following separate processing steps: (1) irradiation of the template material (typically polymer foils with thickness 10–100 μm) with energetic heavy ions and creation of latent iontracks (**Figure 1a**); (2) selective ion-track dissolution and formation of channels by chemical etching (**Figure 1b**); (3) preparation of a conductive back-electrode (**Figure 1c**); (4) electrodeposition of Au in the nanochannels (**Figure 1d**) and (5) dissolution of the polymer membrane (**Figure 1e**).

Etched ion-track membranes are widely used as templates for nanowire growth since the late 1990s. Control over the irradiation and etching conditions enables the production of various

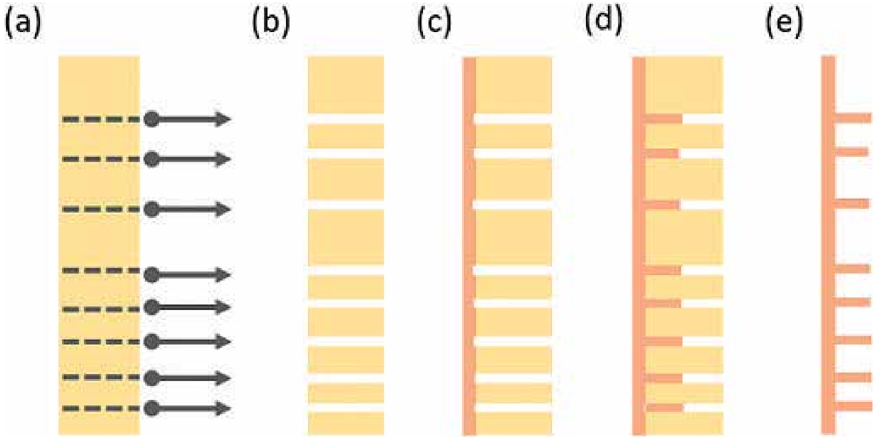

**Figure 1.** Schematics of the steps involved in the synthesis of Au-based nanostructures by the template method: (a) swift heavy ion irradiation of a polycarbonate foil and formation of ion-tracks (dotted lines), (b) selective chemical etching of the ion-tracks, (c) sputtering and electrochemical reinforcement of an electrical contact layer, (d) Au electrodeposition in the channels and (e) dissolution of the polymer foil.

membranes with channels of predefined geometries (e.g., cylindrical, conical, bi-conical), with lengths varying between 1 and 100 μm, diameter ranging between ~15 nm up to several μm and aspect ratio (length *L* over diameter *D*) of up to 1000. Under suitable experimental conditions, the synthesized nanowires adopt the exact shape and size of the host channel, enabling thus the fabrication of wires with very well-controlled geometrical parameters. By varying the electrodeposition parameters, composition, crystallinity and crystallographic orientation of the deposited material can be adjusted. This unique combination of electrochemical deposition and etched ion-track membranes has demonstrated to be very powerful to synthesize nanowires with controlled and independently adjusted characteristics. In addition, a large number of wires up to $10^{10}$ $cm^{-2}$ can be grown simultaneously.

Au nanowires with smooth contour were first electrodeposited using a two-electrode configuration, with the sputtered Au film as initial cathode and an Au rod as anode. Optimized growth conditions enabled the synthesis of both single- and polycrystalline cylindrical Au wires with diameters between 20 and 1000 nm [42–44] in a controlled manner. It was found that the employed electrolyte strongly influenced the crystalline structure of the deposited material. Thus, Au nanowires deposited with ammonium gold(I) sulfite (gold content = 15 g/L, Metakem GmbH, Usingen, Germany) or sodium disulfitoaurate (I) Imabrite 24 bath (gold content = 12.3 g/L, Schloetter Galvanotechnik, Geislingen/Steige, Germany) electrolytes exhibit a polycrystalline structure. In contrast, Au wires grown in a solution of potassium dicyanoaurate(I) (Puramet 402 bath, gold content = 10 g/L, Doduco, Pforzheim, Germany) yield single crystals at temperatures between 50 and 65°C under both direct-current and reverse-pulse deposition conditions. The resulting single-crystalline wires have a preferred [110] orientation independently of applied voltage and temperature.

Recently, this method has also been applied to prepare Au nanowires with smooth and rough contour, by electrodepositing Au in polycarbonate and polyethylene theraphthalate membranes, whose etched nanochannels exhibit smooth and rough contours, respectively. **Figure 2** shows the SEM images of two representative Au nanowire arrays deposited using a two electrode configuration in **Figure 2a** polycarbonate and in **Figure 2b** polyethylene terephthalate membranes using a sulfite-based electrolyte (Metakem, pH 7.5).

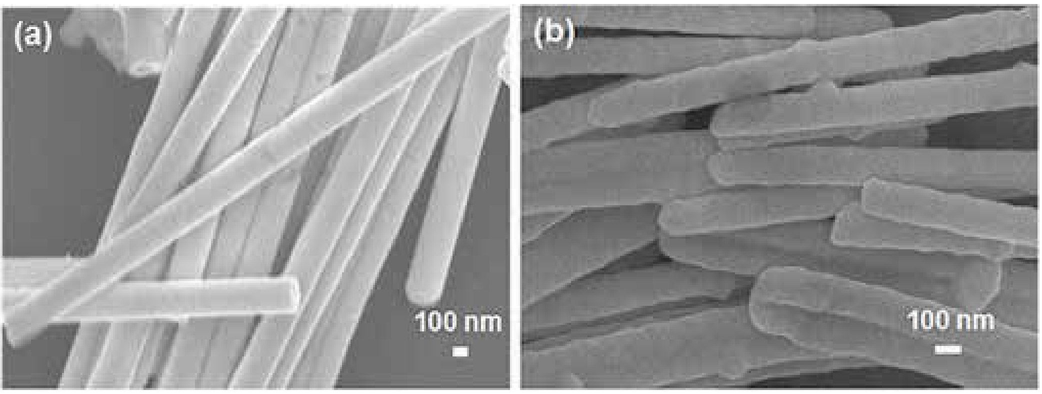

**Figure 2.** SEM image of Au nanowires deposited in (a) polycarbonate and (b) polyethylene terephthalate membranes. Reproduced with permission from [32]. Copyright VBRI press.

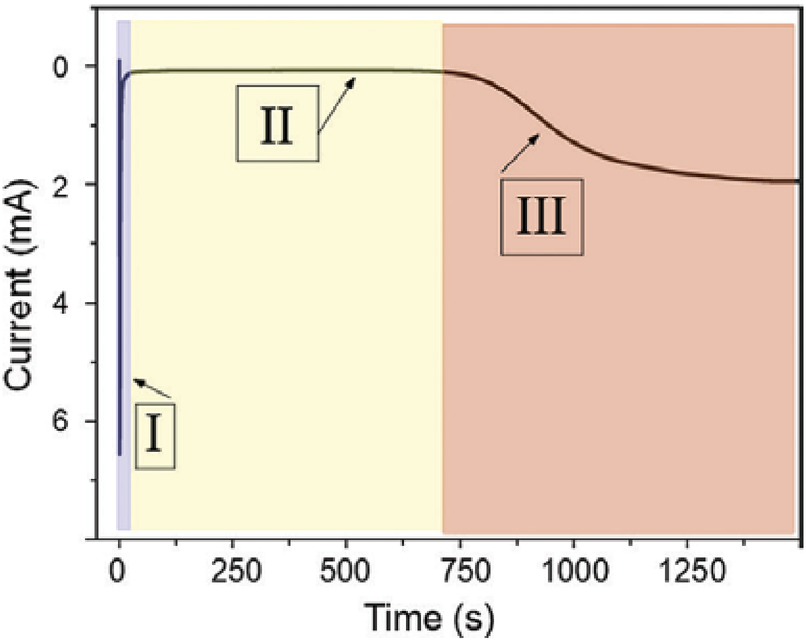

**Figure 3.** Current-versus-time curve recorded during the deposition of Au nanowires with a cyanide-based electrolyte. The three characteristic zones of nanowire growth are highlighted by the different colors.

For large-scale synthesis and industrial applications, two-electrode set-ups are most usual. However, it is known that the use of three electrodes improves the reproducibility and the control over the experiments. Therefore, subsequent synthesis of Au nanowires was investigated in a three-electrode configuration. The process was potentiostatic, using a Pt rod as counter electrode and a Ag/AgCl (Sat. KCl) reference electrode. In this case, a cyanide-based electrolyte consisting of $KAu(CN)_2$ (20 or 50 mM) and $Na_2CO_3$ (0.25 M) is employed. The voltage applied ranges between $U = -0.5$ and $-1.1$ vs. Ag/AgCl, and the temperature is kept constant at $T = 60°C$. The process is monitored by recording the current as a function of deposition time, that is, by chronoamperometry.

**Figure 3** shows a representative current vs. time (*I-t*) curve recorded during the electrodeposition of Au nanowires from a cyanide solution. It reveals three different zones that are highlighted in the figure with different colors. In zone (I) at the moment of applying the potential, the absolute current increases and subsequently decreases (purple). This is due to the reduction of ions in the vicinity of the cathode and the formation of the diffusion layer, respectively. In zone (II), the current density remains almost constant (yellow). Due to their cylindrical geometry, the deposition area is constant during the growth of the material inside the channels. Once the nanochannels are filled, caps start to grow on top of the wires on the template surface. This enlarged surface area results in an increase of the absolute current value in zone (III) (red).

According to Faraday's law, the weight of a product of electrochemical reaction at an electrode is proportional to the electric charge *Q*, passing through the electrochemical cell. If the growth is homogeneous and the efficiency of the deposition reaction is 100%, the experimental charge, being the integral of the *I-t* curve, is thus equivalent to the theoretical value calculated applying Faraday's law:

$$Q_{theo} = z\,F\,L \cdot \left(\frac{D}{2}\right)^2 \cdot \rho \cdot \frac{N_{\mathrm{pores}}}{A_{\mathrm{wt}}}, \tag{1}$$

where $A_{\mathrm{wt}}$ is the atomic weight of the deposit, $z$ the number of electrons involved in the deposition, $F$ Faraday's constant, $D$ and $L$ the nanowire diameter and length, $\rho$ the density, and $N_{\mathrm{pores}}$ the number of pores in the membrane. For homogeneous nanowire growth, this enables to control the nanowire length. The deposition process is therefore stopped after the amount of charge necessary to obtain a specific wire length has been reached. In this way, Au nanowires with the same $D$ and the same crystallography but different $L$, for example, between ~0.8 and ~30 μm can be synthesized.

### 2.2. Synthesis of porous Au nanowires

Compared to cylindrical smooth Au nanowires, porous Au wires exhibit larger surface areas and small nanovoids that can act as plasmonic hotspots, for example, for sensing [45, 46]. Porous Au wires can be also synthesized by the template method. Their fabrication was first demonstrated by Searson et al. [47, 48]. By using a single-bath electrolyte $Au_{1-x}Ag_x$ ($0 < x < 1$) alloy was deposited in the nanochannels. After dissolution of the template, the less noble material, in this case Ag, was selectively dissolved. Since then, various groups studied the influence of both initial AuAg wire composition and dealloying parameters on the resulting porosity, in most cases for wire diameters larger than 200 nm [49–52].

Recently, we reported the potentiostatic electrodeposition and characterization of thinner $Au_{1-x}Ag_x$ nanowires with controlled composition and size. The cylindrical $Au_{1-x}Ag_x$ nanowires exhibited three different $D$, namely, 85, 45 and 30 nm, and $L$ between 10 and 20 μm and were analyzed with respect to their composition and morphology before and after dealloying.

Electrodeposition was performed at 60°C from aqueous electrolytes containing 0.25 M $Na_2CO_3$, as well as $KAu(CN)_2$ and $KAg(CN)_2$ in different ratios, namely (1) 50 mM of $KAu(CN)_2$ and 50 mM of $KAg(CN)_2$ (Au:Ag ratio 1:1) and (2) 50 mM of $KAu(CN)_2$ and 20 mM of $KAg(CN)_2$ (Au:Ag ratio 5:2). A constant potential of −1.1 V vs. Ag/AgCl reference electrode was applied and a platinum wire served as the counter electrode in all cases. After dissolution of the polymer foil, the wires were transferred onto silicon nitride TEM grids for posterior dealloying and analysis. For dealloying, the silicon nitride membranes with randomly distributed nanowires were immersed in 65% nitric acid ($HNO_3$, LS labor-Service GmbH) at room temperature for 3 h. The dealloying process of individual cylindrical wires with various sizes and compositions was characterized by means of TEM for the crystallinity and energy-dispersive X-ray spectroscopy (EDX) for the elemental analysis. The average composition measured by EDX-TEM for $Au_{1-x}Ag_x$ nanowires deposited using two different electrolyte compositions, before and after dealloying are reported in **Table 1**.

The EDX analysis of the as-grown nanowires before dealloying reveals two types of wires: Ag-rich nanowires (i.e., $Au_{0.4}Ag_{0.6}$) and Au-rich nanowires (i.e., $Au_{0.6}Ag_{0.4}$). The resulting wire compositions do not vary significantly as a function of channel diameter. **Figure 4** shows the corresponding dark-field TEM images of the nanowires. **Figure 4a, b** (left images) display the $Au_{0.4}Ag_{0.6}$ wires synthesized using an electrolyte with a ratio of $KAu(CN)_2$:$KAg(CN)_2$ = 1:1 with diameters of 85 nm (**Figure 4a**) and 45 nm (**Figure 4b**), respectively. **Figure 4c, d** (left images) display

$Au_{0.6}Ag_{0.4}$ wires with 85 and 45 nm diameter electrodeposited using a $KAu(CN)_2$:$KAg(CN)_2$ ratio of 5:2. Before dealloying, all nanowires are cylindrical and exhibit very smooth surfaces for all diameters and compositions. EDX with very high spatial resolution (below 1 nm) revealed the presence of a Ag-rich layer in $Au_{0.4}Ag_{0.6}$ wires and Au-rich layer in $Au_{0.6}Ag_{0.4}$ wires [31]. The thickness of these surface layers amounted 1–4 nm. After dealloying (right images), wires with very different morphologies are obtained. After dealloying in nitric acid, Ag-rich wires exhibit porous morphologies, whereas Au-rich wires remain solid cylinders displaying only a small increase in surface roughness. In **Figure 4e**, the EDX line scan shows the composition of a ligament of a dealloyed $Au_{0.4}Ag_{0.6}$ and evidences its almost pure Au composition across the ligament except for a small region (2–3 nm) with 20 at% of remaining Ag content. In turn, after dealloying,

| | Before dealloying | | | After dealloying | |
|---|---|---|---|---|---|
| | Atomic % of Ag | | | Atomic % of Ag | |
| Initial wire diameter (nm) | 85 | 45 | 30 | 85 | 45 |
| Electrolyte: | | | | | |
| 50 mM $KAu(CN)_2$<br>50 mM $KAg(CN)_2$ | 62 ± 4 | 60 ± 4 | 63 ± 3 | 8 ± 6 | 5 ± 6 |
| 50 mM $KAu(CN)_2$<br>20 mM $KAg(CN)_2$ | 41 ± 4 | 38 ± 4 | 39 ± 3 | 39 ± 5 | 36 ± 3 |

Reproduced with permission from Ref. [31]. Copyright 2015 American Chemical Society.

**Table 1.** Averaged Ag content (at%) in the nanowires measured by EDX spectroscopy before and after dealloying as a function of the initial wire diameter.

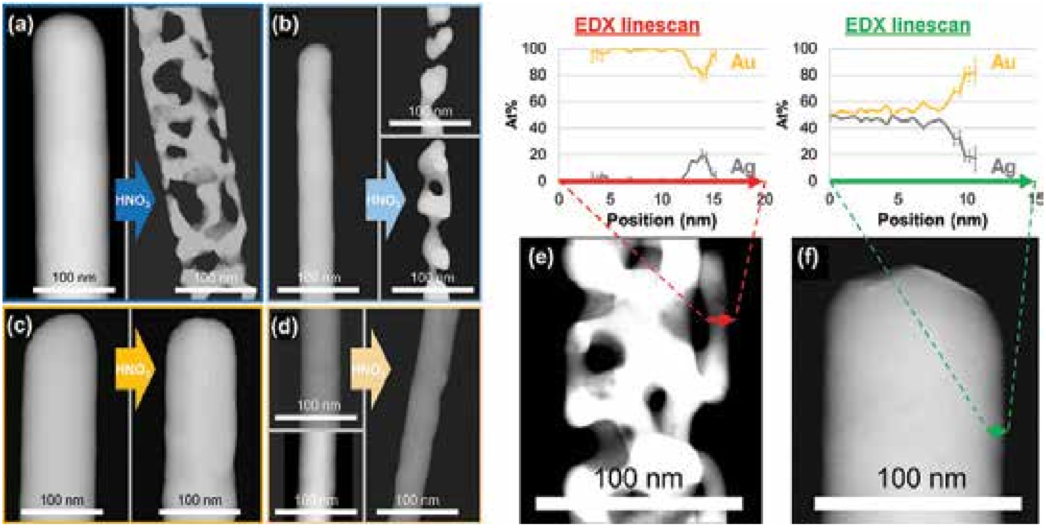

**Figure 4.** Dark-field TEM images of AuAg nanowires before (right) and after (left) dealloying in $HNO_3$: (a) $Au_{0.4}Ag_{0.6}$ nanowire, initial diameter 85 nm, (b) $Au_{0.4}Ag_{0.6}$ nanowire, initial diameter 45 nm, (c) $Au_{0.6}Ag_{0.4}$ nanowire, initial diameter 85 nm, (d) $Au_{0.6}Ag_{0.4}$ nanowire, initial diameter 45 nm. TEM image and EDX line scan across (e) a ligament of an $Au_{0.4}Ag_{0.6}$ dealloyed nanowire and (f) the surface of an $Au_{0.6}Ag_{0.4}$ nanowire after dealloying. Adapted with permission from [31] copyright 2015 American Chemical Society.

the $Au_{0.6}Ag_{0.4}$ nanowires exhibit a diameter and composition similar to that of the initial nanowires (**Figure 4f**). They also have a relatively homogeneous Au-rich shell. This detailed analysis of the different Au-based nanowires, and in particular of their surface composition, is very important in order to interpret the plasmonic measurements presented in the following subsections, as well as for setting realistic inputs for simulations.

### 2.3. STEM-EELS of individual Au nanowires

Single cylindrical smooth Au nanowires with different aspect ratio were investigated by EELS to analyze their multipolar surface plasmon modes. **Figure 5** shows an example of a STEM-EELS map of a single Au nanowire with $L$ = 895 nm ± 5 nm and $D$ = 95 ± 5 nm. The map consists of 100 spectra that were recorded by scanning the electron beam along the red line on the right of the nanowire (distance to wire surface ~10 nm). Each horizontal line in the map corresponds to one single spectrum. The energy loss increases from left to right. The color in the map indicates the energy loss probability. The energy loss of an incident electron depends on the electromagnetic local density of states, projected in the direction of the traveling electron [25]. Thus, the energy loss maxima in the EELS map can be interpreted as the position of field maxima of standing surface plasmon waves. We can therefore identify different multipolar surface plasmon modes by counting these maxima. A single spectrum extracted from the map can be seen in **Figure 5b**, and the spectrum was recorded at the position of the red dot in the TEM image on the right.

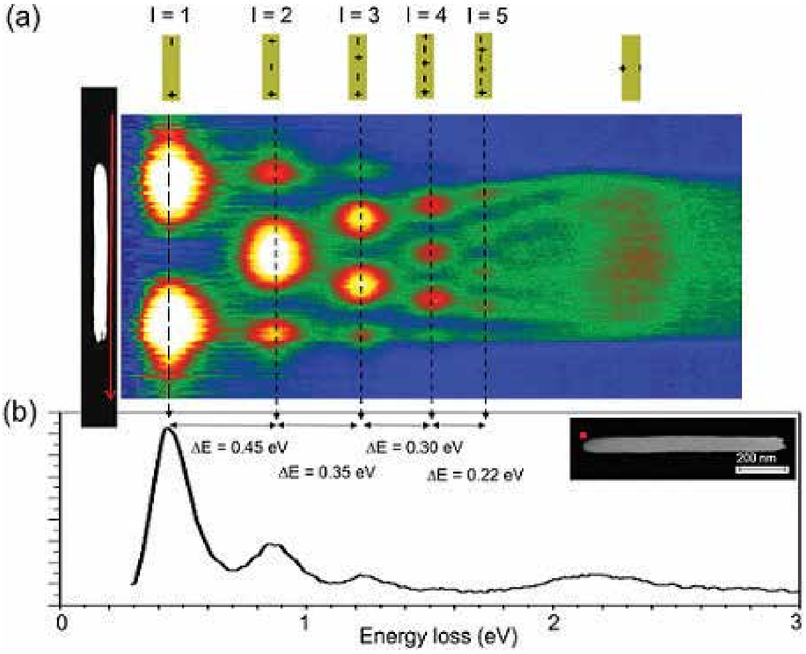

**Figure 5.** (a) STEM-EELS map of a single Au nanowire ($L$ = 895 nm ± 5 nm; $D$ = 95 ± 5 nm). The map consists of 100 spectra measured along the red arrow in the TEM image on the left. The schemes on top show the corresponding surface charge distributions; (b) single spectrum extracted from the map at the position of the red dot in the TEM image. Adapted with permission from [32]. Copyright VBRI press.

From the STEM-EELS map, it is possible to resolve surface plasmon modes of the wire in a broad energy interval between 0.4 and 2.7 eV. At low energies, the map clearly shows five different longitudinal modes of the Au nanowire as shown in the schemes on top of the map. At an energy of 2.3 eV, a transversal mode is excited all along the wire. To study the dependency of resonance energy versus nanowire dimensions, **Figure 6a** shows the energy of several multipole order longitudinal modes for 3 Au nanowires with different aspect ratios. It is seen that tuning the dimensions of the nanowire is a perfect tool to adjust the resonance energy of all multipole modes. TEM images of the three nanowires are depicted in **Figure 6b–d**. With increasing nanowire aspect ratio (*L* over *D*), the energies of all the longitudinal modes are shifted to lower energies, which is in accordance with results obtained with other measurement techniques and simulations (e.g., see [8–10]). The specific curve shape of the resonance energy versus multipole order for all three wires points toward a simple relation between these parameters. Using simulations, in 2007, Klebtsov et al. [6] have proposed the relation

$$\frac{1}{E} = A_0 + A_1 \cdot \frac{L/D}{l} \tag{2}$$

*E* is the energy of the respective mode and $A_0$ and $A_1$ are constants. Eq.(2) is motivated by the direct proportionality between *L* and the resonance wavelength *λ* of a perfect conductor, but is modified since penetration of light into the gold wire is possible in this frequency regime. **Figure 6e** shows a linear regression plot to the data of the three wires. Plotted is the inverse of the energy versus *L*/*D* over *l* according to Eq. 1. The relation follows well the data. As can be seen for the two wires with similar *D* (marked in black and green in **Figure 6e**), for wires of the same diameter and material of the same relation can be used to analytically calculate the multipole resonance energies.

## 2.4. STEM-EELS of porous nanowires

Another advantage of STEM-EELS is that wire details such as surface roughness or porosity can be resolved by the TEM together with the recording of the corresponding EELS map, enabling the investigation of how such specific parameters influence the resonance energies. **Figure 7** shows an example of a STEM-EELS map of a porous nanowire with *L* = 1000 ± 10 nm

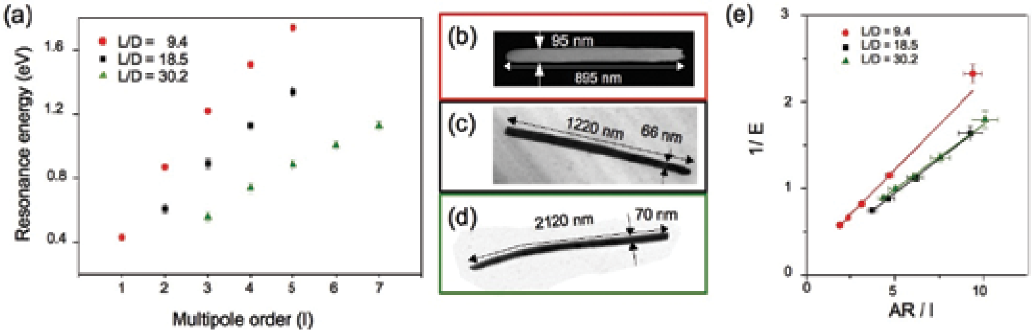

**Figure 6.** (a) Resonance energies for three different nanowires are plotted versus multipole order for the corresponding mode, (b) TEM images of the three different wires and (c) the inverse of the energy plotted versus aspect ratio over *l* for all three wires together with linear regression curves according to Eq. (2). Adapted with permission from [14]. Copyright 2011 American Chemical Society.

and $D = 90 \pm 10$ nm, thus with similar dimensions to the wire analyzed in **Figure 5**. For the longitudinal modes, the map resembles the one of the pure Au wire. However, at the higher energies (around approx. 2.2 eV, where we expect from the single Au wire the transversal mode), it is seen that the transversal mode of the porous wire is not excited at the same energy all along the nanowire, but the transversal mode energy shifts in a broad range between 1.9 and 2.3 eV dependent on the position. We account this to the varying pore sizes along the wire that can be seen in the TEM image in **Figure 7b**.

Since the porous wire is only slightly longer than the single Au wire in **Figure 5**, we can compare the energies of the respective modes. For all modes including the transversal, the energies measured for the porous wire are systematically lower than the corresponding mode energies of the continuous Au wire. This result is in agreement with further studies that we have conducted on the dipolar mode of Au nanowires by infrared spectroscopy [53] as well as results reported by other authors on shorter rods [54]. We believe that it can be explained by a change in the intrinsic parameters such as the lower bulk plasma frequency that follows from introducing an effective medium consisting of gold and empty voids to describe the porous material [53, 55].

### 2.5. Surface plasmon dispersion

EELS maps along individual nanowires allow deducing a surface plasmon dispersion relation. For this, the distance between two maxima, which corresponds to the half-surface plasmon wavelength of the respective mode, is measured [13, 40, 41]. Using this technique, different authors have derived dispersion relations for Ag [13, 40] and Al [41] nanowires by EFTEM

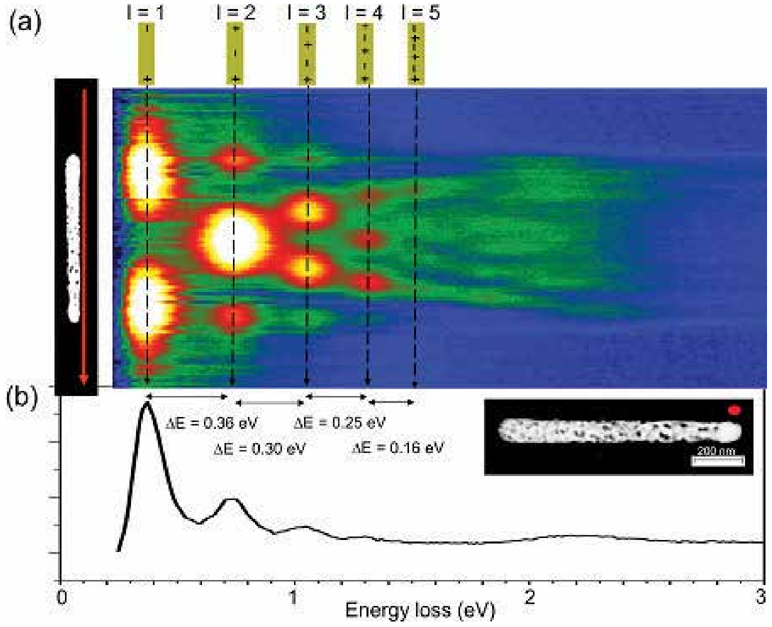

**Figure 7.** (a) STEM-EELS map consisting of 100 spectra measured along a porous Au nanowire ($L = 1000 \pm 10$ nm, $D = 90 \pm 10$ nm) together with the corresponding surface charge distributions; (b) single spectrum extracted from the map at the position of the red dot in TEM image. Adapted with permission from [32]. Copyright VBRI press.

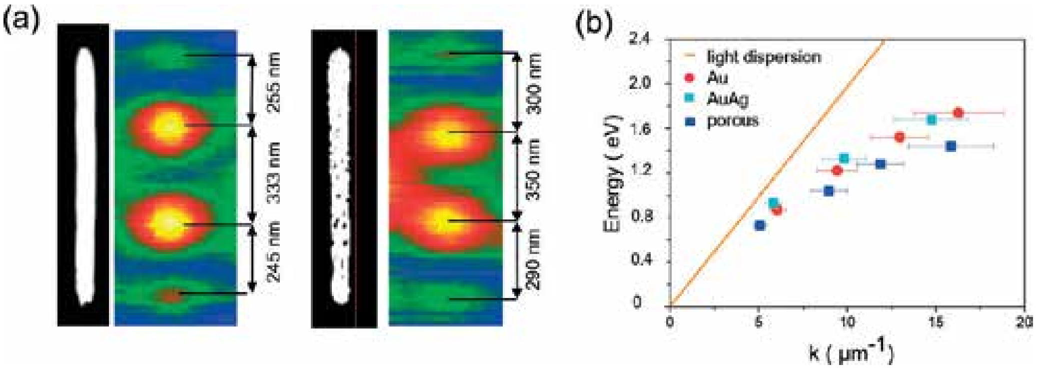

**Figure 8.** (a) Extract of the EELS map in **Figure 5** and **Figure 7** showing the surface plasmon half-wavelength of the third-order mode of smooth and porous nanowire and (b) dispersion relation for different Au-based nanowires together with the dispersion of light.

and STEM-EELS. For both materials, it was demonstrated that the distance between the maxima at the nanowire edges is shorter than the one between two maxima in the middle. The phenomenon is called antinode bunching [13] or $\lambda_{sp}$ - compression [40]. It has been explained by a phase jump of the surface plasmon mode that is most probably due to the shape of the edges of the nanowire [13]. As it can be clearly seen exemplarily for the third-order mode of smooth and porous wires in **Figure 8a**, our data confirm this effect also for the Au wires. For both Ag and Al, it has been shown that the dispersion follows the shape of the calculated dispersion relation of fundamental surface plasmon polaritons sustained by an infinite Ag or respectively Al cylinder and that the low-order modes are close to the light line, which makes them easily excitable with light. **Figure 8b** shows the dispersion relation for a single Au nanowire, an $Au_{0.7}Ag_{0.3}$ alloy nanowire, and a porous Au wire. Values for the Au and AuAg alloy wire follow almost the identical curve shape, which we attribute to the similar dielectric function of Au and Ag at low energies and the small Ag content of only 30% in the wire. In contrast for the porous wire, the curve lies by trend below the one of the pure Au wire which we assign to a lower bulk plasma frequency as mentioned previously.

## 3. Coupled nanowire systems

Interaction between surface plasmons in several nanostructures that are separated by distances smaller than the decay length of the electric field is attracting a lot of attention in the field of plasmonics (see e.g., [15, 17, 19, 56–58]). In such systems, the plasmonic modes couple resulting in a splitting or hybridization (in analogy to molecular orbitals) in new plasmonic modes, called bonding and antibonding modes [16, 19, 56]. Nanowires are very interesting structures to study such hybridization phenomena, since their elongated shape results in a large energetic splitting of the modes even for higher multipole orders, which makes the splitting clearly resolvable in the energy loss spectrum. We have used systems consisting of two nanowires separated by small gaps [14, 35] or connected by small conductive bridges [34] to study such coupling effects. Taking up the terminology of molecular orbitals, the structures are called ‘nanowire dimers’ [16]. After presenting our synthesis technique, we start the discussion with a dimer consisting of two wires with almost identical *L* and separated by a small gap, and continue with more complex structures such as wires connected by bridges or consisting of wires of different *L*.

### 3.1. Synthesis of nanowire dimers

The template method enables the synthesis of axially segmented nanowires composed by two or more materials. Back in the 1990s, the synthesis of segmented Cu/Co and Ni/Cu multilayer nanowires was reported [59, 60]. Since then, many different segmented structures combining, for example, polymers, semiconductors, and metals, have been fabricated by the template method [61, 62]. Segmented nanowires can be grown either by sequential exchange of the electrolyte [63, 64] or using a single-bath electrolyte and controlling the composition of the segments by tuning reduction potential and electrolyte composition [65, 66]. The combination of electrodeposition of segmented nanowires formed by two different materials, and the selective dissolution of the less noble, is known as on-wire lithography [67]. The Au nanowire dimers analyzed in this chapter are synthesized also in a similar two-step process. The first step consists of depositing segmented Au-rich/Ag-rich/Au-rich nanowires by sequential potentiostatic deposition, using the same electrolyte mentioned in Section 2.2, namely 0.25 M $Na_2CO_3$, and $KAu(CN)_2$ and $KAg(CN)_2$ in different concentrations [33]. The length of the Ag and Au segments is controlled by the duration of the corresponding pulses. Each segment contains a certain amount of the second metal. However, potential and electrolyte concentration can be chosen such that the relative concentration of the second material remains low (< 40%). After dissolution of the polycarbonate template using dichloromethane, the nanowires are transferred on to silicon nitride membranes. By immersing the substrate into concentrated nitric acid for 3 h, the middle silver segment is selectively etched. The gap size is determined by the length of the Ag segment. Using this method, we reported the fabrication of nanogaps with sizes between 7 and 30 nm [33].

**Figure 9** shows SEM images of two wires with $D$ ~65 nm consisting of 6 Au-rich and 6 Ag-rich segments (a) before and (b) after the nitric acid treatment. It can be seen in **Figure 9b** that in some cases a small metallic connection remains between the Au-rich segments. In this case, adjacent nanowire segments are electrically connected by the small junction. The small connections can be efficiently removed by thermal annealing at 300°C for 30 min, resulting in adjacent Au segments of similar length separated by a well-defined gap, as shown exemplary in **Figure 9c**.

This method has been applied to produce adjacent nanowires of controlled length separated by a gap of predesigned properties. Thus, two adjacent nanowires with similar length separated by a narrow gap are referred to as “nanowire dimers.” If different pulse durations are applied for the first and third pulses, dimers consisting of Au segments with different length are produced. These are referred to as “nanowire heterodimers” or “symmetry broken dimers.” In addition, two nanowires joined by a small metallic remaining connection (**Figure 9b**) are conductively coupled, while the two wires separated by a well-defined gap (**Figure 9c**) are capacitively coupled. In the next sections, we discuss the plasmonic properties of different nanowire dimers and heterodimers produced by this method.

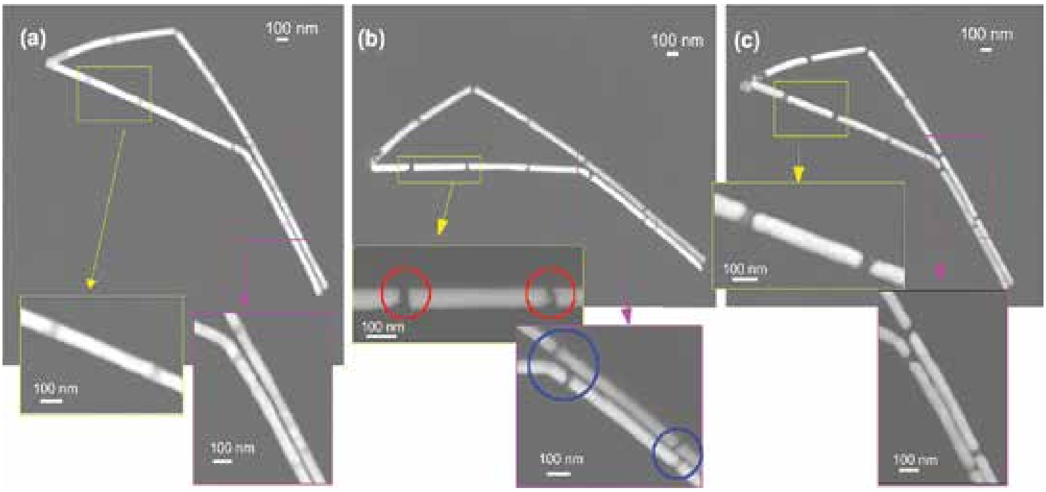

**Figure 9.** (a) SEM image of two segmented nanowires obtained applying a six pulse sequences consisting each of $U_1 = -1.1$ V (25 s) and $U_2 = -0.5$ V (15 s) vs. Ag/AgCl. (b) the same two nanowires after treatment with nitric acid. Small metal junctions are seen between some of the nanowires. (c) Nanowires after nitric acid treatment and annealing at 300°C for 30 min. Well-defined gaps are formed. Adapted from [33], an article distributed under public license https://www.beilstein-journals.org/bjnano/copyright; copyright the authors of [33].

## 3.2. Finite element simulation of coupled systems

Experimental results can be predicted, verified, or complemented by theoretical calculations of surface plasmons. For nanogaps larger than 1 nm quantum phenomena can usually be excluded [58]. In this case, classical calculations based on solving Maxwell's equation are conducted. Several different numerical methods are usually applied to study surface plasmon modes, such as the discrete dipole approximation [68], the boundary-element method [10, 15], or, as in our case, finite element simulations [69]. To conduct finite element simulations, commercial programs such as, for example, Comsol, Lumerical and CST Microwave Studio allow defining the plasmonic nanostructures with high accuracy. In the finite element codes, the structures are subdivided into a large amount of small volume elements. The electric field is numerically calculated by solving Maxwell's equations for these elements using suitable boundary conditions.

To analyze the surface plasmons in nanowires and coupled systems, we have performed finite element simulations with CST Microwave Studio [34]. To simulate the excitation of surface plasmons by a small point source, as it is the case during EELS measurements, we selected as excitation source a small dipole of impedance 5 kΩ located at 1 nm from the surface of the simulated Au nanostructure. This point source excites both bright and dark modes, and can be placed at different positions to analyze plasmon excitation as a function of the relative distance to the wire. **Figure 10** shows the finite element simulations of the electric field strength versus energy for four different structures: a nanowire dimer with gap of 19 nm (red line), two dimers with connections (green line: bridge length 19 nm and bridge diameter 20 nm; blue line: bridge length 19 nm and bridge diameter 40 nm) and a continuous wire. All nanostructures have a total $L = 1145$ nm including gap or connection and $D = 90$ nm. The spectra are normalized to the electric field of the dipole at the specific position for the situation that no Au nanostructure is present. In this simulation, the dipole is located 1 nm from one end of the nanostructures. All spectra are calculated 1 nm from the opposite end of the structures.

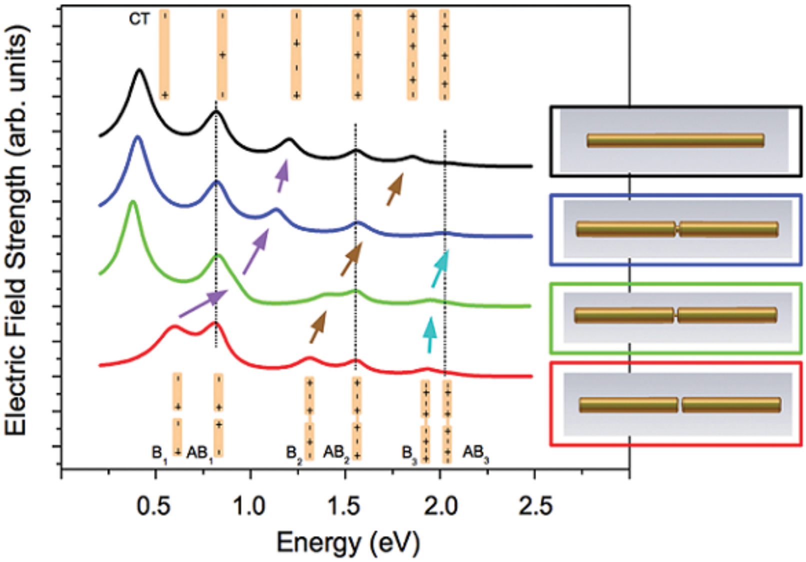

**Figure 10.** Finite element simulation of the electric field strength 1 nm from the end of a nanowire with gap (red), a dimer with small connection of diameter 20 nm (green), with larger connection of diameter 40 nm (blue) and a continuous wire (black). Reprinted with permission from [34]. Copyright 2012 American Chemical Society.

The figure also shows the corresponding charge distributions of the various modes that were obtained from the simulation. In the following sections, we refer to this figure when analyzing the STEM-EELS maps of the corresponding structures.

### 3.3. STEM-EELS of nanowire dimers with gaps

**Figure 11a** shows a STEM-EELS map of nanowire dimer consisting of two wires separated by a gap of about 8 nm. The two wires have length $L_1 = 784 \pm 5$ nm, $L_2 = 808 \pm 5$ nm, and a diameter of $D = 112 \pm 5$ nm. The map of the dimer differs from the ones of single wires by the energy separation between consecutive modes. For a single wire, the energy difference between two consecutive modes decreases with energy (see **Figure 5**). In contrast, for this dimer we find three pairs of modes that are closer in energy than the difference to the next pair. The black arrows below the map depict the energy difference between two modes corresponding two a pair. Each pair consists of a bonding and an antibonding mode that are generated from the coupling of the modes of the two individual wires. The bonding mode is the one having two surface charge maxima of different polarity at the two gap sides, whereas the antibonding mode possesses two maxima of same polarity at this position. In **Figure 11c**, the hybridization scheme of the dimer is schematically shown for the first three multipole orders. These mode pairs of bonding and antibonding modes can also be clearly seen in the red spectrum of **Figure 10** showing the simulation of a nanowire dimer.

The missing energy loss maxima of the bonding modes at the position of the gap can be understood from symmetry reasons. When placing the electron beam at the position of the gap no asymmetric charge distribution can be excited. In addition to the longitudinal modes, the map reveals also a transversal mode of the dimer that can be excited all along the two wires but not at the position of the gap. In the case of dimers, both aspect ratio of the wires and gap

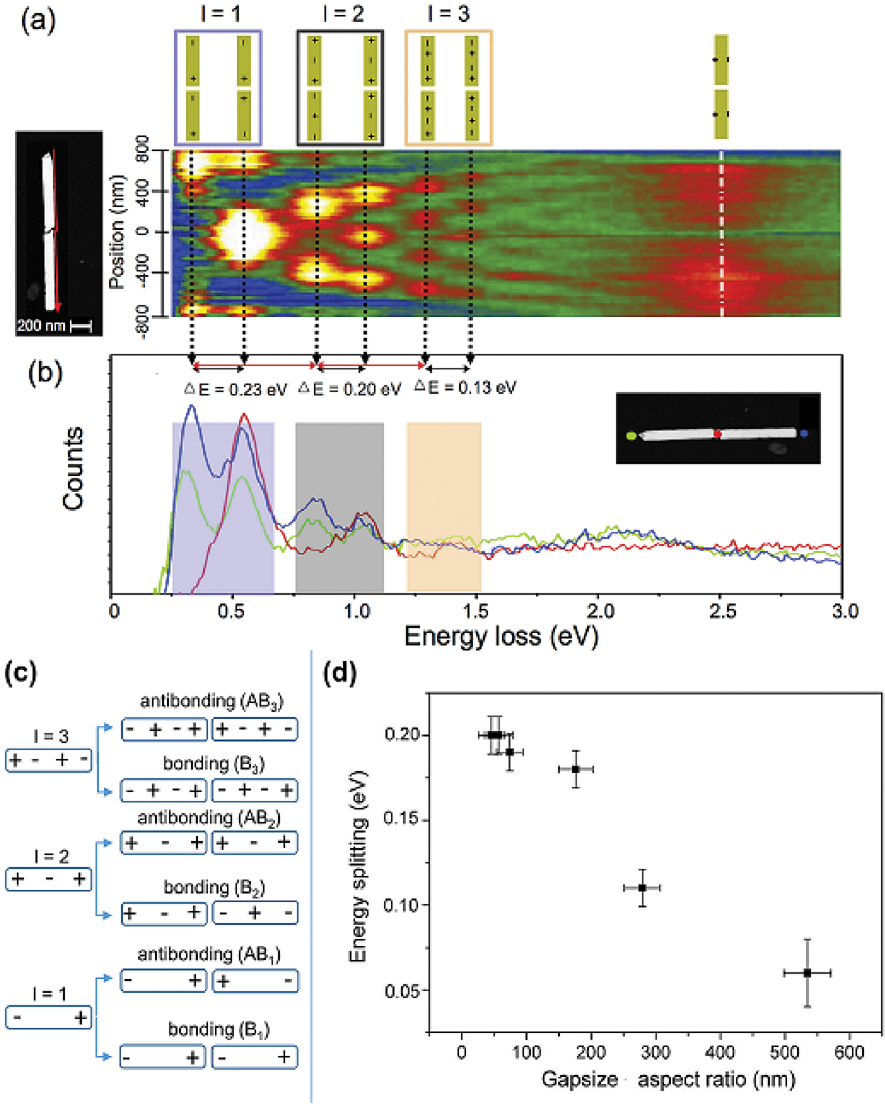

**Figure 11.** (a) STEM-EELS map of nanowire dimer with a gap of about 8 nm. On top of the map the corresponding surface charge distributions of the modes are shown, (b) three spectra measured at the position of the colored dots in the TEM image, (c) hybridization scheme of the dimer for the first three multipole orders and (d) energy splitting for the *l* = 2 bonding and antibonding modes versus gap size times aspect ratio. Adapted with permission from [14] copyright 2011 American Chemical Society.

size influence the energy splitting of the bonding and antibonding modes. For the *l* = 2 modes, the energy difference between bonding and antibonding mode is plotted in **Figure 11d** versus aspect ratio times gap size.

## 3.4. STEM-EELS of coupled nanowires connected by small bridges

Calculations reported in several publications predict that conductively coupled metallic objects can result in extremely conductance sensitive shifts of the resonance energies [18, 57, 70–74].

Such structures are therefore promising platforms for sensing and optical switching applications [18, 74]. Due to difficulties in preparing such structures with controlled dimensions, experimental studies are still rare [21]. As explained in Section 3.1, during the synthesis of nanowire dimers by on-wire lithography from segmented AuAg nanowires, small conductive junctions can remain between two adjacent wires (e.g., **Figure 9b**). This allowed us to perform STEM-EELS analysis on such nanowire dimers with small connections attaining reliable data on the plasmonic properties of these promising systems [34].

**Figure 12** shows a STEM-EELS map of a nanowire dimer where the gap is not completely dissolved, so that a conductive gold bridge remains between the two nanowires. For the dimer, $L$ = 1145 ± 10 nm and $D$ = 90 ± 10 nm. Clearly, seven different multipolar modes can be distinguished that reveal a complex arrangement in energy that differs from the one of a capacitively coupled dimer and as well from the one of a single wire. The schematics on top of the map reveal the charge distribution of these modes that have been identified by simulations of such connected structures (**Figure 10**).

In **Figure 10**, one can see that modes with symmetrical charge distribution (the antibonding modes of the nanowire dimer) do not shift in energy independent on connection size or if a gap is present, whereas all modes of unsymmetrical charge distribution (the bonding modes

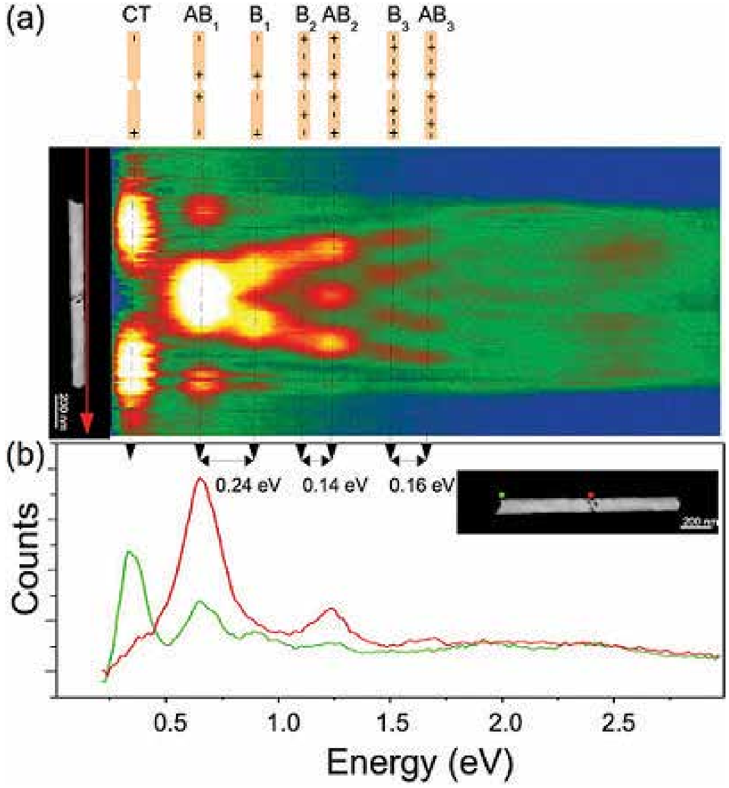

**Figure 12.** (a) STEM-EELS map of a nanowire dimer with metallic connection. (b) Two spectra extracted at the positions of the colored dots in the TEM image. Reprinted with permission from [34]. Copyright 2012 American Chemical Society.

of the nanowire dimer) shift continuously to higher energies with increasing connection size. The strength of the shift decreases with increasing multipole order and results thus in the arrangement seen in **Figure 12** where the bonding mode of first order (labeled with $B_1$ in the figure) is located at higher energy than the corresponding antibonding mode ($AB_1$). However, bonding modes of second and third order ($B_2$ and $B_3$) are observed at lower energies than the corresponding antibonding modes ($AB_2$ and $AB_3$).

The shift of the bonding modes is related to the electric field distribution of the wire in the gap. Therefore, the field distribution of a connected dimer and a continuous wire for modes with formally same number of surface charge maxima should be compared. **Figure 13** shows the electric field distributions of the second-order antibonding mode of the connected dimer (**Figure 13a**) and the $l$ = 4-mode of the continuous wire (**Figure 13b**). Since for antibonding modes the space in the gap is almost field-free, these two modes have identical field distributions and are excited at the same energy. For the field distributions of the second-order bonding mode of the dimer (**Figure 13c**) and the $l$ = 5-mode or the continuous wire (**Figure 13d**) the situation is different: Here a strong field is excited in the gap, shifting the charge maxima in the direction of the gap. The shift to higher energies of the bonding modes is linked to this electric field strength in the gap and decreases thus with increasing multipole order resulting in a completely new mode arrangement compared to dimers with gap.

### 3.5. Mode coupling in heterodimers

Up to now, we have focused only on surface plasmon coupling in structures consisting of two wires with very similar dimensions. In literature, several examples of mode coupling in nanostructures of different material [74–78] or dimensions [35, 79–82] have been reported. **Figure 14** shows clear evidence that surface plasmon coupling is also possible in heterodimers even between modes of different multipole order. The dimer has a diameter $D = 76$ nm ± 5 nm and consists of two wires with length $L_1 = 656$ nm ± 10 nm and $L_2 = 1036$ nm ± 10 nm; the gap size is ~12 nm. **Figure 14a** presents a STEM-EELS map of the dimer. In this map, nine different modes can be identified that are labeled with Arabic numbers on top of the map. In addition, **Figure 14b** shows an EFTEM series of the same dimer. A step size between the images of 0.2 eV (which corresponds also to the slit width) was used. Each image of the series is plotted next to the corresponding mode in the STEM-EELS map. It can be seen that for

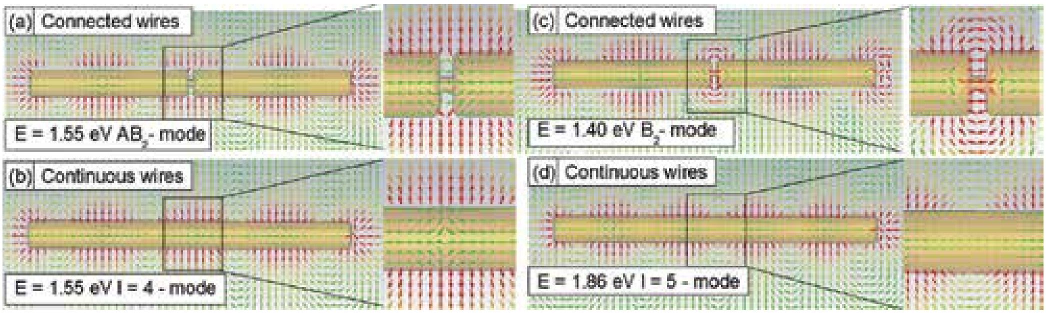

**Figure 13.** Calculated field distributions for the second-order (a) antibonding and (b) bonding mode of the connected dimer and the (c) $l$ = 4 and (d) $l$ = 5 mode of the continuous wire. Reprinted with permission from [34]. Copyright 2012 American Chemical Society.

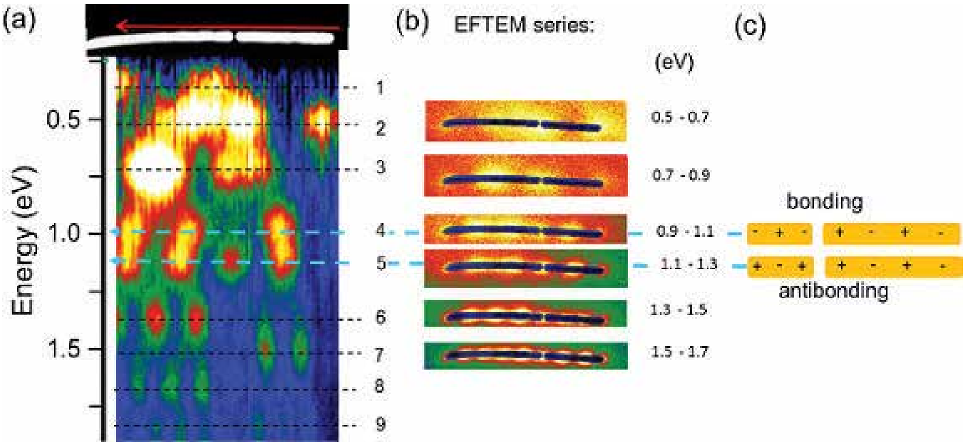

**Figure 14.** (a) EFTEM series of a nanowire heterodimer with 12 nm gap, (b) STEM-EELS map of the same dimer; (c) scheme of the bonding and antibonding mode pair. Adapted from [35] with permission from the Royal Society of Chemistry.

most of the modes, the plasmon mode is more intense either in the long or in the short wire. However, for the modes labeled with 4 and 5, the maxima are very intense along both wires: in this energy interval, in the short wire, the second-order mode ($l_1 = 2$) is active, whereas in the longer wire the third-order mode ($l_2 = 3$) is excited. Both modes couple and form a pair of bonding and antibonding modes as shown schematically in **Figure 14c**. An evidence of such a pair is visible in particular in the STEM map since no maxima can be seen at the gap for mode number 4 which is a typical feature of the bonding mode. The required condition for mode splitting in such unsymmetrical dimers is that in both of the individual wires a mode is excited at almost the same energy as another mode in the second wire, that is, spectral overlap between the two modes of the individual wires has to occur. As follows from Eq. (2), for nanowires, this can, for example, be achieved by designing dimers with length ratio $L_2/L_1 = l_2/l_1$, where $l_2$ and $l_1$ are the multipole orders of the two corresponding modes of the individual wires. In the shown dimer, $L_2/L_1 = 1.58 \pm 0.03$, is deviating only slightly from the ratio between the corresponding multipole orders $l_2/l_1 = 3/2$. Simulations also confirm the spectral overlap of these two modes (see [35]).

## 4. Conclusions

We have shown that STEM-EELS is an extremely powerful technique to analyze surface plasmon modes in nanostructures, and in particular, in nanowires and nanowire dimers. Thanks to its very high spatial resolution, it has been possible to investigate resonance energies of multipole order surface plasmon modes, measure surface plasmon dispersion relations, as well as to analyze surface plasmon excitation on specific positions along the nanostructures.

Cylindrical nanowires are synthesized by electrodeposition in etched ion-track membranes, combined with dealloying. This combination enables the fabrication of nanowires with excellent control on dimension (length, diameter), porosity and composition. These wires are, therefore, excellent model systems to analyze the influence of each parameter on the surface plasmons. Thus, EELS data evidence lower resonance energies for porous wires compared to smooth ones of similar dimensions for both longitudinal and transversal modes. Also, the dispersion relation for the porous nanowires is slightly different from the one of Au and $Au_{0.7}Ag_{0.3}$ nanowires, most probably due a lower bulk plasma frequency of the porous material.

Symmetric and asymmetric dimers separated by small gaps, that is, capacitively coupled, are fabricated by the selective dissolution of short Ag segments in electrodeposited Au/Ag/Au segmented nanowires. In these structures, energy splitting in bonding and antibonding modes was experimentally visualized clearly up to the third multipolar order. If a small metallic junction remains between two adjacent wires, the wires are conductively coupled, and a completely new mode arrangement arises due to an energy shift of the bonding modes. The modes are strongly dependent on the connection size. Finally, mode coupling was also demonstrated for heterodimers consisting of two wires with different length. In these structures, mode coupling is possible if two modes of the individual wires do spectrally overlap. All experimental results are in excellent agreement with finite element calculations.

## Acknowledgements

We acknowledge W. Sigle and P.A. van Aken from MPI Stuttgart for Solid State Physics for their help with EELS measurements and TEM-EDX of our nanowires. The authors thank C. Trautmann for fruitful discussion and her continuous support during the project, as well as L. Burr for his contribution in the synthesis and characterization of Au-based nanowires.

## Author details

Ina Schubert* and Maria Eugenia Toimil-Molares

*Address all correspondence to: i.schubert@gsi.de

GSI Helmholtz Center for Heavy Ion Research GmbH, Darmstadt, Germany

## References

[1] Neubrech F, Pucci A, Cornelius TW, Karim S, Garcia-Etxarri A, Aizpurua J. Resonant plasmonic and vibrational coupling in a tailored nanoantenna for infrared detection. Physical Review Letters. 2008;**101**:157403. DOI: 10.1103/PhysRevLett.101.157403

[2] Maier SA, Kik PG, Atwater HA, Meltzer S, Harel E, Koel BE, Requicha AAG. Local detection of electromagnetic energy transport below the diffraction limit in metal nanoparticle plasmon waveguides. Nature Materials. 2003;**2**:229-232. DOI: 10.1038/nmat852

[3] Clavero C. Plasmon-induced hot-electron generation at nanoparticle/metal-oxide interfaces for photovoltaic and photocatalytic devices. Nature Photonics. 2014;**8**:95-103. DOI:10.1038/nphoton.2013.238

[4] Link S, Mohamed MB, El-Sayed MA. Simulation of the optical absorption spectra of gold nanorods as a function of their aspect ratio and the effect of the medium dielectric constant. The Journal of Physical Chemistry. B. 1999;**103**:3073-3077. DOI: 10.1021/jp990183f

[5] Link S, Wang ZL, El-Sayed MA. Alloy formation of gold−silver nanoparticles and the dependence of the plasmon absorption on their composition. The Journal of Physical Chemistry. B. 1999;**103**:3529-3533. DOI: 10.1021/jp990387w

[6] Khlebtsov BN, Khlebtsov NG. Multipole plasmons in metal nanorods: Scaling properties and dependence on particle size, shape, orientation, and dielectric environment. Journal of Physical Chemistry C. 2007;**111**:11516-11527. DOI: 10.1021/jp072707e

[7] Schider G, Krenn JR, Hohenau A, Ditlbacher H, Leitner A, Aussenegg FR, Schaich WL, Puscasu I, Monacelli B, Boreman G. Plasmon dispersion relation of Au and Ag nanowires. Physical Review B. 2003;**68**:155427. DOI: 10.1103/PhysRevB.68.155427

[8] Dorfmüller J, Vogelgesang R, Weitz RT, Rockstuhl C, Etrich C, Pertsch T, Lederer F, Kern K. Fabry-Pérot resonances in one-dimensional plasmonic nanostructures. Nano Letters. 2009;**9**:2372-2377. DOI: 10.1021/nl900900r

[9] Neubrech F, Kolb T, Lovrincic R, Fahsold G, Pucci A, Aizpurua J, Cornelius TW, Toimil-Molares ME, Neumann R, Karim S. Resonances of individual metal nanowires in the infrared. Applied Physics Letters. 2006;**89**:253104. DOI: 10.1063/1.2405873

[10] Bryant G, Garcia de Abajo FJ, Aizpurua J. Mapping the Plasmon resonances of metallic Nanoantennas. Nano Letters. 2008;**8**:631-636. DOI: 10.1021/nl073042v

[11] Cortie MB, McDonagh AM. Synthesis and optical properties of hybrid and alloy plasmonic nanoparticles. Chemical Reviews. 2011;**111**:3713-3735. DOI: 10.1021/cr1002529

[12] Alkilany AM, Thompson LB, Boulos SP, Sisco PN, Murphy CJ. Gold nanorods: Their potential for photothermal therapeutics and drug delivery, tempered by the complexity of their biological interactions. Advanced Drug Delivery Reviews. 2012;**64**:190-199. DOI: 10.1016/j.addr.2011.03.005

[13] Rossouw D, Couillard M, Vickery J, Kumacheva E, Botton GA. Multipolar plasmonic resonances in silver nanowire antennas imaged with a subnanometer electron probe. Nano Letters. 2011;**11**:1499-1504. DOI: 10.1021/nl200634w

[14] Alber I, Sigle W, Müller S, Neumann R, Picht O, Rauber M, van Aken PA, Toimil-Molares ME. Visualization of multipolar longitudinal and transversal surface plasmon modes in nanowire dimers. ACS Nano. 2011;**5**:9845-9853. DOI: 10.1021/nn2035044

[15] Aizpurua J, Bryant GW, Richter LJ, Garcia de Abajo FJ. Optical properties of coupled metallic nanorods for field-enhanced spectroscopy. Physical Review B. 2005;**71**:235420. DOI: 10.1103/PhysRevB.71.235420

[16] Willingham B, Brandl DW, Nordlander P. Plasmon hybridization in nanorod dimers. Applied Physics B: Lasers and Optics. 2008;**93**:209-216. DOI: 10.1007/s00340-008-3157-5

[17] Qin L, Zou S, Xue C, Atkinson A, Schatz GC, Mirkin CA. Designing, fabricating, and imaging Raman hot spots. PNAS. 2006;**103**:13300-13303. DOI: 10.1073/pnas.0605889103

[18] Perez-Gonzalez O, Zabala O, Borisov AG, Halas NJ, Nordlander P, Aizpurua J. Optical spectroscopy of conductive junctions in plasmonic cavities. Nano Letters. 2010;**10**:3090-3095. DOI: 10.1021/nl1017173

[19] Nordlander P, Oubre C, Prodan E, Li K, Stockman MI. Plasmon hybridization in nanoparticle dimers. Nano Letters. 2004;**4**:899-903. DOI: 10.1021/nl049681c

[20] Chu MW, Myroshnychenko V, Chen CH, Deng JP, Mou CY, Garcia de Abajo FJ. Probing bright and dark surface-plasmon modes in individual and coupled noble metal nanoparticles using an electron beam. Nano Letters. 2009;**9**:399-404. DOI: 10.1021/nl803270x

[21] Duan H, Fernandez-Dominguez AI, Bosman M, Maier SA, Yang JKW. Nanoplasmonics: Classical down to the nanometer scale. Nano Letters. 2012;**12**:1683-1689. DOI: 10.1021/nl3001309

[22] Nelayah J, Kociak M, Stéphan O, Garcia de Abajo FJ, Tencé M, Henrard L, Taverna D, Pastoriza-Santos I, Liz-Marzán LM, Colliex C. Mapping surface plasmons on a single metallic nanoparticle. Nature Physics. 2007;**3**:348-353. DOI: 10.1038/nphys575

[23] Myroshnychenko V, Nelayah J, Adamo G, Geuquet N, Rodríguez-Fernández J, Pastoriza-Santos I, MacDonald KF, Henrard L, Liz-Marzán LM, Zheludev NI, Kociak M, García de Abajo FJ. Plasmon spectroscopy and imaging of individual gold nanodecahedra: A combined optical microscopy, cathodoluminescence, and electron energy-loss spectroscopy study. Nano Letters. 2012;**12**:4172-4180. DOI: 10.1021/nl301742h

[24] Koh AL, Bao K, Khan I, Smith WE, Kothleitner G, Nordlander P, Maier SA, McComb DW. Electron energy-loss spectroscopy (EELS) of surface plasmons in single silver nanoparticles and dimers: Influence of beam damage and mapping of dark modes. ACS Nano. 2009;**3**:3015-3022. DOI: 10.1021/nn900922z

[25] Garcıa de Abajo FJ, Kociak M. Probing the photonic local density of states with electron energy loss spectroscopy. Physical Review Letters. 2008;**100**:106804. DOI: 10.1103/PhysRevLett.100.106804

[26] Garcia de Abajo FJ. Optical excitations in electron microscopy. Reviews of Modern Physics. 2010;**82**:210-262. DOI: 10.1103/RevModPhys.82.209

[27] Sigle W. Analytical transmission electron microscope. Annual Review of Materials Research. 2005;**35**:239-314. DOI: 10.1146/annurev.matsci.35.102303.091623

[28] Kociak M, Stéphan O, Gloter A, Zagonel LF, Tizei LH, Tencé M, March K, Blazit JD, Mahfoud Z, Losquin A, Meuret S, Colliex C. Seeing and measuring in colours: Electron microscopy and spectroscopies applied to nano-optics. Comptes Rendus Physique. 2014;**15**:158-175. DOI: 10.1016/j.crhy.2013.10.003

[29] Kociak M, Stéphan O. Mapping plasmons at the nanoscale in an electron microscope. Chemical Society Reviews. 2014;**43**:3865. DOI: 10.1039/C3CS60478K

[30] Colliex C, Kociak M, Stéphan O. Electron energy loss spectroscopy imaging of surface plasmons at the nanometer scale. Ultramicroscopy. 2016;**162**:A1-A24. DOI: 10.1016/j.ultramic.2015.11.012

[31] Burr L, Schubert I, Sigle W, Trautmann C, Toimil-Molares ME. Surface enrichment in Au-Ag alloy nanowires and investigation of the dealloying process. Journal of Physical Chemistry C. 2015;**119**:20949-20956

[32] Schubert I, Sigle W, Burr L, van Aken PA, Trautmann C, Toimil-Molares ME. Fabrication and plasmonic characterization of Au nanowires with controlled surface morphology. Advanced Materials Letters. 2015;**6**:377-382. DOI: 10.5185/amlett.2015.572

[33] Schubert I, Burr L, Trautmann C, Toimil-Molares ME. Growth and morphological analysis of segmented AuAg alloy nanowires created by pulsed electrodeposition in iontrack etched membranes. Beilstein Journal of Nanotechnology. 2015;**6**:1272-1280. DOI:10.3762/bjnano.6.131

[34] Alber I, Sigle W, Demming-Janssen F, Neumann R, Trautmann C, van Aken PA, Toimil-Molares ME. Multipole surface plasmon resonances in conductively coupled metal nanowire dimers. ACS Nano. 2012;**6**:9711-9717. DOI: 10.1021/nn303149p

[35] Schubert I, Sigle W, van Aken PA, Trautmann C, Toimil-Molares ME. STEM-EELS analysis of multipole surface plasmon modes in symmetry-broken AuAg nanowire dimers. Nanoscale. 2015;**7**:4935. DOI: 10.1039/C4NR06578F

[36] Schaffer B, Hohenester U, Trügler A. High-resolution surface plasmon imaging of gold nanoparticles by energy-filtered transmission electron microscopy. Physical Review B. 2009;**79**:041401. DOI: 10.1103/PhysRevB.79.041401

[37] Bosman M, Keast VJ, Watanabe M, Maaroof AI, Cortie MB. Mapping surface plasmons at the nanometre scale with an electron beam. Nanotechnology. 2007;**18**:165505. DOI: 10.1088/0957-4484/18/16/165505

[38] N'Gom M, Li S, Schatz G, Erni R, Agarwal A, Kotov A, Norris TB. Electron-beam mapping of plasmon resonances in electromagnetically interacting gold nanorods. Physical Review B. 2009;**80**:113411. DOI: 10.1103/PhysRevB.80.113411

[39] Guiton BS, Iberi V, Li S, Leonard DN, Parish CM, Kotula PG, Varela M, Schatz GC, Pennycook SJ, Camden JP. Correlated optical measurements and plasmon mapping of silver nanorods. Nano Letters. 2011;**11**:3482-3488. DOI: 10.1021/nl202027h

[40] Nicoletti O, Wubs M, Mortensen NA, Sigle W, van Aken PA, Midgley PA. Surface plasmon modes of a single silver nanorod: An electron energy loss study. Optics Express. 2011;**19**:15371-15379

[41] Martin J, Kociak M, Mahfoud Z, Proust J, Gerard D, Plain J. High-resolution imaging and spectroscopy of multipolar plasmonic resonances in aluminum nanoantennas. Nano Letters. 2014;**14**:5517-5523. DOI: 10.1021/nl501850m

[42] Karim S, Toimil-Molares ME, Maurer F, Miehe G, Ensinger W, Liu J, Cornelius TW, Neumann R. Synthesis of gold nanowires with controlled crystallographic characteristics. Applied Physics A: Materials Science & Processing. 2006;**84**:403-407. DOI: 10.1007/s00339-006-3645-6

[43] Liu J, Duan JL, Toimil-Molares ME, Karim S, Cornelius TW, Dobrev D, Yao HJ, Sun JM, Hou MD, Mo D, Wang ZG, Neumann R. Electrochemical fabrication of singlecrystalline and polycrystalline Au nanowires: The influence of deposition parameters. Nanotechnology. 2006;**17**:1922-1926. DOI: 10.1088/0957-4484/17/8/020

[44] Dobrev D, Vetter J, Angert N, Neumann R. Periodic reverse current electrodeposition of gold in an ultrasonic field using ion-track membranes as templates: Growth of gold single-crystals. Electrochimica Acta. 2000;**45**:3117-3125. DOI: 10.1016/S0013-4686(00)00478-3

[45] Lee HO, Kim EM, Yu H, Jung JS, Chae WS. Advanced porous gold nanofibers for highly efficient and stable molecular sensing platforms. Nanotechnology. 2009;**20**:325604. DOI: stacks.iop.org/Nano/20/325604

[46] Zhang Q, Large N, Nordlander P, Wang H. Porous Au nanoparticles with tunable plasmon resonances and intense field enhancements for single-particle SERS. Nano Letters. 2014;**5**:370-374. DOI: 10.1021/jz402795x

[47] Ji C, Searson PC. Synthesis and characterization of nanoporous gold nanowires. The Journal of Physical Chemistry. B. 2003;**107**:4494-4499. DOI: 10.1021/jp0222200

[48] Ji C, Searson PC. Fabrication of nanoporous gold nanowires. Applied Physics Letters. 2002;**81**: 4437-4439. DOI: 10.1063/1.1526920

[49] Liu Z, Searson PC, Single PC. Single nanoporous gold nanowire sensors. The Journal of Physical Chemistry. B. 2006;**110**:4318-4322. DOI: 10.1021/jp056940t

[50] Ji C, Oskam G, Ding Y, Erlebacher JD, Wagner AJ, Searson PC. Deposition of AuxAg$_{1-x}$/AuyAg$_{1-y}$ multilayers and multisegment nanowires. Journal of the Electrochemical Society. 2003;**150**:C523. DOI: 10.1149/1.1585053

[51] Johnson LP, Matisons JG. Synthesis of high aspect ratio gold nanowires with highly porous morphology. ISRN Nanomater. 2012;**2012**:1-9. DOI: 10.5402/2012/502960

[52] Yoo SH, Park S. Platinum-coated, nanoporous gold nanorod arrays: Synthesis and characterization. Advanced Materials. 2007;**19**:1612-1615. DOI: 10.1002/adma.200602551

[53] Schubert I, Huck C, Kröber P, Neubrech F, Pucci A, Toimil-Molares ME, Trautmann C, Vogt J. Porous gold nanowires: Plasmonic response and surface-enhanced infrared absorption. Advanced Optical Materials. 2016;**4**:1838-1845. DOI: 10.1002/adom.201600430

[54] Bok HM, Shuford KL, Kim S, Kim SK, Park S. Multiple surface plasmon modes for a colloidal solution of nanoporous gold nanorods and their comparison to smooth gold nanorods. Nano Letters. 2008;**8**:2265-2270. DOI: 10.1021/nl800924r

[55] Brueggeman DAG. Berechnung verschiedener physikalischer Konstanten von heterogenen Substanzen. I. Dielektrizitätskonstanten und Leitfähigkeiten der Mischkörper aus isotropen Substanzen. Annalen der Physik. 1935;**5**:656-679. DOI: 10.1002/andp.19354160802

[56] Prodan E, Radloff C, Halas NJ, Nordlander P. A hybridization model for the plasmon response of complex nanostructures. Science. 2003;**302**:419. DOI: 10.1126/science.1089171

[57] Schnell M, Garcia-Etxarri A, Huber AJ, Crozier K, Aizpurua J, Hillenbrand R. Controlling the near-field oscillations of loaded plasmonic nanoantennas. Nature Photonics. 2009;**3**: 287-291. DOI: 10.1038/nphoton.2009.46

[58] Zuloaga J, Prodan E, Nordlander N. Quantum description of the plasmon resonances of a nanoparticle dimer. Nano Letters. 2009;**9**:887-891. DOI: 10.1021/nl803811g

[59] Piraux L, George JM, Despres JM, Leroy C, Ferain E, Legras R, Ounadjela K, Fert A. Giant magnetoresistance in magnetic multilayered nanowires. Applied Physics Letters. 1994;**65**:2484-2486. DOI: 10.1063/1.112672

[60] Liu K, Nagodawithana K, Searson PC, Chien CL. Perpendicular giant magnetoresistance of multilayered Co/Cu nanowires. Physical Review B. 1995;**51**:7381-7384. DOI: 10.1103/PhysRevB.51.7381

[61] Hernández RM, Richter L, Semancik S, Stranick S, Mallouk TE. Template fabrication of protein-functionalized gold−polypyrrole−gold segmented nanowires. Chemistry of Materials. 2004;**16**:3431-3438. DOI: 10.1021/cm0496265

[62] Valizadeh S, Hultman L, George GM, Leisner P. Template synthesis of Au/Co multilayered nanowires by electrochemical deposition. Advanced Functional Materials. 2002;**12**:766-772. DOI: 10.1002/adfm.200290005

[63] Wang AA, Lee J, Jenikova G, Mulchandani A, Myung NV. Controlled assembly of multisegment nanowires by histidine-tagged peptides. Nanotechnology. 2006;**17**:3375. DOI:10.1088/0957-4484/17/14/006

[64] Nicewarner-Pena SR, Carado AJ, Shale KE, Keating CD. Barcoded metal nanowires: Optical reflectivity and patterned fluorescence. The Journal of Physical Chemistry. B. 2003;**107**:7360-7367. DOI: 10.1021/jp034139i

[65] Burdick J, Alonas E, Huang HC, Rege K, Wang J. High-throughput templated multisegment synthesis of gold nanowires and nanorods. Nanotechnology. 2009;**20**:065306. DOI: 10.1088/0957-4484/20/6/065306

[66] Cho JU, Wu JH, Min JH, Lee JH, Liu HL, Kim YK. Effect of field deposition and pore size on Co/Cu barcode nanowires by electrodeposition. Journal of Magnetism and Magnetic Materials. 2007;**310**:2420-2422. DOI: 10.1016/j.jmmm.2006.10.809

[67] Qin L, Park S, Huang L, Mirkin CA. On-wire lithography. Science. 2005;**309**:113-115. DOI: 10.1126/science.1112666

[68] Bosman M, Ye E, Tan SF, Nijhuis CE, Yang JKW, Marty R, Mlayah A, Arbouet A, Girard C, Han MY. Surface Plasmon damping quantified with an Electron Nanoprobe. Scientific Reports. 2013;**3**:1312. DOI: 10.1038/srep01312

[69] Khoury CG, Norton SJ, Vo-Dinh T. Plasmonics of 3-D nanoshell dimers using multipole expansion and finite element method. ACS Nano. 2009;**3**:2776-2788. DOI: 10.1021/nn900664j

[70] Atay T, Song JH, Numikko AV. Strongly interacting plasmon nanoparticle pairs: From dipole-dipole interaction to conductively coupled regime. Nano Letters. 2004;**4**:1627-1631. DOI: 10.1021/nl049215n

[71] Romero I, Aizpurua J, Bryant GW, Garcia de Abajo FJ. Plasmons in nearly touching metallic nanoparticles: Singular response in the limit of touching dimers. Optics Express. 2006;**14**:9988-9999. DOI: 10.1364/OE.14.009988

[72] Lassiter JB, Aizpurua J, Hernandez JI, Brandl DW, Romero I, Lal S, Hafner JH, Nordlander P, Halas NJ. Close encounters between two nanoshells. Nano Letters. 2008;**8**:1212-1218. DOI: 10.1021/nl080271o

[73] Chau YF, Lin YJ, Tsai DP. Enhanced surface plasmon resonance based on the silver nanoshells connected by the nanobars. Optics Express. 2010;**18**:3510-3518. DOI: 10.1364/OE.18.003510

[74] Perez-Gonzalez O, Zabala N, Aizpurua J. Optical characterization of charge transfer and bonding dimer plasmons in linked interparticle. New Journal of Physics. 2011. DOI:13:083013. DOI: 10.1088/1367-2630/13/8/083013

[75] Bachelier G, Russier-Antoine I, Benichou I, Jonin C, Del Fatti N, Vallée F, Brevet BF. Fano profiles induced by near-field coupling in heterogeneous dimers of gold and silver nanoparticles. Physical Review Letters. 2008;**101**:197401. DOI: 10.1103/Phys RevLett.101.197401

[76] Tumkur T, Yang X, Zhang C, Yang J, Naik GV, Nordlander P, Halas NJ. Wavelength-dependent optical force imaging of bimetallic Al-Au heterodimers. Nano Letters. 2018;**18**:2040-2046. DOI: 10.1021/acs.nanolett.8b00020

[77] Sheikholeslami S, Jun YW, Jain PK, Alivisatos AP. Coupling of optical resonances in a compositionally asymmetric plasmonic nanoparticle dimer. Nano Letters. 2010;**10**:2655-2660. DOI: 10.1021/nl101380f

[78] Flauraud V, Bernasconi GD, Butet J, Alexander DTL, Martin OJF, Brugger J. Mode coupling in plasmonic heterodimers probed with electron energy loss spectroscopy. ACS Nano. 2017;**11**:3485-3495. DOI: 10.1021/acsnano.6b08589

[79] Abb M, Wang Y, Albella P, de Groot CH, Aizpurua J, Muskens OL. Interference, coupling, and nonlinear control of high-order modes in single asymmetric nanoantennas. ACS Nano. 2012;**6**:6462-6470. DOI: 10.1021/nn3021579

[80] Shao L, Fang X, Chen H, Man YC, Wang J, Lin HQ. Distinct plasmonic manifestation on gold nanorods induced by the spatial perturbation of small gold nanospheres. Nano Letters. 2012;**12**:1424-1430. DOI: 10.1021/nl2041063

[81] Bigelow NW, Vaschillo A, Camden JP, Masiello DJ. Signatures of Fano interferences in the electron energy loss spectroscopy and cathodoluminescence of symmetry-broken nanorod dimers. ACS Nano. 2013;**7**:4511-4519. DOI: 10.1021/nn401161n@proofing

[82] Abdulla HM, Thomas R, Swathi RS. Overwhelming analogies between plasmon hybridization theory and molecular orbital theory revealed: The story of plasmonic heterodimers. Journal of Physical Chemistry C. 2018;**122**:7382-7388. DOI: 10.1021/acs.jpcc.8b00503

Chapter 5

# Arbitrary Form Plasmonic Structures: Optical Realization, Numerical Analysis and Demonstration Applications

Quang Cong Tong, Fei Mao, Mai Hoang Luong,
Minh Thanh Do, Rasta Ghasemi, Tran Quoc Tien,
Tho Duc Nguyen and Ngoc Diep Lai

Additional information is available at the end of the chapter

http://dx.doi.org/10.5772/intechopen.79236

## Abstract

Surface plasmon resonance has attracted more and more attention thanks to its wide range of applications in numerous fields (physics, chemistry, biology, etc.). In this chapter, we present different aspects, from theoretical calculation and experimental fabrication to applications demonstration, related to arbitrary shape plasmonic nanostructures. First, numerical calculations based on finite-difference time-domain method were realized to investigate the plasmonic properties of gold nanostructures having various size and shapes. Then the direct laser writing method was demonstrated as an excellent tool for fabrication on demand of arbitrary nanostructures. Plasmonic structures were obtained indirectly by a standard lift-off method from a polymeric template and directly by tightly focusing a continuous-wave laser beam onto a metallic thin film. Finally, demonstration of various applications of fabricated plasmonic structures, namely plasmonic-based data storage, color nanoprinter, tunable filters, and plasmonic-magneto-optics sensors will be shown.

**Keywords:** plasmonics, direct laser writing, one-photon absorption, tunable filter, data storage, color printer, sensor

## 1. Introduction

Since the first scientific observation by Wood in 1902 [1], surface plasmon resonance (SPR) has attracted considerable interest in different domains: physics, chemistry, biology, and so

IntechOpen

© 2018 The Author(s). Licensee IntechOpen. This chapter is distributed under the terms of the Creative Commons Attribution License (http://creativecommons.org/licenses/by/3.0), which permits unrestricted use, distribution, and reproduction in any medium, provided the original work is properly cited. cc BY

on [2–4]. The physical phenomenon of SPR is arisen by light-matter interaction at the interface of metallic and dielectric materials, especially in noble metals, for example, silver and gold [2–4]. The physical mechanism of the SPR can be briefly explained as following. Under irradiation of an electromagnetic (EM) wave, the free electrons in metallic materials are driven to oscillate at the frequency of the external EM field. This electron oscillation at the metallic surface causes a charge separation with respect to the ionic lattice, forming a dipole oscillation along the direction of the electric field of the light. The amplitude of the oscillation reaches maximum at a specific frequency, called SPR frequency, when the incident EM frequency matches the eigenfrequency that relates to the restoring force stemming from the lattice of positive nuclei. For a metallic object with finite dimension, only the electrons on its surface are the most significant since the EM wave can only penetrate a limited depth in metal. Therefore, the collective oscillations of such electrons are called SPR [2].

The SPR band intensity and spectra depend on several factors affecting the electron charge density on the metallic surface, such as the metal type, the dielectric constant of the surrounding medium, particle size, shape, structure, and composition [5]. The plasmonic structures are therefore distinguished into three categories: (i) surface plasmon polariton; (ii) localized surface plasmon resonance; and (iii) plasmonic nano-structures.

Surface plasmon polaritons (SPPs) are EM excitations propagating along the interface between a dielectric and a metal. These EM surface waves arise via the coupling of the EM field to oscillations of the conductor's electron plasma. As a SPP loses energy to the metal due to absorption and scattering, it can only propagate for a finite distance along the interface. Likewise, perpendicularly to the interface, electric field falls off evanescently and can only penetrate into the metal a certain tiny "skin depth" [2], while such an evanescent electric field extends more in the dielectric. Therefore, SPPs are very sensitive to any perturbation within the skin depth and are often used as a very sensitive chemical, biological, or gas sensor [6].

In contrast to SPP, localized surface plasmon resonance (LSPR) occurs when collective oscillations of free electrons are confined to a finite volume, such as metal nanoparticles (NPs), as EM standing waves. The LSPR is excited when the frequency of the incident photons matches the resonance frequency of the NPs. Generally, the LSPR in visible range is obtained with noble NPs with dimensions below 100 nm. The plasmonic properties of metallic NPs vary with their shape and size and are also affected by the refractive index of the surrounding medium. This results in various applications of metallic NPs in different domains, from fundamental science to practical applications [7].

Clearly, the LSPR can strongly and locally amplify the EM field near the metallic surface. It is recently demonstrated that this effect becomes much stronger when two or multiple metallic nano-objects are arranged very close to form the so-called plasmonic nanostructure (PNS) [8]. Two NPs, for example, under an EM illumination can be described as two point dipoles. When (i) NPs are closely spaced (separation $\ll$ light wavelength) and (ii) light polarization is appropriated (longitudinally), these two point dipoles can interact via their near-fields: the restoring force acting on the oscillation electrons of each NP is increased by the charge distribution of their neighboring NP. Therefore, EM field in between this "dimer" can be locally and intensely enhanced, resulting in a hotspot [9]. Following this idea, the plasmonic effect can be also amplified and coupled in an aligned array of metallic NPs (NPA) [10]. A prominent example for coupled SPP nanostructures (NSs) is a nano-hole array (NHA), which is considered as an inverse structure of an NPA [11]. In such a system, the SPP can propagate throughout the NHA surface thanks to the coupling of multiple nano-holes perforated appropriately in a metallic thin film. The properties of plasmon resonance of NHAs and NPAs can be tuned by characteristic length scales and types of arrays such as periodic, quasiperiodic, and aperiodic structures. Such PNSs have great promise for many interesting applications, such as tunable filter and nano-scaled color printing [12].

This chapter deals with different aspects, from theoretical calculation and experimental fabrication to applications demonstration, of two last kinds of SPR, namely, LSPR of metallic NPs and SPP coupling of metallic NHAs. In the first section, numerical calculations based on finite-difference time-domain method will be used to investigate the plasmonic properties of different metallic NSs. We first demonstrate LSPR in individual NPs and show strong relations of plasmon-optical properties on the sizes and shapes of NPs and surrounding media. We also demonstrate a quasi-complete work of gold NHAs for optical bandpass filter and sensing applications. Then, the use of direct laser writing (DLW) technique will be presented in detail, as an excellent method for realization of PNSs on demand. Two practical ways will be demonstrated indirectly via the use of a polymeric template and directly by using an optically induced thermal effect. The advantages of this DLW fabrication method will also be discussed and compared with other fabrication techniques. Finally, plasmonic applications of fabricated PNSs, namely plasmonics-based data storage, color nanoprinter, tunable filters, and plasmonic-magneto-optics sensors will be demonstrated and discussed.

In the last section, some conclusions of the newly developed plasmonic structures and fabrication technique, advantages this technology brings to the plasmonic/nanophotonic field, as well as some prospects, will be shown.

## 2. Numerical investigation of plasmonic nanostructures

Since the discovery of the plasmonic effect, many text books have been produced [2, 13–16] and the theory of this interesting effect can be found easily. We present here only a numerical method to model the analytical theories, especially for some particular plasmonic structures. Actually, there exist different simulation methods which allow to create models of an arbitrary plasmonic structure and to obtain its plasmo-optical properties. Each method presents its own advantages and disadvantages, such as required time processing, computer memory, and simulation precision. We have adopted a very well-known simulation method, which allowed us to achieve rapidly and precisely the plasmo-optical properties of any metallic NSs.

### 2.1. Simulation methodology

Finite-difference time-domain (FDTD) is a numerical analysis method allowing to obtain approximate solutions of electrodynamics problems. FDTD workground was first set in 1928 [17]. However, it only became popular since the1980s thanks to the revolution of information technology [18]. Recently, with the assistance of modern computers, FDTD has become a powerful technique for researchers to predict the EM response of any structure, in particular PNSs. As other finite-difference modeling methods, FDTD is grid-based. It means that computational domains will be meshed into minor units, mostly in a cube shape, with associated vector components of the electric (**E**) field and magnetic (**H**) field, which are determined by Maxwell's equations. In simulation, the **E** and **H** fields are calculated at every point in space, forward in time. Additionally, FDTD is a time-domain method, so it can cover a wide range of frequencies with a single simulation run [19]. Thanks to these advantages, FDTD provides us a natural way to treat any electrodynamics problem, especially periodic structures and broadband sources in PNSs complications.

For calculation of plasmonic properties of all gold (Au) nanostructures (NSs) presented in this chapter, we have performed simulations by using the FDTD method (Lumerical software). **Figure 1** shows the FDTD simulation model. The simulation area was bounded in x- and y-directions by parallel planes in which periodical boundary conditions are defined, while perfectly matched layer metal boundary conditions were applied in top and bottom boundaries to prevent any reflections. The absorbance spectra were calculated from Fourier transform time-dependent transmission monitor. These metallic NSs could be computationally created or imported from real structures, which are reconstructed by using the scanning electron microscope (SEM) and atomic force microscope (AFM) data. Indeed, by using Lumerical software, it is possible to construct models for single or multiple NPs, with changeable particle parameters (size, shape, materials, compositions, etc.). It is also able to simulate NPs organized in order, such as dimer and arrays, with uniform distribution or random distribution. This software also allows to import real SEM and AFM images to simulate with true fabricated structures. Other FDTD model parameters are set as close to characterization conditions: the optical properties of materials were taken from [20] for $SiO_2$ substrate and from [21] for Au thin films.

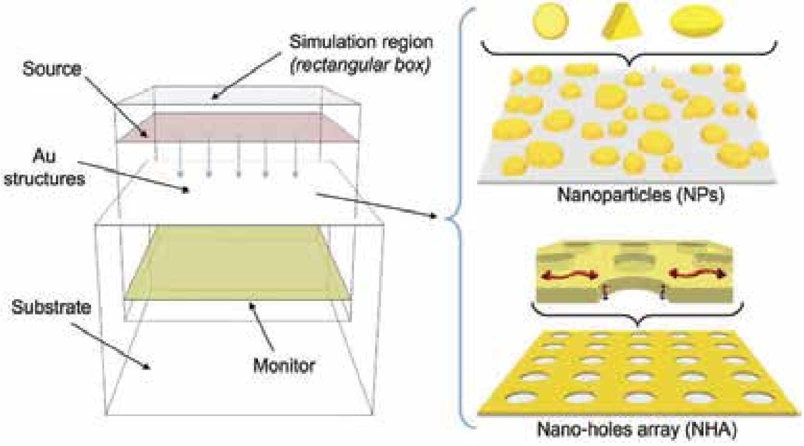

**Figure 1.** FDTD model used to simulate the plasmonic properties of Au NSs, including Au NPs of different shapes and Au NHAs. These NSs could be computationally created or imported from real structures, which are reconstructed by using SEM and AFM data.

### 2.2. Localized surface plasmon resonance

Au NPs possessing particular shapes, such as nano-sphere, nano-rod, and nano-prism, are often fabricated by standard chemical methods, for example, the Turkevich [22], Brust [23] seeded growth [24] or other miscellaneous methods [25]. Those NPs are usually randomly distributed and initially suspended in a solvent such as water. Therefore, they are totally independent, that is, the plasmonic resonance is purely localized and uncoupled. To study the plasmon effect of Au NPs, a simple model consisting of a single NP is demonstrated. The simulation region is a 1 × 1 × 1 $\mu m^3$ box with perfectly matched layer boundary conditions (PML BCs) for all x-, y-, and z-axis. The mesh size of 1 × 1 × 1 $nm^3$ is set in the region encompassing the Au NP and Au-medium interface.

The plasmon resonance frequency is highly sensitive to the refractive index (n) of the surrounding environment. Hence, a change of n results in a shift in the resonant frequency. We have considered a spherical Au NP immersed in various media, such as air, water, or glass. As n near the NP surface increases, the absorption coefficients increase and the absorption spectrum shifts to longer wavelengths as shown in **Figure 2(a)**. Theoretically, this means that the LSPR peak location will be red-shifted if the surrounding medium changes from air to water and to oil.

Optical properties of Au NPs can also be tuned by varying their sizes and shapes. **Figure 2(b)** shows the calculated absorption spectra of Au nano-rods with different aspect ratios (the diameter a was fixed at 15 nm, and the ratio R = 1, 2, 2.5, and 3). We can see that the longitudinal mode, which is commonly referred to the plasmonic band induced by exciting along the long axis of nano-rods, is significantly red-shifted, while the transverse mode, which is commonly referred to the plasmonic band when exciting along the short axis, exhibits a slight blue shift as the aspect ratio R increases.

Consider now another kind of NP, namely Au nano-prism. The size and shape dependence of plasmonic band can also be seen clearly in this case. The LSPR position is highly sensitive to the edge length and the aspect ratio (defined as the ratio d/t between the edge length, d, and

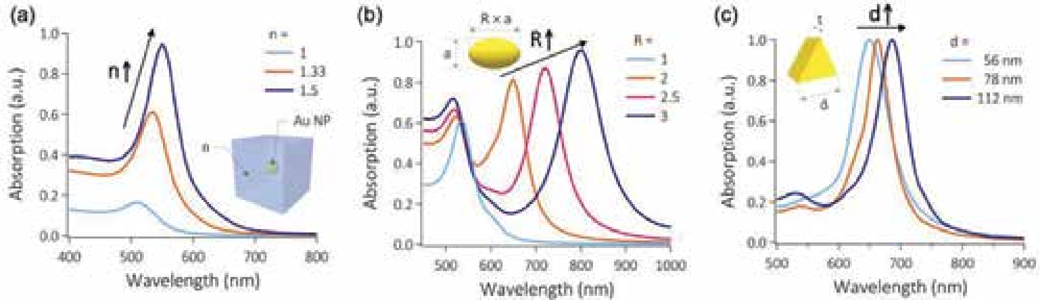

**Figure 2.** (a) Numerical calculation of absorption spectra of Au NPs (diameter d = 50 nm) in different media (air, water, and glass, indicated by its refractive index, n = 1, 1.33, and 1.5, respectively). Inset: Illustration of a single Au NP in a medium with refractive index n. (b) Calculated absorption spectra of Au nano-rods in water with different aspect ratios, R. The diameter of the Au nano-rod is fixed at a = 15 nm. Inset: design of Au nano-rod. (c) Size-dependent absorption spectra of Au prism in water, calculated with different edge-lengths, d. The thickness of the Au prism is fixed at t = 25 nm. Inset: design of Au nano-prism.

thickness, t, of nano-prisms). The larger edge lengths and higher aspect ratio generally result in red shifted resonances. The red shift of the position of the peak maxima (from 642 to 684 nm) corresponds to the edge length of Au nano-prism increases (from 56 to 112 nm) as illustrated in **Figure 2(c)**. This result is quite interesting as compared to that obtained by a spherical NP having a similar size. That allows to easily create different colors by using metallic NPs with different shapes.

From three examples of nano-sphere, nano-rod, and nano-prism, there exists thus a strong dependence of the LSPR peaks (number of modes, location, and intensity) on metallic NPs shape, size, and surrounding medium. Generally, a red shift of absorption spectrum is noticed when NPs size increases. In addition, increment of surrounding refractive index can increase absorption coefficient and enlarge red-shift absorption spectrum. This general observation gives us an insight to construct a numerical model for multiple-sizes/shape nano-islands (NIs) as well as to qualitatively explain their use as plasmonic sensors and/or data storage and color nanoprinter.

### 2.3. Surface plasmon resonance of randomly distributed Au nanoparticles

Another method, called thermal annealing dewetting technique [19, 26, 27], has recently been demonstrated as an excellent way to produce monolayers of randomly distributed Au NPs on a substrate. In this technique, discontinuous thin metallic films are first deposited on a substrate, such as a glass, and then annealed at a temperature of about 500°C. The discontinuous metallic films are thermally melted resulting in isolated metallic NIs. In this case, it is not correct if one calculates the plasmonic properties of only a single NP but it should be done for an ensemble of NPs of various sizes. There exist a few of works in literature, which attempted to model the optical properties of a monolayer of Au NIs [28, 29]. However, most of the works were based on statistical methods to estimate the median parameters of NIs, which required a lot of raw data and statistical analysis efforts. Moreover, in order to simplify the models, an assumption of semispherical NIs was generally used, which might greatly alter the final calculation results since LSPR is highly sensitive to size and shape of NIs.

The calculation method shown in **Figure 1** allowed thus solving completely the problem. This process required only a SEM image and an AFM image. SEM image is utilized to extract the top-view sizes/shapes and (x,y) position coordinates of NIs. This two-dimensional (2D) map is then extruded to three-dimensional (3D) structures with the estimated height from AFM data. **Figure 3** shows the plasmonic resonant spectra of monolayer films of Au NIs with different average NIs sizes. The plasmonic peak located around 550 nm is clearly evidenced. When the particles size increases, the corresponding resonant peaks of the absorption spectra are red-shifted. Theoretically, the resonance peak shifts by a quantity of about 48.5 nm when the average size of NIs changes from 20 to 100 nm. This shift suggests that the structuration of Au NPs by the dewetting method can be a good idea for applications such as tunable absorbers and color nanoprinter.

### 2.4. Surface plasmon resonance in periodic Au nano-holes array

Recently, several strategies have been employed to realize a metallic optical filter, including plasmonic resonators [30], plasmonic metasurfaces for perfect light absorption [31],

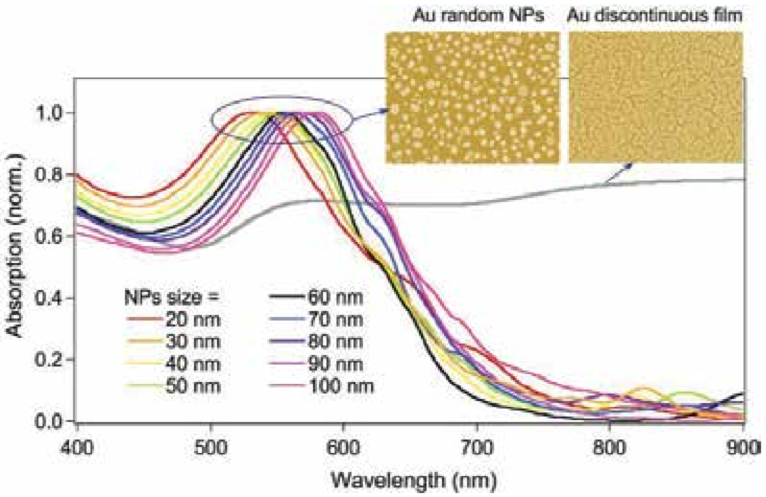

**Figure 3.** Simulation result of absorbance spectra of Au NPs randomly distributed on glass substrates. Different curves correspond to samples having different average NPs sizes. Insets show SEM images of a thin film Au sample obtained before annealing, corresponding to the absorption spectrum of gray color, and of an Au NPs sample obtained after thermal annealing, corresponding to one of the plasmonic resonance absorption spectra.

plasmonic-photonic crystal cavity [32], grating coupler with waveguide resonant grating [33], and so on. In this section, Au NHAs are demonstrated theoretically as an excellent optical bandpass filter via the well-known extraordinary optical transmission (EOT) phenomenon [34]. For complete simulations of NHAs, the parameters were selected and categorized into two groups as described below:

**Fixed parameters**: NHA structures with round holes were chosen because it is the most similar to the structure fabricated by direct laser writing lithography, which will be shown in the fabrication section. The optical constants of silica, Au, and Cr were taken from [20, 21], respectively. Note that Cr is usually used for enhancing the adhesion of Au material with substrates, and it should be thin to avoid the influence of plasmonic properties of Au structures. The periodicity of NHAs was fixed at 1000 nm. The net transmission light was calculated using the arithmetic average of the simulation results of individual and orthogonal polarizations.

**Swept parameters**: the thickness of Au layer and Cr layer were swept from $t_{Au}$ = 10 to 90 nm and $t_{Cr}$ = 0 to 20 nm, respectively. Diameter of the hole was also varied from $d_{hole}$ = 300 to 900 nm. In addition, monitors were set within computation domain to analyze transmission spectra along with EM field distributions. Results were normalized to the transmission spectra obtained from a glass substrate (no NHA) and evaluated right after each simulation to confine the parameters, with a purpose of the fastest convergence.

**Figure 4** shows calculated transmission spectra of Au NHA as a function $t_{Au}$, $t_{Cr}$, and $d_{hole}$. As can be seen in **Figure 4(a)**, the EOT peak position and width depend strongly on the thickness of Au NHA. In detail, this peak was blue-shifted and became shaper when the Au thickness increased. In contrast, an increase of Cr layer thickness suppresses the transmission peaks dramatically (**Figure 4(c)**). Another parameter, which influences greatly the transmission spectrum, is hole diameter, $d_{hole}$. Bigger holes allow higher transmission coefficients; however,

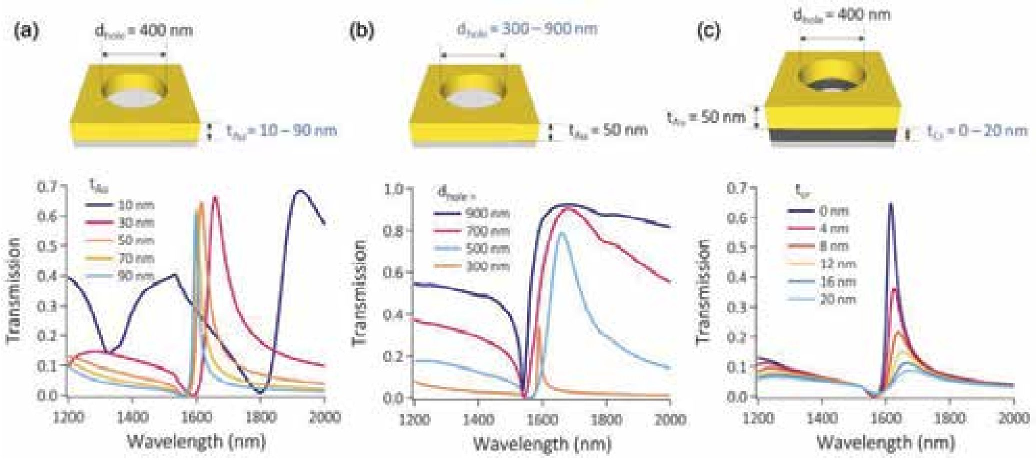

**Figure 4.** Calculated transmission spectra of Au NHAs as a function of Au layer thickness, $t_{Au}$ (a); of nano-hole diameter, $d_{hole}$ (b); and of Cr layer thickness, $t_{Cr,}$ (c), respectively.

band selection is poor. Conversely, smaller holes allow fewer transmission resonance modes, which make transmission peak sharper but also decrease the transmission coefficients. Based on this insight along with advantages and disadvantages of the direct laser writing method, an optimum NHA should have the following parameters: $t_{Au} = 50$ nm, $t_{Cr} = 3$ nm, $\Lambda = 1000$ nm, and $d_{hole} = 400$ nm, respectively.

## 3. Realization of desired plasmonic nanostructures

Different fabrication methods of PNSs have been demonstrated, each possessing its own advantages and drawbacks. For each application, particular metallic NPs or PNSs are required and then a specific fabrication method could be adopted. To form Au NPs and NSs in a small area but with a desired configuration, electron-beam lithography [35, 36] and direct laser writing (DLW) method [37] are two best choices and both are commercially available. Generally, these two methods allow creating PNSs by an indirect way, namely, PNSs are obtained by evaporation of metals on polymeric templates and lift-off. Recently, a direct fabrication method was also demonstrated by using optically induced thermal effect via DLW technique [38]. In this section, the use of DLW will be presented in detail for realization of desired PNSs indirectly and directly.

### 3.1. Direct laser writing method

**Figure 5(a)** illustrates the experimental setup of the DLW system. For realization of 2D PNSs, this DLW involves with a one-photon absorption (OPA) mechanism by using a continuous-wave (cw) laser beam. The sample is a commercial positive photoresist, S1805, for fabrication of PNS by the indirect way. This setup is also used to realize PNSs by the direct way using a sputtered Au film sample. The laser beam, whose wavelength (532 nm) locates the absorption

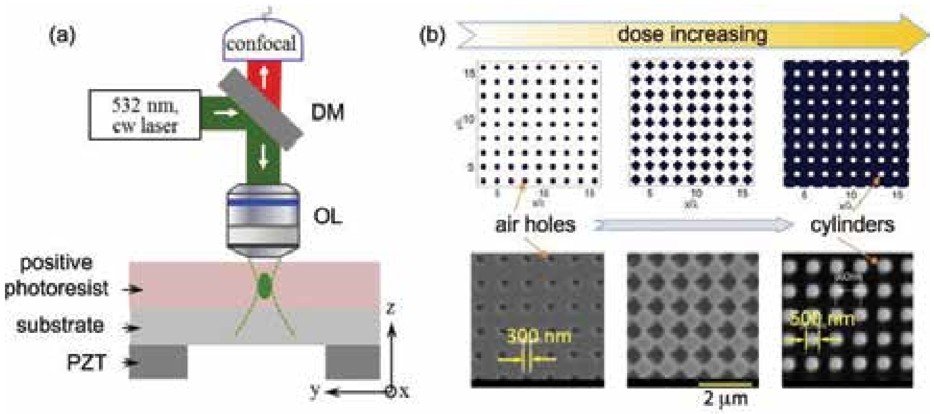

**Figure 5.** (a) Illustration of the DLW technique used to realize arbitrary 2D structures on photoresist and Au film. PZT: piezoelectric translator; DM: dichroic mirror; OL: objective lens. (b) Control of filling factor of structures fabricated on a positive photoresist by adjusting the exposure dose. A 2D square structure is obtained by scanning continuously the focal spot in x- and y-directions. Top: theoretical light pattern; bottom: experimental demonstration. The separation between lines, that is, the period of structure, is Λ = 0.8 μm, and the structures change from negative (air-holes) to positive (polymeric cylinders) forms.

spectrum of both S1805 and Au materials, is tightly focused into samples by a high numerical aperture (NA) objective lens (OL). Since the DLW operates with an OPA mechanism, the required laser power is very modest, in the range of few microwatts for S1805 photoresist and a few dozens of milliwatts for Au films. Thanks to the use of a high NA OL, the light intensity at the focusing region is, however, very high, which is enough for depolymerizing the S1805 photoresist and thermally dewetting the Au films. 3D piezoelectric translator (PZT) connected to a computer control allows the focusing spot to move through the sample following a desired trajectory. By controlling the laser power and the exposure time, the exposure doses are adjusted resulting in structures with desired sizes and forms, as illustrated in **Figure 5(b)**. A detection system consisting of a lenses ensemble, a pinhole, and an avalanche photodiode is used to determine the focusing position, which should be practically located on substrate surface. It should be noted that this DLW is time consuming, like e-beam lithography. Also, in order to keep high resolution, the total area of fabricated structures is limited, generally of about 100x100 μm$^2$. This surface should be enough for various applications, and in case necessary, it could be enlarged by using a PZT with a larger scanning range, together with an increase of fabrication time.

### 3.2. Realization of plasmonic structure by an indirect method

The indirect fabrication of PNSs consists of two steps: (i) fabrication of photoresist templates by DLW method and (ii) transferring templates to metallic structures by evaporation of method and template lift-off. **Figure 6(a)** illustrates the fabrication process of Au NSs by this indirect method. This process is very similar to the fabrication of PNSs by e-beam lithography [35–37]. To fabricate desired structures, the positive photoresist was first coated on cleaned glass substrates and exposed by the DLW system. The samples were then developed, removing all exposed parts and leaving unexposed parts as desired structures. It is demonstrated that the final structures depend strongly on the exposure dose, that is, the laser intensity and the exposure time. Therefore, the filling factor is controlled precisely and both air-holes and dielectric-cylinder structures can be easily and reliably realized (**Figure 5(b)**).

The thin Au film (typical thickness is about 50 nm) is then deposited on the top surface of the polymeric structures by a thermal evaporation technique. As indicated previously, a thin layer of Cr (3 nm) was sputtered in between polymeric templates and the Au film in order to enhance the adhesion of the Au film. The samples were then immersed in acetone to remove the polymeric template, leaving the Au PNSs.

**Figure 6(b)–(d)** shows some examples of 2D PNSs. Depending on the polymeric templates, it is possible to obtain both Au films containing air-holes, that is, NHAs and Au microdisks. The minimum size of the Au microdisks or air-holes is about 300 nm, which is larger than the size limit (about 100 nm) of the polymeric structure fabricated by the DLW. That is because when the polymeric holes or cylinders are small (100 nm), their walls are not vertical and the evaporated Au film is connected between the top and bottom parts of the polymeric structures, influencing the lift-off process. Besides, due to the diffraction limit of the DLW system and also the quality of the positive photoresist during development process, the size of fabricated metallic structures is still large, as compared to those realized by the e-beam lithography technique. A strong effort is currently being made to realize polymeric structures with smaller size and vertical wall, by using, for example, an OL having higher NA, a super-resolution technique to reduce the focusing spot, or a laser with shorter wavelength. Finally, as the most major advantage of the DLW, arbitrary Au NSs can be also realized as shown in **Figure 6(d)**.

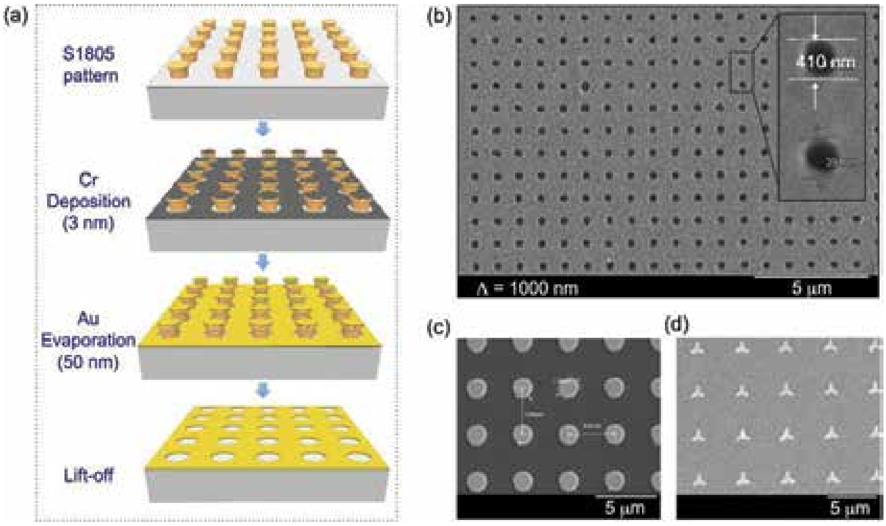

**Figure 6.** (a) Fabrication of plasmonic structures by using polymeric templates. The S1805 structures with controllable period and filling factor are fabricated by the DLW technique. Plasmonic structures are then obtained by a combination of Au evaporation and lift-off techniques. (b–d) SEM images of experimental plasmonic structures: (b) 2D periodic air-holes Au array; (c) periodic array of Au submicrometer disks; (d) arbitrary Au structure.

### 3.3. Direct laser writing of gold nanostructures

In Section 2.3, it is shown that the thermal annealing dewetting technique is a simple and cheap way to realize Au NSs [19, 26, 27]. Conventionally, the dewetting effect is performed on a hot plate or in an oven with an annealing temperature of about 500°C, which results in a large Au NIs areas. In the above section, it is demonstrated that that DLW is a very efficient method that allows the realization of any NS on demand. Recently, this technique is also demonstrated as an excellent method to realize PNSs consisting of Au NPs [38]. For that, the DLW technique employed a cw laser to generate a strong and local heating effect in Au material. This is called optically induced thermal effect by the DLW. This opens up numerous applications of PNSs, which could be experimentally achievable at low cost.

A theoretical model is proposed to investigate the optically induced thermal effect at the focusing spot of the optical system. Physically, due to the strong absorption of the Au material at the excitation wavelength and thanks to the optical intensity distribution, a temperature distribution is produced at the focusing region. **Figure 7** illustrates a tightly focused light beam inside an absorbing medium and the light intensity distribution as well as the heat profile at the focusing region. The light intensity distribution (**Figure 7(b)**) is rigorously calculated by using the vector Debye method [39]. By using finite element method with MATLAB PDE solver, the thermal effect model is numerically solved providing the heat profile as shown in **Figure 7(c)**. By using a DLW method with a cw laser, it is theoretically demonstrated that the induced temperature at the focusing spot rises up quickly as a function of exposure time

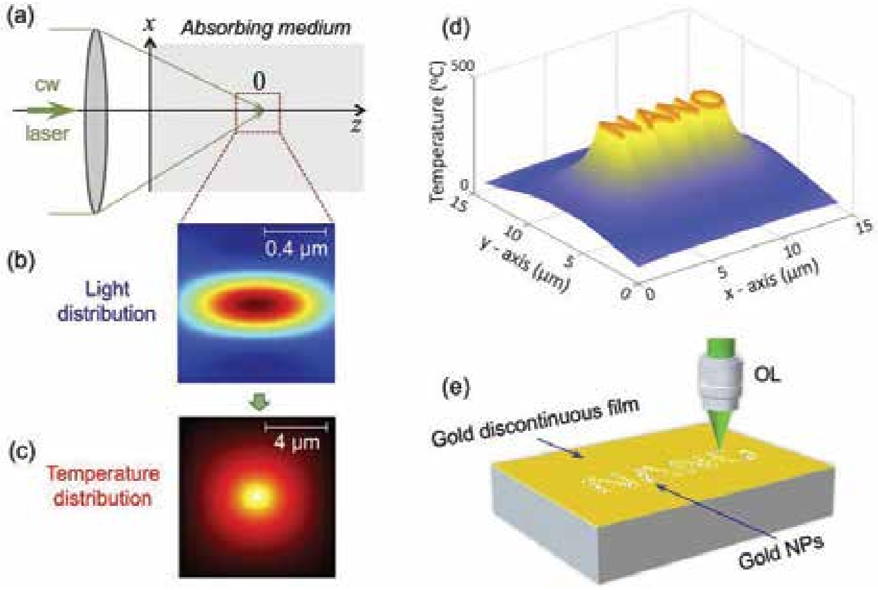

**Figure 7.** (a) Illustration of a tightly focused light beam inside an absorbing medium. (b) Theoretical calculation of light intensity distribution in xz-plane at the focal region of a high NA OL. (c) Corresponding temperature distribution at the focal region. (d) Temperature pattern (NANO letter) obtained by scanning the focusing spot in xy-plane. (e) Illustration of the formation of arbitrary Au NSs by optically induced thermal effect.

and reaches a stable temperature, approximately 500°C, with an excitation laser power of 40 mW. By moving the focusing spot following a desired trajectory, it is possible to create an arbitrary pattern, such as the "NANO" letter as shown in **Figure 7(d)**. This high temperature can significantly change the morphologies and optical responses of the Au thin film [38]. This thus allows one to realize in a direct way the desired PNSs.

The DLW setup used to directly realize PNSs is same as that illustrated in **Figure 5(a)**, except that the photoresist sample is replaced by a sputtered Au thin sample. These samples were prepared on pretreated glass substrates by a magnetron sputtering technique, with an Au thickness of about 12 nm. The laser focusing spot is moved in 2D space (xy-plane) following a desired trajectory. The typical laser power is a range of 40 mW, which results in a local light intensity of about $10^{11}$ W/m$^2$. This high intensity induces a local temperature of about 500°C, which could then locally form Au NIs via the dewetting effect. Using an appropriate laser power, the reasonable exposure times are about 1–100 ms for a single spot or the scanning speeds are about 1–50 μm/s for patterns.

First of all, the optically induced thermal effect is demonstrated by the creation of Au NIs as a function of the scanning speed and of the laser power. In order to obtain a well-defined area of Au NPs, the raster scan is used by the DLW technique. **Figure 8(a)** shows the optical microscope image of the fabricated samples. As the laser exposure dose changes, the color of Au NIs samples changes, suggesting a variation of the NIs sizes. **Figure 8(b)** shows the SEM image confirming the creation of Au NPs, whose size was estimated by a histogram to be about 60 nm. **Figure 8(c)** shows the measured absorption spectra of the corresponding samples, obtained before and after light exposure. The plasmonic resonance peak is clearly observed at a wavelength of about 550 nm.

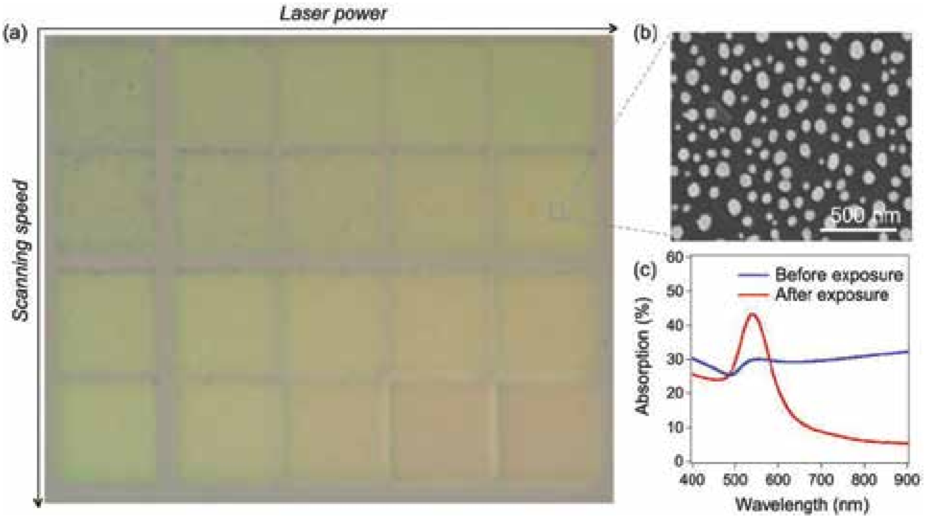

**Figure 8.** (a) Optical microscope image of Au NPs samples realized by using different exposure doses (laser powers and scanning speeds) of the DLW. (b) SEM image of Au NPs sample. (c) Experimental measurement of the plasmon resonance spectrum of the Au NSs obtained before and after laser exposure.

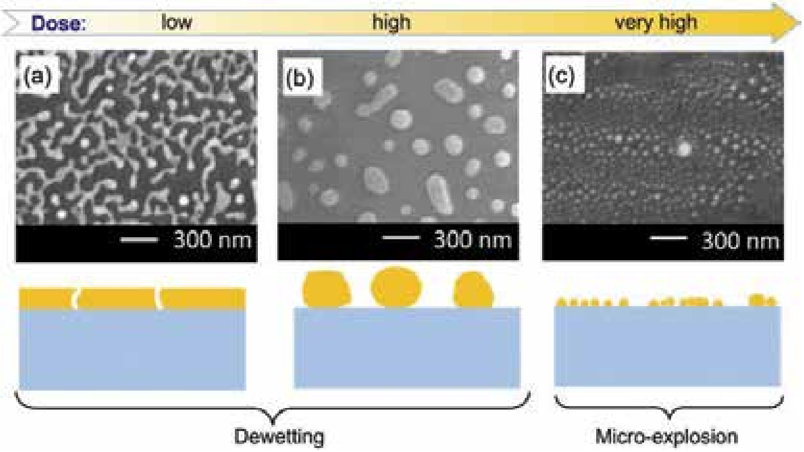

**Figure 9.** Dependence of the exposure dose on the formation of Au NPs. (a) SEM image of an Au discontinuous film, sputtered on a glass substrate. (b), (c) SEM images of Au NPs obtained by scanning a focused laser beam with a power of 40 mW and with scanning velocities of 20 μm/s (b) and 0.5 μm/s (c), respectively. Bottom line: Illustrations of Au film morphological transformation and mechanism as a function of the exposure dose.

It is worth to mention that there is some limit for the laser intensities, otherwise the induced temperature becomes too high, in particular after the formation of NPs, resulting in an explosion effect. **Figure 9** shows the effect of exposure dose, that is, laser intensity, on the formation of Au NPs. First, when the exposure dose is increased, the induced temperature increased resulting in the formation of well-separated Au NPs (**Figure 9(b)**). However, if the exposure dose increased strongly, the Au NPs exploded resulting in very small Au NPs (**Figure 9(c)**). When the laser intensity became too high, the Au material totally evaporated. Thus, by controlling the fabrication parameters, the morphology of Au NIs could be varied, which is quite important for further development of this method in various applications such as data storage, plasmonic band-pass filter, and color printing.

Indeed, thanks to the flexibility and versatility of the laser induced local thermal dewetting method, it is possible to write PNSs at high levels of complexities. **Figure 10** shows two

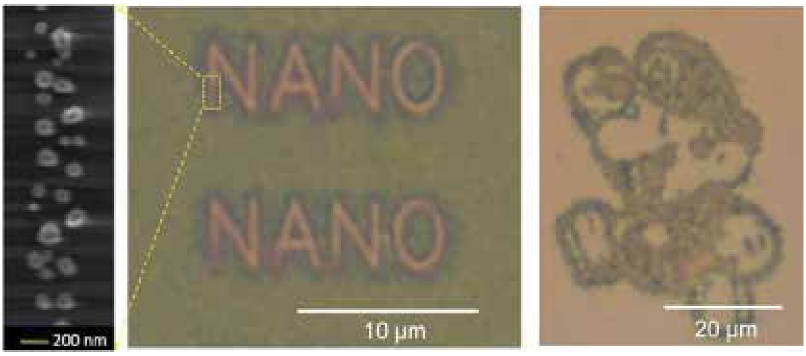

**Figure 10.** Optical microscope images of plasmonic patterns consist of Au NPs, realized by the optically induced thermal effect via DLW technique: “NANO” letter and “Mario” image. In the left: a SEM image of the Au NPs.

examples of the PNSs consisting of Au NIs: a "NANO" letter consisted of Au NPs as demonstrated by the SEM image and a "Mario" image consisted of Au NPs having different sizes, as seen by different colors.

## 4. Potential applications of fabricated plasmonic nanostructures

Nowadays, plasmonics appear in many different domains with numerous interesting applications and continue to attract more and more attention. Of course, these applications depend strongly on the fabrication technologies that may or may not allow to produce PNSs as desired. In this section, a few interesting applications related to PNSs fabricated by the DLW method will be presented, particularly for plasmonics-based sensor, optical filter, data storage, and color nanoprinter.

### 4.1. Applications of plasmonic nano-hole arrays

**Figure 11(a)** shows an experimental setup used to measure the transmission of NHAs fabricated previously by the indirect method. A supercontinuum laser ($\lambda$ = 1200–1700 nm) is used as the illumination source. The beam was expanded and focused through NHA structure by an OL (NA = 0.4). The surrounding media of NHA can be easily changed from air to water

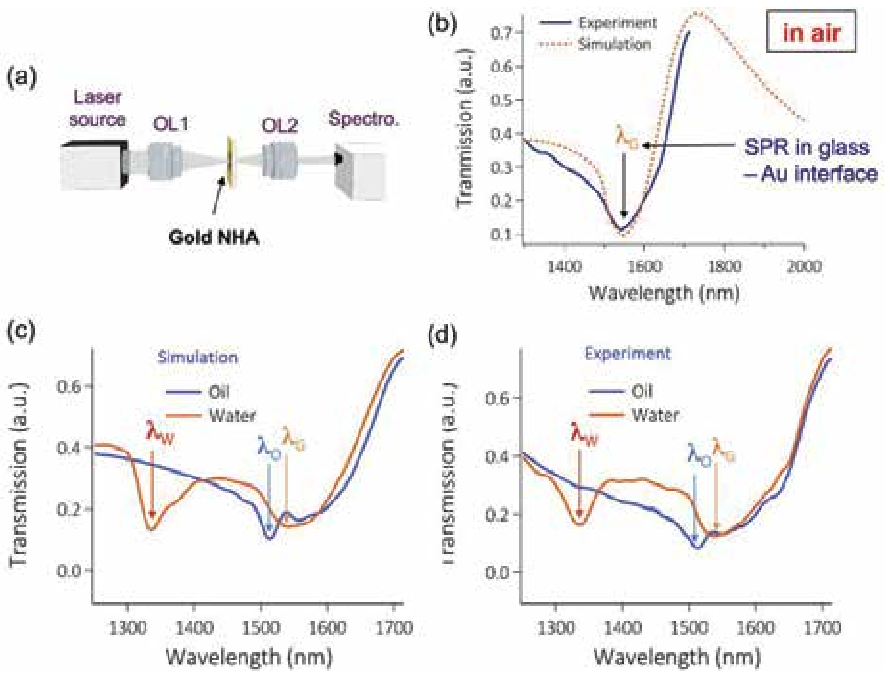

**Figure 11.** (a) Experimental setup of Au NHA transmission measurement. (b) Experimental and theoretical results of transmission spectra in air of fabricated Au NHA structures. (c) Experimental and (d) calculating transmission spectra of Au NHA structures in different media. For all simulations: $\Lambda$ = 1000 nm, $d_{hole}$ = 400 nm, $t_{Au}$ = 50 nm, and $t_{Cr}$ = 15 nm.

and to oil by simply casting a drop of desired medium. The transmission spectra was collected by another OL and transmitted to a spectrometer. The experimental results were summarized and compared to predicted simulation results.

A remarkable similarity between experimental results and theoretical calculations is emphasized in **Figure 11(b)** for a sample immersed in air. We can observe a transmission dip around 1535 nm and a transmission peak located at about 1750 nm. The experimental transmission spectrum follows the evolution trend of calculation. However, due to the limitation of the detection range of the spectrometer, it is not possible to fully characterize this transmission band of the fabricated NHA, in particular, for the transmission peak. Therefore, the transmission dip corresponding to SPR band on the interface of gold-glass substrate is exploited further. From simulation (**Figure 11(c)**), a transmission dip is predicted approximately close to the wavelength of $\Lambda \times n$ with n as the refractive index of surrounding media, that is, transmission dips around 1330 and 1500 nm for water and oil, respectively. Those dips are effectively observed experimentally and shown in **Figure 11(d)**. The transmission dip at $\lambda_G \approx 1535$ nm (corresponding to SPR at glass-Au interface, called glass-mode) was unchanged in all three cases of water, oil, and air. Another dip appears at $\lambda_W \approx 1335$ nm when the NHA was embedded in water, called water-mode. This dip red-shifted to $\lambda_O \approx 1510$ nm when the NHA was immersed in oil, called oil-mode. This suggests a great application as plasmonics-based sensor if the surrounding medium of the NHA changes.

### 4.2. Plamonic-based data storage and color nanoprinters

The newly developed optically induced thermal effect by DLW technique allows imaging many applications at nanoscale. For a demonstration, different PNS were realized and several examples are shown in **Figure 12**. By this way, stereoscopic images can be encoded in the NSs and can be potentially used as elements for data storage and color nanoprinter applications. The stored data can be coded (binary code, alphabet letter, etc.) and programmed into the trajectory of laser scanning to directly write data on metallic materials.

**Figure 12(a)** shows an example of the "NANO LETTERS" words made by Au NIs. The height of the word can be as small as 1 μm. Generally, any nano text can be written by this DLW

**Figure 12.** (a) Optical microscope image of the plasmonic text ("NANO LETTERS" with different sizes) realized by the DLW technique. (b) Optical image of a quick response (QR) code, which links to the website of the author's laboratory (LPQM).

method and read by plasmonic effect. **Figure 12(b)** illustrates a quick response (QR) code, which links to the website of the author's laboratory (LPQM). Bar code (1D) or QR code (2D) is a fast, easy, and accurate data storage method enabling products to be tracked efficiently and accurately. In particular, QR code attracts more attention in e-commerce because it also improves mobile user experience by convenient and easy operation.

Furthermore, as mentioned previously, the DLW technique allows production of any structures at nanoscale. **Figure 13** shows the result of a real image: a real "experiment book" of French laboratories. The real photo was imported to a MATLAB image, and each pixel was transferred to an exact dose of the light exposure, resulting in a plasmonic image of this "experiment book" at microscale. The image color is quite faithful to the original one, but theoretically and experimentally limited in the green and yellow color domain. That could be explained by the result shown in the simulation section, which predicted that the plasmonic resonance shifts only about 48 nm when the particles size changes from 20 to 100 nm. It is theoretically expected that a variety of colors could be obtained by organizing these Au NIs in order, like 1D and 2D PNSs [10, 11]. The combination of LSPR and PNS will offer a large possibility to tune the color.

### 4.3. About resonantly enhanced plasmonic magneto-optics

The magneto-optical (MO) sensors are a powerful sensing platform based on the Faraday or Kerr effects, that is, the rotation of linearly polarized light when it passes through or reflects from a magnetic thin film under influence of an external magnetic field [40]. However, conventional MO sensor cannot be used as a refractometer since it is not sensitive to minute

**Figure 13.** The color printed image fabricated by the DLW method on Au film. Left: a real "experiment book". Right: a plasmonic image of corresponding book at microscale.

changes of refractive index; therefore, such a sensor is not suitable for gas, chemical, and biological sensing applications. Recently, it has been discovered that when the MO active media is coupled with PNSs, the strong local EM fields produced through LSPR or SPP interact strongly with ambient magnetic materials. Consequently, the MO property of the magnetic media could be significantly enhanced at these LSPR/SPP resonance wavelengths [41, 42]. Since magnetic materials possess weak plasmonic property, most current PMO materials for sensors are layered films made by noble metal (Au, Al, and Ag) films and magnetic (Ni, Co, Fe, or magnetic insulators) films [43]. The DLW method is an excellent tool for fabrication on demand of arbitrary NHAs, whose plasmonic property and hence PMO performance may be significantly enhanced. It is expected that the PMO sensors have advantages over the corresponding plasmonic sensors and will be fully explored.

## 5. Conclusion

In summary, this chapter reports systematically most aspects related to arbitrary plasmonic nanostructures, in particular those realized by the direct laser writing technique. In the first section, the optical properties of very basic nanostructures are completely investigated by using a well-known FDTD simulation method. Real fabricated metallic structures are also imported to a simulation model and calculated accurately. These investigations offer a short but understandable image of plasmonic properties of various nanostructures and guide for applications of plasmonic nanostructures in different domains. In the second section, the direct laser writing technique is demonstrated as an excellent method for realization of desired plasmonic nanostructures on demand. The fabrication of plasmonic nanostructures is demonstrated in two ways: indirectly via the use a polymeric template and directly by exploiting the optically induced local thermal effect. Any plasmonic microstructures with desired size, shape, and color were obtained by controlling the writing pattern and the exposure doses (laser power and writing speed). Finally, several important applications of plasmonic nanostructures, in particular those realized by direct laser writing method, have been demonstrated. Namely, the nano-holes arrays are demonstrated as excellent optical bandpass filters and also sensitive plasmonics-based sensor. The plasmonic nano-islands realized by optically induced thermal effect offered an excellent way for data storage and color nanoprinter. It is clear that those fabricated structures could be useful for a wide range of applications in numerous fields (physics, chemistry, biology, etc.).

## Acknowledgements

This work is supported by a public grant overseen by the French National Research Agency (ANR) (project: GRATEOM) and by a public grant of Ministry of Science and Technology of Vietnam (project: DTDLCN.01/2017).

## Author details

Quang Cong Tong[1,2], Fei Mao[1], Mai Hoang Luong[1,3], Minh Thanh Do[1,4], Rasta Ghasemi[5], Tran Quoc Tien[2], Tho Duc Nguyen[3] and Ngoc Diep Lai[1]*

*Address all correspondence to: ngoc-diep.lai@ens-paris-saclay.fr

1 Laboratoire de Photonique et Moléculaire, UMR 8537, Ecole Normale Supérieure de Cachan, CentraleSupélec, CNRS, Université Paris-Saclay, Cachan, France

2 Institute of Materials Sciences, Vietnam Academy of Science and Technology, Hanoi, Vietnam

3 Department of Physics and Astronomy, University of Georgia, Athens, Georgia, USA

4 Hanoi National University of Education, Hanoi, Vietnam

5 Institute D'Alembert, Ecole Normale Supérieure Paris-Saclay, Cachan, France

## References

[1] Wood RW. On a remarkable case of uneven distribution of light in a diffraction grating spectrum. The London, Edinburgh, and Dublin philosophical magazine and. Journal of Science. 1902;**4**:396-402. DOI: 10.1080/14786440209462857

[2] Maier SA. Plasmonics: Fundamentals and Applications. New York Inc.: Springer Science & Business Media; 2007. DOI: 10.1007/0-387-37825-1

[3] Stewart ME, Anderton CR, Thompson LB, Maria J, Gray SK, Rogers JA, Nuzzo RG. Nanostructured plasmonic sensors. Chemical Reviews. 2008;**108**:494-521. DOI: 10.1021/cr068126n

[4] Halas NJ, Lal S, Chang WS, Link S, Nordlander P. Plasmons in strongly coupled metallic nanostructure. Chemical Reviews. 2011;**111**:3913-3961. DOI: 10.1021/cr200061k

[5] Hutter E, Fendler JH. Exploitation of localized surface plasmon resonance. Advanced Materials. 2004;**16**:1685-1706. DOI: 10.1002/adma.200400271

[6] Homola J, Yee SS, Gauglitz G. Surface plasmon resonance sensors: review. Sensors and Actuators B: Chemical. 1999;**54**:3-15. DOI: 10.1016/S0925-4005(98)00321-9

[7] Jimenez de Aberasturi D, Serrano-Montes AB, Liz-Marzán LM. Modern applications of plasmonic nanoparticles: From energy to health. Advanced Optical Materials. 2015;**3**:602-617. DOI: 10.1002/adom.201500053

[8] Barnes WL, Dereux A, Ebbesen TW. Surface plasmon subwavelength optics. Nature. 2003;**424**:824-830. DOI: 10.1038/nature01937

[9] Ringler M, Schwemer A, Wunderlich M, Nichtl A, Kurzinger K, Klar TA, Feldmann J. Shaping emission spectra of fluorescent molecules with single plasmonic nanoresonators. Physical Review Letters. 2008;**100**:203002. DOI: 10.1103/PhysRevLett.100.203002

[10] Wang X, Gogol P, Cambril E, Palpant B. Near- and far-field effects on the plasmon coupling in gold nanoparticle arrays. Journal of Physical Chemistry C. 2012;**116**:24741-24747. DOI: 10.1021/jp306292r

[11] Chanda D, Shigeta K, Truong T, Lui E, Mihi A, Schulmerich M, Braun PV, Bhargava R, Rogers JA. Coupling of plasmonic and optical cavity modes in quasi-three-dimensional plasmonic crystals. Nature Communications. 2011;**2**:479. DOI: 10.1038/ncomms1487

[12] Zijlstra P, Chon JWM, Gu M. Five-dimensional optical recording mediated by surface plasmons in gold nanorods. Nature. 2009;**459**:410-413. DOI: 10.1038/nature08053

[13] Brongersma ML, Kik PG, editors. Surface Plasmon Nanophotonics. Vol. 131. Springer Series in Optical Sciences. Netherlands: Springer; 2007. 268 p. DOI: 10.1007/978-1-4020-4333-8

[14] Enoch S, Nicolas B, editors. Plasmonics: From Basics To Advanced Topics. Springer Series in Optical Sciences. Vol. 167. Berlin Heidelberg: Springer-Verlag; 2012. 321 p. DOI 10.1007/978-3-642-28079-5

[15] Bozhevolnyi SI, Martin-Moreno L, Garcia-Vidal F, editors. Quantum Plasmonics. Vol. 185. Springer Series in Solid-State Sciences. Switzerland: Springer International Publishing; 2017. 327 p. DOI 10.1007/978-3-319-45820-5

[16] Shahbazyan TV, Stockman MI, editors. Plasmonics: Theory and Applications. Springer Series in Challenges and Advances in Computational Chemistry and Physics. Vol. 15. Netherlands: Springer; 2013. 577 p. DOI 10.1007/978-94-007-7805-4

[17] Courant R, Friedrichs K, Lewy H. Über die partiellen Differenzengleichungen der mathematischen Physik. Mathematische Annalen. 1928;**100**:32-74. DOI: 10.1007/BF01448839

[18] Taflove A, Hagness SC, editors. Computational Electrodynamics: The Finite-Difference Time-Domain Method. 2nd ed. Norwood MA: Artech House; 1995. 1006 p

[19] Do MT, Tong QC, Luong MH, Lidiak A, Ledoux- Rak I, Lai ND. Fabrication and characterization of large-area unpatterned and patterned plasmonic gold nanostructures. Journal of Electronic Materials. 2016;**45**:2347-2353. DOI: 10.1007/s11664-015-4291-6

[20] Palik ED editor. Handbook of Optical Constants of Solids. USA: Academic Press; 1985. 804 p

[21] Johnson PB, Christy RW. Optical constants of the noble metals. Physical Review B. 1972; **6**:4370. DOI: 10.1103/PhysRevB.6.4370

[22] Turkevich J, Stevenson PC, Hillier J. A study of the nucleation and growth process in the synthesis of colloidal gold. Discussions of the Faraday Society. 1951;**11**:55-75. DOI: 10.1039/DF9511100055

[23] Brust M, Walker M, Bethell W, Schriffin DJ, Whyman R. Synthesis of thiol-derivatised gold nanoparticles in a two phase liquid system. Journal of the Chemical Society, Chemical Communications. 1994;**0**:801-802. DOI: 10.1039/C39940000801

[24] Xu ZC, Shen CM, Xiao CW, Yang TZ, Zhang HR, Li JQ, Li HL, Gao HJ. Wet chemical synthesis of gold nanoparticles using silver seeds: A shape control from nanorods to hollow spherical nanoparticles. Nanotechnology. 2007;**18**:115608. DOI: 10.1088/0957-4484/18/11/115608

[25] Karakouz T, Tesler AB, Bendikov TA, Vaskevich A, Rubinstein I. Highly stable localized plasmon transducers obtained by thermal embedding of gold island films on glass. Advanced Materials. 2008;**20**:3893-3899. DOI: 10.1002/adma.200703092

[26] Gupta G, Tanaka D, Ito Y, Shibata D, Shimojo M, Furuya K, Mitsui K, Kajikawa K. Absorption spectroscopy of gold nanoisland films: Optical and structural characterization. Nanotechnology. 2009;**20**:025703. DOI: 10.1088/0957-4484/20/2/025703

[27] Kang M, Park S, Jeong K. Repeated solid-state dewetting of thin gold films for nanogap-rich plasmonic nanoislands. Scientific Reports. 2015;**5**:14790. DOI: 10.1038/srep14790

[28] Axelevitch A, Apter B, Golan G. Simulation and experimental investigation of optical transparency in gold island films. Optics Express. 2013;**21**:4126-4138. DOI: 10.1364/OE.21.004126

[29] Ozhikandathil J, Packirisamy M. Simulation and implementation of a morphology-tuned gold nano-islands integrated plasmonic sensor. Sensors. 2014;**14**:10497-10513. DOI: 10.3390/s140610497

[30] Xu T, Wu YK, Luo X, Guo LJ. Plasmonic nanoresonators for high-resolution colour filtering and spectral imaging. Nature Communications. 2010;**1**:59. DOI: 10.1038/ncomms1058

[31] Cheng F, Gao J, Luk TS, Yang X. Structural color printing based on plasmonic metasurfaces of perfect light absorption. Scientific Reports. 2015;**5**:11045. DOI: 10.1038/srep11045

[32] Wang X, Palpant B. Large and ultrafast optical response of a one-dimensional plasmonic-photonic cavity. Plasmonics. 2013;**8**:164-1653. DOI: 10.1007/s11468-013-9583-1

[33] Daghestani HN, Day BW. Theory and applications of surface plasmon resonance, resonant mirror, resonant waveguide grating, and dual polarization interferometry biosensors. Sensors. 2010;**10**:9630-9646. DOI: 10.3390/s101109630

[34] Ebbesen TW, Lezec HJ, Ghaemi H, Thio T, Wolff R. Extraordinary optical transmission through sub-wavelength hole arrays. Nature. 1998;**391**:667-669. DOI: 10.1038/35570

[35] Grigorenko AN, Geim AK, Gleeson HF, Zhang Y, Firsov AA, Khrushchev IY, Petrovic J. Nanofabricated media with negative permeability at visible frequencies. Nature. 2005; **438**:355-338. DOI: 10.1038/nature04242

[36] Steinbruck A, Choi JW, Fasold S, Menzel C, Sergeyev A, Pertsch T, Grange R. Plasmonic heating with near infrared resonance nanodot arrays for multiplexing optofluidic applications. RSC Advances 2014;**4**:898. DOI: 10.1039/C4RA13312A

[37] Tong QC, Luong MH, Tran TM, Remmel J, Do MT, Kieu DM, Ghasemi R, Nguyen DT, Lai ND. Realization of desired plasmonic structures via a direct laser writing technique. Journal of Electronic Materials. 2017;**46**:3695-3701. DOI: 10.1007/s11664-016-5131-z

[38] Tong QC, Luong MH, Remmel J, Do MT, Nguyen DTT, Lai ND. Rapid direct laser writing of desired plasmonic nanostructures. Optics Letters. 2017;**42**:2382. DOI: 10.1364/OL.42.002382

[39] Li Q, Do MT, Ledoux-Rak I, Lai ND. Concept for three-dimensional optical addressing by ultralow one-photon absorption method. Optics Letters. 2013;**38**:4640-4643. DOI: 10.1364/OL.38.004640

[40] Scott G, Lacklison D. Magnetooptic properties and applications of bismuth substituted iron garnets. IEEE Transactions on Magnetics. 1976;**12**:292-311. DOI: 10.1109/TMAG.1976.1059031

[41] Armelles G, Cebollada A, García-Martín A, González MU. Magnetoplasmonics: Combining magnetic and plasmonic functionalities. Advanced Optical Materials. 2013;**1**:10-35. DOI: 10.1002/adom.201200011

[42] Clavero C, Yang K, Skuza JR, Lukaszew RA. Magnetic field modulation of intense surface plasmon polaritons. Optics Express. 2010;**18**:7743-7752. DOI: 10.1364/OE.18.007743

[43] Escobedo C. On-chip nanohole array based sensing: A review. Lab on a Chip. 2013;**13**: 2445-2463. DOI: 10.1039/C3LC50107H

## Section 3

# Applications

## Chapter 6

# Surface Magneto Plasmons and Their Applications

Bin Hu

Additional information is available at the end of the chapter

http://dx.doi.org/10.5772/intechopen.79788

### Abstract

Due to their promising properties, surface magneto plasmons have attracted great interests in the field of plasmonics. Apart from flexible modulation of the plasmonic properties by an external magnetic field, surface magneto plasmons also promise nonreciprocal effect and multi-bands of propagation, which can be applied into the design of integrated plasmonic devices for biosensing and telecommunication applications. In the visible frequencies, hybrid nanodevices consisting of metals and magnetic materials based on surface magneto plasmon are proposed. In the infrared frequencies, highly-doped semiconductors can replace metals, owning to the lower incident wave frequencies and lower plasma frequencies. Furthermore, a promising 2D material-graphene shows great potential in infrared magnetic plasmonics. In this book chapter, we will review the magneto plasmonics with a focus on device designs and applications. We will give the basic theory of surface magneto plasmons propagating in different structures, including plane surface structures and slot waveguides. Based on the fundamental investigation and theoretical studies, we will illustrate various magneto plasmonic micro/nanodevices, such as tunable waveguides, filters, and beam-splitters. Novel plasmonic devices such as one-way waveguides and broad-band waveguides will also be introduced.

**Keywords:** surface magneto plasmons, plasmonics, magnetic field tuning

## 1. Introduction

Surface plasmons (SPs) are electromagnetic waves that are confined on and propagate along and the surface of a conductor, usually a metal or a semiconductor [1]. SPs are caused by the resonant oscillation of the free electrons in the conductor with the incident electromagnetic waves. The resonant oscillation can be denoted by a characteristic frequency—the plasma frequency $\omega_p$, which decides the scale of the free electrons response to time-varying perturbations [2]. Since SPs depend on the free electron motions, it can be imagined that an external

IntechOpen

© 2018 The Author(s). Licensee IntechOpen. This chapter is distributed under the terms of the Creative Commons Attribution License (http://creativecommons.org/licenses/by/3.0), which permits unrestricted use, distribution, and reproduction in any medium, provided the original work is properly cited.

magnetic field may have modulations on the SPs, due to the Lorentz force which can change the response of carriers. In this situation, another characteristic frequency called cyclotron frequency $\omega_c$ is often used, which is a function of the effective mass of the charge carriers and the strength of the applied magnetic field [3]. One of the important consequences of magnetizing the plasmons is that the polarizability becomes highly anisotropic (the permittivity of the conductor becomes a tensor)—even though the medium is isotropic when the magnetic field is not applied. Therefore, SPs may have different properties when they are propagating under an external magnetic field. In this situation, they are usually called surface magneto plasmons (SMPs) [4].

SMPs can be divided in three principal configurations, according to three directions—the orientation of applied magnetic field **B**, the propagation of the surface wave **k**, and the surface. The first one is called perpendicular geometry, in which **B** is perpendicular to both the surface and **k**. The second one is called Faraday geometry, in which **B** is parallel to the surface and **k**. The third one is called Voigt geometry, in which **B** is parallel to the surface and perpendicular to **k**. Compared with traditional SPs, SMPs have several unique properties. For instance, SMPs in perpendicular geometry and Faraday geometry can support pseudo-surface waves, which means they attenuate on only one side of the surface [5, 6]. SMPs in this Voigt configuration support nonreciprocal effect, which means the SMP dispersions are different when they propagate along two opposite directions. In addition, unlike SPs only has one propagating frequency band which is below the plasma frequency [2], SMPs support two propagating bands.

The basic theory of SMPs in the perpendicular configuration was first given by Brion et al. [5] in 1974. Then, in the same year, Wallis et al. reported the theoretical study of SMPs in the Faraday configuration [6]. In 1987, Kushwaha [7] gave the theoretical derivation of SMP on a thin film in the Faraday configurations. For the Voigt configuration, the pioneer work was implemented by Chiu et al. [8] and Brion et al. [4] as early as 1972, separately. Then De Wames and coworkers studied the dispersion relation of Voigt-configured SMPs on a thin film [9]. Then SMP properties considering holes [10], optical phonons [11–13], diffuse electron density profiles [14], and metal screen [15] were theoretically proposed. They were also studied both theoretically and experimentally in various structures [16–27]. In 2001, a review work of SMP was given [28].

In recent years, due to the extraordinary optical transmission through periodic holds in nanometer scale, which is found in 1998 [29], numerous plasmonic devices, made of metals, have been theoretically proposed and experimentally realized in the visible frequencies [1, 30]. Compared with studies about SPs before 2000 [31–40], these structures have been mostly focused on the subwavelength confinement of electromagnetic waves [41]. For example, in the slot waveguides [42] or metal-insulator-metal structures [43], electromagnetic waves can be confined in a space as small as $\sim 0.1\lambda$. Inspired by these structures, some SMP devices composed of metals were proposed [44–49]. However, all of these SMP structures are difficult to realize because they require unreachable magnetic fields. The reason is that in order to observe the effect of an external magnetic field, it requires $\omega_p$, $\omega_c$ and the incident angular frequency $\omega$ be comparable. However, for a metal in the visible frequencies, $\omega_p$ and $\omega$ are usually in the order of $\sim 10^{16}$ and $\sim 10^{15}$ Hz, respectively. Therefore, it needs a magnetic field as strong as $\sim 10^3$ Tesla, which is difficult to realize in laboratories. So far, there are two ways to solve this problem. One is using ferromagnetic materials, such as Ni and Co in nanostructures [50–57]. By this method, the intensity of the applied magnetic field can be decreased to a scale of ~mT. But it introduces large loss. The other solution is using semiconductors instead of metals in THz regime to decrease both $\omega_p$ and $\omega$. $\omega_p$ of a doped semiconductor can be decreased in an order of $\sim 10^{13}$ Hz. Therefore, the required external magnetic field can be less than 2 Tesla. Some researches of SMP devices consisting of semiconductors have also been proposed recently [58–62].

In this chapter, we will introduce the basic theory of SMPs in the Voigt configuration and their applications in SMP devices design. In Section 2, we will give the dispersions of SMPs on a surface, in a metal-insulator-semiconductor structure, and in a semiconductor-insulator-semiconductor structure of the Voigt configuration. The nonreciprocal effect and the two propagating bands will be discussed. In Section 3, some intriguing plasmonic devices based on the SMPs will be presented, including one-way waveguides, broadly tunable THz slow light waveguides, and focal-length-tunable plasmonic lenses.

## 2. Theory of SMPs on a surface and in a slot waveguide

The first theory of SMPs on a conductor plane surface in the Voigt configuration was presented by Chiu et al. [8]. However, they only found the nonreciprocal effect. In the same year, Brion et al. gave a more comprehensive study on SMPs, including the nonreciprocal effect and the two propagating bands [4]. They also gave an explanation of why the higher band appears. We will give a review of his research in this section. Although the energy of SMPs is confine on the plane surface, the confinement is not subwavelength scale (in the order of ~2–3$\lambda$). In order to solve this problem, in this section, we derive the dispersion of SMPs in a slot waveguide, which can confine light in 1/10 $\lambda$ in the lateral direction [63–66]. Some results are very similar with that in Ref. [4], while some are quite different. For example, the nonreciprocal effect is eliminated in a symmetric structure [63].

### 2.1. Dispersion of SMPs on a plane surface

The schematic structure is shown in **Figure 1**. The material of $x < 0$ is a metal or a semiconductor, and its surface is oriented to +x-axis. The SMPs is propagating along the z-axis. In the Voigt configuration, the applied magnetic field **B** is applied along the y-axis. Then the permittivity of the metal/semiconductor becomes a tensor:

$$\varepsilon = \begin{bmatrix} \varepsilon_{xx} & 0 & \varepsilon_{xz} \\ 0 & \varepsilon_{yy} & 0 \\ -\varepsilon_{xz} & 0 & \varepsilon_{xx} \end{bmatrix}. \tag{1}$$

The parameters in Eq. (1) have the expressions of

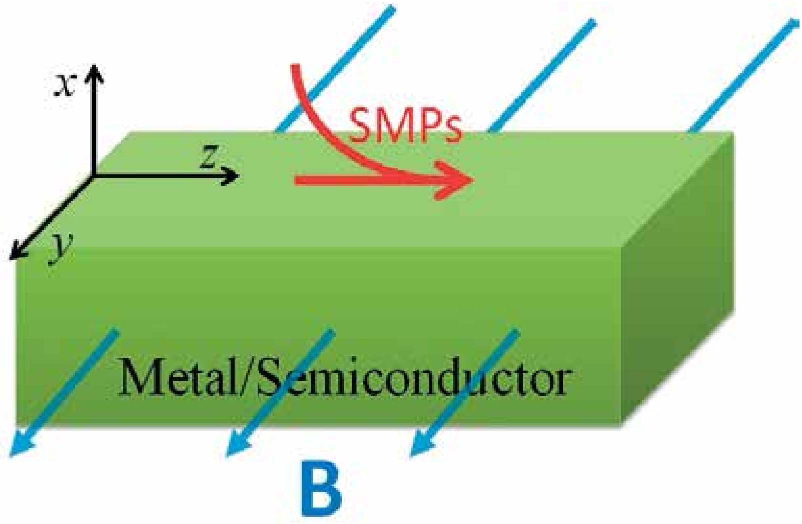

**Figure 1.** Schematic structure of SMPs propagating on a metal/semiconductor surface in the Voigt configuration. The external static magnetic field B is applied along the y-axis.

$$\varepsilon_{xx} = \varepsilon_\infty \left\{ 1 - \frac{\omega_p{}^2(\omega + iv)}{\omega\left[(\omega + iv)^2 - \omega_c{}^2\right]} \right\} \tag{2}$$

$$\varepsilon_{xz} = -i\varepsilon_\infty \frac{\omega_p{}^2\omega_c{}^2}{\omega\left[(\omega + iv)^2 - \omega_c{}^2\right]} \tag{3}$$

$$\varepsilon_{yy} = \varepsilon_\infty \left[ 1 - \frac{\omega_p{}^2}{\omega(\omega + iv)} \right] \tag{4}$$

in which $\omega_p$ is the plasma frequency of the conductor, $\omega$ is the angular frequency of the incident wave, $\varepsilon_\infty$ is the high-frequency permittivity, and $\omega_c = eB/m^*$ is the cyclotron frequency. $e$ and $m^*$ are the charge and the effective mass of electrons, respectively. $B$ is the applied external magnetic field. $v = e/(\mu m^*)$ is the collision frequency of free electrons, $\mu$ is the carrier mobility.

From the Maxwell equations, the wave equation can be derived as

$$\nabla \times (\nabla \times \mathbf{E}) - k_0^2 \varepsilon \mathbf{E} = 0 \tag{5}$$

where $k_0$ is the wave vector in vacuum. $\varepsilon$ is the permittivity of the material (for a conductor, it is the dielectric constant tensor of Eq. (1)). $c$ is the light velocity in vacuum. If we assume that the material of the region $x > 0$ is a dielectric with permittivity of $\varepsilon_d$, and considering SMPs are TM polarized (with the magnetic field component parallel to the y-axis), the electromagnetic fields in the metal/semiconductor and the dielectric have the form:

$$\mathbf{E} = (E_{1x}, 0, E_{1z})e^{\alpha_0 x}e^{i(\beta z-\omega t)}, x\geq 0 \tag{6}$$

$$\mathbf{E} = (E_x, 0, E_z)e^{\alpha x}e^{i(\beta z-\omega t)}, x < 0 \tag{7}$$

where $\beta$ is the wave vector of SMPs. From Eqs. (6), (7) and (1), we have a nontrivial solution of Eq. (5) only if

$$\alpha_0^2 = \beta^2 - \frac{\omega^2}{c^2}\varepsilon_d \tag{8}$$

$$\alpha^2 = \beta^2 - \frac{\omega^2}{c^2}\varepsilon_V \tag{9}$$

where $\varepsilon_V = \varepsilon_{xx} + \varepsilon_{xz}^2/\varepsilon_{xx}$ is the Voigt dielectric constant. With the consideration of the characteristics of the surface mode and the continuity of $H_y$ and $E_z$ at the surface, the dispersion relation of the waveguide is given by

$$\varepsilon_d\sqrt{\beta^2 - \frac{\omega^2}{c^2}\varepsilon_V} + \varepsilon_V\sqrt{\beta^2 - \frac{\omega^2}{c^2}\varepsilon_d} + i\beta\varepsilon_d\frac{\varepsilon_{xz}}{\varepsilon_{xx}} = 0. \tag{10}$$

It can be clearly seen from Eq. (10) that this dispersion is non-reciprocal with respect to the direction of propagation, i.e., the positive and negative values of the wave vector $\beta$ are not equivalent. The dispersion equation can be solved numerically by Eq. (10). In **Figure 2**, the dispersion of SMPs on a plane surface is plotted, assuming that the conductor material is InSb in the lossless case ($\upsilon = 0$) with $\omega_c = 0.5\omega_p$, and the dielectric material is air ($\varepsilon_d = 1$). The other corresponding parameters of InSb are chosen as $m^* = 0.014\ m_0$ ($m_0$ is the free electron mass in vacuum), $\omega_p = 12.6$THz, and $\varepsilon_\infty = 15.68$ [4].

As shown in the dispersion equation, the nonreciprocal effect is immediately observed. We first discuss the case of $\beta > 0$. An interesting feature is that the dispersion curve consists of two propagation bands with a gap between them. The lower curve starts from the origin, rises just to the right of the light line (the line marked as $\alpha_0 = 0$), bends over, and terminates when it reaches the dispersion curve of the bulk magneto plasmons (the line marked as $\alpha = 0$). The higher branch starts from the line of $\varepsilon_{xx} = 0$, and approaches the asymptotic frequency for the non-retarded magneto plasmons defined by $\varepsilon_d + \varepsilon_{xx}\text{-}i\varepsilon_{xz} = 0$. The reduced wave vector at which the upper band starts is specified by the equation of

$$\zeta_s^2 \equiv \left(\frac{c\beta}{\omega_p}\right)^2 = \frac{1+\Omega_c^2}{1-(\varepsilon_d/\varepsilon_\infty)^2\left(1+\Omega_c^2\right)/\Omega_c^2}, \tag{11}$$

where $\Omega_c = \omega_c/\omega_p$. In order to let $\zeta_s$ to be positive and finite, it must be satisfied that $\varepsilon_\infty/\varepsilon_d > \omega_H/\omega_c$, where $\omega_H = \text{sqrt}(\omega_p^2 + \omega_c^2)$ is the hybrid cyclotron-plasmon frequency. For InSb and air, this is given by $\Omega_c \geq 0.064$. Therefore, the magnetic field should be at least 0.0643 Tesla to observe the higher band.

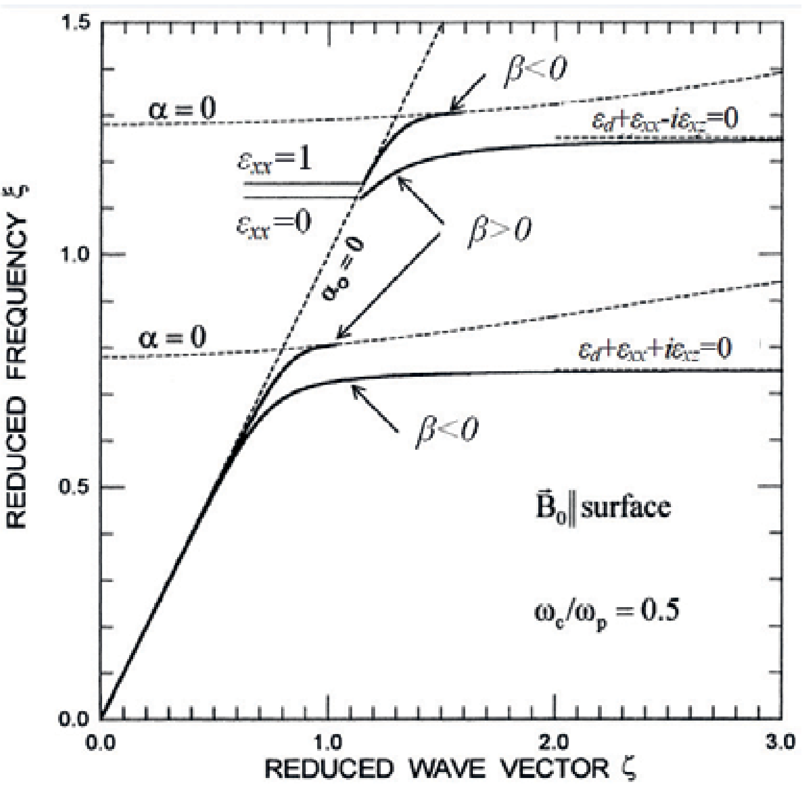

**Figure 2.** Dispersion curves of SMPs at the interface of InSb and air in the Voigt configuration (solid lines). $\omega_c = 0.5\omega_p$. $\xi = \omega/\omega_p$ and $\zeta = \beta c/\omega_p$ are normalized frequency and wave vector.

For $\beta < 0$, the lower band starting from the origin to the asymptotic value defined by $\varepsilon_d + \varepsilon_{xx} + i\varepsilon_{xz} = 0$. The higher band starts at the light line $\varepsilon_{xx} = 1$, rises to the right of the light line, and cutoff when it meets the higher bulk magneto plasmon curve $\alpha = 0$.

The two propagating band can be explained by **Figure 3**, where the Voigt dielectric constant is plotted as a function of the normalized angular frequency $\xi = \omega/\omega_p$. It can be seen that when $\omega_c = 0.5\omega_p$, there are two regions, where $\varepsilon_V < 0$. Because SMPs can only propagate on the surface of a material with negative permittivity, SMPs have two propagating bands on a plane surface.

## 2.2. Dispersion of SMPs in a symmetric slot waveguide

In order to expand the theory of SMPs in a subwavelength scale, we study the dispersion of SMPs in a slot waveguide with a lateral width in subwavelength scale. In this part, we study a symmetric structure, which is shown in **Figure 4**. An insulator layer (the permittivity is denoted by $\varepsilon_d$) with a width of $w$ is sandwiched by two conductor layers. A TM-polarized electromagnetic wave (the magnetic field component is parallel to the $y$-axis) is propagating along the $z$-direction where $E_x(\mathbf{r}, \omega)$, $E_z(\mathbf{r}, \omega)$, $H_y(\mathbf{r}, \omega) \propto \exp[i(\beta z - \omega t)]$. An external static magnetic field $B$ is applied uniformly along the $y$-axis, in a Voigt configuration. Therefore, according to the Maxwell equations, the electromagnetic field components in region I, II, and III can be written as

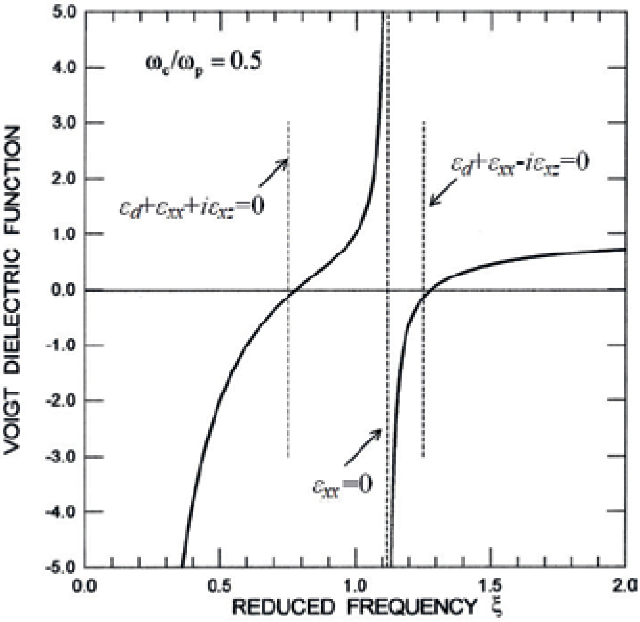

**Figure 3.** Voigt dielectric constant $\varepsilon_V$ as a function of frequency.

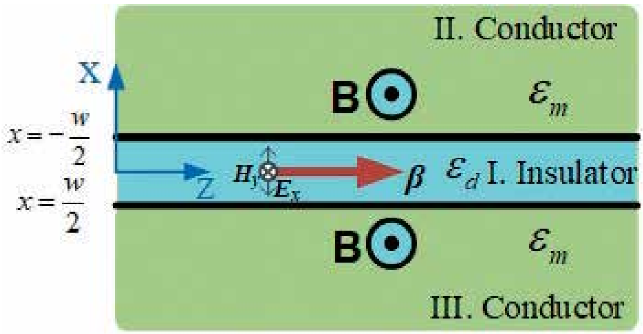

**Figure 4.** Schematic of SMPs propagating in a symmetric conductor-insulator-conductor structure in the Voigt configuration. The external static magnetic field B is applied along the y-axis.

$$H_y{}^{(I)} = Ae^{-\kappa_1 x} + Be^{\kappa_1 x} \tag{12}$$

$$E_z{}^{(I)} = -\frac{i\kappa_1}{\omega\varepsilon_0\varepsilon_d}\left(Ae^{-\kappa_1 x} - Be^{\kappa_1 x}\right) \tag{13}$$

$$H_y{}^{(II)} = Ce^{-\kappa_2(x-w/2)} \tag{14}$$

$$E_z{}^{(II)} = \frac{1}{i\omega\varepsilon_0\left(\varepsilon_{xx}{}^2 + \varepsilon_{xz}{}^2\right)}\left(i\beta\varepsilon_{xz}Ce^{-\kappa_2(x-w/2)} + \varepsilon_{xx}\kappa_2 Ce^{-\kappa_2(x-w/2)}\right) \tag{15}$$

$$H_y{}^{(III)} = De^{\kappa_3(x+w/2)} \tag{16}$$

$$E_z{}^{(III)} = \frac{1}{i\omega\varepsilon_0({\varepsilon_{xx}}^2 + {\varepsilon_{xz}}^2)}\left(i\beta\varepsilon_{xz}De^{\kappa_3(x+w/2)} - \varepsilon_{xx}\kappa_3 De^{\kappa_3(x+w/2)}\right) \tag{17}$$

where A, B, C, and D are undetermined coefficients. $\kappa_1$, $\kappa_2$ and $\kappa_3$ are expressed by

$${\kappa_1}^2 = \beta^2 - k_0^2\varepsilon_d \tag{18}$$

$${\kappa_2}^2 = {\kappa_3}^2 = \beta^2 - k_0^2\varepsilon_V \tag{19}$$

Employing the boundary conditions at the two interfaces ($x = -w/2$ and $x = w/2$) yields

$$\left\{\begin{matrix} \left[\frac{(\beta\varepsilon_{xz} - i\varepsilon_{xx}\kappa_2)}{({\varepsilon_{xx}}^2 + {\varepsilon_{xz}}^2)} + \frac{i\kappa_1}{\varepsilon_d}\right]e^{-\kappa_1 w/2} & \left[\frac{(\beta\varepsilon_{xz} - i\varepsilon_{xx}\kappa_2)}{({\varepsilon_{xx}}^2 + {\varepsilon_{xz}}^2)} - \frac{i\kappa_1}{\varepsilon_d}\right]e^{\kappa_1 w/2} \\ \left[\frac{(\beta\varepsilon_{xz} + i\varepsilon_{xx}\kappa_2)}{({\varepsilon_{xx}}^2 + {\varepsilon_{xz}}^2)} + \frac{i\kappa_1}{\varepsilon_d}\right]e^{\kappa_1 w/2} & \left[\frac{(\beta\varepsilon_{xz} + i\varepsilon_{xx}\kappa_2)}{({\varepsilon_{xx}}^2 + {\varepsilon_{xz}}^2)} - \frac{i\kappa_1}{\varepsilon_d}\right]e^{-\kappa_1 w/2} \end{matrix}\right\}\begin{pmatrix} A \\ B \end{pmatrix} = 0 \tag{20}$$

The nontrivial solution of these linear equations requires the vanishing of the coefficients determinant, and then we can derive the following relation:

$$\tanh\left(w\sqrt{\beta^2 - \varepsilon_d k_0^2}\right)\left[1 + \left(\frac{\varepsilon_d}{\varepsilon_V}\right)^2\frac{\beta^2 - \varepsilon_V k_0^2}{\beta^2 - \varepsilon_d k_0^2} + \left(\frac{\varepsilon_d}{\varepsilon_V}\right)^2\left(\frac{\varepsilon_{xz}}{\varepsilon_{xx}}\right)^2\frac{\beta^2}{\beta^2 - \varepsilon_d k_0^2}\right] + 2\frac{\varepsilon_d}{\varepsilon_V}\frac{\sqrt{\beta^2 - \varepsilon_V k_0^2}}{\sqrt{\beta^2 - \varepsilon_d k_0^2}} = 0 \tag{21}$$

Eq. (21) is the dispersion relation of TM-polarized SMPs in the Voigt configurations for the symmetric slot structure. It should be noted that, when B = 0, Eq. (21) becomes the dispersion relations of SPs in a MIM structure [43]; when $w \to \infty$, it becomes Eq. (10).

An intriguing feature of Eq. (21) is that due to the symmetric structure, the nonreciprocal effect of Eq. (10) is eliminated because only $\beta^2$ can be found in the equation. The dispersion curve is shown in **Figure 5**. Without loss of generality, here we also assume the conductor material is n-doped InSb. The width of the dielectric is $w = 0.1 \times 2\pi c/\omega_p$. It is found that $\beta > 0$ and $\beta < 0$ SMP waves have same dispersion curve when the magnetic field is applied (blue lines). In addition, the two propagating bands are remained. The higher band can also be explained by the effect of the applied magnetic field on the Voigt dielectric constant $\varepsilon_V$ in **Figure 3**.

Although the dispersion curve is reciprocal, the mode distribution is still nonreciprocal in this structure, which is shown in **Figure 6**. The normalized electric field intensities of the SMPs modes indicate that with the magnetic field, the mode distribution becomes asymmetric. For the SMPs mode in the lower band, most of the energy is confined on the lower surface of the dielectric layer, while the energy is mostly confined on the upper surface in the higher frequency band.

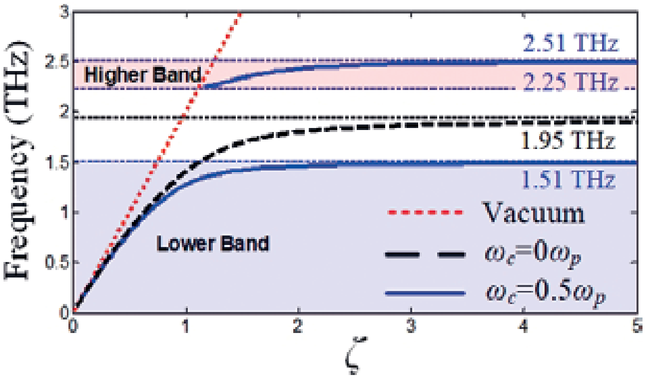

**Figure 5.** Dispersion curves of SMPs in a slot waveguide of InSb-air-InSb in the Voigt configuration (solid lines). $w = 0.1 \times 2\pi c/\omega_p$. $\zeta = \beta c/\omega_p$ is the normalized wave vector.

### 2.3. Dispersion of SMPs in an asymmetric slot waveguide

In this part, we study the dispersion of SMPs in an asymmetric slot waveguide with a lateral width in subwavelength scale, which is shown in **Figure 7**. The structure is similar with **Figure 4**,

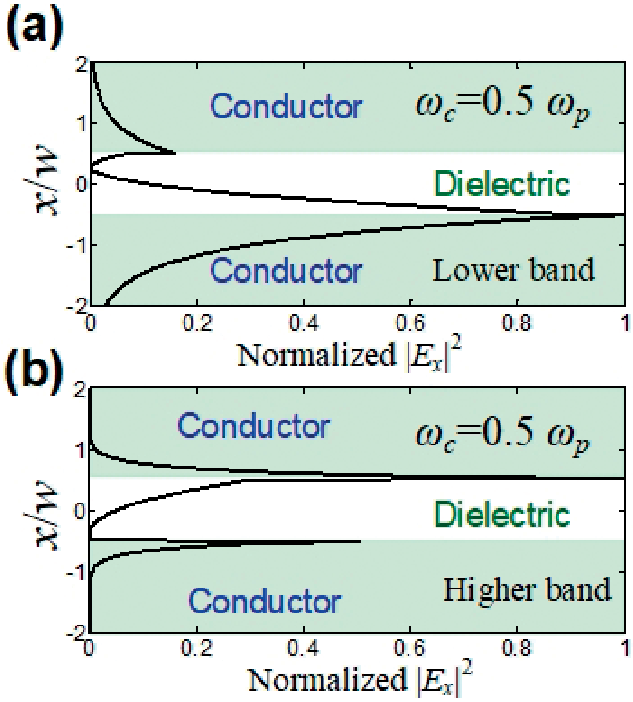

**Figure 6.** Normalized $E_x$ intensities of SMPs mode along the x-axis under an external magnetic field of $\omega_c = 0.5\ \omega_p$. (a) Lower band; (b) higher band.

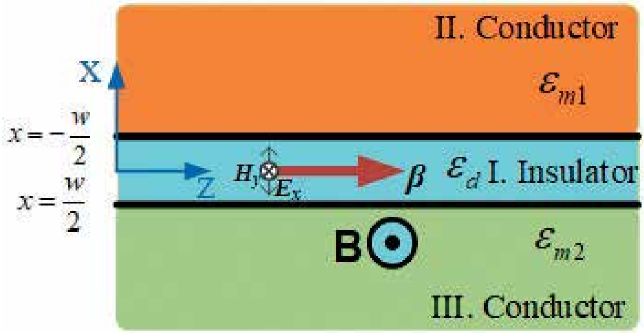

**Figure 7.** Schematic of SMPs propagating in an asymmetric conductor-insulator-conductor structure in the Voigt configuration. The external static magnetic field B is only applied on the conductor below the insulator.

an insulator layer is sandwiched by two conductor layers. However, the external magnetic field is only applied on one of the two conductor layers. In this geometry, the conductor of region III is anisotropic, and its permittivity is a tensor, as we discussed earlier, but the conductor of region II is isotropic. Therefore, according to the Maxwell equations, the electromagnetic field components in region I, II, and III can be written as

$$H_y{}^{(I)} = Ae^{-\kappa_1 x} + Be^{\kappa_1 x} \tag{22}$$

$$E_z{}^{(I)} = -\frac{i\kappa_1}{\omega\varepsilon_0\varepsilon_d}\left(Ae^{-\kappa_1 x} - Be^{\kappa_1 x}\right) \tag{23}$$

$$H_y{}^{(II)} = Ce^{-\kappa_2(x-w/2)} \tag{24}$$

$$E_z{}^{(II)} = -\frac{i\kappa_2}{\omega\varepsilon_0\varepsilon_m}Ce^{-\kappa_2(x-w/2)} \tag{25}$$

$$H_y{}^{(III)} = De^{\kappa_3(x+w/2)} \tag{26}$$

$$E_z{}^{(III)} = \frac{1}{i\omega\varepsilon_0\left(\varepsilon_{xx}{}^2 + \varepsilon_{xz}{}^2\right)}\left(i\beta\varepsilon_{xz}De^{\kappa_3(x+w/2)} - \varepsilon_{xx}\kappa_3 De^{\kappa_3(x+w/2)}\right) \tag{27}$$

where A, B, C, and D are undetermined coefficients. $\varepsilon_m$ is the isotropic permittivity of region II. $\kappa_1$, $\kappa_2$ and $\kappa_3$ are expressed by

$$\kappa_1{}^2 = \beta^2 - k_0^2\varepsilon_d \tag{28}$$

$$\kappa_2{}^2 = \beta^2 - k_0^2\varepsilon_m \tag{29}$$

$$\kappa_3{}^2 = \beta^2 - k_0^2\varepsilon_V \tag{30}$$

Employing the boundary conditions at the two interfaces ($x = -w/2$ and $x = w/2$), it can be derived

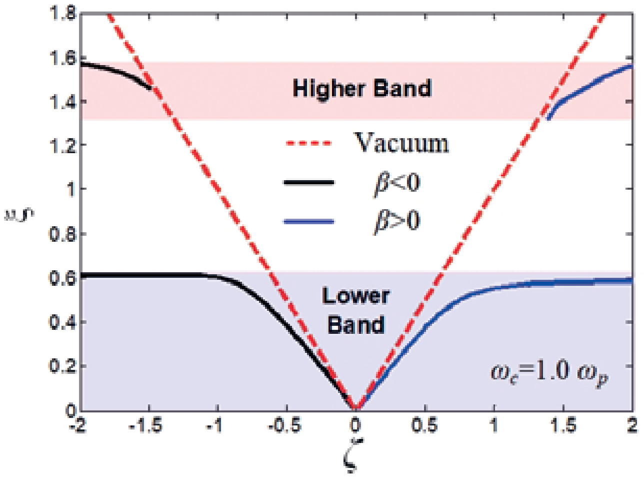

**Figure 8.** Dispersion curves of SMPs in an asymmetric slot waveguide in the Voigt configuration (solid lines). $w = 0.1 \times 2\pi c/\omega_p$. $\xi = \omega/\omega_p$ and $\zeta = \beta c/\omega_p$ are normalized frequency and wave vector, respectively.

$$\begin{Bmatrix} \left[\frac{i\kappa_2}{\varepsilon_m}-\frac{i\kappa_1}{\varepsilon_d}\right]e^{i\kappa_1 w/2} & \left[\frac{i\kappa_2}{\varepsilon_m}+\frac{i\kappa_1}{\varepsilon_d}\right]e^{-i\kappa_1 w/2} \\ \left[\frac{(i\beta\varepsilon_{xz}-\varepsilon_{xx}\kappa_3)}{i(\varepsilon_{xx}{}^2+\varepsilon_{xz}{}^2)}+\frac{i\kappa_1}{\varepsilon_d}\right]e^{-i\kappa_1 w/2} & \left[\frac{(i\beta\varepsilon_{xz}-\varepsilon_{xx}\kappa_3)}{i(\varepsilon_{xx}{}^2+\varepsilon_{xz}{}^2)}-\frac{i\kappa_1}{\varepsilon_d}\right]e^{i\kappa_1 w/2} \end{Bmatrix} \begin{pmatrix} A \\ B \end{pmatrix} = 0 \tag{31}$$

Then we can derive the dispersion equation of SMPs in an asymmetric slot waveguide by the nontrivial solution of these linear equations:

$$\begin{aligned} &\left\{\frac{\sqrt{\beta^2-k_0^2\varepsilon_m}\sqrt{\beta^2-k_0^2\varepsilon_V}}{\beta^2-\varepsilon_d k_0^2}\frac{1}{\varepsilon_m\varepsilon_V}+\frac{1}{\varepsilon_d^2}-i\frac{\beta\sqrt{\beta^2-k_0^2\varepsilon_m}}{\beta^2-\varepsilon_d k_0^2}\frac{\varepsilon_{xz}}{\varepsilon_m\varepsilon_V\varepsilon_{xx}}\right\}\tanh\left(\sqrt{\beta^2-\varepsilon_d k_0^2}w\right) \\ &+\left[\frac{\sqrt{\beta^2-k_0^2\varepsilon_V}}{\sqrt{\beta^2-\varepsilon_d k_0^2}}\frac{1}{\varepsilon_d\varepsilon_V}+\frac{\sqrt{\beta^2-k_0^2\varepsilon_m}}{\sqrt{\beta^2-\varepsilon_d k_0^2}}\frac{1}{\varepsilon_m\varepsilon_d}-i\frac{\beta}{\sqrt{\beta^2-\varepsilon_d k_0^2}}\frac{\varepsilon_{xz}}{\varepsilon_d\varepsilon_V\varepsilon_{xx}}\right]=0 \end{aligned} \tag{32}$$

One can know by a glance from Eq. (32) that in an asymmetric slot waveguide, SMPs have nonreciprocal dispersion as those on a plane surface. In **Figure 8**, the dispersion curves of both $\beta > 0$ and $\beta < 0$ are plotted, when $w = 0.1 \times 2\pi c/\omega_p$, $\omega_c = 0.1\omega_p$. It can be seen that due to nonreciprocal effect, forward propagating and backward propagating SMPs have different cutoff frequencies.

## 3. Applications of slot SMPs

In recent years, several kinds of SMP devices that can manipulate electromagnetic fields in subwavelength scale have been proposed [46–49, 52–56]. However, most of them are focused on the magnetic-field tunable property. The nonreciprocal effect and the two propagating bands are rarely utilized. In this section, we give three applications using the nonreciprocal effect, two propagating bands and magnetic field tuning properties, respectively. The SMPs applications are realized by semiconductors in the terahertz regime. However, the design principle can be used in any SMP devices.

### 3.1. Broadly tunable one-way terahertz plasmonic waveguides based on nonreciprocal effect of slot SMPs

With the rapid development in Terahertz (THz) technology in recent years, THz plasmonic components, e.g. waveguides, have been proposed due to the sub-wavelength confinement for miniaturized devices. However, most plasmonic waveguides are two-way waveguides, i.e. light waves propagate in both the forward and the backward directions. One-way-propagating waveguides are highly desired in splitters, switches and isolators. One method to realize one-way plasmonic devices are based on interference of SPs [66]. This effect is strongly sensitive to geometric structure variations. Another approach is by the nonreciprocal effect of SMPs under an external magnetic field. The dispersions of the forward and backward propagating SMPs terminate at different cut-off frequencies, making it possible to realize an absolute one-way plasmonic waveguide.

In this section, we propose a simple THz one-way sub-wavelength plasmonic waveguide that needs only 1 Tesla. By tuning the applied MF, the central frequency of the one-way-propagating frequency band is shifted from 1.5 to 0.36 THz when the MF is increased from 0.5 to 5 Tesla.

The schematic structure of the proposed waveguide is depicted in **Figure 9(a)**. It is composed of a metal-dielectric-semiconductor. The metal and the semiconductor layers are half-infinite and the thickness of the dielectric layer is $w$. The external static magnetic field is applied uniformly on the whole structure along the y-axis (as indicated by B), forming a Voigt configuration. Without loss of generality, we assume the metal, dielectric and semiconductor are Au, air and InSb, respectively. Although Au is a conductor, it resembles perfect conductors in the THz regime [67]. Therefore, it can be considered as an isotropic material even though the magnetic field is applied. In this approximation, the conclusion of Section 2.3 can be applied. **Figure 9(b)** shows the dispersion

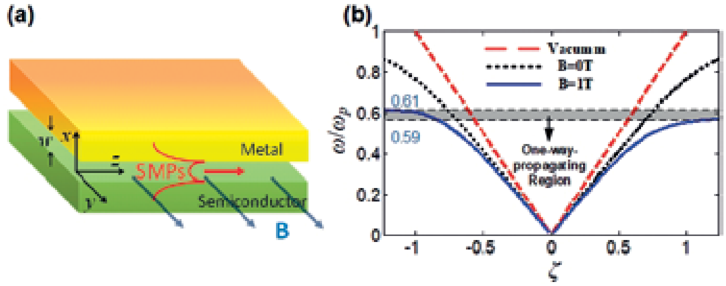

**Figure 9.** (a) Schematic structure of the one-way THz plasmonic waveguide. It is composed of metal (upper), dielectric (middle), and semiconductor (lower) layers. (b) Dispersion relations of the THz SMPs without and with an external magnetic field.

curves of the lower band of SMPs waves with (B = 1 Tesla) and without the external magnetic fields. It can be found that the dispersion curves are symmetric without the magnetic field. While, when magnetic field is applied, the dispersion curves of the two propagating waves become different. The cutoff frequency of the forward-propagating mode is $\omega/\omega_p = 0.59$, while that of the backward propagating mode is $\omega/\omega_p = 0.61$. This means that the THz waves in the frequency region of $\omega/\omega_p = [0.59, 0.61]$ (corresponding to $f = [1.18, 1.23]$ THz) can only propagate backwards.

Then simulations are then conducted by the finite element method (FEM) using COMSOL Multiphysics to verify the one-way effect. The results are plotted in **Figure 2 (a)-(d)**. When the magnetic field is not applied, the field distributions of the forward and backward propagating waves are the same (see (a) and (b), respectively). However, when there is 1 Tesla magnetic field, the forward-propagating THz wave is blocked (see **Figure 2(c)**), while the backward-propagating wave can still propagate through the slit (see **Figure 2(d)**) (there is no bright-dark field distribution in the slit as that in **Figure 2(a)** and **(c)** also confirms that no reflected SMP wave can be realized in the slit to interfere with the incident wave). The compared transmitted intensities of the forward and the backward propagating waves of Figure (c) and (d) are depicted in **Figure 2(e)**. It can be seen the one way region located at $\omega = [0.592, 0.612]\omega_p$, which agrees very well with the theoretical results.

The tuning ability of the one-way frequency band is also studied. By applying the non-retardation limit [22], i.e. substitute $\beta >> k_0$ into Eq. (32), we have $\kappa_1 \approx \kappa_2 \approx \kappa_3 \approx \beta$, and $\beta w >> 1$. Thus the cutoff frequencies of the forward and the backward propagating modes $\omega_{Vf}$ and $\omega_{Vb}$ can be calculated as

$$\omega_{Vf} = \frac{1}{2}\left[\sqrt{{\omega_c}^2 + 4\omega_{ps}^2 \varepsilon_\infty/(\varepsilon_d + \varepsilon_\infty)} - \omega_c\right] \tag{33}$$

$$\omega_{Vb} = \frac{1}{2}\left[\sqrt{{\omega_c}^2 + 4\omega_{ps}^2} - \omega_c\right] \tag{34}$$

Therefore both $\omega_{Vf}$ and $\omega_{Vb}$ are functions of $\omega_c$, which indicate the one-way region can be tuned by the external magnetic field. The one-way bandwidth is obtained analytically as $\Delta\omega = \omega_{Vf} - \omega_{Vb}$, which increases with $\varepsilon_d$. According to Eq. (32), we calculate $\omega_{Vf}$ and $\omega_{Vb}$ versus $B$, and the permittivity of the dielectric layer, shown in **Figure 11(a)** and **(b)**, respectively. It is found that the magnetic field affects both the cutoff frequencies of the forward and backward propagating modes. However, the bandwidth of the one-way band $\Delta\omega$ depends little on $B$, but determined by the permittivity of the dielectric layer $\varepsilon_d$. This effect is owing to the asymmetry of the mode distribution caused by the magnetic field.

Based on this one-way waveguide structure, we also proposed a THz plasmonic switch. It should be noted that if we change the propagation direction of the applied magnetic field, the dielectric tensor matrix in Eq. (1) is transposed. As a result, the one-way-propagating band will not block the forward wave, but the backward wave. According to this principle, a T-shape waveguide is designed, as shown in **Figure 12**. The width of the waveguide, the magnetic field intensity, and the incident frequency are the same as those in **Figure 10(c)** and **(d)**. It is clearly seen that when the direction of the external MF is changed, a tunable THz plasmonic switch can be realized.

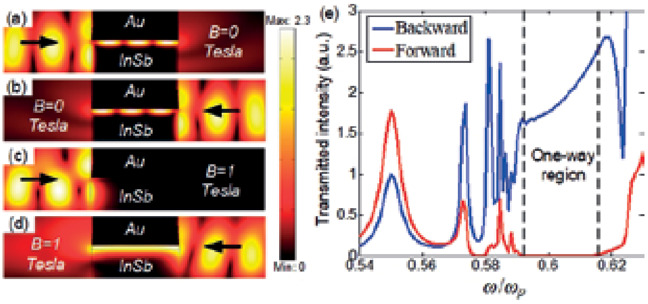

**Figure 10.** (a)-(d) FEM-simulated $|H_y|^2$ distribution of the forward and backward propagating waves in a sub-wavelength slit. The width and length of the slit are $0.1 \times 2\pi c/\omega_p$ and 300 $\mu m$, respectively. The incident frequency is $\omega = 0.6\omega_p$, which is in the one-way frequency band. (e) Transmitted intensities of the forward (corresponding to (c)) and backward propagating (corresponding to (d)) waves when 1 Tesla magnetic field is applied.

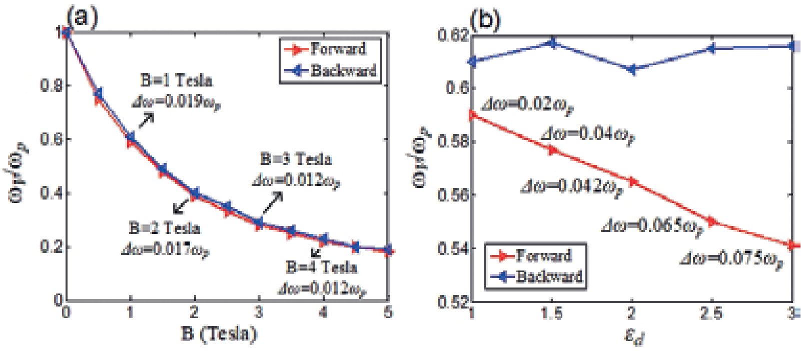

**Figure 11.** Effects of the applied magnetic field B (a) and the permittivity of the dielectric layer (b) on the one-way frequency band. $\omega_V$ represents the cutoff frequency. $\Delta\omega$ is the bandwidth of the one-way band.

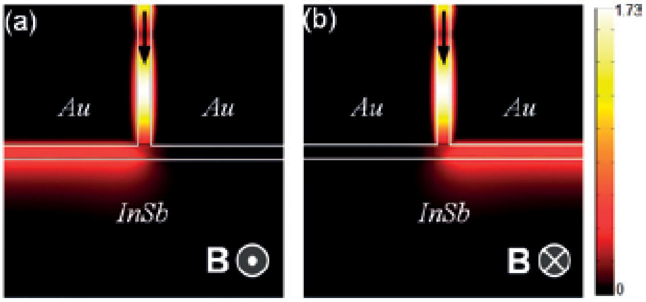

**Figure 12.** Field distributions of a designed THz plasmonic switch tuned by an external magnetic field. (a) the magnetic field is along +$y$-axis. (b) the magnetic field is along -$y$-axis.

http://dx.doi.org/10.5772/intechopen.79788

### 3.2. A terahertz slow-light system with tunable group velocities in a broad frequency range by SMPs

In this part, we will apply the two bands of SMPs to a THz slow light system. Slow-light technology has great application potentials in telecommunications, data processing, and light-matter interactions. Compared with traditional electronic approaches [68], plasmonic approaches are easy to achieve because its subwavelength confinement of electromagnetic (EM) fields [69]. However, most slow light systems are not tunable so far, especially in the THz frequency region. In this section, we propose a tunable THz slow-light system based on SMPs with a semiconductor-insulator-semiconductor (SIS) structure. In this structure, both the frequency and the group velocity of the slowed-down THz wave can be tuned. More importantly, due to the existence of two SMPs bands, especially the higher band which has a wider tunable bandwidth, the proposed system has a very broad tunable bandwidth.

Because a plasmonic slow-light system is expected to have the same slow-light effect in both forward- and backward-propagating directions, we use a symmetric structure as shown in **Figure 13(a)** in which the nonreciprocal effect is eliminated. By the dispersion equation of Eq. (21), the dispersion curves of the SMPs in the structure when the external magnetic field is applied with intensities of 0, 0.5, 1 and 2 Tesla are plotted in **Figure 13(b)**. The width of the waveguide is $w = 0.1 \times 2\pi c/\omega_p = 15$ μm ($\sim 1/20\lambda$ of 1 THz wave). It can be seen from the figure that with the increase of the magnitude of the external magnetic field, the two bands move toward opposite directions (as indicated by the blue arrow). In addition, the shift of the higher band dispersion curve is more obvious than the lower band dispersion curve. When the magnetic field increases from 0 to 2 T, the cutoff frequency of the lower band changes from 1.9 to 0.8 THz, while that of the higher band changes from 1.9 to 4.8 THz.

We then study the slowed-down characteristics of the structure. Since the analytical expression of the group velocity defined as $v_g = d\omega/d\beta$ cannot be obtained from Eq. (21), we calculate $v_g$ numerically by fitting the dispersion curves in **Figure 13**. In **Figure 14(a)**, the normalized group velocity $v_g$ with respect to $c$ as a function of the incident frequency is plotted when the external magnetic fields are 0, 0.5, 1, and 2 Tesla. It shows that $v_g$ can achieve $\sim 10^{-6}c$ in the structure for both the lower and higher modes in the lossless case. When the magnetic field is

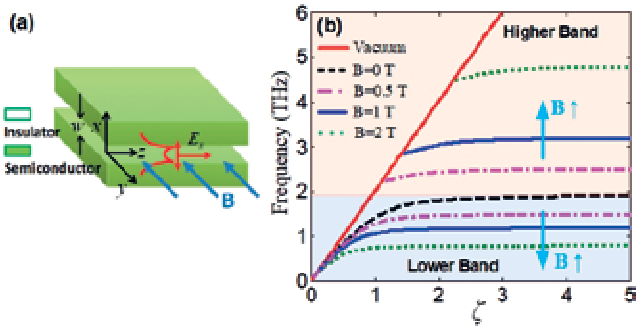

**Figure 13.** (a) Schematic structure of the THz plasmonic slow-light system. (b) Dispersion relations of the SMPs without and with an external magnetic field.

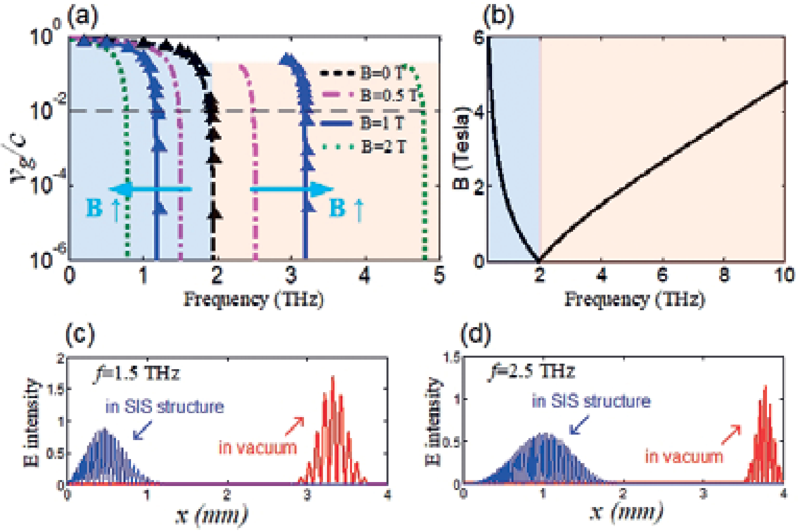

**Figure 14.** Slow-light effect of the structure tuned by an external magnetic field. The lower and the higher bands under the magnetic field are indicated by the blue and the pink shadows, respectively. (a) Normalized group velocity of the structure with 0 to 2 Tesla external magnetic fields (lines: Numerical results by fitting dispersion curves in **Figure 13(b)**; triangular points: FDTD simulation results). (b) Incident frequencies versus their corresponding needed magnetic fields. (c) and (d) FDTD simulations of THz pulses propagating in the slow-light waveguide compared with that propagating in vacuum after 15 ps for $f$ = 1.5 THz and $f$ = 2.5 THz, respectively, when a 0.5 Tesla magnetic field is applied. The pulse is launched at $x$ = 0. Both the lower and higher band can slow down the THz waves.

increased from 0 to 2 Tesla, the corresponding frequency for $v_g < 10^{-6}c$ moves from 1.9 to 0.8 THz for the lower band, while that of the higher band moves from 1.9 to 4.8 THz. To verify these results, finite-difference time-domain (FDTD) simulations are conducted for B = 0 and 1 Tesla, respectively (shown as the triangular points). The group velocities of the simulation results agree well with the analytical results from Eq. (21). This verifies the slow-light effects of the system. More obvious FDTD simulated results of a slowed THz pulse in the structure are shown in **Figure 14(c)** and **(d)**. The incident frequencies are chosen as $f$ = 1.5 THz and $f$ = 2.5 THz, which are the frequencies corresponding to $v_g/c = 10^{-2}$ of the lower band and the higher band when a 0.5 Tesla magnetic field is applied, respectively. In the simulations, the THz pulses propagating in the slow-light system and in vacuum along the $x$-axis are compared. It shows that, for $f$ = 1.5 THz, the THz pulse moves 3.3 mm in vacuum while only 0.4 mm in the structure after 15 ps. For $f$ = 2.5 THz, the THz pulse moves 3.8 mm in vacuum while 1 mm in the structure after 15 ps. The reason on the larger simulated group velocity compared with the calculated one is that we added losses to InSb material in order to keep the simulation more stable, which may dramatically limit the achievable slow down factors and introduce losses [70]. Furthermore, the pulse is broadened because of the high dispersion of the system in the frequency region where the signal group velocity is low (the dispersion is proportional to $dv_g/d\omega$), which could be solved by using solitons in Kerr dielectrics [71].

Although direct relation of the magnetic field intensity $B$ and the incident angular frequency $\omega$ is difficult to obtain, it is found that the slow light region is always close to the cut-off frequency of the SMPs modes, which can be derived analytically. From the non-retarded limit of Eq. (21), the cutoff frequencies of the lower and the higher modes can be obtained by $1 + \varepsilon_{xx} + i\varepsilon_{xz} = 0$ and $1 + \varepsilon_{xx} - i\varepsilon_{xz} = 0$, respectively. Then we have

$$B = \pm \frac{m^*}{e}\left[\frac{\omega_p^2 \varepsilon_\infty}{\omega(\varepsilon_d + \varepsilon_\infty)} - \omega\right] \tag{35}$$

where '+' represents $\omega < \omega_{sp}$, '−' denotes $\omega > \omega_{sp}$. $\omega_{sp} = \mathrm{sqrt}[\omega_p{}^2/(1 + \varepsilon_d)]$ is the surface plasma frequency. From Eq. (35), one can calculate the magnetic field needed to slow down the THz waves. In **Figure 14(b)**, the calculated magnetic fields versus the frequencies of the incident THz waves are depicted. It is found that when the magnetic field increases to 6 Tesla, the group velocities of waves in the region of [0.3, 10] THz can all be decreased. Therefore, a plasmonic slow-light system with broad band tuning range is achieved.

From the results in **Figure 14(a)**, it is inferred that the group velocity can also be tuned by changing the intensity of the magnetic field. We choose 1 and 3 THz in the lower and higher bands, respectively. We then calculate their corresponding group velocities dependent on $B$, which are shown in **Figure 15(a)** and **(b)**, respectively. When the magnetic field is increased, the frequency-$v_g$ curves corresponding to the lower band and higher bands moves to the

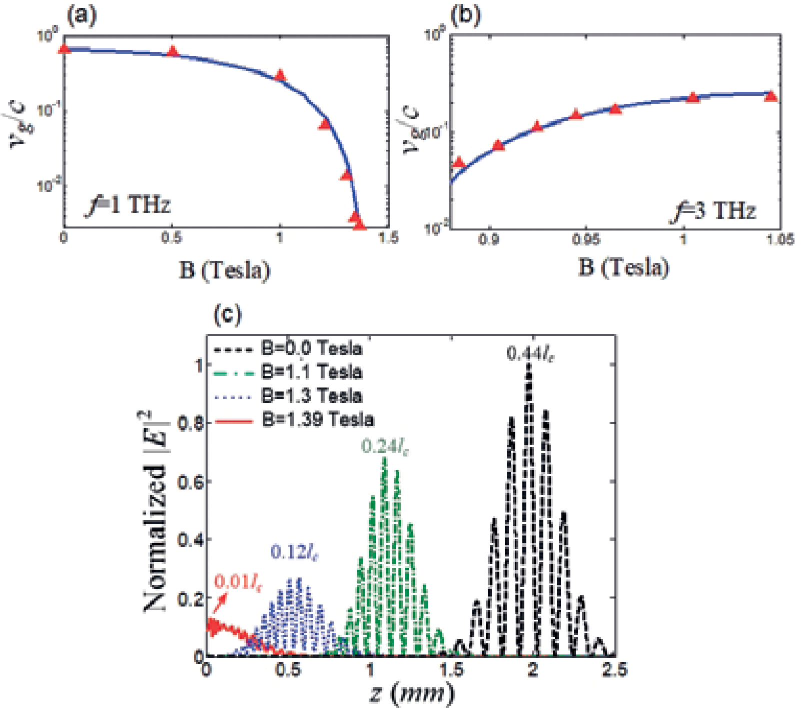

**Figure 15.** Group velocity of a monochromatic wave tuning by the magnetic field. (a) and (b) $f = 1$ THz (in the lower band) and $f = 3$THz (in the higher band), respectively. Blue lines: Results from the analytical model. Red dots: FDTD simulation results. (c) FDTD simulations of THz pulses propagating in the slow-light waveguide. The frequency of the incident wave is 1THz. When the magnetic fields are 0, 1.1, 1.3, and 1.4 Tesla, the peak of the pulse moves $0.01l_c$, $0.12l_c$, $0.24l_c$, and $0.44l_c$ after the THz pulse is launched 15 $ps$, respectively, where $l_c$ is defined as $l_c = 15\ ps \times c$.

opposite directions. Therefore, $v_g$ in the lower band decreases with the magnetic field, while $v_g$ in the higher band increases. When the magnetic field increases from 0 to 1.36 Tesla, the group velocity of 1 THz frequency deceases from 0.65*c* to $10^{-3}c$. For frequency at 3 THz, the required magnetic field is from 1.04 to 0.88 Tesla in order to slow down the wave from 0.23*c* to 0.048*c*. In **Figure 15(c)**, the FDTD simulated magnetic-field-tunable group velocity of a THz pulse is depicted. The incident frequency is 1 THz. It can be found that when $B$ is increased, the distance Terahertz pulse moves become shorter and shorter. When $B$ = 1.39 Tesla, it can be found that the THz pulse moves only $0.01l_c$ after it is launched 15 ps, where $l_c$ is the corresponding moving distance of light in vacuum. It is worth noting that the loss also increases with the magnetic field. Therefore, in addition to the broad tuning range, the group velocity can also be flexibly tuned in the proposed slow-light system.

We then discuss the effects of the material loss on the tuning properties of the slow-light system. It is reported that the slowdown factor may be limited by the material losses [70]. This phenomenon is also observed with this structure. In a semiconductor, the loss is mainly caused by the collision of charge carriers, characterized by the collision frequency $\upsilon$ in Eqs. (2)–(4). For a small loss, we have $\upsilon = 0.01\omega_p$, the group velocity $v_g$ is in the order of $10^{-2}$~$10^{-1}c$. It is increased with the loss, which can be found in **Figure 16**. In addition, owing to the loss, the group velocity no longer decreases monotonously with the frequency, but increases dramatically at a resonant frequency after reaching the minimum value. Therefore, the tuning mechanism of the proposed structure is still valid in a lossy system. The tunable range restricted by the material loss could be effectively compensated by using active materials [71], designing doping levels, etc.

### 3.3. Terahertz plasmonic slit lenses with tunable focal length

Among various plasmonic devices, planar plasmonic slit lenses (PSLs) are often used to realize integrated optical collimators [72–74]. Plasmonic slit lenses consist of a metallic slab with several nanoslits with various widths, thicknesses and material compositions. When light wave propagates through these slits, it has different phase retardations. By adjusting the materials and geometric parameters of the slits, phase control is able to be realized. Compared

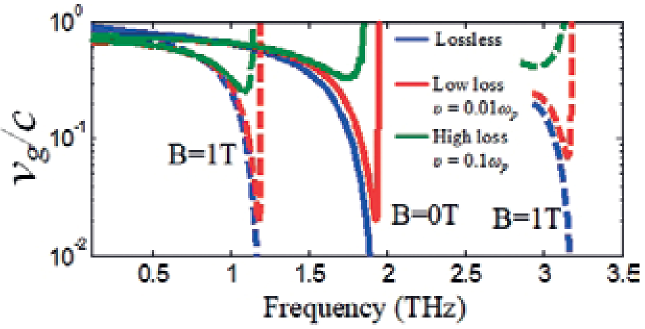

**Figure 16.** Effects of loss on the tuning properties of the slow-light system. The loss is characterized by the collision frequency $\upsilon$ of free carriers.

to other lenses, PSLs have relatively simple structures. In this part, using the magnetic field tuning ability of SMPs, we present an active THz PSL. The focal length of the PSL can be actively tuned by an external magnetic field.

The PSL structure is shown in **Figure 17**. It is composed a symmetric 2D InSb slab surrounded by air, and perforated with 2 $N$-1 slits. The thickness of the slab is $h$; the lens width is $d$; and the width of the $i$-th slit is denoted by $w_i$. The incident plane wave is TM-polarized with frequency $f$. Therefore, each slit can be considered as an SIS waveguide structure with finite length in $z$-direction, or a single-mode Fabry-Perot (F-P) cavity, with the refractive index of $n_1$ above the slit, $n_3$ below the slit, and $n_{eff} = \beta/k_0$ the effective refractive index of the slit. $\beta$ is the propagating constant of SMPs that can be calculated by Eq. (21). In consequence, according to Fresnel equations, the phase retardation $\Delta\varphi$ of the magnetic field component $H_y$ through a slit is expressed as

$$\Delta\varphi = \arg\left[\frac{H_{yo}}{H_{yi}}\right] = \arg\left[\frac{t_{01}t_{12}e^{i\alpha}}{1 - r_{10}r_{12}e^{i2\alpha}}\right] \tag{36}$$

where $H_{yi}$ and $H_{yo}$ are the incident magnetic field at the entrance and transmitted magnetic field at the exit, respectively. $\alpha = k_0 \times h \times neff$, $r_{10} = (n_1 - neff)/(n_1 + neff)$, $r_{12} = (n_2 - neff)/(n_2 + neff)$, $t_{01} = 1 - r_{10}$, $t_{12} = 1 + r_{12}$. Therefore, according to Eq. (21), different slit widths and magnetic fields provide different propagation constants, and also the phases. In the following design procedures, without loss of generality, we set the thickness of the slab as $h$ = 300 μm, and the incident frequency is $f$ = 1 THz, thus $\varepsilon_V = -45.6 + 16.4i$ for B = 0 Tesla and $\varepsilon_V = -14.3 + 6.6i$ for B = 1 Tesla.

Since phase retardation is the key factor in the design, we study the impact of the external magnetic field on $\Delta\varphi$ first. The dispersion of SMPs in an InSb-air-InSb structure considering the loss of InSb is depicted in **Figure 18(a)**, according to Eq. (21). It is found from the figure

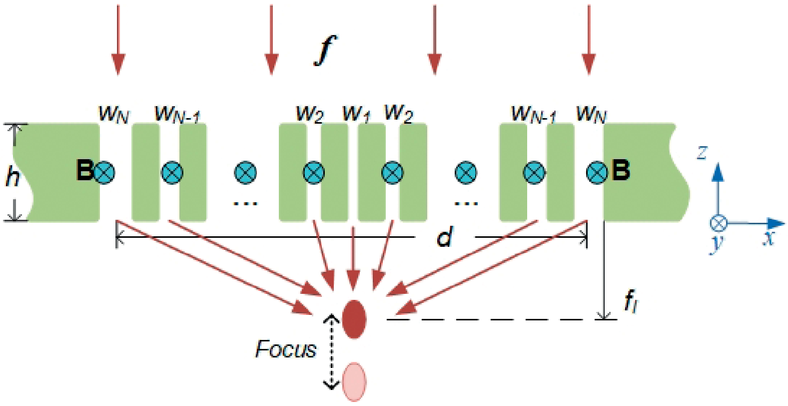

**Figure 17.** Schematic structure of the tunable THz PSL. The structure consists of an InSb slab tunable by an external magnetic field $B$, and perforated with 2 $N$-1 sub-wavelength slits. THz waves are indicated by the red arrows. They have different phase retardations after the slits, thus focusing can be realized by modulating those phases. The thickness of the slab is denoted by $h$. the width of the $i$-th slit from the middle to the two sides is $w_i$. $f_l$ denotes the focal length of the lens. The external magnetic field B is applied along the y-axis in order to change the focal length.

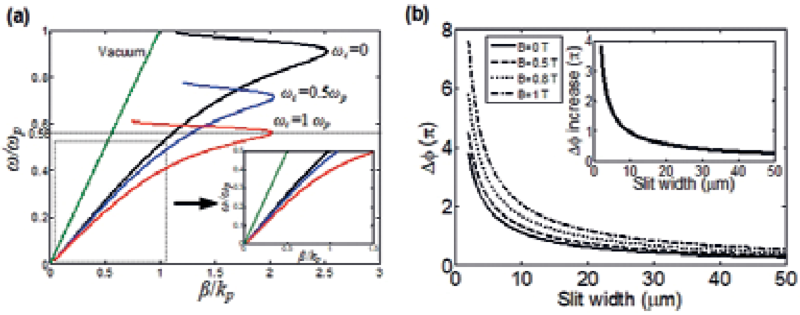

**Figure 18.** (a) Dispersion relation of SMPs in an InSb-air-InSb structure. The electronic dissipation is considered. Electromagnetic wave in vacuum and magnetoplasmons (MPs) under the magnetic field of $\omega_c = 0$, $\omega_c = 0.5\omega_p$, and $\omega_c = 1\omega_p$ are denoted by the green, black, blue and red lines, respectively. The inset shows the enlarged view of the low-frequency region. The insulator width is set as $w = 0.1 \times 2\pi c/\omega_p$. (b) Phase retardation of a single slit under external magnetic field of different intensity. The incident frequency is 1THz, and the thickness of the slab is 300 $\mu m$. The inset shows the corresponding increase of $\Delta\varphi$ against the slit width for a magnetic field from 0 Tesla to 1 Tesla.

that, when the magnetic field is increased, the dispersion curve moves toward lower-frequencies. In other words, for a certain frequency, the propagation constant increases with the increase of the magnetic field, which can be seen clearly in the inset of **Figure 18(a)**. As a result, it can be inferred from Eq. (36) that the phase retardation of the propagation mode in a slit is increased with the increase of the magnetic field. The curves of $\Delta\varphi$ versus slit width under several magnetic field intensities are plotted in **Figure 18(b)**, calculated by Eq. (36). It shows that for a single slit, the phase retardation becomes larger when an external magnetic field is applied. The reason is that with the increase of the external magnetic field, the negative real part of bulk dielectric constant $\varepsilon_V$ increases, which results in an increase of the effective refractive index of the slit. Therefore, the phase retardation is increased. It can also be found from **Figure 18(b)** that the change of the phase retardation of narrower slits is more obvious than that of wider slits under the same magnetic field.

Then following Eqs. (21) and (36), we design a lens with focal length of $f_l = 7\lambda$ for $B = 0$, the slit positions and widths are shown in **Figure 19(a)**. The total width of the lens and slit number are $d$ = 2 mm and 2 $N$-1 = 41, respectively. Therefore, when an external magnetic field is applied, the phase curve at the slab output surface will be more convex (see **Figure 19(b)**) with the magnetic field. In analogous to a conventional lens, the focal length of the proposed lens will be reduced by the magnetic field.

To verify the tunability of the PSL, we calculate the distributions of magnetic field intensity of the electromagnetic field by FDTD simulations. The results are shown in **Figure 20**. The magnetic field intensity distributions of the lens for B = 0 Tesla and B = 1 Tesla are shown in **Figure 20(a)** and **(b)**, respectively. An obvious of focal length change is observed. From the dependence of the focal length on the intensity of applied magnetic field shown in **Figure 20 (c)**, it is found that it is changed by 3λ (from 5.92λ to 2.87λ). There is also a deviation of the calculated focal length (5.92λ) from the designed one (7λ), and some strong side lobes appear. This focal shift effect is caused by both the small Fresnel number (about 1.6 for our structure) and SMPs interactions between the slits [74]. We then change the designed parameters such as

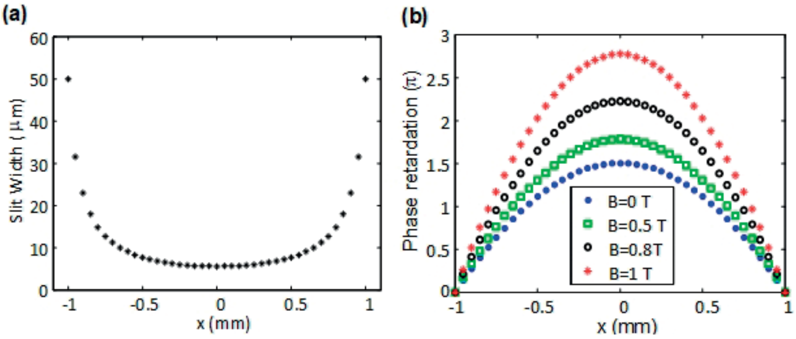

**Figure 19.** Design of a tunable THz plasmonic lens with focal length of $7\lambda$ and $d = 2$ mm, $N = 21$. (a) the slit position and corresponding slit width of the designed structure. (b) the relative phase retardation of the slits under magnetic fields of 0, 0.5, 0.8 and 1 Tesla.

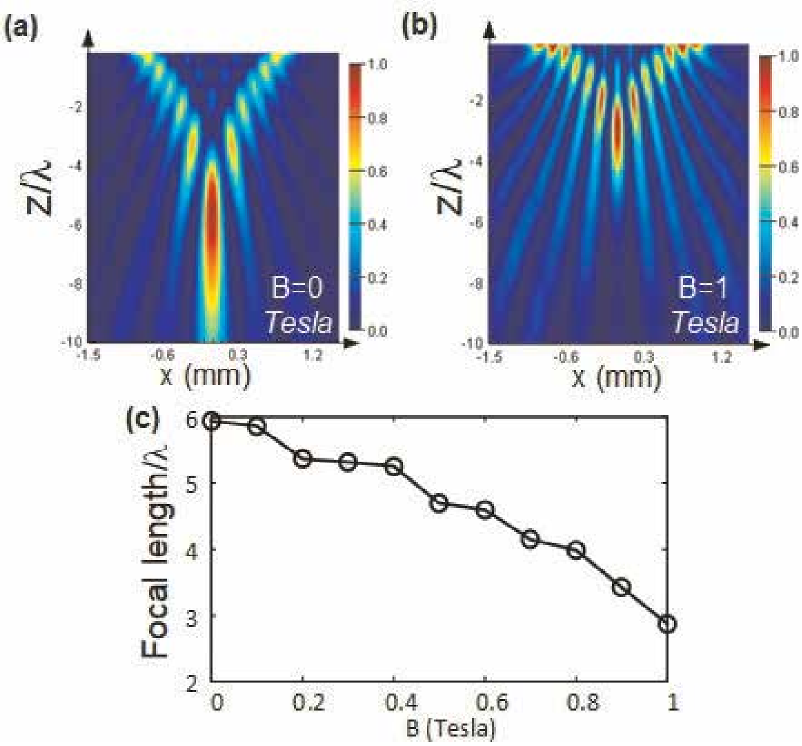

**Figure 20.** Magnetic field modulation on the THz PSL. (a), (b) $|H_y|^2$ distributions of the structure when the external magnetic field is 0 Tesla and 1 Tesla, respectively. (c) FDTD-calculated focal length when the external magnetic field is increased from 0 Tesla to 1 Tesla.

the lens width, the slit number, and designed focal length. The results are shown in **Figure 21**. It is found that, compared with slit number and designed focal length, the slit width $d$ has a greater impact on the focal length change. The reason is that for a larger lens width, the

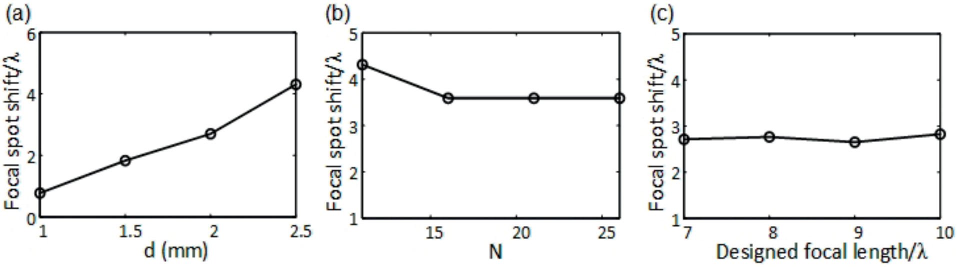

**Figure 21.** Focal length change caused by an external magnetic field increase from 0 to 1 Tesla as a function of various lens parameters. (a) Lens width changes as $d$ = 1 mm, 1.5 mm, 2 mm, and 2.5 mm, when the designed focal length and slit number are fixed at $f_l = 10\lambda$, 2 $N$-1 = 21, respectively; (b) $N$ changes as 11, 16, 21, and 26, when the designed focal length and lens width are fixed at $f_l = 10\lambda$, $d$ = 2.5 mm; (c) designed focal lengths changes as $7\lambda$, $8\lambda$, $9\lambda$, $10\lambda$, and the length width and slit number are fixed as $d$ = 2 mm, 2 $N$-1 = 41.

difference of the side slit width and middle slit width is greater. Therefore, the change of the phase curve on the exit plane of the slab is larger when an external magnetic field is applied.

We then investigate a lens with two monotonically increased sets of slits. The lens width and slit number are set as $d$ = 3 mm and $N$ = 31, as shown in **Figure 22(a)**. The designed focal length remains $7\lambda$. The structure has two monotone intervals: [0 mm, 0.9 mm], and [0.9 mm, 1.5 mm]

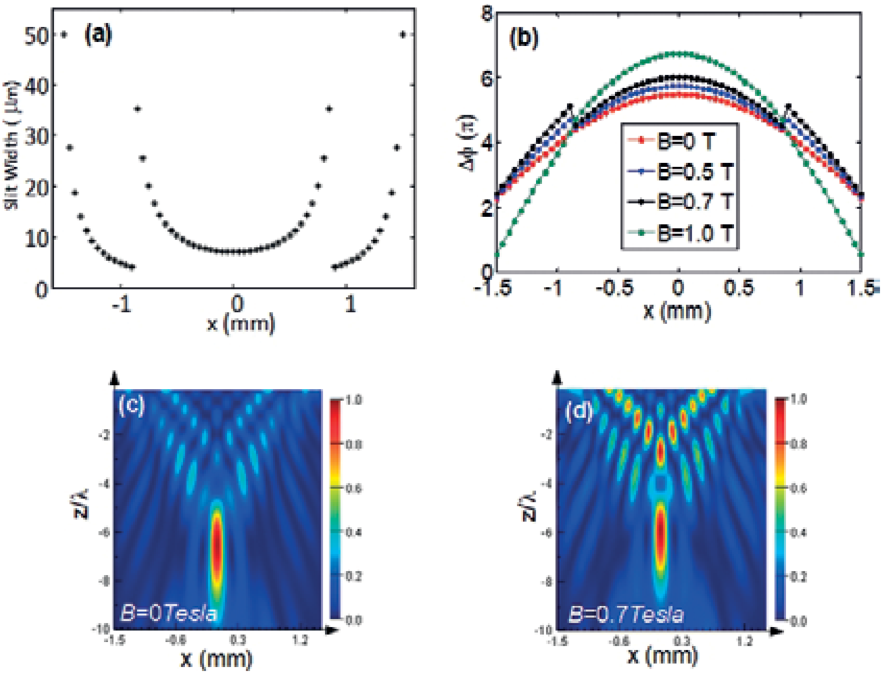

**Figure 22.** Bi-focus pattern by an external magnetic field. The parameters are same as the lens in **Figure 20**, except $d$ = 1 mm, $N$ = 31. (a) the slit position and corresponding slit width of the lens. (b) Phase retardation of the slits under different external magnetic fields. (c) and (d) $|H_y|^2$ distributions under a magnetic field of B = 0 and 0.7 Tesla, respectively.

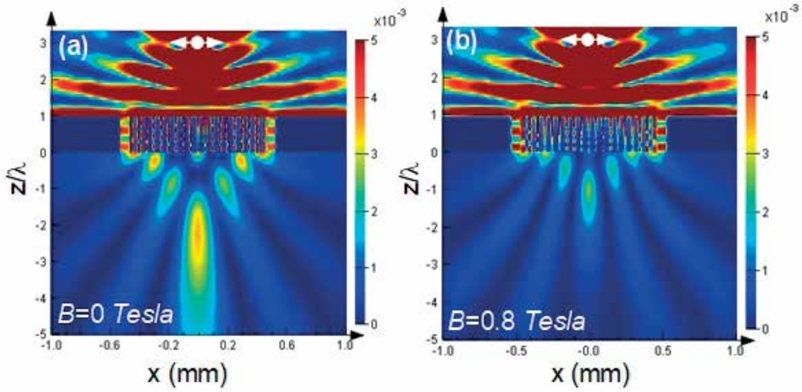

**Figure 23.** Magnetic-field tunable lens for a dipole source imaging. The designed object and image distances are both 3$\lambda$. The source is an electric dipole with the electric field vibration direction perpendicular to the *z*-axis, which is represented by a white circle on the top portion of the two figures. (a) $|H_y|^2$ distribution under a magnetic field of $B$ = 0 Tesla. The obtained image distance is 2.25$\lambda$. (b) $|H_y|^2$ distribution under a magnetic field of $B$ = 0.8 Tesla. The obtained image distance is 0.99$\lambda$.

from the middle to the two sides. The corresponding slit phase retardations are shown in **Figure 22(b)**. When the magnetic field increases, phase retardations of the two intervals grow asynchronously. Therefore, a discontinuous jump appears between the two intervals (see B = 0 and 0.7 Tesla for comparison). The field distribution of the transmitted wave at $B$ = 0 Tesla and $B$ = 0.7 Tesla (where the largest jump appears) are depicted in **Figure 22(c)** and **(d)**. It shows that when the magnetic field is 0.7 Tesla, we can achieve two focal spots along the *z*-axis.

Last but not least, a magnetic-field tunable lens for a dipole source imaging is proposed. The source is an electric dipole with the electric field vibration direction perpendicular to the *z*-axis. The designed object distance and image distance are both 3$\lambda$. The distributions of magnetic field intensity for the external magnetic field of $B$ = 0 Tesla and $B$ = 0.8 Tesla are depicted in **Figure 23(a)** and **(b)**, respectively. It shows that the obtained image distance is 2.25$\lambda$ and 0.99$\lambda$ for B = 0 and 0.8 Tesla, respectively.

## 4. Summary

In this chapter, we give a brief review on surface magneto plasmons. The theory of SMPs on a plane metal/conductor surface is reviewed. Our recent research on the theories of SMPs in symmetric and asymmetric slot waveguide is also presented. We also give the applications of SMPs based on their unique and intriguing properties, such as the nonreciprocal effect, two propagating bands, and tunability by an external magnetic field. A one-way THz waveguide, a THz broadly tunable slow-light system, and a focal length tunable plasmonic slit lens are presented, which show SMPs have big possibilities in applications of tunable plasmonic devices. Although the applications of SMPs have some drawbacks so far, including large loss and strong magnetic fields, with the rapid development of plasmonics, SMPs may open a new avenue of manipulating lights in subwavelength range.

## Author details

Bin Hu

Address all correspondence to: hubin@bit.edu.cn

Beijing Engineering Research Center for Mixed Reality and Advanced Display, School of Optics and Photonics, Beijing Institute of Technology, Beijing, China

## References

[1] Barnes WL, Dereux A, Ebbesen TW. Surface plasmon subwavelength optics. Nature. 2003; **424**(6950):824-830

[2] Raether H. In: Hohler G, editor. Surface Plasmons on Smooth and Rough Surfaces and on Gratings. Berlin: Springer; 1988

[3] Palik ED, Furdyna JK. Infrared and microwave magnetoplasma effects in semiconductors. Reports on Progress in Physics. 1970;**33**(3):1193-1322

[4] Brion JJ, Wallis RF, Hartstein A, Burstein E. Theory of surface magnetoplasmons in semiconductors. Physical Review Letters. 1972;**28**(22):1455-1458

[5] Brion JJ, Wallis RF. Theory of pseudosurface polaritons in semiconductors in magnetic fields. Physical Review B. 1974;**10**(8):3140-3143

[6] Wallis RF, Brion JJ, Burstein E. Theory of surface polaritons in anisotropic dielectric media with application to surface magnetoplasmons in semiconductors. Physical Review B. 1974;**9**(8):3424-3437

[7] Kushwaha MS, Halevi P. Magnetoplasma modes in thin films in the faraday configuration. Physical Review B. 1987;**35**(8):3879-3889

[8] Chiu KW, Quinn JJ. Magnetoplasma surface waves in metals. Physical Review B. 1972; **5**(12):4707-4709

[9] De Wames RE, Hall WF. Magnetic field effect on plasma-wave dispersion in a dielectric layer. Physical Review Letters. 1972;**29**(3):172-175

[10] Flahive PG, Quinn JJ. Surface waves of an electron-hole plasma in a uniform magnetic field. Physical Review Letters. 1973;**31**(9):586-589

[11] Brion JJ, Wallis RF, Hartstein A, Burstein E. Interaction of surface magnetoplasmons and surface optical phonons in polar semiconductors. Surface Science. 1973;**34**(1):73-80

[12] Hartstein A, Burstein E, Palik ED, Gammon RW, Henvis BW. Investigation of optic-phonon—Magnetoplasmon-type surface polaritons on n-InSb. Physical Review B. 1975; **12**(8):3186

[13] Palik ED, Kaplan R, Gammon RW, Kaplan H, Wallis RF, Quinn JJ. Coupled surface magnetoplasmon-optic-phonon polariton modes on InSb. Physical Review B. 1976;**13**(6):2497

[14] Eguiluz A, Quinn JJ. Magnetoplasma surface waves in solids with diffuse electron density profiles. Physical Review B. 1976;**13**(10):4299-4305

[15] Yi KS, Quinn JJ. Magnetoplasma surface waves of a degenerate semiconductor in the Faraday geometry: Effect of the presence of a metallic screen. Physical Review B. 1980; **22**(12):6247-6253

[16] Tyler IL, Fischer B, Bell RJ. On the observation of surface magnetoplasmons. Optics Communications. 1973;**8**(2):145-146

[17] Kaplan H et al. Calculation of attenuated-total-reflection spectra of surface magnetoplasmons on semiconductors. Journal of the Optical Society of America. A. 1974;**64**(11): 1551-1562

[18] Fisher AD. Optical guided-wave interactions with magnetostatic waves at microwave frequencies. Applied Physics Letters. 1982;**41**(9):779

[19] Remer L et al. Nonreciprocity in the optical reflection of magnetoplasmas. Physical Review B. 1984;**30**(6):3277

[20] Stamps RL, Camley RE. Focusing of magnetoplasmon polaritons. Physical Review B. 1985;**31**:4924

[21] Camley RE. Nonreciprocal surface waves. Surface Science Reports. 1987;**7**(3–4):103-187

[22] Kushwaha M, Halevi P. Magnetoplasmons in thin films in the Voigt configuration. Physical Review B. 1987;**36**(11):5960-5967

[23] Glass N. Nonreciprocal diffraction via grating coupling to surface magnetoplasmons. Physical Review B. 1990;**41**(11):7615

[24] Boardman A, Shabat M, Wallis R. Nonlinear surface magnetoplasmon waves on a semiconductor. Optics Communications. 1991;**86**(5):416-422

[25] Elmzughi F, Tilley D. Surface and guided-wave polariton modes of magnetoplasma films in the Voigt geometry. Journal of Physics: Condensed Matter. 1994;**6**(23):4233

[26] Safarov V et al. Magneto-optical effects enhanced by surface plasmons in metallic multilayer films. Physical Review Letters. 1994;**73**(26):3584-3587

[27] Hermann C et al. Surface-enhanced magneto-optics in metallic multilayer films. Physical Review B. 2001;**64**:235422

[28] Kushwaha MS. Plasmons and magnetoplasmons in semiconductor heterostructures. Surface Science Reports. 2001;**41**(1–8):1-416

[29] Ebbesen T et al. Extraordinary optical transmission through sub-wavelength hole arrays. Nature. 1998;**391**(6668):667-669

[30] Ozbay E. Plasmonics: Merging photonics and electronics at nanoscale dimensions. Science (New York, N.Y.). 2006;**311**(5758):189-193

[31] Ritchie RH et al. Surface-plasmon resonance effect in grating diffraction. Physical Review Letters. 1968;**21**(22):1530-1533

[32] Economou E. Surface plasmons in thin films. Physical Review. 1969;**182**(2):539-554

[33] Marschall N, Fischer B, Queisser H. Dispersion of surface plasmons in InSp. Physical Review Letters. 1971;**27**(2):95-97

[34] Knop K. Rigorous diffraction theory for transmission phase gratings with deep rectangular grooves. Journal of the Optical Society of America. 1978;**68**(9):1206

[35] Moreland J, Adams A, Hansma PK. Efficiency of light emission from surface plasmons. Physical Review B. 1982;**25**(4):2297-2300

[36] Sheng P, Stepleman R, Sanda P. Exact eigenfunctions for square-wave gratings: Application to diffraction and surface-plasmon calculations. Physical Review B. 1982;**26**(6): 2907-2916

[37] Weber M, Mills D. Interaction of electromagnetic waves with periodic gratings: Enhanced fields and the reflectivity. Physical Review B. 1983;**27**(5):2698-2709

[38] Sambles J, Bradbery G, Yang F. Optical excitation of surface plasmons: An introduction. Contemporary Physics. 1991;**32**(3):173-183

[39] Yang F, Sambles J, Bradberry G. Long-range surface modes supported by thin films. Physical Review B. 1991;**44**(11):5855-5872

[40] Lochbihler H. Surface polaritons on gold-wire gratings. Physical Review B. 1994;**50**(7): 4795-4801

[41] Ebbesen TW, Genet C, Bozhevolnyi SI. Surface-plasmon circuitry. Physics Today. 2008; **61**(5):44-50

[42] Dionne J et al. Plasmon slot waveguides: Towards chip-scale propagation with subwavelength-scale localization. Physical Review B. 2006;**73**:035407

[43] Kurokawa Y, Miyazaki H. Metal-insulator-metal plasmon nanocavities: Analysis of optical properties. Physical Review B. 2007;**75**:035411

[44] Belotelov V, Doskolovich L, Zvezdin A. Extraordinary magneto-optical effects and transmission through metal-dielectric plasmonic systems. Physical Review Letters. 2007;**98**:077401

[45] Johnson BL, Shiau H-H. Guided magneto-plasmon polaritons in thin films: Non-reciprocal propagation and forbidden modes. Journal of Physics: Condensed Matter. 2008; **20**(33):335217

[46] Yu Z et al. One-way electromagnetic waveguide formed at the interface between a plasmonic metal under a static magnetic field and a photonic crystal. Physical Review Letters. 2008;**100**:23902

[47] Hadad Y, Steinberg B. Magnetized spiral chains of plasmonic ellipsoids for one-way optical waveguides. Physical Review Letters. 2010;**105**:233904

[48] Lan Y-C, Chen C-M. Long-range surface magnetoplasmon on thin plasmon films in the Voigt configuration. Optics Express. 2010;**18**(12):12470

[49] Khanikaev A et al. One-way extraordinary optical transmission and nonreciprocal spoof plasmons. Physical Review Letters. 2010;**105**:126804

[50] Ferreiro-Vila E et al. Intertwined magneto-optical and plasmonic effects in Ag/Co/Ag layered structures. Physical Review B. 2009;**80**:125132

[51] Drezdzon SM, Yoshie T. On-chip waveguide isolator based on bismuth iron garnet operating via nonreciprocal single-mode cutoff. Optics Express. 2009;**17**(11):9276-9281

[52] Temnov V et al. Active magneto-plasmonics in hybrid metal–ferromagnet structures. Nature Photonics. 2010;**4**(February):107-111

[53] Torrado JF et al. Magneto-optical effects in interacting localized and propagating surface plasmon modes. Optics Express. 2010;**18**(15):15635-15642

[54] Zhu H, Jiang C. Nonreciprocal extraordinary optical transmission through subwavelength slits in metallic film. Optics Letters. 2011;**36**(8):1308-1310

[55] Belotelov VI et al. Enhanced magneto-optical effects in magnetoplasmonic crystals. Nature Nanotechnology. 2011;**6**(6):370-376

[56] Ferreiro-Vila E et al. Magneto-optical and magnetoplasmonic properties of epitaxial and polycrystalline Au/Fe/Au trilayers. Physical Review B. 2011;**83**:205120

[57] Bonanni V et al. Designer magnetoplasmonics with nickel nanoferromagnets. Nano Letters. 2011;**11**:5333-5338

[58] Lan Y-C, Chang Y-C, Lee P-H. Manipulation of tunneling frequencies using magnetic fields for resonant tunneling effects of surface plasmons. Applied Physics Letters. 2007; **90**(17):171114

[59] Kong F et al. Analysis of the surface Magnetoplasmon modes in the semiconductor slit waveguide at terahertz frequencies. Progress in Electromagnetics Research. 2008;**82**: 257-270

[60] Hu B et al. Optical transmission resonances tuned by external static magnetic field in an n-doped semiconductor grating with subwavelength slits. Optics Communications. 2008; **281**(24):6120-6123

[61] Liu X-X et al. Dispersion mechanism of surface magnetoplasmons in periodic layered structures. Applied Optics. 2009;**48**(16):3102-3107

[62] Liu Z, Jin G. Extraordinary THz transmission through subwavelength semiconductor slits under antiparallel external magnetic fields. Applied Physics A. 2011;**105**(4):819-825

[63] Hu B, Wang QJ, Zhang Y. Slowing down terahertz waves with tunable group velocities in a broad frequency range by surface magneto plasmons. Optics Express. 2012;**20**(9): 10071-10076

[64] Hu B, Wang QJ, Zhang Y. Broadly tunable one-way terahertz plasmonic waveguide based on nonreciprocal surface magneto plasmons. Optics Letters. 2012;**37**(11):1895-1897

[65] Hu B et al. Active focal length control of terahertz slitted plane lenses by magneto-plasmons. Plasmonics. 2011 published on line: http://www.springerlink.com/content/p53 1745636224004/

[66] Chen J et al. Efficient unidirectional generation of surface plasmon polaritons with asymmetric single-nanoslit. Applied Physics Letters. 2010;**97**(4):041113

[67] Williams CR et al. Highly confined guiding of terahertz surface plasmon polaritons on structured metal surfaces. Nature Photonics. 2008;**2**(3):175-179

[68] Hau LV et al. Light speed reduction to 17 metres per second in an ultracold atomic gas. Nature. 1999;**397**(6720):594-598

[69] Sandtke M, Kuipers L. Slow guided surface plasmons at telecom frequencies. Nature Photonics. 2007;**1**(10):573-576

[70] Fitrakis E, Kamalakis T, Sphicopoulos T. Slow light in insulator-metal-insulator plasmonic waveguides. Journal of the Optical Society of America B. 2011;**28**(9):2159-2164

[71] Fitrakis E, Kamalakis T, Sphicopoulos T. Slow-light dark solitons in insulator-insulator-metal plasmonic waveguides. Journal of the Optical Society of America B. 2010;**27**(9): 1701-1706

[72] Yu N et al. Designer spoof surface plasmon structures collimate terahertz laser beams. Nature Materials. 2010;**9**(9):730-735

[73] Verslegers L et al. Planar lenses based on nanoscale slit arrays in a metallic film. Nano Letters. 2009;**9**(1):235-238

[74] Hu B, Wang QJ, Zhang Y. Systematic study of planar plasmonic slit lenses and the focal shift effect. Nanotechnology. 2012;**23**(44):444002

Chapter 7

# Plasmonic Enhancement of Solar Cells Efficiency: Material Dependence in Semiconductor Metallic Surface Nano-Modification

Janusz E. Jacak and Witold A. Jacak

Additional information is available at the end of the chapter

http://dx.doi.org/10.5772/intechopen.79113

**Abstract**

Recent experimental data shown a promising direction in employing nano-plasmonics for increasing efficiencies of the solar cells. The effect is due to metallic nanoparticles' plasmons mediating energy transfer from the incoming e-m wave to the semiconductor in a regime violating limits in energy transitions imposed by the momentum conservation, due to translational invariance departure in surface nano-modified system. The chapter presents analysis of material dependence of near-field coupling to band electrons of surface plazmons in metallic nanoparticles deposited on the top of semiconductor substrate in nano-modified solar cells. Various materials for metal and substrate are comparatively studied upon the quantum Fermi Golden Rule approach in theoretical quantitative modeling of the plasmon-electron coupling that enhances ordinary PV effect. The material dependence of the plasmon-mediated efficiency growth in two types of solar cells, multi-crystalline Si and CIGS (copper-indium-gallium-diselenide), modified by various surface-deposited metallic nanoparticles is additionally illustrated by the experimental data.

**Keywords:** plasmons, metallic nanoparticles, photo effect, solar cells

## 1. Introduction

The plasmon-mediated sunlight energy harvesting in metal-nano-modified solar cells is caused by three effects: the strong concentration of electric field of plasmon oscillations close to metallic components with local large curvature, the large amplitude of plasmon oscillations in metallic nanoparticles and the enhancement of the probability of interband excitations in semiconductor substrate caused by breaking of the translational symmetry for a nanoparticle

IntechOpen

© 2018 The Author(s). Licensee IntechOpen. This chapter is distributed under the terms of the Creative Commons Attribution License (http://creativecommons.org/licenses/by/3.0), which permits unrestricted use, distribution, and reproduction in any medium, provided the original work is properly cited.

and the dipole near-field coupling of surface plasmons with semiconductor band electrons [1–7]. The transition probability for transfer of electrons from the valence band to the conduction band in a semiconductor, essential for efficiency of the photovoltaic effect, grows due to the electric field amplitude enhancement and due to admission of all oblique transitions not here prohibited by the momentum conservation [4]. In the ordinary photo effect Kiriejew [8], the interband transitions are confined to only vertical ones between states with almost the same momentum due to the momentum conservation and the fact that the sunlight photons have very small momentum (owing to large light velocity, $c$) which almost does not change electron momentum at scattering: for excitation energy $\hbar\omega$ beyond the forbidden gap, $E_g$, in the substrate semiconductor, $\hbar\omega = cq$ gives $q \ll p$, where $p \sim \frac{\pi\hbar}{l}$ is the semiconductor band quasi-momentum scale in the Brillouin zone ($l$ denotes here the elementary cell linear size). Thus the change of the band electron momentum $\mathbf{p}_1 = \mathbf{p}_2 + \mathbf{q}$ is negligible on the scale of the Brillouin zone and $\mathbf{p}_1 \simeq \mathbf{p}_2$ (because $c = 10^8$ m/s) and only the vertical, conserving momentum, interband transitions contribute to the ordinary photo effect, i.e., when the transition is caused by free photons with momentum $\mathbf{q}$ and energy $\hbar\omega = cq$.

However, for interaction of band electrons with surface plasmon from the metallic nanoparticle deposited on the semiconductor surface, the situation changes significantly. In the near-field regime [9], the potential of the plasmon dipole on the nanosphere is proportional to $\frac{1}{R^2}$ ($R$ is a distance from the sphere center), which has the infinite decomposition in Fourier picture and thus overlaps with all quasi-momenta in the substrate semiconductor Brillouin zone. This is in contrary to the potential of the free photon which contributes via only single $e^{i(\mathbf{q}\cdot\mathbf{r}-\hbar\omega t)/\hbar}$ plane-wave Fourier component.

The resulted effect of oblique interband transitions can be accounted for via the Fermi Golden Rule (FGR). According the FGR scheme [10], the probability of interband transitions is proportional to matrix element of the perturbation potential between initial and final states and summed up over all initial states in the valence band and over all final states in the conduction band assuming only the energy conservation, $E_p(\mathbf{p}_1) + \hbar\omega = E_n(\mathbf{p}_2)$, where $E_{p(n)}(\mathbf{p})$ is the valence-$p$ (conduction-$n$) band dispersion and $\hbar\omega$ is the excitation energy related to damped and forced by sunlight surface plasmon oscillations with the bare self-energy value $\hbar\omega_1 = \frac{\hbar\omega_p}{\sqrt{3}}$ (i.e., the Mie energy [11, 12], $\hbar\omega_p = \hbar\sqrt{\frac{n_e e^2}{m^* \varepsilon_0}}$ is the bulk-plasmon energy in metal [13], $n_e$ is the density of collective electrons in metal, $m^*$ is the effective mass of electron in metal, $e$ is the electron charge and $\varepsilon_0$ is the dielectric constant) with not-defined momentum, however. The initial momentum, $\mathbf{p}_1$, and the final one, $\mathbf{p}_2$, can be arbitrary because the momentum conservation is rule out by the matrix element of the local dipole interaction.

The chapter is organized as follows. In Section 2, we present the quantum calculation of the efficiency of photo effect mediated by plasmons in metallic nanoparticles deposited on the top of a semiconductor photodiode. This efficiency has been accounted by application of the Fermi golden rule to the near-field coupling of dipole-plasmons with band electrons in the semiconductor substrate. The resulted transition probability is next utilized to the derivation of the plasmon damping rate due to coupling with band electrons which we present in Section 3.

Section 4 addressed to analysis of the by-plasmon enhanced photo effect efficiency in various materials, including various metals for nanoparticles with plasmons and various semiconductor substrates. Section 5 contains also comparison with experiment both for laboratory Si photodiode covered with metallic nanoparticles as well as for standard solar cells, Si-multicrystal and CIGS.

## 2. Plasmon-mediated photo effect: Fermi Golden Rule calculus of probability of electron interband excitation due to plasmons

The perturbation of electron band system in the substrate semiconductor due to the presence of dipole surface plasmon oscillations in metallic nanosphere (with a radius $a$) deposited on the semiconductor surface, has the form of the potential of the e-m field of an oscillating dipole. The Fourier components of the electric $\mathbf{E}_\omega$ and magnetic $\mathbf{B}_\omega$ fields produced in the distance $\mathbf{R}$ from the center of considered nanosphere with the dipole of surface plasmon with the frequency $\omega$, have the form [9],

$$\mathbf{E}_\omega = \frac{1}{\varepsilon}\left\{\mathbf{D}_0\left(\frac{k^2}{R}+\frac{ik}{R^2}-\frac{1}{R^3}\right)+\widehat{\mathbf{n}}(\widehat{\mathbf{n}}\cdot\mathbf{D}_0)\left(-\frac{k^2}{R}-\frac{3ik}{R^2}+\frac{3}{R^3}\right)\right\}e^{ikR} \tag{1}$$

and

$$\mathbf{B}_\omega = \frac{ik}{\sqrt{\varepsilon}}[\mathbf{D}_0\times\widehat{\mathbf{n}}]\left(\frac{ik}{R}-\frac{1}{R^2}\right)e^{ikR}, \tag{2}$$

($\varepsilon$ is the dielectric permittivity). In the case of the spherical symmetry, the dipole of plasmon is considered as pinned to the center of the nanosphere (the origin of the reference frame system), $\mathbf{D}=\mathbf{D}_0e^{-i\omega t}$. In Eqs. (1) and (2), we used the notation for the retarded argument, $i\omega\left(t-\frac{R}{c}\right)=i\omega t-ikR$, $\widehat{\mathbf{n}}=\frac{\mathbf{R}}{R}$, $\omega=ck$, momentum $\mathbf{p}=\hbar\mathbf{k}$. The terms with denominators $R^3$, $R^2$ and $R$ are referred to near-, medium- and far-field zones of the dipole radiation, correspondingly. Because we consider the interaction with a closely adjacent layer of the substrate semiconductor, all terms with denominators $R^2$ and $R$ we neglect as small in comparison to the term with $R^3$ denominator—this is the near-field zone approximation (the magnetic field disappears and the electric field is of the form of a static dipole field [9]). Therefore the related perturbation potential added to the system Hamiltonian attains the form,

$$w=e\psi(\mathbf{R},t)=\frac{e}{\varepsilon R^2}\widehat{\mathbf{n}}\cdot\mathbf{D}_0\,sin\,(\omega t+\alpha)=w^+e^{i\omega t}+w^-e^{-i\omega t}. \tag{3}$$

The term $w^+=(w^-)^*=\frac{e}{\varepsilon R^2}\frac{e^{i\alpha}}{2i}\widehat{\mathbf{n}}\cdot\mathbf{D}_0$ describes emission, i.e., the case of our interest.

According to the FGR [10], the interband transition probability is proportional to

$$w(\mathbf{k}_1,\mathbf{k}_2)=\frac{2\pi}{\hbar}|<\mathbf{k}_1|w^+|\mathbf{k}_2>|^2\delta\left(E_p(\mathbf{k}_1)-E_n(\mathbf{k}_2)+\hbar\omega\right), \tag{4}$$

where the Bloch states in the conduction and valence bands are assumed as planar waves (for simplicity), $\Psi_{\mathbf{k}} = \frac{1}{(2\pi)^{3/2}} e^{i\mathbf{k}\cdot\mathbf{R} - iE_{n(p)}(\mathbf{k})t/\hbar}$, $E_p(\mathbf{k}) = -\frac{\hbar^2\mathbf{k}^2}{2m_p^*} - E_g$, $E_n(\mathbf{k}) = \frac{\hbar^2\mathbf{k}^2}{2m_n^*}$ (indices $n, p$ refer to electrons from the conduction and valence bands, respectively, $E_g$ is the forbidden gap).

The matrix element,

$$< \mathbf{k}_1|w^+|\mathbf{k}_2 >= \frac{1}{(2\pi)^3}\int d^3R \frac{e}{\varepsilon 2i} e^{i\alpha}\hat{\mathbf{n}} \cdot \mathbf{D}_0 \frac{1}{R^2} e^{-i(\mathbf{k}_1 - \mathbf{k}_2)\cdot\mathbf{R}}. \tag{5}$$

can be found analytically by a direct integration, which gives the formula ($\mathbf{q} = \mathbf{k}_1 - \mathbf{k}_2$),

$$< \mathbf{k}_1|w^+|\mathbf{k}_2 >= \frac{-1}{(2\pi)^3}\frac{ee^{i\alpha}}{\varepsilon} D_0 \cos\Theta(2\pi)\int_a^\infty dR \frac{1}{q}\frac{d}{dR}\frac{\sin qR}{qR} = \frac{1}{(2\pi)^2}\frac{ee^{i\alpha}}{\varepsilon}\frac{\mathbf{D}_0 \cdot \mathbf{q}}{q^2}\frac{\sin qa}{qa}. \tag{6}$$

Next, we must sum up overall initial and final states in both bands. Thus, for the total interband transition probability we have,

$$\delta w = \int d^3k_1 \int d^3k_2 \left[f_1(1 - f_2)w(\mathbf{k}_1, \mathbf{k}_2) - f_2(1 - f_1)w(\mathbf{k}_2, \mathbf{k}_1)\right], \tag{7}$$

where $f_1, f_2$ assign the temperature dependent distribution functions (Fermi-Dirac distribution functions) for initial and final states, respectively. For room temperatures, $f_2 \simeq 0$ and $f_1 \simeq 1$, which leads to,

$$\delta w = \int d^3k_1 \int d^3k_2 \cdot w(\mathbf{k}_1, \mathbf{k}_2). \tag{8}$$

After some also analytical integration in the above formula, we arrive at the expression,

$$\begin{aligned}\delta w &= \frac{4}{3}\frac{\mu^2\left(m_n^* + m_p^*\right)2\left(\hbar\omega - E_g\right)e^2D_0^2}{\sqrt{m_n^*m_p^*}2\pi\hbar^5\varepsilon^2}\int_0^1 dx \frac{\sin^2(xa\xi)}{(xa\xi)^2}\sqrt{1 - x^2} \\ &= \frac{4}{3}\frac{\mu^2}{\sqrt{m_n^*m_p^*}}\frac{e^2D_0^2}{2\pi\hbar^3\varepsilon^2}\xi^2\int_0^1 dx \frac{\sin^2(xa\xi)}{(xa\xi)^2}\sqrt{1 - x^2},\end{aligned} \tag{9}$$

according to assumed band dispersions, $m_n^*$ and $m_p^*$ denote the effective masses of electrons and holes, $\mu = \frac{m_n^* m_p^*}{m_n^* + m_p^*}$ is the reduced mass, the parameter $\xi = \frac{\sqrt{2\left(\hbar\omega - E_g\right)\left(m_n^* + m_p^*\right)}}{\hbar}$. In limiting cases for a nanoparticle radius $a$, we finally obtain,

$$\delta w = \begin{cases} \dfrac{4}{3}\dfrac{\mu\sqrt{m_n^*m_p^*}\left(\hbar\omega - E_g\right)e^2D_0^2}{\hbar^5\varepsilon^2}, & \text{for } a\xi \ll 1, \\[2ex] \dfrac{4}{3}\dfrac{\mu^{3/2}\sqrt{2}\sqrt{\hbar\omega - E_g}e^2D_0^2}{a\hbar^4\varepsilon^2}, & \text{for } a\xi \gg 1. \end{cases} \tag{10}$$

In the latter case in Eq. (10), the following approximation was applied,

$$\int_0^1 dx \frac{sin^2(xa\xi)}{(xa\xi)^2}\sqrt{1-x^2} \approx (\text{for } a\xi \gg 1)\frac{1}{a\xi}\int_0^\infty d(xa\xi)\frac{sin^2(xa\xi)}{(xa\xi)^2} = \frac{\pi}{2a\xi},$$

whereas in the former one, $\int_0^1 dx\sqrt{1-x^2} = \pi/4$.

With regard to two limiting cases, $a\xi \ll 1$ or $a\xi \gg 1$, $\xi = \frac{\sqrt{2(\hbar\omega - E_g)(m_n^* + m_p^*)}}{\hbar}$, we see that $a \simeq 1/\xi \simeq \begin{cases} > 2 \times 10^{-9}[m] \ for \ \dfrac{\hbar\omega - E_g}{E_g} < 0.02 \\ < 2 \times 10^{-9}[m] \ for \ \dfrac{\hbar\omega - E_g}{E_g} > 0.02 \end{cases}$, and this range weakly depends on effective masses and $E_g$. Thus for nanoparticles with radii $a > 2$ nm, the first regime holds only close to $E_g$ (less than the 2% distance to limiting $E_g$), whereas the second regime holds in the rest of the $\omega$ domain. For comparison, $a \simeq 1/\xi \simeq \begin{cases} > 0.5 \times 10^{-9}[m] \ for \ \dfrac{\hbar\omega - E_g}{E_g} < 0.5 \\ < 0.5 \times 10^{-9}[m] \ for \ \dfrac{\hbar\omega - E_g}{E_g} > 0.5 \end{cases}$, the first region widens considerably (to ca. 50% relative distance to $E_g$), but holds only for ultrasmall size of nanoparticles ($a < 0.5$ nm). For larger nanospheres, e.g., with $a > 10$ nm, the second regime is thus dominating.

One can notice that the above formula, Eq. (9) and its explicit form in limiting situations given by Eq. (10), is the generalization of to the ordinary photo effect, for which the transition probability is different [8],

$$\delta w_0 = \frac{4\sqrt{2}}{3}\frac{\mu^{5/2}e^2}{m_p^{*2}\omega\varepsilon\hbar^3}\left(\frac{\varepsilon E_0^2 V}{8\pi\hbar\omega}\right)\left(\hbar\omega - E_g\right)^{3/2}. \tag{11}$$

The number of photons of the $\omega$ e-m wave with electric field component amplitude $E_0$ in the volume $V$ equals to, $\left(\frac{\varepsilon E_0^2 V}{8\pi\hbar\omega}\right)$, hence the probability of single photon absorption by the semiconductor per time unit, attains the form in the ordinary photo effect [8],

$$q_0 = \delta w_0 \left(\frac{\varepsilon E_0^2 V}{8\pi\hbar\omega}\right)^{-1} = \frac{4(4)\sqrt{2}}{3}\frac{\mu^{5/2}e^2}{m_p^{*2}\omega\varepsilon\hbar^3}\left(\hbar\omega - E_g\right)^{3/2}, \tag{12}$$

(factor (4) corresponds here to spin degeneration of band electrons).

In the case of mediation by plasmons, all oblique interband transitions contribute, not only vertical ones (as it was for the interaction with the planar wave in the ordinary photo effect). This results in an enhancement of the transition probability for the near-field coupling in comparison to the photon (planar wave) absorption rate in a semiconductor in the ordinary photo effect. The enhancement of the probability of transition due to hopping not conserving momentum, is, however, gradually quenched with the radius $a$ growth, as expressed by Eq. (10).

The probability of energy absorption in the semiconductor via mediation of surface plasmons per single photon incident on the metallic nanospheres, $q_m$, equals to the product of $\delta w$ (given by Eq. (10)) and the number, $N_m$, of metallic nanoparticles divided by photon density with additional phenomenological factor $\beta$ responsible for all effects not directly accounted for (as deposition separation and surface properties reducing the coupling strength, as well as energy losses due to electron scattering and irradiation to far-field zone (Lorentz friction [9]) into upper hemisphere, if the metallic nanoparticle is not completely embedded in the substrate semiconductor medium),

$$q_m = \beta N_m \delta w \left( \frac{\varepsilon E_0^2 V}{8\pi\hbar\omega} \right)^{-1}. \tag{13}$$

## 3. Damping rate for plasmons in a metallic nanoparticle deposited on a top of a semicoductor

Assuming that the energy acquired by the semiconductor band system, $\mathcal{A}$, is equal to the output of plasmon oscillation energy (resulting in plasmon damping), one can estimate the corresponding damping rate of plasmon oscillations. Namely, at the damped (lowering in time) plasmon amplitude $D_0(t) = D_0 e^{-t/\tau'}$, one finds for a total transmitted energy,

$$\mathcal{A} = \beta \int_0^\infty \delta w \hbar\omega dt = \beta\hbar\omega\delta w\tau'/2 = \begin{cases} \dfrac{2}{3} \dfrac{\beta\omega\tau'\mu\sqrt{m_n^* m_p^*}(\hbar\omega - E_g)e^2 D_0^2}{\hbar^4\varepsilon^2}, & \text{for } a\xi \ll 1, \\ \dfrac{2}{3} \dfrac{\beta\omega\tau'\mu^{3/2}\sqrt{2}\sqrt{\hbar\omega - E_g}e^2 D_0^2}{a\hbar^3\varepsilon^2}, & \text{for } a\xi \gg 1, \end{cases} \tag{14}$$

where $\tau'$ is the damping time-rate and $\beta$ accounts for losses (not included in the model). Comparing the value of $\mathcal{A}$ given by the formula (14) with the energy loss of damping plasmon estimated in Ref. [4] (the initial energy of the plasmon oscillations which has been transferred step-by-step to the semiconductor, $\mathcal{A} = \frac{D_0^2}{2\varepsilon a^3}$), one can find

$$\frac{1}{\tau'} = \begin{cases} \dfrac{4\beta\omega\mu\sqrt{m_n^* m_p^*}(\hbar\omega - E_g)e^2 a^3}{3\hbar^4\varepsilon}, & \text{for } a\xi \ll 1, \\ \dfrac{4\beta\omega\mu^{3/2}\sqrt{2}\sqrt{\hbar\omega - E_g}e^2 a^2}{3\hbar^3\varepsilon}, & \text{for } a\xi \gg 1. \end{cases} \tag{15}$$

By $\tau'$, we denote here a large damping of plasmons due to energy transfer to the semiconductor substrate highly exceeding the internal damping, characterized by $\tau$, due to scattering of electrons inside the metallic nanoparticle [4] ($\frac{1}{\tau} \ll \frac{1}{\tau'}$). We neglect also the irradiation to far-field upper hemisphere zone of plasmon energy due to the Lorentz friction, which is also smaller than near-field zone energy transfer to the substrate [4].

For example, for nanospheres of Au deposited on the Si layer, we obtain for Mie self-frequency $\omega = \omega_1$,

$$\frac{1}{\tau'\omega_1} = \begin{cases} 44.092\beta\left(\frac{a[nm]}{1[nm]}\right)^3 \frac{\mu}{m}\frac{\sqrt{m_n^* m_p^*}}{m}, & \text{for } a\xi \ll 1, \\ 13.648\beta\left(\frac{a[nm]}{1[nm]}\right)^2 \left(\frac{\mu}{m}\right)^{3/2}, & \text{for } a\xi \gg 1, \end{cases} \tag{16}$$

for light(heavy) carriers in Si, $m_n^* = 0.19(0.98)\ m$, $m_p^* = 0.16(0.52)\ m$, $m$ is the bare electron mass, $\mu = \frac{m_n^* m_p^*}{m_n^* + m_p^*}$ and $E_g = 1.14$ eV, $\hbar\omega_1 = 2.72$ eV. For these parameters and nanospheres with the radius $a$ in the range of $5 - 50$ nm, the lower case of Eq. (16) applies (at $\omega = \omega_1$). The parameter $\beta$ fitted from the experimental data [4, 14] equals to ca 0.001.

In another scenario when the output of the plasmon energy is recovered by continuous income from the sunlight, one can consider the energy-balanced state. In an idealized case, whole incoming energy of the monochromatic $\omega$ e-m wave is transferred to the semiconductor via plasmons, and we deal with the stationary behavior of a driven and damped oscillator for plasmons. Even though the free undamped plasmon has the Mie self-resonance frequency, $\omega_1 = \frac{\omega_p}{\sqrt{3}}$, the frequency of plasma oscillation equals to the driven electric field frequency, $\omega$, of the incident e-m wave of photons. Because of an instant leakage of the plasmon energy in near-field to semiconductor substrate, this large damping of plasmon causes a red-shift and widening of the resonance, as for every damped and driven oscillator. The widened resonance enables the energy transfer from plasmons to electrons to embrace also frequencies lower or larger than Mie frequency but limited from below by the semiconductor gap $E_g/\hbar$.

The incident sunlight dispersion covers the visible spectrum and also some UV and infra-red tails. The total efficiency of the plasmon channel corresponds to a sum (integration) overall Fourier components $\omega > E_g/\hbar$ of light interfered with intensity distribution of sunlight spectrum. To model this behavior, it is necessary to consider separately each single monochromatic e-m mode, i.e., a Fourier component $\omega$. Its electric field excites plasmon with this frequency and this plasmon is damping with the rate $\frac{1}{\tau'}$ (15). This damping causes a red shift of a resonance and reduces the resonance amplitude, which in turn allows for the accommodation to the balance of energy transfer to the semiconductor with incident sunlight e-m wave energy intensity (defined by it electric field amplitude $E_0$) at the frequency $\omega$. Within this damped and driven oscillator model, the amplitude of plasmon oscillations $D_0(\omega)$ is constant in time and shaped by $f(\omega) = \frac{1}{\sqrt{\left(\omega_1^2 - \omega^2\right)^2 + 4\omega^2/\tau'^2}}$. The extremum of red-shifted resonance is attained at $\omega_m = \omega_1\sqrt{1 - 2(\omega_1\tau')^{-2}}$ with corresponding amplitude $\sim \tau'/\left(2\sqrt{\omega_1^2 - \tau'^{-2}}\right)$. The red shift is proportional to $1/\left(\omega_1\tau'^2\right)$. In the case of the described energy transfer balance, one obtains according to Eq. (10),

$$q_m = \begin{cases} \beta C_0 \dfrac{128}{9} \pi^2 a^3 \dfrac{\mu \sqrt{\mu_n^* \mu_p^*}}{m^2} \left(\hbar\omega - E_g\right) \dfrac{e^6 n_e^2 \omega}{\hbar^4 \varepsilon^3} f^2(\omega), & \text{for } a\xi \ll 1, \\ \beta C_0 \dfrac{128}{9} \sqrt{2}\pi^2 a^2 \dfrac{\mu^{3/2}}{m^2} \sqrt{\hbar\omega - E_g} \dfrac{e^6 n_e^2 \omega}{\hbar^3 \varepsilon^3} f^2(\omega), & \text{for } a\xi \gg 1, \end{cases} \tag{17}$$

where $f(\omega) = \frac{1}{\sqrt{\left(\omega_1^2 - \omega^2\right)^2 + 4\omega^2/\tau'^2}}$ corresponds to amplitude factor for driven damped oscillator and $D_0 = \frac{e^2 n_e E_0 4\pi a^3}{3m} f(\omega)$ (in Eq. (10)); the amplitude of the electric field, $E_0$, in the incident e-m wave is next ruled out from Eq. (17) due to normalization per single photon as in Eq. (13); $C_0 = \frac{N_m 4/3\pi a^3}{V}$, $V$ is the volume of the semiconductor, $N_m$ is the number of metallic nanospheres.

The ratio, $\frac{q_m}{q_0}$, revealing the advantage of the plasmon-mediated photo effect over the ordinary photo effect can be expressed as follows

$$\frac{q_m}{q_0} = \begin{cases} \dfrac{4\sqrt{2}\pi^2 a^3 \beta C_0 \sqrt{m_n^* m_p^*} \left(m_p^*\right)^2 e^4 n_e^2 \omega^2 f^2(\omega)}{3\mu^{3/2} m^2 \sqrt{\hbar\omega - E_g} \hbar \varepsilon^2}, & \text{for } a\xi \ll 1, \\ \dfrac{8\pi^2 a^2 \beta C_0 \left(m_p^*\right)^2 e^4 n_e^2 \omega^2 f^2(\omega)}{3\mu m^2 \left(\hbar\omega - E_g\right) \varepsilon^2}, & \text{for } a\xi \gg 1. \end{cases} \tag{18}$$

This ratio turns out to be of order of $10^4 \frac{\beta 40}{H[nm]}$ for the surface density of nanoparticles (as in experiment in Ref. [14]), $n_s \sim 10^8/\text{cm}^2$; note that $C_0 = n_s 4\pi a^3/(3H)$, $H$ is a thickness of the semiconductor layer, which including the phenomenological factor $\beta$, and the thickness $H$ (we have confirmed experimentally that the range of the near-field zone exceeds the Mie wavelength), is sufficient to explain the scale of the experimentally observed strong enhancement of absorption rate in semiconductors due to plasmons. The strong enhancement of this transition probability is linked with the allowance of momentum-non-conserved transitions, which is, however, reduced with the radius $a$ growth. The strengthening of the near-field induced interband transitions, in the case of large nanospheres, is, however, still significant as the quenching of oblique interband transitions is partly compensated by $\sim a^3$ growth of the amplitude of dipole plasmon oscillations. The trade-off between these two competing size-dependent factors is responsible for the observed experimental enhancement of light absorption and emission in diode systems mediated by surface plasmons in nanoparticle surface coverings [7, 14–18].

## 4. Efficiency of the light absorption channel via plasmon for various materials

Nanoparticles of gold and silver (sometimes also of copper) are mostly used in plasmon photovoltaics because their surface plasmon resonances are located within the visible light spectrum. These nanoparticles can be deposited on various semiconductor substrates with different material parameters. We list here the appropriate parameters usable for comparison with experiment for various configurations of the plasmon solar cell systems. In order to compare with the experiment, we can estimate the photocurrent in the case of a semiconductor photodiode with the metallically modified photoactive surface. This photocurrent is given by $I' = |e|N(q_0 + q_m)A$, where $N$ is the number of incident photons and $q_0$ and $q_m$ are the probabilities of single photon absorption in the ordinary photo effect [8] and of single photon absorption mediated by the presence of metallic nanospheres, respectively, as derived in the previous paragraph; $A = \frac{\tau_f^n}{t_n} + \frac{\tau_f^p}{t_p}$ is the amplification factor ($\tau_f^{n(p)}$ is the annihilation time of both sign carriers, $t_{n(p)}$ is the drive time for carriers [the time of traversing the distance between electrodes]). From the above formulae, it follows that (here $I = I'(q_m = 0)$, i.e., the photocurrent without metallic modifications),

$$\frac{I'}{I} = 1 + \frac{q_m}{q_0}, \tag{19}$$

where the ratio $q_m/q_0$ is given by Eq. (18).

In **Tables 1–3**, we list parameters for several semiconductor substrates and for a metallic nanoparticle few materials, which allow for comparison of the ratio $q_m/q_0$ for various material configurations by formula (18).

Formula (18) is exemplified in **Figure 1** for Au nanoparticles deposited on Si semiconductor (continuous line)–this reproduces well the experimental behavior (red dashed/dotted) [14]. Both channels of photon absorption resulting in photocurrent in the semiconductor sample are included, the direct ordinary photo effect absorption with probability of transitions given by $q_0$ and the plasmon-mediated absorption with probability $q_m$, respectively. Note also that

| metal | Bulk pl. (eV) | Surface pl. (eV) |
|---|---|---|
| Li | 6.6 | 3.4 |
| Na | 5.4 | 3.3 |
| K | 3.8 | 2.4 |
| Mg | 10.7 | 6.7 |
| Al | 15.1 | 8.8 |
| Fe | 10.3 | 5.0 |
| Cu | 6 | 3.5 |
| Ag | 3.8 | 3.5 |
| Au | 4.67 | 2.7 |

**Table 1.** Plasmon energies measured in metals.

| metal | Au | Ag | Cu |
|---|---|---|---|
| Mie frequency | $4.11 \times 10^{15}$ 1/s | $5.2 \times 10^{15}$ 1/s | $5.7 \times 10^{15}$ 1/s |

**Table 2.** Mie frequency $\omega_1$ to formula (18).

| Semiconductor | $m_n^*$ | $m_p^*$ | $E_g$ |
|---|---|---|---|
| Si | 0.9 $m$ L[101], 0.19 $m$ T[110] | 0.16 $m$ lh, 0.49 $m$ hh | 1.12 eV |
| GaAs | 0.067 $m$ | 0.08 $m$ lh, 0.45 $m$ hh | 1.35 eV |
| CIGS | 0.09 − 0.13 $m$ | 0.72 $m$ | 1 − 1.7 eV |

**Table 3.** Substrate material parameters to formula (18) ($m = 9.1 \times 10^{-31}$ kg, the mass of bare electron; lh–light holes, hh–heavy holes, L–longitudinal, T–transverse).

some additional effects like reflection of the incident photons or destructive interference on metallic net would contribute and it was phenomenologically accounted in the plasmon-mediated channel by an experiment-fitted factor $\beta$. The collective interference type corrections are rather not strong for the considered low densities of metallic coverings of order of $10^8/\text{cm}^2$, and nanosphere sizes well lower than the resonant wavelength, though for larger concentrations and larger nanosphere sizes, would play a stronger reducing role (reflecting photons) [6, 19]. The resonance threshold was accounted for the damped resonance envelope function in Eq. (19) including also semiconductor band-gap limit. The relatively high value of $\frac{q_m}{q_0} \sim 10^4 \frac{\beta 40}{H[nm]}$ enables a significant growth of the efficiency of the photoenergy transfer to the semiconductor, mediated by surface plasmons in nanoparticles deposited on the active layer, by increasing $\beta$ or reducing $H$ (at constant $n_s$). However, because of the fact that an enhancement of $\beta$ easily induces the overdamped regime of plasmon oscillations, the more prospective would be lowering of $H$ especially convenient in thin film solar cells. The overall behavior of $I'/I(\omega) = 1 + q_m/q_0$ calculated according to the relation (19), and depicted in **Figure 1**, agrees quite well with the experimental observations [14], in the position, height and shape of the photocurrent curves for distinct samples (the strongest enhancement is achieved for $a = 40$ nm, for Au and Si substrate).

In **Figure 2**, we present the spectral dependence of the plasmonic efficiency enhancement with respect to substrate change (Si, CIGS and GaAs) for the same Au nanoparticles with radius $a = 50$ nm and the same nanoparticle concentration $n_s = 10^8/\text{cm}^2$. One can note that for the CIGS substrate (copper-indium-gallium-diselenide) the spectral characteristics is narrower and

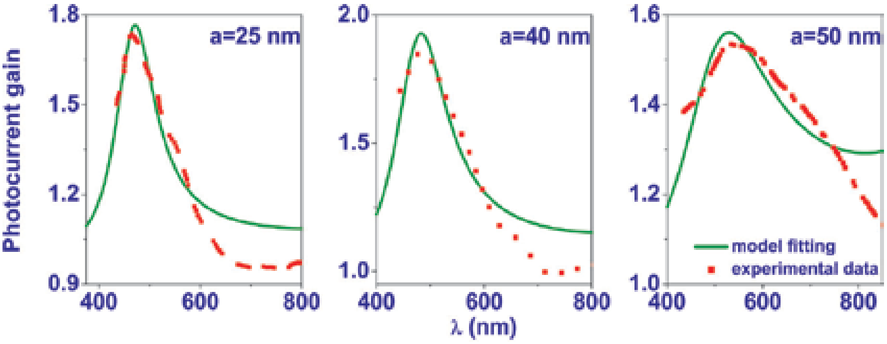

**Figure 1.** Spectral dependence of the normalized photocurrent $\frac{I'}{I}(\lambda)$ according to formulae (19) and (18)—Comparison with the experimental data (red) from Ref. [14]: $a = 25$ nm, $n_s = 6.6 \times 10^8$ 1/cm$^2$, (center): $a = 40$ nm, $n_s = 1.6 \times 10^8$ 1/cm$^2$, (right): $a = 50$nm, $n_s = 0.8 \times 10^8$ 1/cm$^2$ ($H = 3\,\mu$m).

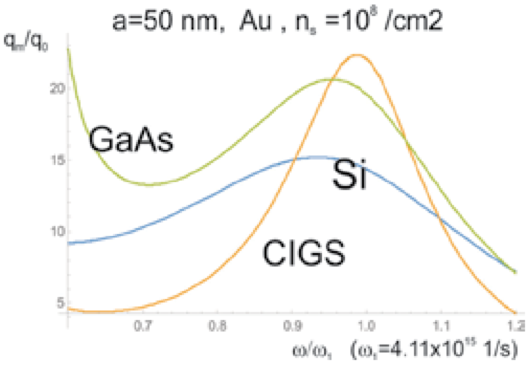

**Figure 2.** Comparison of the effectiveness of the plasmon channel for Si, GaAs and CIGS substrates with the same Au nanoparticles with radius 50 nm and surface density $10^8/\mathrm{cm}^2$.

blue shifted in comparison to Si and GaAs. **Figure 2** reveals an increase in efficiency of the plasmon effect with growth of the value of forbidden gap $E_g$ conserving other parameters not changed. Especially significantly influential material parameter occurs, however, a mass of holes, cf. **Figure 3**, which is also noticeable from Eq. (18). The mass of holes, $\left(m_p^*\right)^2$, enters the denominator in the formula (12) for the ordinary photo effect and next the numerator in Eq. (18). The higher mass $m_p^*$ the lower efficiency $q_0$ of the ordinary photo effect is and higher the ratio $\frac{q_m}{q_0}$. In **Figure 4**, the material comparison of metal material of nanoparticles (Au, Ag and Cu) is presented for two their sizes ($a = 50, 25$ nm). The blue shift of spectral characteristics for Ag and Cu in comparison to Au is noticeable (cf. also **Figure 5**) and even more visible for lower radii of nanoparticles due to narrowing of spectral curves (cf. **Figure 6**). From the comparison in **Figures 5** and **6**, for Si and CIGS substrates with Au, Ag and Cu nanoparticles of size $a = 50, 25\,\mathrm{nm}$ (at the nanoparticle concentration $n_s = 10^8/\mathrm{cm}^2$), one can notice that Au nanoparticles utilize the visible spectrum in the better manner than Ag or Cu ones. The advantage of Au nanoparticles is greater in the case of Si substrate and is reduced for CIGS

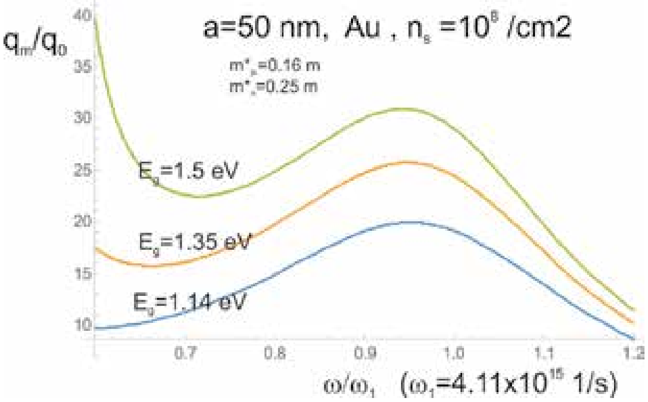

**Figure 3.** Comparison of the effectiveness of the plasmon channel for varying $E_g$ but the same effective masses of substrates covered with the same Au nanoparticles with radius 50 nm and surface density $10^8/\mathrm{cm}^2$.

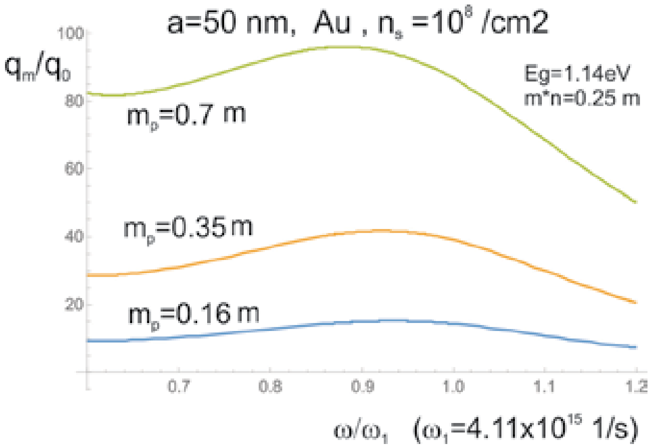

**Figure 4.** Comparison of the effectiveness of the plasmon channel for varying hole mass $m_p^*$ but the same electron mass and $E_g$ of substrates covered with the same Au nanoparticles with radius 50 nm and surface density $10^8/\mathrm{cm}^2$.

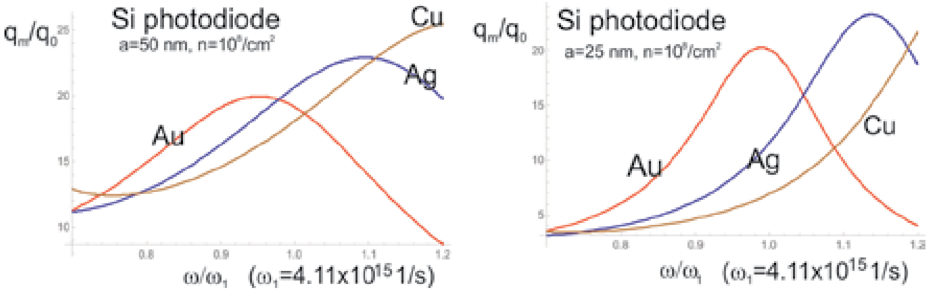

**Figure 5.** Comparison of the effectiveness of the plasmon channel for the same substrate Si with Au (red), Ag (blue) and Cu (brown) nanoparticles of the same radius 50 nm and surface density $10^8/\mathrm{cm}^2$.

substrate because the blue shift of $E_g$ in CIGS with respect to Si. In the case of CIGS (especially for large nanoparticles, $a = 50$ nm), the advantage of Au beyond Ag in overall utilization of sunlight spectrum disappears, whereas is pronounced in the case of Si substrate. Later, we describe an experimental confirmation of this behavior of Si and CIGS substrates, at laboratory sunlight-type illumination by Yamashita DensoYSS-50Aunder AM1.5 [19].

For nanoparticles of gold (Au) and silver (Ag) of size, $a = 50$ nm, optimized due to formula (18), deposited on the multi-crystalline silicon (mc-Si) and on the copper-indium-gallium-diselenide (CIGS) solar cells, the measured [19] overall increase of cell efficiency attains the level of even 5%. The application of suitable concentration of Au and Ag nanoparticles onto mc-Si solar cells increases their efficiency by 5.6 and 4.8%, respectively [19]. Application of Au and Ag nanoparticles onto surface of CIGS solar cells improves their efficiency by 1.2 and 1.4%, respectively [19]. This is visualized in **Figures 7** and **8**, where it is compared an increase in solar cell overall efficiency (the ratio of the field beneath the I-V curve for the metallically improved solar cell and the clean solar cell; the same size (50 nm for radius) and the same

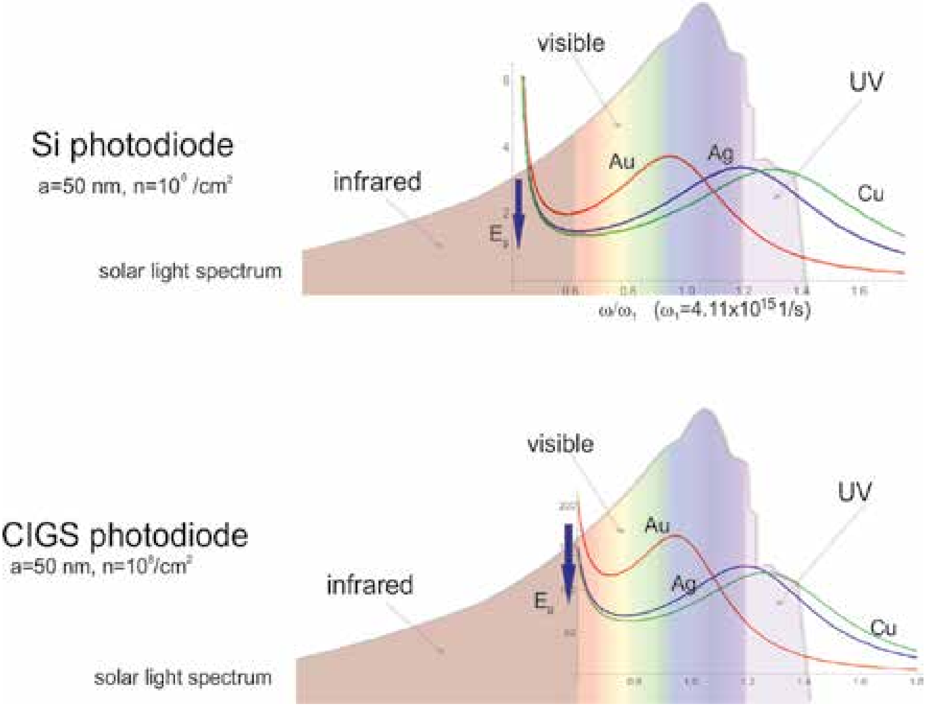

**Figure 6.** Comparison of the effectiveness of the plasmon channel for the same substrate Si (upper) and CIGS (lower) with Au (red), Ag (blue) and Cu (green) nanoparticles of the same radius 50 nm and surface density $10^8/\text{cm}^2$, versus the sunlight spectrum on the earth surface.

concentration (from the 5% colloidal solution sputtering over the surface) has been applied to different samples)—for more detail cf. Ref. [19].

Worth noting is an agreement of experimentally observed difference in the increase of the efficiency due to the plasmon effect in both cases, of mc-Si and CIGS cells, if one compares the results of application of Au and Ag particles (at the same size of metallic nanoparticles and the same their surface concentration). This behavior agrees with the theoretical study of the material dependence of the plasmon effect, as shown above. From **Figures 2–5**, we see that for Si substrate Au nanoparticles with radii 50 nm better utilize the solar light spectrum than Ag or Cu particles (cf. **Figure 5**), and indeed in the experiment (cf. **Figure 8**) for Au nanoparticles the efficiency growth is ca. 10% larger than for Ag nanoparticles of the same size and concentration on the substrate m-Si solar cell. Interestingly, for the substrate CIGS cell, the effect is weaker and inverted, cf. **Figure 9**. This also is noticeable from the theoretical modeling—due to different $E_g$ and effective masses of carriers for CIGS with respect to mc-Si. The maxima for efficiency enhancement for Au and Ag mutually shift in such a way that for CIGS Ag nanoparticles a bit better suit to solar light spectrum than Au nanoparticles. However, to analyze these effects in more detail, a measurement of spectral characteristics of all considered structures at varying but monochromatic illumination uniformly calibrated should be performed.

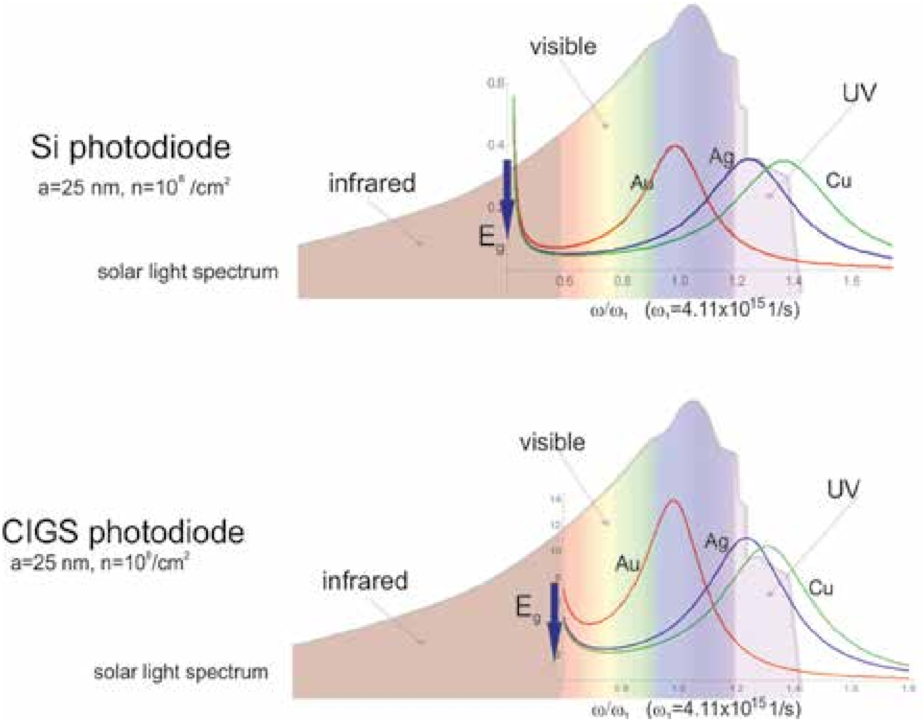

**Figure 7.** Comparison of the effectiveness of the plasmon channel for the same substrate Si (upper) and CIGS (lower) with Au (red), Ag (blue) and Cu (green) nanoparticles of the same radius 25 nm and surface density $10^8/\mathrm{cm}^2$, versus the sunlight spectrum on the earth surface.

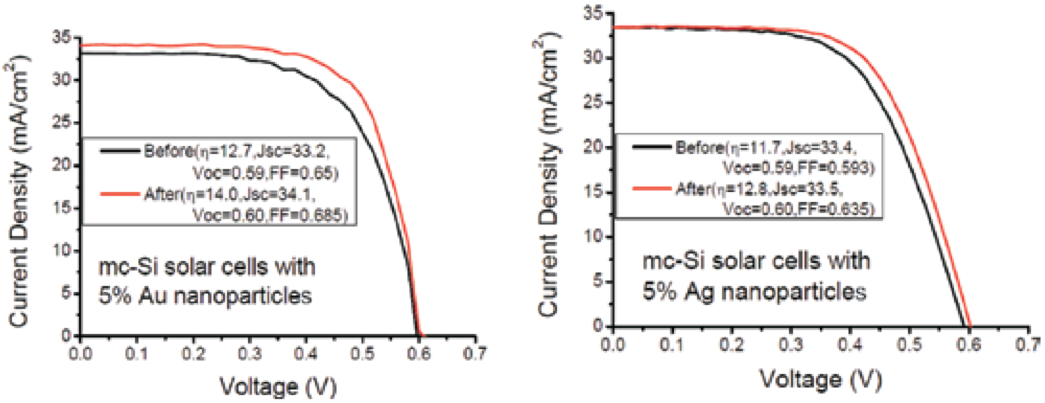

**Figure 8.** Comparison of solar cell efficiency due to plasmon modification for the multi-crystal Si solar cell, (left) modified by Au nanoparticles, (right) by Ag nanoparticles [19].

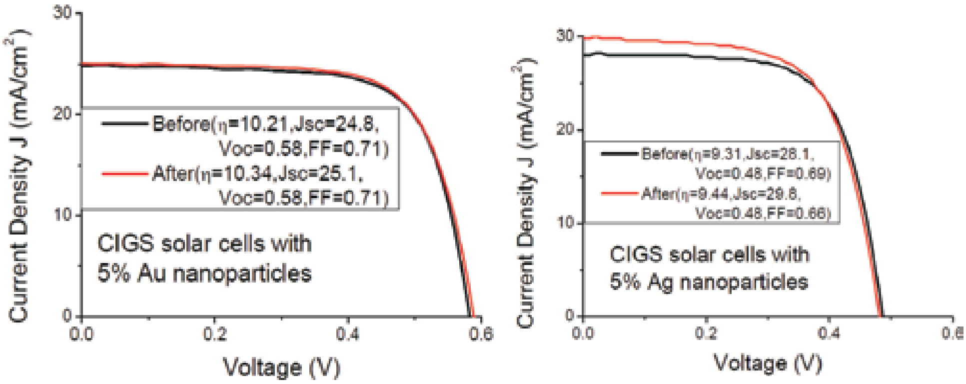

**Figure 9.** Comparison of solar cell efficiency due to plasmon modification for the CIGS cell, (left) modified by Au nanoparticles, (right) by Ag nanoparticles [19].

## 5. Conclusion

We have demonstrated by application of the Fermi Golden Rule scheme, that the efficiency of the energy transfer channel between the surface plasmon oscillations in a metallic nanoparticles and a substrate semiconductor depends on parameters of both deposited metallic particles (its radius and material) as well as on semiconductor parameters (energy gap, and effective masses of electron and holes). Found by us formula which generalizes the ordinary photo effect onto the plasmon-mediated one, agrees well with the experimental measurements in laboratory photodiode configuration. The measured ratio of photocurrent in the setup with and without metallic nano-components is compared with the theoretically predicted scenario. The quantitative consistence is obtained both in the shape of the spectral characteristics and in the particle size dependence (as illustrated for Si diode with deposited Au nanoparticles with radii 25, 40 and 50 nm). The qualitative agreement has been achieved also for complete solar cells where the plasmon effect is obscured by other elements of the long series of effects resulting in overall solar cell efficiency beyond only efficiency of the absorption of photons. We have compared the experimental data for multi-crystalline Si solar cell and CIGS (copper-indium-gallium-diselenide) solar cell covered or not with gold and silver nanoparticles with radii of order of 50 nm. The increase of the overall photovoltaic efficiency for metallically modified cells varies between 1.5 (CIGS) and 6% (Si), depending on nanoparticle concentration (for too dense concentration the efficiency drops down). A bit better increase (ca. 10% difference) causes Au nanoparticles for Si cell in comparison to Ag nanoparticles, whereas for CIGS cell, the difference between effect of Ag nanoparticles and Au ones is inverted and strongly reduced. This also agrees qualitatively with theory predictions taken into account differences in Mie frequency in Au and Ag and also different semiconductor parameters for Si and CIGS.

## Author details

Janusz E. Jacak and Witold A. Jacak*

*Address all correspondence to: witold.aleksander.jacak@pwr.wroc.pl

Department of Quantum Technology, Wrocław University of Science and Technology, Poland

## References

[1] Atwater HA, Polman A. Plasmonics for improved photovoltaic devices. Nature Materials. 2010;**9**:205

[2] Catchpole KR, Mokkapati S, Beck F, Wang E, McKinley A, Basch A, Lee J. Plasmonics and nanophotonics for photovoltaics. MRS Bulletin. 2011;**36**:461-467

[3] Green MA, Pillai S. Harnessing plasmonics for solar cells. Nature Photonics. 2012;**6**:130-132

[4] Jacak J, Krasnyj J, Jacak W, Gonczarek R, Chepok A, Jacak L. Surface and volume plasmons in metallic nanospheres in semiclassical RPA-type approach; near-field coupling of surface plasmons with semiconductor substrate. Physical Review B. 2010;**82**: 035418

[5] Lee J, Peumans P. The origin of enhanced optical absorption in solar cells with metal nanoparticles embedded in the active layer. Optics Express. 2010;**18**:10078

[6] Losurdo M, Giangregorio MM, Bianco GV, Sacchetti A, Capezzuto P, Bruno G. Enhanced absorption in Au nanoparticles/a-Si:H/c-Si heterojunction solar cells exploiting au surface plasmon resonance. Solar Energy Materials & Solar Cells. 2009;**93**:1749

[7] Pillai S, Catchpole KR, Trupke T, Zhang G, Zhao J, Green MA. Enhanced emission from Si-based light-emitting diodes using surface plasmons. Applied Physics Letters. 2006;**88** (161102)

[8] Kiriejew PS. Physics of Semiconductors. Warsaw: PWN; 1969

[9] Landau LD, Lifshitz EM. Field Theory. Moscow: Nauka; 1973

[10] Landau LD, Lifshitz LM. Quantum Mechanics. Nonrelativistic Theory. Pergamon Press; 1965

[11] Bohren CF, Huffman DR. Absorption and Scattering of Light by Small Particles. New York: Wiley; 1983

[12] Mie G. Beitrige zur Optik trüber Medien, speziell kolloidaler Metallösungen. Annals of Physics. 1908;**25**:376

[13] Pines D. Elementary Excitations in Solids. Massachusetts: ABP Perseus Books; 1999

[14] Schaadt DM, Feng B, Yu ET. Enhanced semiconductor optical absorption via surface plasmon excitation in metal nanoparticles. Applied Physics Letters. 2005;**86**:063106

[15] Okamoto K, Niki I, Shvartser A, Narukawa Y, Mukai T, Scherer A. Surface plasmon enhanced spontaneous emission rate of InGaN/GaN QW probed by time-resolved photolumimnescence spectroscopy. Nature Materials. 2004;**3**:601

[16] Stuart HR, Hall DG. Enhanced dipole-dipole interaction between elementary radiators near a surface. Physical Review Letters. 1998:80

[17] Wen C, Ishikawa K, Kishima M, Yamada K. Effects of silver particles on the photovoltaic properties of dye-sensitized $TiO_2$ thin films, *Sol*. Cell. 2000;**61**:339

[18] Westphalen M, Kreibig U, Rostalski J, Lüth H, Meissner D. Metal cluster enhanced organic solar cells. Solar Energy Materials & Solar Cells. 2000;**61**:97

[19] Jeng M, Chen Z, Xiao Y, Chang L, Ao J, Sun Y, Popko E, Jacak W, Chow L. Improving efficiency of multicrystalline silicon and CIGS solar cells by incorporating metal nanoparticles. Materials. 2015;**8**:6761

Chapter 8

# Plasmonic Intracellular Delivery

Marinna Madrid

Additional information is available at the end of the chapter

http://dx.doi.org/10.5772/intechopen.79384

## Abstract

This chapter describes the significance of plasmonics to the field of intracellular delivery. We begin by discussing the significance of intracellular delivery, its applications in biology and medicine, and the currently available intracellular delivery techniques. Next, we discuss the field of plasmonic intracellular delivery, beginning with the discovery of optoporation. In optoporation, a laser beam is tightly focused onto a cell membrane to generate a transient pore, through which membrane-impermeable cargo can enter the cell. To improve the throughput of this technique, plasmonic materials were used for their ability to efficiently absorb laser light and generate spatially confined electric fields. Here, we describe the process by which plasmonic materials absorb laser light energy and generate plasmons. These plasmons transfer their energy to their surroundings, resulting in a rise in temperature and the subsequent creation of a bubble or shockwave. Finally, we describe how the properties of plasmons and plasmon-mediated effects facilitate cell poration for intracellular delivery.

**Keywords:** plasmonic, thermoplasmonic, intracellular delivery, cell poration, cell membrane perforation, cell transfection

## 1. Introduction

Plasmonic materials have found utility in biological applications ranging from photothermal therapy (killing cancer cells) to bio-sensing to intracellular delivery [1–3]. The ability to deliver membrane-impermeable cargoes into cells is a critical step in the development of many therapeutics and an important problem in the field of biology [4–7]. Light-activated thermoplasmonic nanostructures are a potential solution to this problem and can be used to deliver a range of cargoes into a range of cell types at high efficiency and high throughput, with spatial selectivity, while maintaining cell viability [8–10].

IntechOpen

© 2018 The Author(s). Licensee IntechOpen. This chapter is distributed under the terms of the Creative Commons Attribution License (http://creativecommons.org/licenses/by/3.0), which permits unrestricted use, distribution, and reproduction in any medium, provided the original work is properly cited.

## 2. Currently available intracellular delivery techniques

The delivery of membrane-impermeable cargoes such as nanoparticles, genetic materials, or functional proteins directly into cells is a critical step for applications in biology and medicine [4]. For instance, the delivery of gene-editing tools could be used to manipulate cells and tissues for regenerative medicine or engineer cells for personalized cell therapies [4–7]. Intracellular delivery methods include biological vectors such as viruses, chemical modifications of delivery cargoes such as lipofection, and physical techniques such as microinjection, electroporation, and optoporation [11–24]. While research efforts have led to a continuous increase in efficiency and sophistication, each of the currently available approaches has its own advantages and disadvantages. To this point, no platform technology exists that combines high-efficiency delivery, high-throughput processing, low-toxicity, versatility with respect to type of cell and cargo, and simple, cheap and affordable production. The research presented in this thesis is an attempt toward developing a solution to this problem.

Viral-based delivery is a popular biological technique that offers high-efficiency delivery at high throughput. However, it is limited in terms of cargo-carrying capacity, the ability to only deliver genetic material, the requirement to customize the virus for each cargo and cell type, and the potential for immunologic and oncogenic risks [11–15].

Lipofection, a chemical method, offers high throughput but varies in efficiency depending on cell type, can require complex chemical customization depending on the cargo, and risks endosomal trapping of the cargo [7, 25, 26].

Electroporation, the most widely used physical delivery method, offers high-efficiency delivery and high throughput for a range of cargo types, but can lead to high cell death, particularly for sensitive cell types [27, 28]. Nucleofection, a variation of electroporation, offers improved viability but can require expensive customized reagents and can still be low viability for the most sensitive cell types. Ultrasound-mediated methods offer a low-cost high-throughput technique for delivering membrane-impermeable cargo into cells [12]. However, the cavitation dynamics are not spatially localized, which can lead to nonuniform results and high cell death. Other physical methods such as microinjection, nanowire-mediated delivery, and microfluidic squeezing are promising, but offer limited throughput and/or reproducibility [14, 29–32].

## 3. Laser-mediated cell poration for intracellular delivery

Optoporation, a physical delivery technique, utilizes a tightly focused laser beam to create a transient pore in the cell membrane [18, 19, 33, 34]. This technique offers high delivery efficiency, high cell viability and is versatile with respect to cargo and cell type. However, each cell has to be porated individually by focusing the laser beam directly onto the membrane, causing optoporation to have an extremely low throughput. Modifications, including the use of active flow in microfluidic channels and a nondiffracting beam, slightly increase the throughput but not to the scale necessary for applications such as cell therapy, which can require on the order of $10^8$ cells [35, 36].

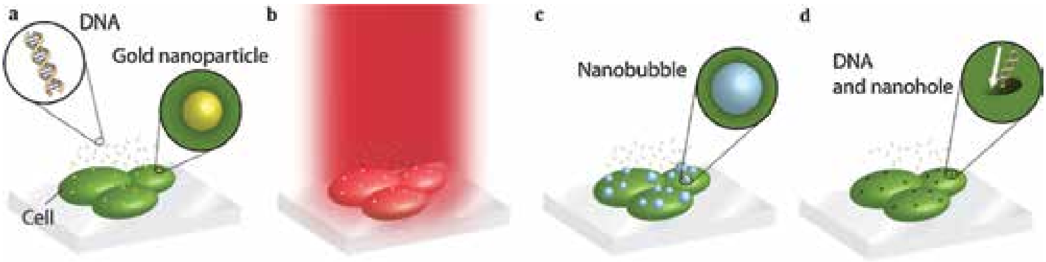

**Figure 1.** Schematic of gold nanoparticle-mediated intracellular delivery. (a) Gold nanoparticles adhere to the cell membrane. (b) The gold nanoparticles are illuminated by a pulsed laser system. (c) Laser illumination of the gold nanoparticles leads to the formation of a bubble around the gold nanoparticle. (d) The bubble creates a temporary pore in the cell membrane, through which membrane-impermeable cargo can enter. Reprinted with permission from [1]. Copyright 2013, Elsevier.

Laser-activated thermoplasmonic nanostructures improve the throughput of optoporation by efficiently absorbing the laser energy at multiple localized hotspots, generating a rise in temperature, and transferring the energy to the surrounding medium [2, 8–10, 31, 37–39]. This transfer of energy to the surrounding solution results in the creation of a bubble or pressure wave that can generate sufficient mechanical stress to create a transient pore in the cell membrane, through which membrane-impermeable cargo can diffuse into the cell [1, 3, 8–10, 40]. This process is shown briefly in **Figure 1**, and the physics of this process will be explained in greater detail in the following section of this thesis. Gold nanoparticles are the most commonly used plasmonic nanostructures for intracellular delivery and have been successfully used to porate cell membranes for a range of cell types [37, 38, 41–46]. Gold nanoparticles potentially outperform other physical techniques by offering high efficiency, viability, and throughput [1, 45]. However, the gold nanoparticles remain in the cell after delivery as metallic residue and can form aggregates, and the long-term toxicity of these gold nanoparticles is still not fully understood [47, 48].

Laser-activated nanostructured substrates bypass this potential toxicity problem, as cells can be cultured on the substrates, porated, and removed from the substrates (which remain intact) after intracellular delivery without leaving metallic particles within the cells [31, 39, 49–52]. In this thesis we explore the fabrication of various thermoplasmonic nanostructured substrates for intracellular delivery and use the fabricated substrates to deliver a wide range of membrane-impermeable cargoes (dyes, dextrans, proteins, etc.) to a wide range of cell types (HeLa CCL2 cells, induced pluripotent stem cells (iPSCs), etc.).

## 4. Physics of plasmonic intracellular delivery

### 4.1. Properties of localized surface plasmons

Plasmonic structures have proven valuable in intracellular delivery as well as numerous other applications requiring the ability to generate electric fields in a highly localized manner [1]. These structures are capable of supporting plasmons, or quanta of plasma oscillations.

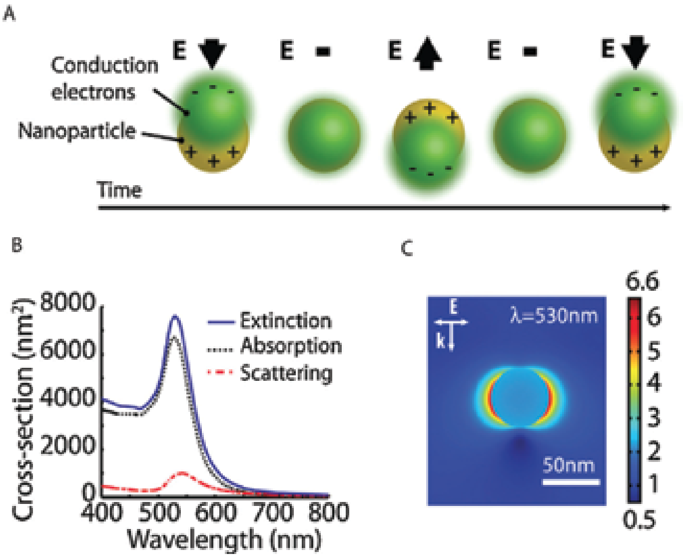

**Figure 2.** (a) Principle of localized surface plasmons. At any point in time, the gold nanoparticle experiences a uniform electric field. The electrons accelerate in the direction of the electric field and are displaced from the positive lattice ions. The electrons are then attracted back to the positive lattice ions by Coulomb forces. This electromagnetic oscillator is called a plasmon. (b) The gold nanoparticles are illuminated by a pulsed laser system. (c) For a gold nanoparticle with a 50-nm diameter, resonance occurs at a wavelength of approximately 550 nm [1]. Copyright 2013, Elsevier.

Plasmons can be described classically as the collective oscillations of free electrons with respect to the positively-charged ion lattice in a metallic nanoparticle in the presence of an oscillating electromagnetic field [53, 54].

It is simplest to picture a spherical metallic nanoparticle immersed in an aqueous environment in the presence of an electromagnetic wave, such as laser light. If the diameter of the nanoparticle is less than half the wavelength of the light, then at any point in time the entire nanoparticle will experience a uniform electric field pointing in one direction, as shown in **Figure 2a**. The free electrons in the metallic nanoparticle will accelerate in the direction of the uniform electric field. As a result, the electrons are displaced from the positively-charged lattice ions of the metallic nanoparticle. The electrons experience an attractive Coulomb force that drives them back toward the positively-charged lattice ions, and this movement results in a collective oscillation of the free electrons with respect to the fixed positively-charged lattice ions. The oscillator is termed a localized surface plasmon, and the electromagnetic wave, for instance laser light, is the driving force.

For this phenomenon to occur, the real part of the permittivity, $\varepsilon_r$, of the plasmonic material must be negative (a condition satisfied by metals), and the real part of the permittivity of the surrounding material must be positive (a condition satisfied by dielectrics) [1]. This allows the following boundary condition in electrodynamics to be satisfied:

$$(D_1 - D_2) \cdot \widehat{n} = D_{1,\perp} - D_{2,\perp} = \sigma_f \tag{1}$$

given that

$$D = \varepsilon E \tag{2}$$

where $D$ is the electric displacement field, $E$ is the electric field, $\varepsilon$ is the permittivity of the material, $\sigma_f$ is the free charge density and $\hat{n}$ points in the direction from medium 2 to medium 1 [55].

When the eigen frequency of the collective electron oscillation, or the plasma frequency, matches the frequency of the electromagnetic wave, the system is said to be in resonance. Resonance results in enhanced absorption of the laser light energy by the metallic nanoparticle, and a greater near field enhancement, as shown in **Figure 2b** and **c** [1]. The resonance wavelength is affected by the shape, size and material of the nanoparticle as well as the dielectric constant and refractive index of the environment [1, 56]. Although resonance results in more efficient absorption and a higher near-field enhancement, resonance is not a necessary condition for the thermoplasmonic cell poration described in this thesis [57].

### 4.2. Interactions of laser pulses and plasmonic structures in an aqueous environment

#### *4.2.1. Energy transfer from light source to plasmonic nanostructure to aqueous environment*

When a plasmonic nanostructure in an aqueous environment is illuminated with laser light, the resulting absorption of laser energy and near-field enhancement initiates a series of energy transfers. Depending on the conditions of the laser pulse, these energy transfers can result in the creation of a shockwave or vapor bubble [1, 57–59]. In our theoretical discussions, we will use water as the aqueous environment, as cell media is water-based and biological tissue has a refractive index (1.36–1.39) comparable to that of water (1.33) [60].

First, the photons in the laser light are absorbed by the electrons in the plasmonic nanostructure, causing them to collectively oscillate, generating plasmons. The plasmons generate an enhanced near field. For ultrashort pulses in the fs regime, the peak intensities of the laser pulses and therefore of the enhanced near-field can be high enough to photo-ionize the water and generate a plasma [1]. Because the research presented in this thesis makes use of a ns-pulsed laser system rather than a fs-pulsed laser system, we will not focus on the effects of the enhanced near-field. We will instead focus on other effects of laser energy absorption by the plasmonic structure. As the plasmon oscillations decay, the energy is transferred into a distribution of nonthermal electrons (**Figure 3**) [1]. Over approximately 500 fs, the nonthermal electrons decay into a population of thermalized electrons via electron–electron scattering. It takes 1–3 ps for the thermalized electrons to couple with the phonon lattice of the plasmonic nanostructure and reach thermal equilibrium. According to Boulais et al., over a timescale of approximately 100 s of ps, thermal energy is transferred from the phonon lattice to the surrounding medium. However, it is worth noting that the characteristic timescale over which energy is transferred from a gold plasmonic nanostructure to water can vary depending on the laser system used and the laser power.

The research presented in this thesis makes use of a ns-pulsed laser system with 11-ns pulses. These pulse widths are relatively long compared to the electron-phonon coupling

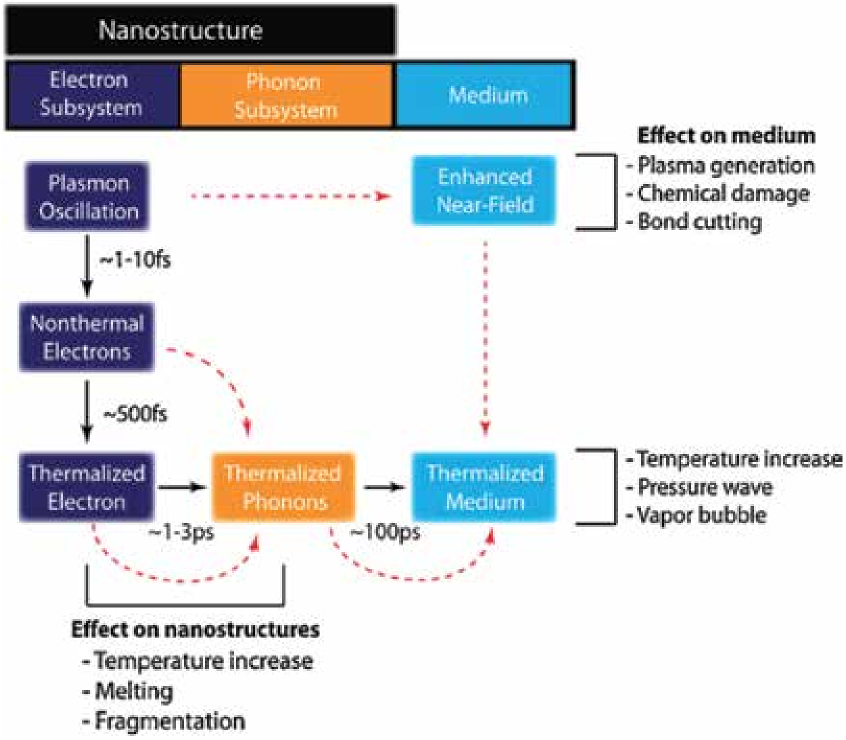

**Figure 3.** Energy transfers following laser illumination of a plasmonic nanostructure. The photons in the laser light couple with the electrons in the plasmonic nanostructure, generating plasmon oscillations. The plasmons decay into a nonthermal electron distribution, which thermalizes within 100s of fs. The thermalized electrons transfer energy to the phonon lattice of several ps. The phonons transfer thermal energy to the surrounding medium within a timescale on the order of 100 ps. This can result in effects such as temperature increase, the formation of a pressure wave, and/or the formation of a vapor bubble. Reprinted with permission from [1]. Copyright 2013, Elsevier.

time and the time over which the thermalized phonon lattice couples to the surrounding medium. These subsystems therefore reach thermal equilibrium during the lifetime of the laser pulse, and the laser pulse can be considered as heating the electrons, phonon lattice, and surrounding medium at the same time.

### *4.2.2. Heat-mediated bubble and/or shockwave formation*

Absorption of laser energy by a plasmonic nanostructure can result in a temperature increase that generates a shockwave or a bubble, among other possible effects [1, 3, 8–10, 40]. The exact event that results from the laser energy absorption is dependent on the conditions of the laser pulse—most importantly, the fluence and the width of the laser pulse. **Figure 4** shows the various effects on a plasmonic gold nanoparticle immersed in water after absorption of an incoming laser pulse, ranging from a relatively low fluence on the left to increasingly higher fluences on the right [3].

The laser fluences used in the research presented in this thesis are sufficient to cause protein denaturation and to generate acoustic waves and water vapor bubbles, and we will therefore

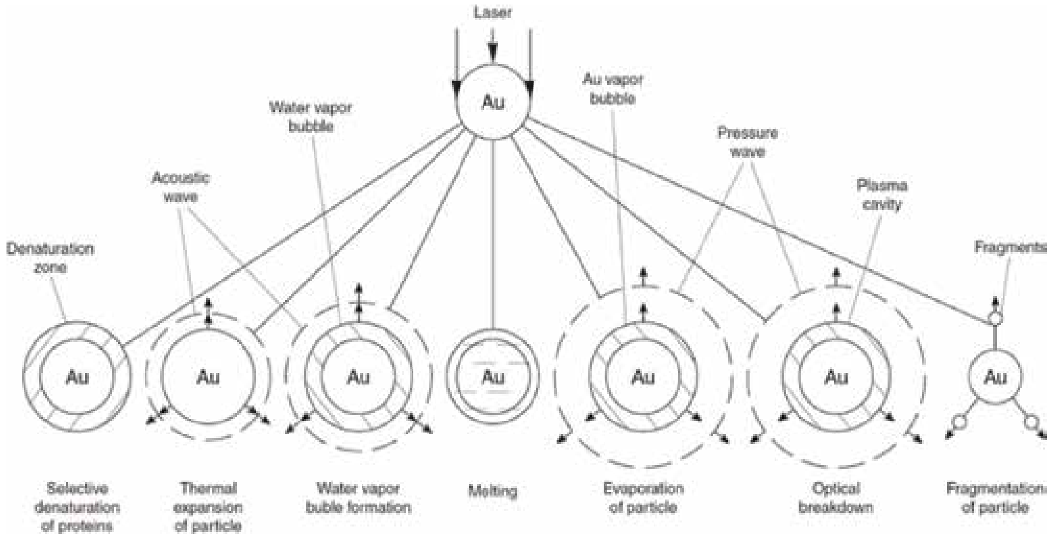

**Figure 4.** Various effects of laser illumination of plasmonic gold nanoparticle in liquid environment. Laser fluence increases from left to right. Reprinted with permission from [3]. Copyright 2008, Astro Ltd.

focus the discussion in this section on these events. Because the research presented in this thesis is based on the use of an 11-ns pulsed laser system, we will restrict the discussion to mechanism processes that can be initiated by laser pulses of this width.

Proteins can denature at temperatures above 50–160°C [3]. The distance from the plasmonic material at which proteins are denatured is also dependent on the width of the laser pulse. For instance, proteins 18 nm away from a gold nanoparticle illuminated with a microsecond laser pulse of sufficient energy are denatured, whereas only proteins up to 4 nm away from a gold nanoparticle illuminated with a femtosecond pulse are denatured [3]. In the case of nanosecond pulses, as are used in the research presented here, proteins 6 nm away from a gold nanoparticle are denatured [3]. This is because heat is able to diffuse further for longer pulse widths; in other words, shorter pulse widths result in greater thermal confinement.

When the plasmonic material absorbs light from a pulsed laser source, the material undergoes thermal expansion. If the rate of thermal expansion is greater than or approximately equal to the speed of sound in the surrounding media, compression waves can form, known as the photoacoustic effect [3]. These acoustic waves can form at lower temperatures, and thus at lower fluences, than those required for bubble formation [3].

If the laser fluence is high enough for the surrounding media to reach 90% of the critical temperature, ($T_c = 373.9^{\circ}C$) bubbles can be generated via phase explosion, which is a combination of spinodal decomposition and homogenous nucleation [1, 61–63]. Thermal energy is deposited rapidly into the system, and the water temperature rises rapidly as a consequence. The heating occurs too rapidly for the water to build up pressure at a sufficient rate, and the pressure drops below the saturation pressure. The system crosses the binodal line into the metastable region, and crosses the kinetic spinodal line into the unstable region. In the

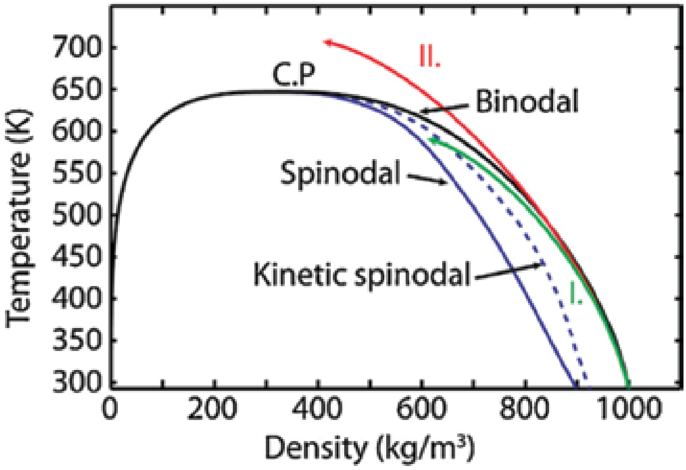

**Figure 5.** Density-temperature phase diagram for water. The green line labeled "I" shows the trajectory for phase explosion. The system crosses the binodal line into the metastable region before crossing the kinetic spinodal line into the unstable region, where there is no energy barrier between the two phases. The red line labeled "II" shows the trajectory for trivial fragmentation. CP is the critical point. Reprinted with permission from [1]. Copyright 2013, Elsevier.

unstable region, there is no energy barrier between the liquid and vapor phases. The water relaxes into an equilibrium state of both liquid and vapor. This process is accompanied by an increase in pressure, termed phase explosion. The green line in **Figure 5** represents the pathway of this process [1].

For nanosecond pulses and longer, the damage caused to the cells is most likely due to bubble formation and collapse, and not due to the formation of acoustic shockwaves. This is because the timescale for the shockwaves generated by a nanosecond pulse (on the order of $10^{9}$ s) is longer than the characteristic relaxation time for thermomechanical stress in biological tissues ($10^{11}$–$10^{12}$ s) [3].

### *4.2.3. Bubble dynamics*

For a nanosecond laser pulse, bubbles can grow and collapse on the timescale of 100 ns to 5 μs [3]. The bubble grows due to its high relative temperature and pressure, but loses energy as it grows due to friction with the surrounding liquid. The pressure of the surrounding liquid and surface tension eventually cause the bubble to collapse, which occurs over approximately the same timescale as the bubble's growth [1]. When the bubble collapses, it can generate a shockwave [3]. It is also possible for the bubble to contract and expand repeatedly, resulting in bubble oscillations [3].

The formation of a bubble or pressure wave can be measured using pump-probe spectroscopy [1]. Pump-probe spectroscopy measures scattered light, or a drop in transmitted light. The lifetime of the drop in transmitted light is equivalent to the lifetime of a bubble, which can be used to calculate the diameter of the bubble [1]. Operating under the assumptions that the surrounding liquid is incompressible and there is no heat or mass transfer from the bubble

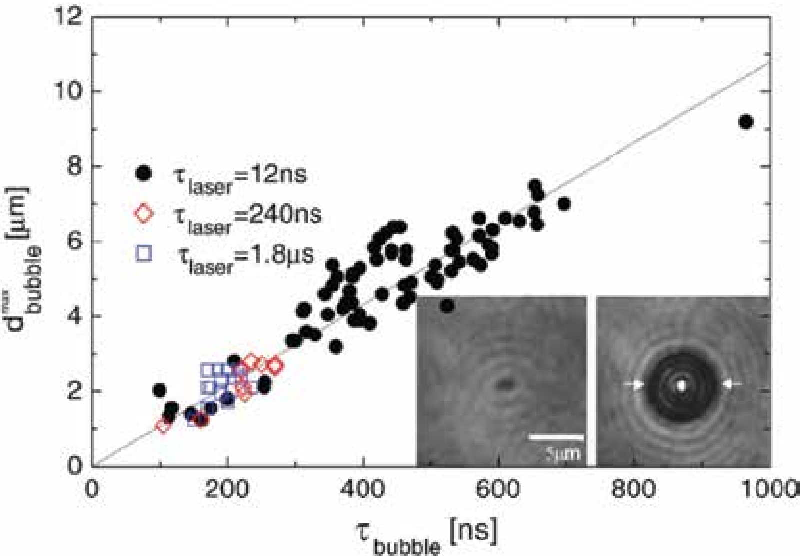

**Figure 6.** Plot showing fit of Rayleigh-Plesset equation to experimental data measuring the maximum diameters and lifetimes of bubbles generated by light-irradiated melanosomes. Photographic image on left shows melanosome before irradiation; image on right shows melanosome and bubble after irradiation. Ambient pressure of 101 kPa, saturated vapor pressure of 2.33 kPa, and water density of 998 kg/m$^3$. Reprinted with permission from [1]. Copyright 2013, Elsevier.

(water vapor has relatively low heat conduction), and given that the temperature $T$ of the surrounding water is 293 K, the mass density $\rho_L = 998\,\text{kg/m}^3$ and the saturation pressure $\rho_{sat} = 2.3$ kPa for water, one can simplify the Rayleigh-Plesset equation to obtain the following relation between the lifetime of a bubble and its diameter [1]:

$$\tau_{bubble} = 0.0915\left(\frac{s}{m}\right)d^{max}_{bubble} \tag{3}$$

This estimation is well supported by experimental results, as shown in **Figure 6** [1].

The growth and collapse of thermoplasmonic bubbles can generate sufficient thermomechanical stress to porate cells [1, 3, 8, 9, 40]. In addition to this effect, the formation of a vapor bubble affects the interaction between the incoming laser light and the plasmonic nanostructure by modifying the refractive index of the system and by scattering the incoming light and reducing the absorption of light by the plasmonic structure [1, 3]. The presence of the bubble also prevents significant heat conduction to the surrounding liquid, because the vapor of the bubble consists of relatively low thermal conductivity [1].

## 5. Conclusion

The challenge of delivering membrane-impermeable cargoes into living cells is an important problem in the fields of biology and medicine [4–7]. Over the past few decades, solutions such as viral vectors, lipofection, electroporation, nucleofection, microfluidic squeezing, and microinjection have offered potential solutions to this complex and critical problem [11, 14–17, 19, 20, 22–24, 28, 29, 35, 64–66]. However, there is still a need for a high-efficiency, high-throughput, low-toxicity, cost-effective intracellular delivery technique that is applicable to a range of cells types for a range of cargoes. Plasmonic nanostructured surfaces may be a promising alternative to the currently available intracellular delivery techniques and utilize the unique ability of plasmonic structures to absorb laser light energy and transfer the energy to a confined volume within the nearby surrounding medium [31, 39, 49–52]. Upon illumination with a short laser pulse, the laser light energy is strongly absorbed by the plasmonic nanostructures, resulting in a rise in temperature [1, 57–59]. Thermal energy is transferred to the surrounding medium; if the rise in temperature is sufficient, a bubble is formed in the surrounding medium [1, 57–59]. The subsequent growth and collapse of the bubble can generate sufficient thermomechanical stress to create a transient pore in nearby cell membranes [1, 3].

## Author details

Marinna Madrid[1,2,3]*

*Address all correspondence to: marinnamadrid@gmail.com

1 Cellino Biotech, Inc., USA

2 Applied Physics, Harvard University, USA

3 Biophysics, UCLA, USA

## References

[1] Boulais E, Lachaine R, Hatef A, Meunier M. Plasmonics for pulsed-laser cell nanosurgery: Fundamentals and applications. Journal of Photochemistry and Photobiology C-Photochemistry Reviews. 2013;**17**:26-49

[2] Schomaker M, Heinemann D, Kalies S, Willenbrock S, Wagner S, Nolte I, Ripken T, Escobar H, Meyer H, Heisterkamp A. Characterization of nanoparticle mediated laser transfection by femtosecond laser pulses for applications in molecular medicine. Journal of Nanobiotechnology. 2015;**13**(1):10

[3] Pustovalov VK, Smetannikov AS, Zharov VP. Photothermal and accompanied phenomena of selective nanophotothermolysis with gold nanoparticles and laser pulses. Laser Physics Letters. 2008;**5**(11):775-792

[4] Rusk N. Seamless delivery. Nature Methods. 2010;**8**(1):44

[5] Lorden ER, Levinson HM, Leong KW. Integration of drug, protein, and gene delivery systems with regenerative medicine. Drug Delivery and Translational Research. 2015;**5**(2):168-186

[6] Srivastava S, Riddell SR. Engineering CAR-T cells: Design concepts. Trends in Immunology. 2015;**36**(8):494-502

[7] D'Astolfo DS, Pagliero RJ, Pras A, Karthaus WR, Clevers H, Prasad V, Lebbink RJ, Rehmann H, Geijsen N. Efficient intracellular delivery of native proteins. Cell. 2015;**161**(3):674-690

[8] Baffou G, Quidant R. Thermo-plasmonics: Using metallic nanostructures as nano-sources of heat. Laser and Photonics Reviews. 2013;**7**(2):171-187

[9] Baffou G, Berto P, Ureña EB, Quidant R, Monneret S, Polleux J, Rigneault H. Photoinduced heating of nanoparticle arrays. ACS Nano. 2013;**7**(8):6478-6488

[10] Baffou G, Polleux J, Rigneault H, Monneret S. Super-heating and micro-bubble generation around plasmonic nanoparticles under cw illumination. Journal of Physical Chemistry C. 2014;**118**(9):4890-4898

[11] Thomas CE, Ehrhardt A, Kay MA. Progress and problems with the use of viral vectors for gene therapy. Nature Reviews. Genetics. 2003;**4**(5):346-358

[12] Cavalli R, Bisazza A, Lembo D. Micro- and nanobubbles: A versatile non-viral platform for gene delivery. International Journal of Pharmaceutics. 2013;**456**(2):437-445

[13] Bessis N, GarciaCozar FJ, Boissier MC. Immune responses to gene therapy vectors: Influence on vector function and effector mechanisms. Gene Therapy. 2004;**11**:S10-S17

[14] Mark Meacham J, Kiranmai Durvasula FLD, Fedorov AG. Physical methods for intracellular delivery: Practical aspects from laboratory use to industrial-scale processing. Journal of Laboratory Automation. 2014;**19**(1):1-18

[15] Mancheño-Corvo P, Martn-Duque P. Viral gene therapy. Clinical & Translational Oncology. 2006;**8**(12):858-867

[16] Capecchi MR. High efficiency transformation by direct microinjection of DNA into cultured mammalian cells. Cell. 1980;**22**(November):479-488

[17] Davis AA, Farrar MJ, Nishimura N, Jin MM, Schaffer CB. Optoporation and genetic manipulation of cells using femtosecond laser pulses. Biophysical Journal. 2013;**105**(4):862-871

[18] Breunig HG, Uchugonova A, Batista A, König K. Software-aided automatic laser optoporation and transfection of cells. Scientific Reports. 2015;**5**:1-11

[19] Waleed M, Hwang SU, Kim JD, Shabbir I, Shin SM, Lee YG. Single-cell optoporation and transfection using femtosecond laser and optical tweezers. Biomedical Optics Express. 2013;**4**(9):1533-1547

[20] Stracke F, Rieman I, König K. Optical nanoinjection of macromolecules into vital cells. Journal of Photochemistry and Photobiology. B. 2005;**81**(3):136-142

[21] Antkowiak M, Torres-Mapa ML, McGinty J, Chahine M, Bugeon L, Rose A, Finn A, Moleirinho S, Okuse K, Dallman M, French P, Harding SE, Reynolds P, Gunn-Moore F,

Dholakia K. Towards gene therapy based on femtosecond optical transfection. Biophotonics: Photonic Solutions for Better Health Care Iii. 2012;**8427**

[22] Stevenson D, Agate B, Tsampoula X, Fischer P, Brown CTA, Sibbett W, Riches A, Gunn-Moore F, Dholakia K. Femtosecond optical transfection of cells: Viability and efficiency. Optics Express. 2006;**14**(16):7125-7133

[23] Stevenson D, Agate B, Paterson L, Lake T, Comrie M, Brown T, Riches A, Bryant P, Sibbett W, Gunn-Moore F, Dholakia K. Optical transfection of mammalian cells—Art. no. 61910D. Biophotonics and New Therapy Frontiers. 2006;**6191**:D1910-D1910

[24] Stevenson DJ, Gunn-Moore FJ, Campbell P, Dholakia K. Single cell optical transfection. Journal of the Royal Society Interface. 2010;**7**(47):863-871

[25] Ewert KK, Ahmad A, Evans HM, Safinya CR. Cationic lipid-DNA complexes for non-viral gene therapy: Relating supramolecular structures to cellular pathways. Expert Opinion on Biological Therapy. 2005;**5**(1):33-53

[26] Godbey WT, Mikos AG. Recent progress in gene delivery using non-viral transfer complexes. Journal of Controlled Release. 2001;**72**(1–3):115-125

[27] Lee Y, Deng P. Review of micro/nano technologies and theories for electroporation of biological cells. Science China Physics, Mechanics & Astronomy. 2012;**55**(6):996-1003

[28] Yarmush ML, Golberg A, Sersa G, Kotnik T, Miklavcic D. Electroporation-based technologies for medicine: Principles, applications, and challenges. Annual Review of Biomedical Engineering. 2014;**16**:295-320

[29] Lee J, Sharei A, Sim WY, Adamo A, Langer R, Jensen KF, Bawendi MG. Non-endocytic delivery of functional engineered nanoparticles into the cytoplasm of live cells using a novel, high through-put microfluidic device (supplementary information). Nano Letters. 2012;**12**(2):6322-6327

[30] Sharei A, Zoldan J, Adamo A, Sim WY, Cho N, Jackson E, Mao S, Schneider S, Han M-J, Lytton-Jean A, Basto PA, Jhunjhunwala S, Lee J, Heller DA, Kang JW, Hartoularos GC, Kim K-S, Anderson DG, Langer R, Jensen KF. A vector-free microfluidic platform forintracellular delivery. Proceedings of the National Academy of Sciences. 2012;**110**(6):2082-2087

[31] Messina GC, Dipalo M, La Rocca R, Zilio P, Caprettini V, Zaccaria RP, Toma A, Tantussi F, Berdondini L, De Angelis F. Spatially, temporally, and quantitatively controlled delivery of broad range of molecules into selected cells through plasmonic nanotubes. Advanced Materials. 2015;**27**(44):7145-7149

[32] Matsumoto D, Sathuluri RR, Kato Y, Silberberg YR, Kawamura R, Iwata F, Kobayashi T, Nakamura C. Oscillating high-aspect-ratio monolithic silicon nanoneedle array enables efficient delivery of functional bio-macromolecules into living cells. Scientific Reports. 2015;**5**:15325

[33] Soman P, Zhang WD, Umeda A, Zhang ZJ, Chen SC. Femtosecond laser-assisted optoporation for drug and gene delivery into single mammalian cells. Journal of Biomedical Nanotechnology. 2011;**7**(3):334-341

[34] König K, Tirlapur UK. Targeted transfection byfemtosecond laser. Nature. 2002;**418**:290-291

[35] Breunig HG, Uchugonova A, Batista A, Konig K. High-throughput continuous flow femtosecond laser-assisted cell optoporation and transfection. Microscopy Research and Technique. 2014;**77**(12):974-979

[36] Rendall HA, Marchington RF, Praveen BB, Bergmann G, Arita Y, Heisterkamp A, Gunn-Moore FJ, Dholakia K. High-throughput optical injection of mammalian cells using a bessel light beam. Lab on a Chip. 2012;**12**(22):4816-4820

[37] Heinemann D, Schomaker M, Kalies S, Schieck M, Carlson R, Murua Escobar H, Ripken T, Meyer H, Heisterkamp A. Gold nanoparticle mediated laser transfection for efficient siRNA mediated gene knock down. PLoS One. 2013;**8**(3):e58604

[38] Lukianova-Hleb EY, Belyanin A, Kashinath S, Wu X, Lapotko DO. Plasmonic nanobubble-enhanced endosomal escape processes for selective and guided intracellular delivery of chemotherapy to drug-resistant cancer cells. Biomaterials. 2012;**33**(6):1821-1826

[39] Wu YC, Wu TH, Clemens DL, Lee BY, Wen X, Horwitz MA, Teitell MA, Chiou PY. Massively parallel delivery of large cargo into mammalian cells with light pulses. Nature Methods. 2015;**12**(5):439-444

[40] Chen X, Chen Y, Yan M, Qiu M. Nanosecond photothermal effects in plasmonic nanostructures. ACS Nano. 2012;**6**(3):2550-2557

[41] Yao C, Rudnitzki F, Hüttmann G, Zhang Z, Rahmanzadeh R. Important factors for cell-membrane permeabilization by gold nanoparticles activated by nanosecond-laser irradiation. International Journal of Nanomedicine. 2017;**12**:5659-5672

[42] Plech A, Kotaidis V, Lorenc M, Boneberg J. Femtosecond laser near-field ablation from gold nanoparticles. Nature Physics. 2006;**2**(1):44-47

[43] Murphy CJ, Gole AM, Stone JW, Sisco PN, Alkilany AM, Goldsmith EC, Baxter SC. Gold nanoparticles in biology: Beyond toxicity to cellular imaging. Accounts of Chemical Research. 2008;**41**(12):1721-1730

[44] Lukianova-Hleb EY, Hanna EY, Hafner JH, Lapotko DO. Tunable plasmonic nanobubbles for cell theranostics. Nanotechnology. 2010;**21**(8)

[45] Kalies S, Birr T, Heinemann D, Schomaker M, Ripken T, Heisterkamp A, Meyer H. Enhancement of extracellular molecule uptake in plasmonic laser perforation. Journal of Biophotonics. 2014;**7**(7):474-482

[46] Pitsillides CM, Joe EK, Wei XB, Anderson RR, Lin CP. Selective cell targeting with light-absorbing microparticles and nanoparticles. Biophysical Journal. 2003;**84**(6):4023-4032

[47] Alkilany AM, Murphy CJ. Toxicity and cellular uptake of gold nanoparticles: What we have learned so far? Journal of Nanoparticle Research. 2010;**12**(7):2313-2333

[48] Schaeublin NM, Braydich-Stolle LK, Schrand AM, Miller JM, Hutchison J, Schlager JJ, Hussain SM. Surface charge of gold nanoparticles mediates mechanism of toxicity. Nanoscale. 2011;**3**(2):410-420

[49] Courvoisier S, Saklayen N, Huber M, Chen J, Diebold ED, Bonacina L, Wolf JP, Mazur E. Plasmonic tipless pyramid arrays for cell poration. Nano Letters. 2015;**15**(7):4461-4466

[50] Saklayen N, Huber M, Madrid M, Nuzzo V, Vulis DI, Shen W, Nelson J, McClelland AA, Heisterkamp A, Mazur E. Intracellular delivery using nanosecond-laser excitation of large-area plasmonic substrates. ACS Nano. 2017;**11**(4):3671-3680

[51] Saklayen N, Kalies S, Madrid M, Nuzzo V, Huber M, Shen W, Sinanan-Singh J, Heinemann D, Heisterkamp A, Mazur E. Analysis of poration-induced changes in cells from laser-activated plasmonic substrates. Biomedical Optics Express. 2017;**8**(10):4756-4771

[52] Kalim S, Wu T-H, Callahan C, Teitell MA, Chiou P-Y. Image patterned molecular delivery into live cells using gold particle coated substrates. Optics Express. 2010;**18**(2):938-946

[53] Myroshnychenko V, Rodrguez-Fernández J, Pastoriza-Santos I, Funston AM, Novo C, Mulvaney P, Liz-Marzán LM, Javier Garca de Abajo F. Modelling the optical response of gold nanoparticles. Chemical Society Reviews. 2008;**37**(9):1792-1805

[54] Jain PK, Huang X, El-Sayed IH, El-Sayed MA. Review of some interesting surface plasmon resonance-enhanced properties of noble metal nanoparticles and their applications to biosystems. Plasmonics. 2007;**2**(3):107-118

[55] Griffiths DJ. Introduction to Electrodynamics. Upper Saddle River, NJ: Prentice-Hall; 1999

[56] Mock JJ, Barbic M, Smith DR, Schultz DA, Schultz S. Shape effects in plasmon resonance of individual colloidal silver nanoparticles. The Journal of Chemical Physics. 2002;**116**(15): 6755-6759

[57] Baumgart J, Humbert L, Boulais E, Lachaine R, Lebrun JJ, Meunier M. Off-resonance plasmonic enhanced femtosecond laser optoporation and transfection of cancer cells. Biomaterials. 2012;**33**(7):2345-2350

[58] Lachaine R, Boulais É, Meunier M. From thermo- to plasma-mediated ultrafast laser-induced plasmonic nanobubbles. ACS Photonics. 2014;**1**(4):331-336

[59] Boulais E, Lachaine R, Meunier M. Plasma mediated off-resonance plasmonic enhanced ultrafast laser-induced nanocavitation. Nano Letters. 2012;**12**(9):4763-4769

[60] Liu PY, Chin LK, Ser W, Chen HF, Hsieh C-M, Lee C-H, Sung K-B, Ayi TC, Yap PH, Liedberg B, Wang K, Bourouina T, Leprince-Wang Y. Cell refractive index for cell biology and disease diagnosis: Past, present and future. Lab on a Chip. 2016;**16**(4):634-644

[61] Vogel A, Venugopalan V. Mechanisms of pulsed laser ablation of biological tissues. Chemical Reviews. February 2003;**103**(2):577-644

[62] Qin Z, Bischof JC. Thermophysical and biological responses of gold nanoparticle laser heating. Chemical Society Reviews. 2012;**41**(3):1191-1217

[63] Vogel A, Noack J, Huttman G, Paltauf G. Mechanisms of femtosecond laser nanosurgery of cells and tissues. Applied Physics B-Lasers and Optics. 2005;**81**(8):1015-1047

[64] Zhang Y, Yu LC. Microinjection as a tool of mechanical delivery. Current Opinion in Biotechnology. 2008;**19**(5):506-510

[65] Dhakal K, Black B, Mohanty S. Introduction of impermeable actin-staining molecules to mammalian cells by optoporation. Scientific Reports. 2014;**4**

[66] Antkowiak M, Torres-Mapa ML, Stevenson DJ, Dholakia K, Gunn-Moore FJ. Femtosecond optical transfection of individual mammalian cells. Nature Protocols. 2013;**8**(6):1216-1233

Chapter 9

# Plasmonics in Sensing: From Colorimetry to SERS Analytics

Christian Kuttner

Additional information is available at the end of the chapter

http://dx.doi.org/10.5772/intechopen.79055

**Abstract**

This chapter gives a brief overview of plasmonic nanoparticle (NP)-based sensing concepts ranging from classical spectral-shift colorimetry to the highly active field of surface-enhanced Raman scattering (SERS) spectroscopy. In the last two decades, colloidal approaches have developed significantly. This is seen with, for example, refractive-index sensing, detection of ad−/desorption and ligand-exchange processes, as well as ultrasensitive chemical sensing utilizing well-defined nanocrystals or discrete self-assembled superstructures in 2D and 3D. Apart from individual NPs, the rational design of self-assembled nanostructures grants spectroscopic access to unprecedented physicochemical information. This involves selected research examples on molecular trapping, ligand corona analysis, SERS-encoding, and biosensing. The origin of the SERS effect, also in regard to hot spot formation by off-resonant excitation, is reviewed and discussed in the context of the current challenge to formulate a generalized metric for high SERS efficiency. Special emphasis lies in addressing the fundamental design criteria and the specific challenges of these particle-based sensing techniques.

**Keywords:** colorimetry, SERS, LSPR, colloidal sensors, optically functional materials, self-assembled nanostructures

## 1. Introduction

The field of plasmonics has advanced immensely over the years and is spreading more and more into the area of sensor technology [1–4]. This is due to the unique interaction of light with noble metals [5]. The excitation of conduction electrons to perform collective vibrations, both in volume as well as at the surface, shows in brilliant colors, which have fascinated

© 2018 The Author(s). Licensee IntechOpen. This chapter is distributed under the terms of the Creative Commons Attribution License (http://creativecommons.org/licenses/by/3.0), which permits unrestricted use, distribution, and reproduction in any medium, provided the original work is properly cited. (cc) BY

people since the medieval times. Countless prominent examples of art objects still exist today, such as the Lycurgus Cup (4th century AD) and stained-glass windows of cathedrals.

As early as 1857, Michael Faraday published his groundbreaking findings (The Bakerian Lecture of the Royal Society of London [6]) on the experimental interactions of gold and other metals with light [7]. *"Light has a relation to the matter which it meets with in its course, and is affected by it, being reflected, deflected, transmitted, refracted, absorbed, etc. by particles very minute in their dimensions* [6]." He studied the emergence of different colors for *fluids containing gold reduced to diffused particles* and described the *metallic character of the divided gold*: "*Hitherto it may seem that I have assumed the various preparations of gold, whether ruby, green, violet, or blue in color, to consist of that substance in a metallic divided state* [6]."

Between 1900 and 1920, the famous contributions of James Clerk Maxwell Garnett [8], Gustav Mie [9], Richard Gans [10, 11], and Richard Adolf Zsigmondy [12], just to name a few, proved that plasmonic colors were based on optical resonances that occur for particles smaller than the wavelength of light and that can be theoretically described and precisely predicted [13–15]. This birthed the field of colloidal plasmonic nanoscience [16]. During the last few decades, a variety of different nanostructures, both in the form of individual NPs and particle assemblies [17], have been developed with a special focus on their use as colorimetric or SERS spectroscopy sensors [18, 19].

Today's pronounced diversity of available nanostructures demonstrates the high level of interest in these *optically functional materials*. Within the scope of this book chapter, this diversity can, of course, only be covered to a limited extent. For this reason, the focus here is on NPs as defined building blocks for discrete nanostructures by guided self-assembly [20–22]. **Figure 1** provides a rough overview of functional structures which have been found to be particularly suitable for sensor applications. The first area is represented by individual nanocrystals, for example, in spherical, rod-shaped, triangular, or star-shaped morphologies with strong *intrinsic* electromagnetic hot spots. This can be extended by coupling these particles to a metal surface or thin-film, the formation of branched structures by overgrowth, or hollow, core/shell, and nested structures with nanoscale interior gaps. Nanoparticles at short distances form *extrinsic* hot spots by strong electromagnetic interactions [23], referred to as plasmonic coupling [24]. Even in the disordered state, particle aggregates produce strong field enhancements. However, it is the ordered assembly of particles that allows plasmonic hybridization to emerge [25]. Hybridization can result in highly sensitive modes for spectral shift sensing and intense near-field enhancement for chemical sensing [14]. Again, the diversity ranges from discrete single nanoclusters with uniform coordination numbers to complex superstructures, supercrystals, and patterned structures both in 2D and 3D, which can be fabricated by colloidal engineering.

In this chapter, we will first address the field of plasmonic colorimetric sensing. Here, the fundamental concepts for sensing of surface plasmon resonances of metallic thin films are reviewed and then extended to localized surface plasmon resonances [26] of NPs and ordered NP assemblies by guided self-assembly [20–22]. Second, we will review SERS analytics divided into several steps: the first principles of SERS [27] and off-resonance excitation, SERS analytics of dispersed particles with a focus of the tasks of functional shells, SERS analytics using disordered aggregates under controlled conditions, and finally ordered assemblies designed for high SERS activity [28, 29].

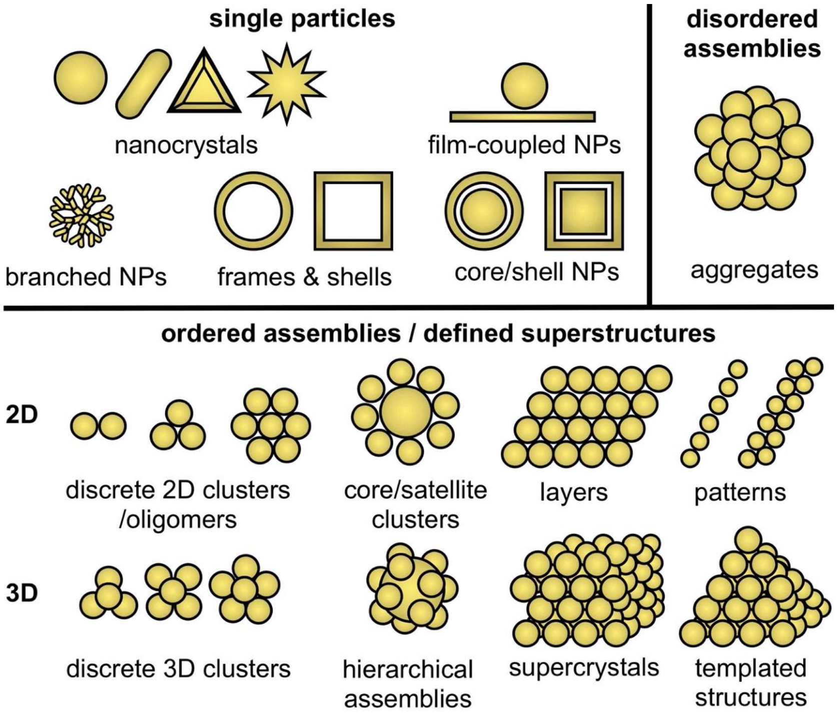

**Figure 1.** Schematic overview of the diversity in plasmonic nanoparticles and -structures: (top, left) nanocrystals, film-coupled particles, and hollow/nested morphologies on single particle level; (top, right) disordered assemblies of aggregated NPs; (bottom) ordered assemblies of discrete NP oligomers, clusters, and defined superstructures in 2D and 3D.

## 2. Plasmonic colorimetric sensing

To begin, we will first briefly review SPR spectroscopy of thin metallic films as a foundation for LSPR spectroscopy. Colorimetric sensing describes the optical determination of chemical or physicochemical properties of a sample. Subsequently, we will discuss concepts in which the plasmonic response is used to obtain information at interfaces or at the near-field environment of metal structures, which would otherwise be inaccessible.

### 2.1. SPR spectroscopy of thin metal films

Surface plasmons (SPs) are electromagnetic waves, emerging from surface plasmon resonances (SPRs), that propagate along the surface or interface of a conductor, usually a metal/dielectric interface [30]. Essentially, surface plasmons are light waves *trapped at interfaces* because of their strong interaction with the free electrons of the conductor. Surface structuring can guide this interaction [31]. The response of the free electrons takes place collectively in the form of oscillations in resonance with the light wave. The consequent charge density oscillation at the surface leads to a concentration of light and thus an enhancement of the local electric nearfield. The high sensitivity of this light-matter interaction renders it attractive for sensing applications. SP-based sensing builds on a *simple* resonance condition:

$$k_{\mathrm{sp}} = k_0 \cdot \sqrt{\frac{\varepsilon_{\mathrm{d}}\ \varepsilon_{\mathrm{m}}}{\varepsilon_{\mathrm{d}} + \varepsilon_{\mathrm{m}}}} \tag{1}$$

The resonance condition requires the SP mode (with frequency-dependent wave-vector $k_{\mathrm{sp}}$) to be greater than that of a free-space photon of the same frequency (free-space wave-vector $k_0$). In addition, for SPRs, the frequency-dependent permittivity of metal ($\varepsilon_{\mathrm{m}}$) and dielectric ($\varepsilon_{\mathrm{d}}$) need to be of opposite signs. As a consequence, the SP resonance phenomenon has been employed for biochemical sensing [32] and clinical diagnosis [33]. Under appropriate conditions, the reflectivity of a thin metal film is extremely sensitive to changes in the local refractive index environment. **Figure 2A** (left) shows an exemplary SPR sensor in a fluidic channel in Kretschmann configuration using a prism for coupling p-polarized light into the metallic film interface [34]. The resulting evanescently decaying field reaches beyond the metallic interface into the sensing medium. When the SPR condition is satisfied, the reflection spectrum for monochromic light shows a characteristic resonance dip (**Figure 2A**, right). Here, the resonance condition is

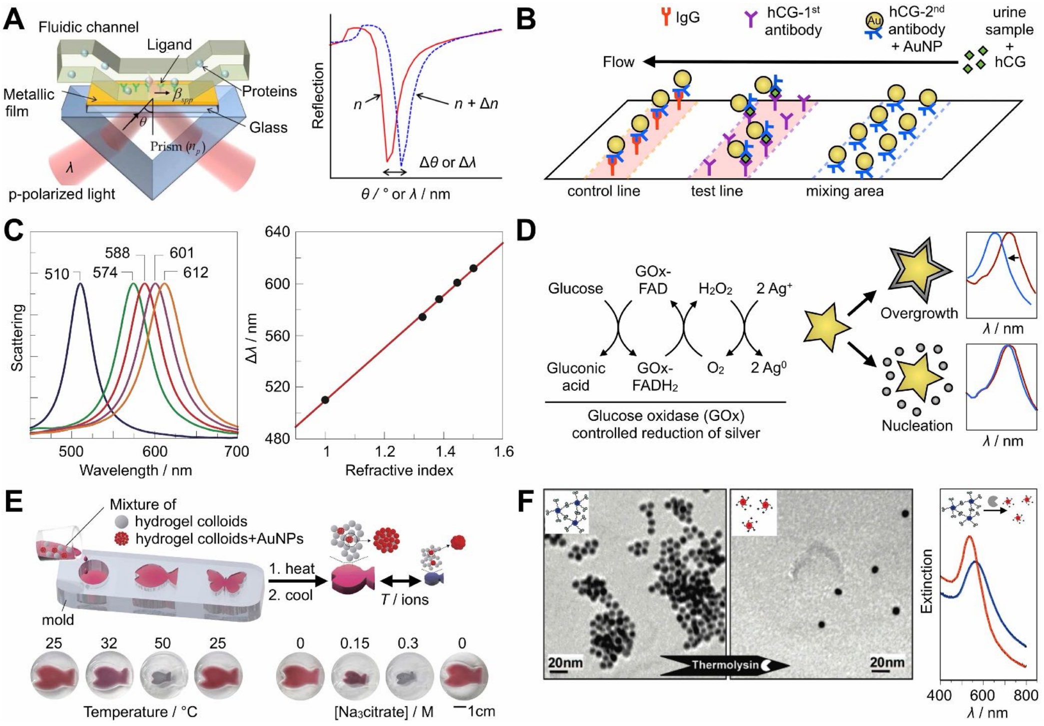

**Figure 2.** Fundamental concepts of colorimetric plasmonic sensing. (A) SPR sensor in a fluidic channel. Copyright 2011 MDPI, adapted with permission [34]. (B) Pregnancy test using AuNPs as inert dye. (C) Refractive index sensitivity of an AgNP-based optical sensor. Copyright 2003 ACS, adapted with permission [44]. (D) LSPR sensor concept for enzyme-guided inverse sensitivity [45]. (E) Dual-responsive hydrogel/AuNP hybrid particles. Copyright 2016 NPG, adapted with permission [47]. (F) Protease-triggered dispersion of AuNP assemblies. Copyright 2007 ACS, adapted with permission [48].

$$\frac{2\,\pi}{\lambda} \cdot n_{\mathrm{p}} \cdot \sin\theta = \mathrm{Re}\left(\frac{\omega}{\mathrm{c}} \cdot \sqrt{\frac{n_{\mathrm{s}}^2\,\varepsilon_{\mathrm{m}}}{n_{\mathrm{s}}^2 + \varepsilon_{\mathrm{m}}}}\right) \tag{2}$$

where $n$ denotes the refractive indices of the dielectric prism (p) and the sensing medium (s), $\lambda$ is the wavelength in free space, and $\theta$ is the incident angle of light [34]. Thus, changes of the refractive index ($\Delta n$) of the sensing medium will shift the resonance dip by altering the resonance angle ($\Delta\theta$) and/or the resonance wavelength ($\Delta\lambda$). The sensing of this resonant spectral response can be realized in different micro- and nanostructured sensor configurations (e.g., prism-, waveguide-, channel-, grating-based setups) [35]. Oates et al. demonstrated that the established methods of SPR spectroscopy for chemical and biological sensing can be enhanced by using the ellipsometric phase information [31]. Next, we focus on colorimetric sensing using plasmonic NPs.

### 2.2. LSPR spectroscopy of single NPs and disordered NP assemblies

The transition from SPR to localized surface plasmon resonance (LSPR) sensing is accompanied by the step from sensors using metallic thin-films to nanosensors in the form of particulate matter [36–38]. The plasmon generated on a small nanoparticle, for example, a sphere, experiences strong spatial confinement because of its hindered and limited propagation [39]. This confinement, also known as localization, results in discrete charge density oscillations [9, 40], which manifest themselves by intensive colors [41]. The excitation frequency of localized plasmons (absorbance band) is highly sensitive for the size, shape, composition, and refractive index environment of the NP. Though LSPRs were capitalized for various nanophotonic applications covering many fields [16, 26, 42], this chapter is limited to their use as sensor elements. For this purpose, we briefly survey the most commonly used and prominent concepts for colorimetric sensing.

**Figure 2** summarizes the fundamental colorimetric sensing concepts using single NPs and disordered NP assemblies. The first example shows the working principle of a pregnancy test for which AuNPs (conjugated to anti-hCG antibodies, blue) serve as an inert dye to detect the presence of hCG antigens (green, **Figure 2B**) [43]. The test is basically a lateral flow sandwich immunoassay consisting of a test line with anti-hCG antibodies (violet), a control line with immunoglobulin G (IgG, red) antibodies, and a mixing with immobilized anti hCG-conjugated AuNPs. By application of a urine sample, the NPs bind to available hCG antigens (which are indicative for a pregnancy). This is followed by the selective binding of AuNPs to the control and test line, while the latter only happens in the presence of hCG antibodies. In this example, the AuNPs serve as an inert dye which does not interfere with the antibody–antigen binding by biorecognition and possesses high chemical stability.

**Figure 2C** highlights the refractive index sensitivity of an AgNP-based optical sensor in various solvent environments (left) [44]. Van Duyne et al. found a linear relationship between the refractive index environment and the LSPR position. This enabled to detect the adsorption of fewer than 60,000 1-hexadecanethiol molecules on single AgNPs which corresponded to a 41 nm shift followed by dark-field spectroscopy. However, for ultralow concentrations, the variations in the physical property (e.g., LSPR shift) become increasingly smaller, and thus, harder to detect with confidence. Contrary to conventional transducers which generate a signal that is directly proportional to the concentration of the target molecule, Stevens and coworkers proposed an LSPR sensor with inverse sensitivity (**Figure 2D**) [45]. The key for this inverse sensitivity is the enzymatic control over the rate of nucleation of Ag on Au nanostars (top: overgrowth; bottom: nucleation), accompanied by a blueshift of the LSPR. Different biosensing strategies have been proposed building on enzymatic reactions and NPs [46].

Apart from dispersed NPs, the plasmonic coupling between NPs, which is dependent on their spatial interspacings, can be utilized for colorimetry. Song and Cho reported dual-responsive architectures by mixing hydrogel and AuNP-decorated hydrogel particles (**Figure 2E**) [47]. This hybrid ensemble responds to both temperature and ions by means of a volume and color change in aqueous systems. Both stimuli can be used to reversibly trigger the transition of uncoupled well-separated AuNPs (red tint) to a state that allows for plasmonic coupling (blue tint), mediated by the hydrogel matrix. Ulijn and Stevens et al. demonstrated the bioresponsive transition from aggregated to dispersed state [48]. **Figure 2F** shows the protease-triggered dispersion of AuNP assemblies using thermolysin for the removal of attractive self-assembly groups and revelation of repulsive charged groups. The consequent blueshift of the LSPR allowed for simple and highly sensitive detection of the presence of thermolysin, which could be tailored for different proteases.

Another approach builds on measuring the orientation of a sample. For this, it is necessary to align the ensemble of NPs macroscopically. This was achieved for anisotropic NPs homogenously dispersed in an elastic polymer matrix [49, 50]. By uniaxial stretching of the material, the NPs are oriented along the direction of elongation. As a result, the material exhibits uniform plasmonic response, which enables for optical detection of the orientation of the material. Continuing on, we will examine assemblies containing ordered NPs and patterns.

### 2.3. LSPR spectroscopy of ordered NP assemblies and defined patterned superstructures

**Figure 3** highlights colorimetric sensing examples of ordered NP assemblies and defined patterned superstructures. Because the LSPR depends on the local dielectric environment at the NP surface, the LSPR shift can be evaluated to detect changes in effective refractive index. The first example is a macroscopic *plasmonic library* consisting of well-separated non-coupling AuNPs with a gradient in size, induced by Au overgrowth [51]. Along the array, the size increase goes along with a color change from colorless to pink (**Figure 3A**, left). Aided by electromagnetic simulations, it was possible to evaluate the effective refractive index and thus changes in the local density of the hydrogel shell around the substrate-supported particles (right). The initial increase of the refractive index indicated a densification of the hydrogel network upon particle growth from 10 to 30 nm. The subsequent decrease above 30 nm might result from internal breakup/rupture of the network.

Sönnichsen et al. proposed the use of core/satellite assemblies for highly sensitive refractive index sensing [52]. **Figure 3B** (left) shows 60 nm AuNPs as cores linked to 20 nm AuNPs as satellites. The average number of satellites allowed tuning the LSPR from 543 to 575 nm. The core/satellite nanostructures showed about twofold higher colorimetric sensitivity ($\Delta\lambda/\Delta n$) than similar sized gold NPs (right). Lee et al. developed a theory-based design of such core/

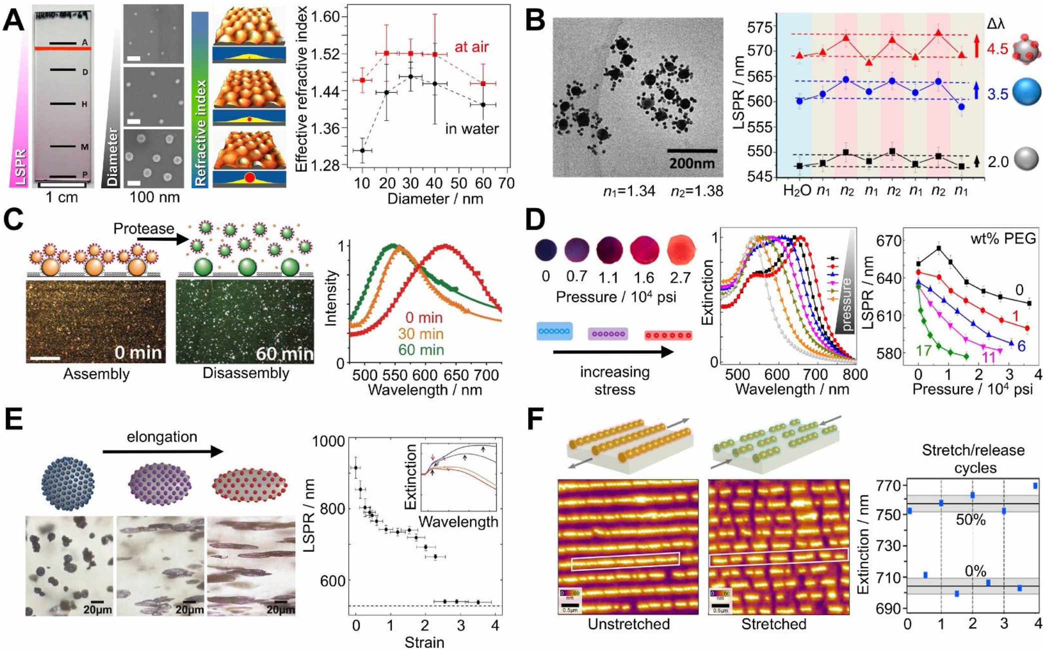

**Figure 3.** Colorimetric sensing concepts of ordered NP assemblies and defined patterned superstructures: (A) Effective refractive index of a substrate-supported array of particles with a gradient in sizes. Copyright 2014 ACS, adapted with permission [51]. (B) Core/satellite assemblies for highly sensitive refractive index sensing. Copyright 2015 ACS, adapted with permission [52]. (C) Biomolecular detection by disassembly of core/satellite assemblies. Copyright 2011 ACS, adapted with permission [54]. (D) Stress memory sensor based on disassembly of AuNP chains. Copyright 2014 ACS, adapted with permission [56]. (E) Mechanochromic strain sensor based on AuNP-decorated microparticles dispersed in a polymer matrix. Copyright 2017 Wiley, adapted with permission [59]. (F) Reversible strain-induced fragmentation of quasi-infinite linear assemblies to defined plasmonic oligomers. Copyright 2017 ACS, adapted with permission [62].

satellite assemblies to optimize the spectral shift due to satellite attachment or release. They provided clear strategies for improving the sensitivity and signal-to-noise ratio for molecular detection, enabling simple colorimetric assays [53]. **Figure 3C** depicts the disassembly of substrate-supported core/satellite assemblies for biomolecular detection [54]. By addition of trypsin, the cysteine/biotin-streptavidin peptide tethers were proteolytically cleaved to release the satellites into solution enabling colorimetric detection of the protease.

Different concepts have been developed for opto-mechanic sensitivity and control [55]. Yin et al. reported a stress-responsive colorimetric film that can memorize the stress it has experienced (**Figure 3D**, left) [56]. This stress memory sensor is based on the LSPR shift associated with the disassembly of chains of AuNPs embedded in a polymer matrix (middle). By plastic deformation, the LSPR experiences a blueshift by irreversible breaking of the linear AuNP assemblies, initially formed in colloidal suspension [57]. The sensitivity of the optical change to stress could be tuned by doping with different amounts of PEG as plasticizer (right) [56]. Instead of mixing NPs with an elastic matrix, AuNPs can also be grown at the surface of a flexible substrate [58]. This enables mechanical control of the plasmonic coupling and electromagnetic fields at the surface. Dreyfus and coworkers designed mechanochromic AuNP-decorated microparticles as strain sensor (**Figure 3E**) [59]. After dispersion in an elastic polymer matrix of PVA, the capsules change in color upon elongation. When the film is stretched, the capsules are deformed into elongated ellipsoidal shapes and the distance between the AuNPs, embedded in their shells, concomitantly increases. Another mechano-plasmonic approach has been proposed for substrate-supported chains of AuNPs. **Figure 3F** (left) shows oriented linear assemblies, above the so-called infinite chain limit [60, 61], in a periodic pattern over cm$^2$ areas on an elastic support [62]. Upon external strain, the assemblies experience a transition from long to short chains by reversible strain-induced fragmentation. The transition from plasmonic polymers to oligomers was accompanied by a pronounced spectral shift (right). A similar strain sensing approach was reported by Minati and coworkers using 1D arrays of broader line widths [63]. These multiparticle arrays showed a blueshift of the reflectance, lineally scaling with the external strain. Here, we will leave the field of colorimetric sensing and turn our attention to the enhancement of the electric field and the concomitant SERS activity.

## 3. SERS analytics

Since its discovery by Martin Fleischmann, Patrick J. Hendra, and A. James McQuillan in 1974, surface-enhanced Raman scattering has become an indispensable tool for analytical chemistry [64]. In this study, two types of pyridine adsorptions have been identified at Ag electrodes [65]. At the same time, the detected signal strengths were far beyond what could be expected to arise from local concentration of absorbed molecules. In 1977, two enhancement theories were proposed independently, namely *chemical enhancement* [66] by Albrecht and Creighton and *electromagnetic enhancement* [67] by Jeanmaire and Van Duyne. Here, we will limit our discussion on the electromagnetic theory, because it is most closely linked to the optical and structural properties of nanocrystals and their assemblies. After an initial review of the origin of SERS enhancement [68, 69], we will go over prominent examples for the application of SERS for chemical spectroscopy.

### 3.1. From basic principles to off-resonance SERS enhancement

The Raman process describes the inelastic scattering of light by atoms or molecules discovered by C. V. Raman in 1928 [70]. This process had already been proposed theoretically by Adolf Smekal in 1923 [71]. In principle, Raman scattering builds on the interaction of a photon and a molecule (or crystal) for which an energy transfer can occur (**Figure 4A**) [72]. However, the Raman process has an inherently low cross-section because the probability of this transfer is *very low* and only 1 in $10^7$ photons are scattered inelastically. For that reason, long measurement times are necessary to compensate for the low photon yield. Therefore, the low time resolution and the limitation of the spatial resolution demand on excellent optics. The SERS effect dramatically improves the photon yield, overcoming these limitations. To clarify this, it is necessary to look at the origin of the enhancement [68].

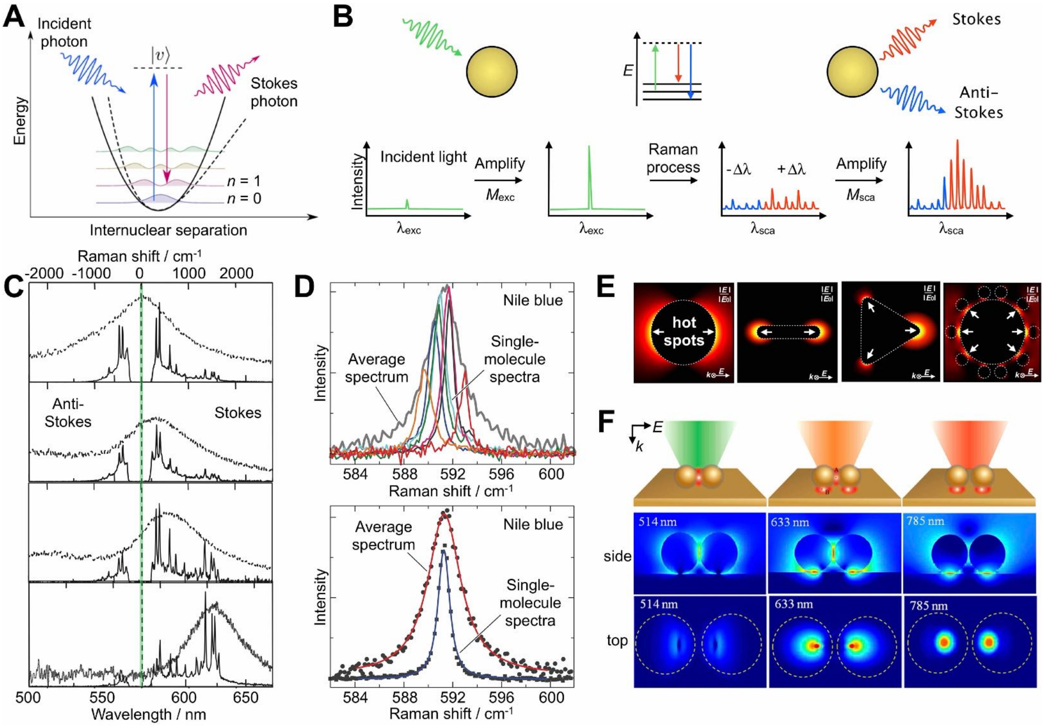

**Figure 4.** First principles of surface-enhanced Raman scattering: (A) schematic of the two-photon non-resonant stokes scattering between two vibrational states of a molecule ($n$ = 0 - > $n$ = 1) mediated by a virtual state $v$. A harmonic potential (solid line) approximates the energy landscape of the ground electronic level (dashed line). Copyright 2016 ACS, adapted with permission [72]. (B) Schematic of the twofold amplification process. (C) Single-molecule spectra of rhodamine Rh123 of AgNP aggregates (solid lines) reflecting the approximate shape of their corresponding Rayleigh scattering spectra (dotted lines). Copyright 2007 APS, adapted with permission [79]. (D) Comparison of individual single-molecule events to average signal (7500 spectra). Copyright 2010 ACS, adapted with permission [75]. (E) Electric field confinement of nanosphere, nanorod, nanotriangle, and core/satellite nanocluster; scaled to maximum visibility. Copyright 2016 ACS, adapted with permission [77]. (F) Selective excitation and spatial transfer of hot spots in dimer gap, in both junctions, or only in the particle–film junctions. Copyright 2016 ACS, adapted with permission [78].

### 3.1.1. *The origin of the SERS enhancement*

Raman scattering is, in its most basic and phenomenological form, the emission of a molecular Raman dipole ($\lambda_{sca} = \lambda_{exc} \pm \Delta\lambda$) [27]. Induced by the electric field $E_{exc}$ of the exciting laser light $\lambda_{exc}$, a Raman dipole $p_0$ oscillates at a Raman-shifted frequency ($\omega_{sca} = 2\pi c/\lambda_{sca}$).

$$p_0(\omega_{\mathrm{sca}}) = \alpha_0(\omega_{\mathrm{exc}}, \omega_{\mathrm{sca}})\ E_0(\omega_{\mathrm{exc}}) \tag{3}$$

For a randomly oriented Raman scatterer, the radiated power is proportional to $|p_0|^2$ [68]. Thus, in order to enhance the Raman signal either the polarizability $\alpha$ or the electric field $E$ need to be magnified. The former refers to chemical enhancement, this is the modification of the local polarizability of the molecule ($\alpha_0$ -> $\alpha_{loc}$), whereas the latter is called electromagnetic enhancement EM and describes the augmentation and confinement of the local near-field ($E_0$ -> $E_{loc}$). The enhanced dipole $p$ can be written as

$$p(\omega_{\mathrm{sca}}) = \alpha_{\mathrm{loc}}(\omega_{\mathrm{exc}}, \omega_{\mathrm{sca}})\ E_{\mathrm{loc}}(\omega_{\mathrm{exc}}) \tag{4}$$

The dipole enhancement upon excitation can be expressed by

$$\frac{|p|^2}{|p_0|^2} \propto \frac{|E_{\mathrm{loc}}(\omega_{\mathrm{exc}})|^2}{|E_0(\omega_{\mathrm{exc}})|^2} = M_{\mathrm{exc}}(\omega_{\mathrm{exc}}) \tag{5}$$

Likewise, the dipole enhancement upon emission, that is, the Raman scattering, is given by

$$\frac{|p|^2}{|p_0|^2} \propto \frac{|E_{\mathrm{loc}}(\omega_{\mathrm{sca}})|^2}{|E_0(\omega_{\mathrm{sca}})|^2} = M_{\mathrm{sca}}(\omega_{\mathrm{sca}}) \tag{6}$$

Although it is convenient from a theoretical point of view to separate the excitation and scattering into two steps, the Raman scattering process is instantaneous and both occur simultaneously [27]. The combined enhancement $M_{\mathrm{SERS}}$ contains both contributions of the twofold amplification process (**Figure 4B**) [73]: the augmented excitation of a molecular dipole by an incident photon ($\lambda_{\mathrm{exc}}$) and the stimulated emission of a scattered photon ($\lambda_{\mathrm{sca}}$) of higher (anti-Stokes, $\lambda_{\mathrm{sca}} < \lambda_{\mathrm{exc}}$) or lower energy (Stokes, $\lambda_{\mathrm{sca}} > \lambda_{\mathrm{exc}}$).

$$M_{\mathrm{SERS}}\left(\lambda_{\mathrm{exc}}, \lambda_{\mathrm{sca}}\right) = M_{\mathrm{exc}}\left(\lambda_{\mathrm{exc}}\right) \times M_{\mathrm{sca}}\left(\lambda_{\mathrm{sca}}\right) \tag{7}$$

Often, the total enhancement is simplified by the so-called $|E|^4$-approximation, which neglects the Raman shift. However, this approximation needs to be treated with caution as many cases have shown [74].

$$M_{\mathrm{exc}}(\lambda_{\mathrm{exc}}) \times M_{\mathrm{sca}}(\lambda_{\mathrm{sca}}) = \frac{|E_{\mathrm{loc}}(\lambda_{\mathrm{exc}})|^2}{|E_0(\lambda_{\mathrm{exc}})|^2} \times \frac{|E_{\mathrm{sca}}(\lambda_{\mathrm{sca}})|^2}{|E_0(\lambda_{\mathrm{sca}})|^2} \approx \frac{|E_{\mathrm{loc}}(\lambda_{\mathrm{exc}})|^4}{|E_0(\lambda_{\mathrm{exc}})|^4} \tag{8}$$

The questions of why and how the shapes of SERS spectra change has been addressed by Yamamoto and Itoh [73]. The transformation of the Raman spectrum, in principle the Raman cross section $\sigma_{\mathrm{RS}}$, by the SERS process can be described as follows:

$$\sigma_{\mathrm{SERS}} = M_{\mathrm{exc}}\left(\lambda_{\mathrm{exc}}\right) \times \sigma_{\mathrm{RS}} \times M_{\mathrm{sca}}\left(\lambda_{\mathrm{sca}}\right) = \sigma_{\mathrm{RS}} \times M_{\mathrm{SERS}}\left(\lambda_{\mathrm{exc}}, \lambda_{\mathrm{sca}}\right) \tag{9}$$

If Eq. 9 holds true, this would enable the reconstruction of a SERS spectrum from the unenhanced Raman spectrum and an enhancement function $M_{\mathrm{SERS}}(\lambda)$. Yamamoto and Itoh proposed that this reconstruction might be given by the product of the Raman spectrum times the Rayleigh scattering spectrum, based on observations using AgNP nanoaggregates (**Figure 4C**) [73]. They found that single-molecule spectra of rhodamine Rh123 (solid lines) were well reflecting the approximate shape of their corresponding Rayleigh scattering spectra (dotted lines) both for Stokes as well as Anti-Stokes scattering [43, 47]. **Figure 4D** shows a comparison of individual single-molecule events to average signal (7500 spectra) for Nile blue measured with Ag aggregates at high spectral resolution [75]. The ensemble averaging of many events revealed the characteristic broadening of the average spectrum (top) and fitted to Lorentzian line shapes (bottom).

All the reviewed examples, up to now, have capitalized from aggregated Ag nanocolloids as, for example, introduced by Lee and Meisel [76]. Such disordered aggregates enabled breakthrough results in regard to pushing the limit for ultrasensitive detection, down to single-molecule resolution, as well as nurtured the fundamental understanding of the origin of SERS enhancement. In the following section, we will turn our attention from disordered aggregated systems to individual nanocrystals and their ordered assemblies. The main aim is to find appropriate criteria for the design of nanostructures with both high and robust enhancement.

### *3.1.2. Hot spot formation*

As a first step, we address the formation of *hot spots*, so-called confined locations with the highest electric field strengths. For individual nanoparticles, hot spots can be found at the poles of nanospheres (e.g., in respect to an excited dipolar mode, see **Figure 4E**, left) or near areas of high surface curvatures, as at the tips of nanorods and nanotriangles (middle). In multiparticle systems, hot spots form inside interparticle gaps, cavities, or crevices, as depicted for an exemplary core/satellite assembly (right) [77]. Depending on the nature of the excited LSPR modes and considering plasmonic hybridization in multiparticle systems, the distribution of hot spots can be quite diverse. For instance, the lighting of special hot spots has been demonstrated for film-coupled multiparticle configurations [78]. **Figure 4F** shows the basic example for selective excitation and spatial transfer of hot spots in a AuNP dimer. Depending on the excitation wavelength, the hot spots can be formed either in the dimer gap, in the particle-film junctions, or in both junctions at the same time [78]. Electromagnetic simulations can give valuable guidance for the design of targeted hot spots in plasmonic nanostructures, especially for complex systems [15, 23].

### *3.1.3. Off-resonance SERS enhancement*

However, the design of NPs for SERS has shown to be more involved than simply maximizing the local electric field [80]. Murphy et al. initially reported the surprising finding of the highest SERS signals for LSPRs, blue-shifted from the wavelength of laser excitation. They studied an ensemble of Au nanorods of different aspect ratios (but uniform tip curvature) for which the longitudinal LSPRs shifted from 650 nm to 800 nm (**Figure 5A**, left). Contrary to expectations, the batches with matching of LSPR and laser excitation performed worse than off-resonant batches (right). This has been explained by a competition between SERS enhancement and extinction. The initial assumption that the LSPR is an adequate prediction for the best SERS performance has been shown to be incorrect.

Further validation was provided by a similar approach, screening the correlation of Au nanotriangle size and SERS performance [81]. Upon overgrowth, the LSPRs showed a continuous shift toward near-infrared (**Figure 5B**, left). Again, the highest SERS enhancement did not coincide with matching of the LSPR to the laser wavelength. Instead, the highest SERS activity was identified in off-resonance conditions (right). To rule out the influence of possible differences in tip/edge sharpness, the nanotriangle morphology was characterized by a close correlation of electron microscopy (TEM, field-emission SEM) and small-angle X-ray scattering (SAXS) analysis [50, 77, 81] combined with 3D atomistic modeling. This revealed a uniform tip curvature for all sizes.

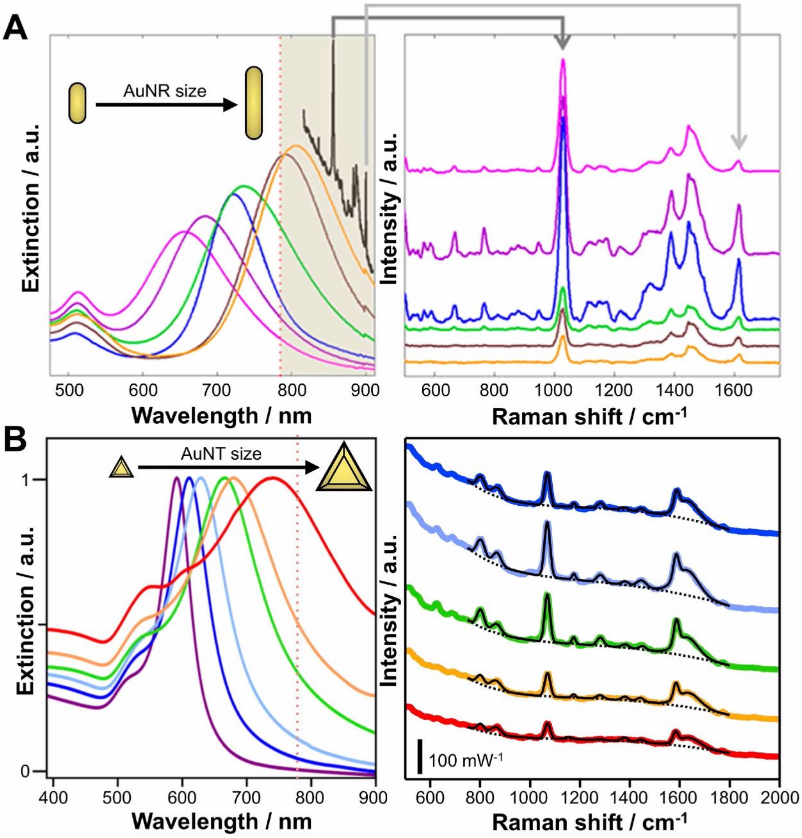

**Figure 5.** Off-resonance SERS enhancement: Non-linear dependency of (left) optical properties and (right) SERS signal intensities for variably sized (A) nanorods and (B) nanotriangles. (A) Copyright 2013 ACS, adapted with permission [80]. (B) Copyright 2018 ACS, adapted with permission [81].

The assumption that aggregation might be the cause for the off-resonant SERS activity was thoroughly investigated. Optical spectroscopy (UV-vis-NIR) before and after addition of the Raman marker did not show any indication of aggregation. Reversible aggregation/association of particles could be ruled out because of the presence of a sufficient amount of stabilizing agent (CTAB) in the solution. The amount of Raman marker (4MBA) added was much lower than that of the available stabilizing agent (>50-fold molar excess). The marker was not expected to act as a molecular linker. Also, in the case of irreversible aggregation, one would expect a loss of particles over time, which was not observed. The video feedback of the Raman microscopy did not give any indication of possible formation of aggregates even after the extended laser exposure. The colloidal dispersions were found to exhibit high colloidal stability for the reported surfactant concentrations, and the SERS signals could be detected reproducibly. Thus, even if aggregation (below the detection limit) was present, it would be of *negligible* contribution and should not have affected the registered SERS spectra [81].

Consequently, in many situations, the hot spot intensity *is not* directly correlated to the optical properties; thus, the extinction maximum is often *not* the best excitation wavelength for SERS [81]. As a rule, an increase in SERS activity can be expected for situations in which the

Stokes-shifted Raman signals lies in the low-energy shoulder of the LSPR band; in other words, when the laser line is shifted to the red, compared to the LSPR extinction maximum.

## 3.2. SERS analytics of single particles

At this point, we move to the application of SERS for analytical purposes. The term "single or individual particles" indicates that the NPs are present in a dispersed state in colloidally stable dispersions and that aggregation is avoided. First, examples will be discussed that highlight the retrieval of chemical information at the NP surface. Then, we will address the specific tasks of the different shells and its versatile functions for SERS applications.

### *3.2.1. Surface chemistry of nanoparticles in dispersion detection, exchange, competition, and chemical reaction of ligands*

SERS analytics have proven to be a valuable tool for the detection, studies of the exchange and competitive adsorption, as well as localized chemical reactions of ligands at NP surfaces in dispersion.

Hafner et al. applied SERS analytics to study the structural transition in the surfactant layer that surrounds Au nanorods (**Figure 6A**, left) [82]. This was achieved by following the displacement of surfactant by thiolated poly(ethylene glycol). At the same time, they characterized the surfactant bilayer, revealing the absorbed layer of counterions at the gold surface $Au^+X^-$, the ammonium head group $CN^+$, and the skeletal vibrations of the alkane chain of the surfactant (right). Building on these findings, Chanana et al. investigated the quantitative exchange of surfactant against protein (bovine serum albumin) on Au nanorods (**Figure 6B**, left) [83]. In the context of biotoxicity, the cationic surfactant ($CTA^+X^-$) needs to be removed

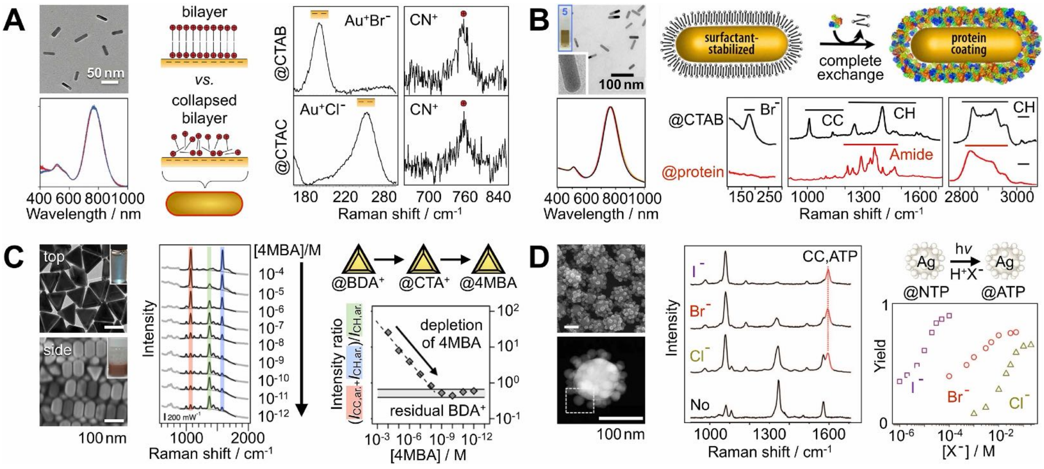

**Figure 6.** Detection, exchange, competition, and chemical reaction of ligands by SERS analytics in dispersion: (A) surfactant bilayer characterization on au nanorods (counter ion $au^+X^-$, ammonium head group $CN^+$). Copyright 2011 ACS, adapted with permission [82]. (B) Quantitative exchange of surfactant against protein on au nanorods. Copyright 2015 ACS, adapted with permission [83]. (C) Competition of aromatic surfactants ($BDA^+$), non-aromatic surfactants ($CTA^+$), and thiol ligands (4MBA) on au nanotriangles. Copyright 2018 ACS, adapted with permission [81]. (D) Hot electron-induced reduction of small ligands (NTP to ATP) on Ag core/satellite assemblies. Copyright 2015 NPG, adapted with permission [85].

from the solution and NP surface. This required analyzing the broad spectral range from 100 to 3100 cm$^{-1}$, covering all the characteristic signals associated with the ligand exchange (right). This evidenced the complete surfactant removal, which is a key step toward safe bioapplication of protein-coated NPs.

The competition of aromatic surfactants (BDA$^+$), non-aromatic surfactants (CTA$^+$), and thiol ligands (4MBA) was studied on Au nanotriangles (**Figure 6C**) [81]. Contrary to expectations, first evidence for the nonquantitative nature of the ligand exchange of aromatic versus non-aromatic surfactants was found. Differences in binding affinity toward the NP surface are attributed to additional π-interactions of the electron-rich benzyl headgroup [84]. It was possible to detect a trace amount of BDA$^+$ of 1–10 nM, which originated from the seed synthesis and could not be removed even after excessive washing with CTAB surfactant [81].

Schlücker and Xie applied SERS analytics to follow nano-localized chemistry on Ag core/satellite assemblies (**Figure 6D**, left) [85]. They reported the hot electron-induced reduction of small ligands (NTP to ATP) in the absence of chemical reduction agents. The reduction was shown to be dependent on the available halide counterions X$^-$ (middle, right).

### *3.2.2. Functional shells for augmented SERS applications*

The shell can provide for different functionalities, such as inertness, hosting of Raman markers, molecular trapping, harvesting/accumulation of analyte molecules, but also by means of improving the SERS activity.

The first examples represent chemically inert shells to protect SERS-active nanostructures from contact with whatever is being probed. This concept has been introduced by Tian et al. and entitled as shell-isolated NP-enhanced Raman spectroscopy (SHINERS) [86]. The silica shell acts as a nanoscale dielectric spacer. Such particles have been applied for the *in-situ* detection of pesticide contaminations on food/fruit [87]. Silica encapsulation can also be used to protect a molecular codification, a layer of Raman markers at the NP surface (**Figure 7A**) [88]. A silica shell enables further functionalization, chemical post-modification, and assembly of superstructures [89]. At the same time, silica overgrowth can stabilize superstructures as well as increase their colloidal stability and robustness (**Figure 7A**).

Pazos-Pérez and Alvarez-Puebla et al. demonstrated the SERS encoding of particles. For this, the NP surface is first partially functionalized by a stabilizing ligand, followed by a codification with a SERS marker (**Figure 7B**), and the final overcoating with silica to create an inert outer surface layer [90]. Also, hyrogel shells have shown the potential for molecular trapping of analyte molecules [91, 92]. The partial hydrophobic/hydrophilic nature of poly(N-isopropylacrylamide) during the reversible volume-phase transition can harvest analyte molecules from solution. After accumulation, the induced collapse of the shell can serve to increase the local concentration of analytes at the NP surface (**Figure 7C**, right) [93].

The shell can serve as a means to improve the SERS activity of NPs. For example, as a template for the growth of complex NP morphologies. Liz-Marzán et al. developed an approach for the templated growth of branched Au structures inside of mesoporous silica shells (**Figure 7D**, left) [94]. The formed tips branching out from the cores (spheres, rods, triangles) improve the

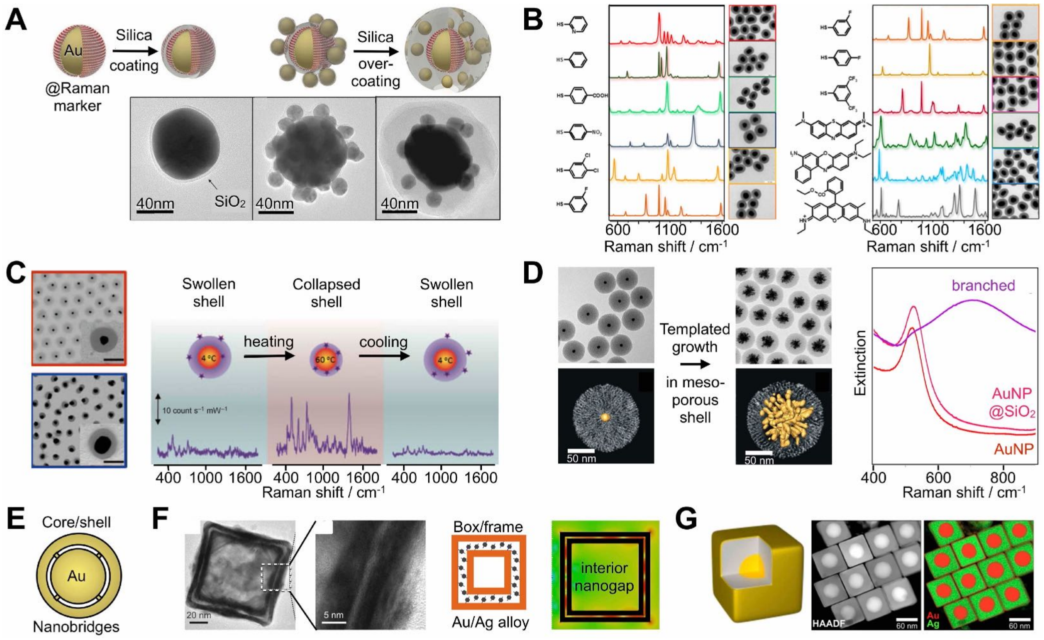

**Figure 7.** Functional shells for augmented SERS applications of single nanoparticles: (A) silica coating of dispersed AuNPs and overcoating of core/satellite superstructures. Copyright 2011 Wiley, adapted with permission [88]. (B) SERS-encoded NPs enclosed in silica. Copyright 2015 ACS, adapted with permission [90]. (C) Hydrogel-encapsulation for thermo-responsive molecular trapping. Copyright 2008 Wiley, adapted with permission [93]. (D) Branched morphologies grown inside radial mesoporous silica shells. Copyright 2015 ACS, adapted with permission [94]. (E) Schematic core/shell particle with nanoscale interior gaps and nanobridges [95]. (F) Interior nanogap within double-shelled au/Ag nanoboxes. Copyright 2015 NPG, adapted with permission [96]. (G) Protective au overcoating of AgNPs to increase their chemical stability. Copyright 2018 Wiley, adapted with permission [99].

plasmonic performance (right) while favoring the localization of analyte molecules at highly SERS-active regions. Another example is the formation of nanoscale DNA-tailorable interior gaps in spherical core/shell particles (**Figure 7F**) [95]. Interestingly, it has been found that the presence of nanobridges between shell and core does not perturb the hot spot formation. In **Figure 7G**, this concept is adopted for cubic NPs [96]. For such shelled Au/Ag nanoboxes and nanorattles, a pronounced electric field confinement was found in the interior nanocavity [50].

Metal overgrowth can increase surface roughness by forming bumpy structures [97] or undulated surfaces [98], which both showed increased SERS activity. At the same time, metal overgrowth can increase the chemical stability of NPs. A sub-skin depth Au layer has been shown to enable oxidant stability and functionality without altering the optical properties of Ag nanocubes (**Figure 7G**) [99].

### 3.3. SERS analytics of particle assemblies

The field of particle assemblies is sophisticated and versatile. Here, we start with disordered aggregates and then progressively move from small discrete oligomers to large organized multiparticle assemblies in dispersion or supported on substrates. The examples shown are by no means to be considered universally valid but should serve as guidelines for a rational design of assemblies for SERS.

### *3.3.1. SERS sensing based on the formation of disordered aggregates under controlled conditions*

In this section, we briefly delve back into the field of disordered aggregates to explore to what extent these can be formed under controlled conditions for SERS analytics. As introduced in Section 3.1, aggregates can exhibit high SERS activities but suffer from problems concerning reproducibility and robustness. Several approaches addressed these issues and proposed conditions under which aggregation can be induced in a controllable manner.

Gucciardi et al. reported the aggregation of Au nanorods mediated by optical forces and plasmonic heating (**Figure 8A**) for SERS detection of biomolecules at physiological pH [100]. The formed disordered NP clusters can embed molecules from solution, even in buffered media at neutral pH. The dynamics of the signal increase during aggregate formation have been studied revealing different states (**Figure 8B**: onset, stabilization, size increase, and saturation). The laser scattering and bright field images showed that such aggregates can reach micron-scale dimensions after extended laser irradiation (over several tens of minutes). Aggregation can also be induced by specific binding, for example, glyco-conjugation of galectin-9 and glycan-decorated AuNPs. The real-time dynamic SERS sensing of galectin-9 in binding buffer, mimicking neutral conditions, revealed three different aggregation ranges, namely an early fast cluster growth, followed by a slower aggregation, before ultimately reaching the final equilibrium state [101]. Similarly, Mahajan et al. employed the selective guest sequestration of cucurbit[*n*]uril (CB[*n*]) molecules for molecular-recognition-based SERS assays (**Figure 8C**) [102]. These macrocyclic host molecules feature sub-nanometer dimensions capable of

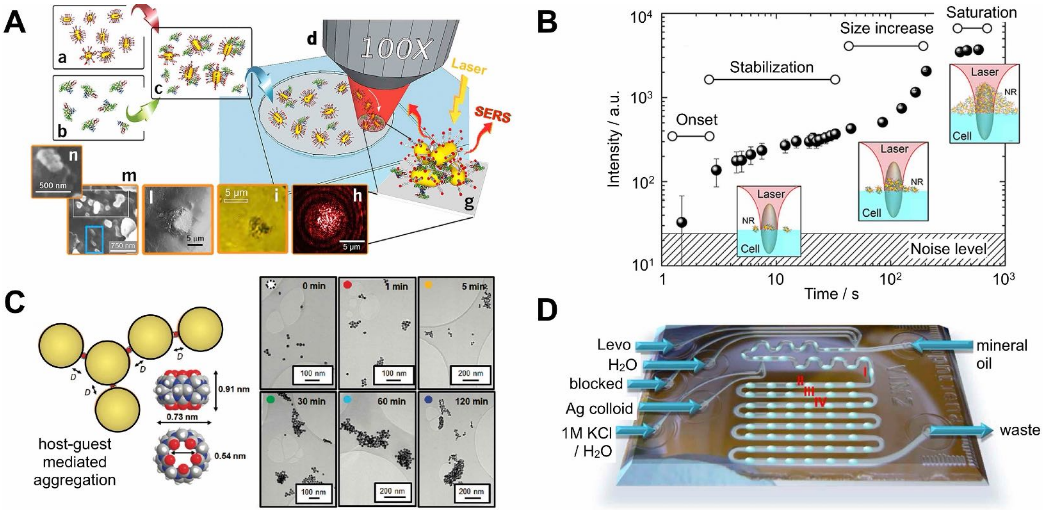

**Figure 8.** SERS sensing based on the formation of disordered aggregates under controlled conditions: (A) laser-induced aggregation by plasmonic heating and (B) aggregation dynamics. Copyright 2016 NPG, adapted with permission [100]. (C) Molecular-recognition-based SERS assay by selective guest sequestration. Copyright 2011 ACS, adapted with permission [102]. (D) Droplet-based microfluidic setup for lab-on-a-chip SERS measurements. Copyright 2016 ACS, adapted with permission [104].

binding AuNPs. The aggregation produces clusters with a defined interparticle spacing of 0.9 nm. The entitled "host-guest SERS" builds on the capturing of analyte guest molecules inside the barrel-shaped geometry of CB[*n*] host molecules [102, 103].

Lab-on-a-chip (LOC) SERS is an approach that is particularly well-suited for diagnostic applications. **Figure 8D** depicts a droplet-based microfluidic setup for LOC SERS measurements [104]. For measurements, equal amounts of Ag colloids and buffer/analyte solutions were mixed and, finally, 1 M KCl was added for inducing the aggregation in a controlled and reproducible manner [105]. Such microfluidic devices with a liquid/liquid segmented flow, where analyte-containing droplets are formed in a carrier liquid e.g. oil, show great potential for bioanalytics because minimal sample amounts are required and only short analysis times are needed, leading to significant cost reduction [106–108].

### *3.3.2. SERS sensing based on ordered assemblies designed for high SERS activity*

The ultimate goal is to obtain full control over the organization of NPs into discrete clusters. In other words, finding appropriate conditions under which the local association of particles proceeds in a controlled way. This would give access to uniform and discrete assemblies of defined coordination numbers both in 2D and 3D.

The first step toward this goal was achieved by efficient fractionation of 3D clusters by density gradient separation. After purification, the mixed ensemble of clusters was separated yielding pure cluster populations (**Figure 9A**) [109]. The obtained fractions of monomers (single NPs), dimers, trimers, tetramers, pentamers, and higher species were characterized for their optical properties as well as their capabilities for SERS. The SERS activity per assembly was found to depend on the coordination number, which determines the number of available gaps in a cluster, but also the respective contribution of each gap.

For the case of substrate-supported "flat" clusters, Bach and coworkers fabricated core/satellite structures using DNA ligands to direct the self-assembly (**Figure 9B**) [110]. Such "nanoflower"-like 2D structures have shown improved SERS activity as compared to commercial SERS substrates. However, the critical parameter is the size ratio of core to satellite as it controls the coupling strength and plasmonic hybridization. For a high mismatch is sizes, this is for satellites of much smaller size than the core NP, the orbit of NPs is effectively uncoupled from the central NP. But the possible sensing applications of such structures go beyond the formation of hot spots for SERS. For matching building block sizes, Fano-like resonances have been predicted and experimentally observed for structures prepared by e-beam lithography [111–113]. Such resonances show the characteristic signature in the form of two LSPR peaks separated by a transparency window, a dip in extinction.

Building on this, one might ask what happens if such core/satellite patterns are formed on a curved surface, such as a microparticle, or if the substrate consists of different metallic layers. The latter results in a complex architecture of multilayered core/satellite assemblies surrounding Au/Ag rattles as cores [114]. The rattles exhibit intrinsic hot spots inside the interior cavity between the central rod-like Au core and the frame of Au/Ag alloy [50, 115, 116]. By adsorption of small NPs at the exterior, the LSPR band broadened and shifted further toward red and additional extrinsic hot spots were formed. This broadening was found to be controlled by the density of the satellite particles.

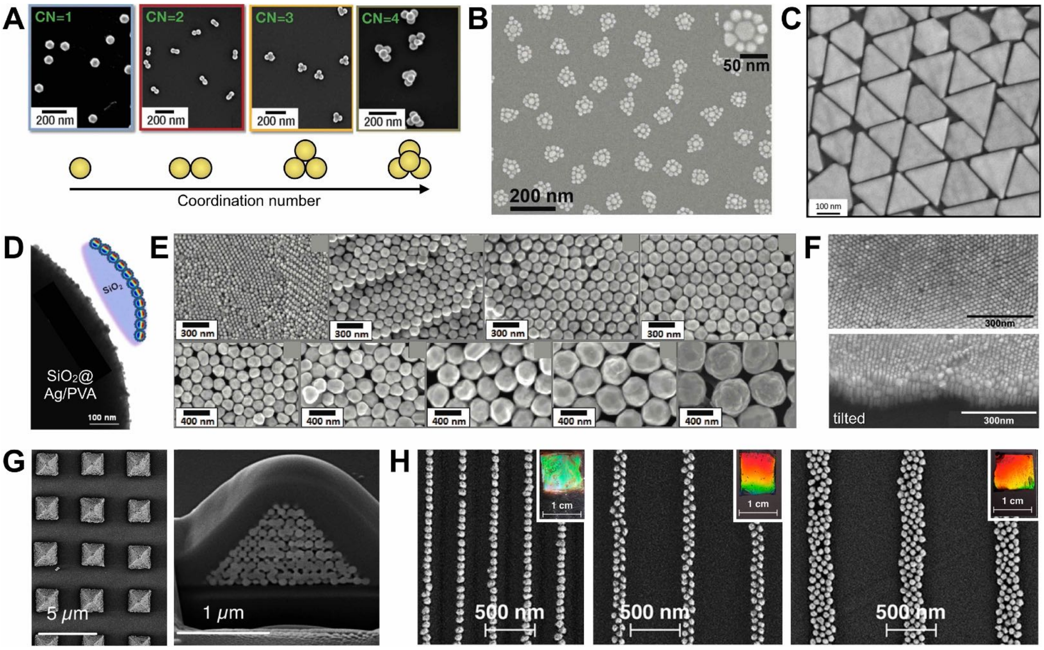

**Figure 9.** Ordered assemblies designed for high SERS activity. (A) Nanoparticle clusters of discrete coordination numbers. Copyright 2012 Wiley, adapted with permission [109]. (B) DNA-directed 2D core/satellite structures. Copyright 2012 Wiley, adapted with permission [110]. (C) Monolayer of close-packed nanotriangles. Copyright 2017 ACS, adapted with permission [118]. (D) AgNP-decorated silica microparticles. Copyright 2015 ACS, adapted with permission [119]. (E) Patterned supercrystal array of close-packed vertically aligned nanorods. Copyright 2012 Wiley, adapted with permission [124]. (F) Supercrystals of NPs ranging from the nano- to the microscale. Copyright 2012 ACS, adapted with permission [121]. (G) Pattern of pyramidal supercrystal architectures. Copyright 2017 ACS, adapted with permission [126]. (H) Macroscale patterns of quasi-infinite linear NP arrangements. Copyright 2014 ACS, adapted with permission [61].

In general, the density of assemblies is a critical parameter for SERS activity. The interparticle distances determine the coupling strength. Here, the coupling threshold of the smallest, in other words, weakest coupling partner limits the interaction strength [117]. For a nanofilm, that is, a dense layer of close-packed particles, this limitation is overcome aided by collective long-range modes. For instance, a layer of nanotriangles prepared by film-casting and solvent evaporation shows nicely arranged edge-to-edge and tip-to-tip ordered arrangements in the monolayer (**Figure 9C**) [118]. The resulting extrinsic hot spots have been shown allowance for hot electron-driven catalytic reactions such as the dimerization of 4-NTP to 4,4′-dimercaptoazobenzene (DMAB), followed by SERS spectroscopy in a dry state. Radziuk and Möhwald reported close-packed nanofilms of 30-nm sized AgNPs on silica microparticles for intracellular SERS (**Figure 9D**) [119]. The primary (of individual microparticles) and secondary hot spots (between adjacent microparticles) were utilized for chemical imaging of live fibroblasts [120]. These AgNP-decorated microparticles have been compared to AgNPs with a 5 nm silica shell and silica NPs with a 5 nm thin Ag coating.

The nanofilm concept can be extended to thicker layers ultimately yielding supercrystals of close-packed NPs. **Figure 9F** presents a study in which supercrystals of NPs ranging from nano- to the microscale dimension have been realized [121]. During this transition, the LSPR band of the building blocks becomes increasingly broad because of higher polar modes. The formed superlattices exhibited pronounced interparticle coupling, whereas only the top layer is available for SERS sensing because of a limited penetration depth. However, patterning can also be utilized to discretize the electromagnetic response of the films/crystals. By comparison of different geometries of discrete supercrystals, it was found that patterning can have a deep impact on the surface electric field generation [122].

In addition to size, the shape of the used building block NPs plays an important role. For anisotropic particles such as nanorods, the local organization becomes essential. Organized nanorod supercrystals in lying-down [123] and standing configurations have shown significant contributions of side-to-side interactions between the close-packed NPs [124]. Bach et al. developed a method for directed nanorod assembly to prepare micropatterned substrates of vertically oriented nanorods (**Figure 9F**).

Finally, we turn our attention toward complex superstructures of organized NPs such as periodical arrays of pyramidal supercrystals. These superstructures accumulate the electric near-field at the apex of the pyramid [125]. The focalization can be expected to strongly depend on the "sharpness" of the pyramid but also on the internal order. Liz-Marzán and coworkers further developed the templated self-assembly to obtain "high quality" pyramids with highly ordered face-centered cubic lattices with one {100} facet oriented parallel to the pyramidal base and the {111} facets corresponding to the four lateral sides (**Figure 9G**) [126].

Further examples, highlighting the importance of structural order, are linear 1D assemblies with uniform interspaces. Here, lateral offsetting of NPs and inconsistent spacing can perturb the coupling along the chain [62, 127]. **Figure 9H** presents macroscale patterns of quasi-infinite linear NP arrangements [61]. The strong plasmonic coupling builds on the regular nanoscale spacing. Both single-line and double-line arrays have been shown to provide for uniform enhancement, with higher values for the single-line arrays [128, 129]. Likewise, the use of anisotropic NPs, which is more challenging, causes the LSPRs to shift further toward the red [130].

Ultimately, the challenge in ordered systems is the control of the interparticle spacings because the gap sizes correlate with the achievable field enhancements. Here, the coating of the NPs plays an essential role, as it may act as a guide for the self-assembly while at the same time act as a spacer in the final nanostructure [20].

## 4. Conclusion and outlook

This chapter gave an overview of plasmonics in the field of sensing. Starting with nanoparticles with specific morphological and optical properties up to the complex arrangements of these into ordered and even hierarchical superstructures, there is *much diversity* of accessible nanostructures. Despite this diversity, it must be considered that the structure-property relations need to be well understood to design *functional materials* with tailored properties.

For colorimetric detection, this represents the fabrication of uniform systems with high spectral sensitivity. Changes in particle size, shape, composition, and arrangement can be used for this purpose. This gives access to many possible applications in the field of biosensing, ion/temperature sensing, mechanosensing, to name a few. In each case, the plasmonic response of a system to a *specific internal or external stimulus* represents the central design criterion. For colorimetry, the task of plasmonics is very direct, meaning that the plasmonic response of a material is evaluated directly. For this reason, the plasmonic material/substrate is often closely linked to the analytical question.

Building on this, SERS spectroscopy demonstrates the power of *surface-enhanced analytics*. Here, plasmonics serve to provide the enhancement as a means to an end. The central task is the detection of chemical information—often independent of the actual plasmonic material. In fact, the analysis is, in many cases, blind to the plasmonic material. This opens the door for optimizing the nanostructure for *higher signal yields*. In this overview, we have found various structural approaches to increase the sensitivity. The confined and localized enhancement in these structures gives access to unprecedented details about the chemistry of and at material interfaces and nanoparticle surfaces [131].

As a final thought, one needs to bear in mind that some questions persist regarding the enhancement mechanism in action. For multiparticle systems and complex nanostructures, the prediction of hot spot localization and intensity becomes increasingly challenging. Several examples have shown the surprising circumstance of highest SERS response at unexpected conditions. In retrospect, it is likely that a fair share of SERS studies in the literature might be affected by particle aggregation. For that reason, targeted investigations are necessary to explain such phenomena. Also, the accurate prediction of SERS activity is still challenging both on a single-particle level as well as in multiparticle assemblies. In view of these points, besides increasing the sensitivity, the *sensing robustness* of the system must be a central design criterion in the development.

## Acknowledgements

C.K. acknowledges funding from the European Union's Horizon 2020 research and innovation programme under the Marie Skłodowska-Curie grant agreement No. 799393 (NANOBIOME). Honest gratitude is addressed to Andreas Fery for his fruitful suggestions, his critical thinking, and his continued support.

## Conflict of interest

The author declares no competing financial interest.

## Author details

Christian Kuttner[1,2,3]*

*Address all correspondence to: christian.kuttner@googlemail.com

1 BioNanoPlasmonics Laboratory, CIC biomaGUNE, Donostia–San Sebastián, Spain

2 Leibniz-Institut für Polymerforschung Dresden e.V., Dresden, Germany

3 Cluster of Excellence Centre for Advancing Electronics Dresden (cfaed), Technische Universität Dresden, Dresden, Germany

## References

[1] Howes PD, Chandrawati R, Stevens MM. Colloidal nanoparticles as advanced biological sensors. Science. 2014;**346**(6205):1247390

[2] Anker JN, Hall WP, Lyandres O, Shah NC, Zhao J, Van Duyne RP. Biosensing with plasmonic nanosensors. Nature Materials. 2008;**7**(6):442-453

[3] Bodelón G, Montes-García V, López-Puente V, Hill EH, Hamon C, Sanz-Ortiz MN, Rodal-Cedeira S, Costas C, Celiksoy S, Pérez-Juste I, Scarabelli L, La Porta A, Pérez-Juste J, Pastoriza-Santos I, Liz-Marzan LM. Detection and imaging of quorum sensing in Pseudomonas aeruginosa biofilm communities by surface-enhanced resonance Raman scattering. Nature Materials. 2016;**15**(11):1203-1211

[4] Zhang S, Geryak R, Geldmeier J, Kim S, Tsukruk VV. Synthesis, assembly, and applications of hybrid nanostructures for biosensing. Chemical Reviews. 2017;**117**(20):12942-13038

[5] Odom TW, Schatz GC. Introduction to plasmonics. Chemical Reviews. 2011;**111**(6): 3667-3668

[6] Faraday M. Experimental relations of gold (and other metals) to light. Philosophical Transactions. Royal Society of London. 1857;**147**:145-181

[7] Edwards PP, Thomas JM. Gold in a metallic divided state—from faraday to present-day nanoscience. Angewandte Chemie, International Edition. 2007;**46**(29):5480-5486

[8] Garnett JCM. Colours in metal glasses and in metallic films. Philosophical Transactions of the Royal Society A. 1904;**203**(359-371):385-420

[9] Mie G. Beitrage zur Optik trüber Medien, speziell kolloidaler Metallösungen. Annals of Physics. 1908;**330**(3):377-445

[10] Gans R. Über die Form ultramikroskopischer Goldteilchen. Annals of Physics. 1912; **342**(5):881-900

[11] Gans R. Über die Form ultramikroskopischer Silberteilchen. Annals of Physics. 1915; **352**(10):270-284

[12] Zsigmondy R, Norton JF, Spear EB. The chemistry of colloids. New York: John Wiley & Sons, Inc; 1917

[13] Myroshnychenko V, Rodríguez-Fernández J, Pastoriza-Santos I, Funston AM, Novo C, Mulvaney P, Liz-Marzan LM, Garcia de Abajo FJ. Modelling the optical response of gold nanoparticles. Chemical Society Reviews. 2008; **37**(9):1792-1805

[14] Zhang R, Bursi L, Cox JD, Cui Y, Krauter CM, Alabastri A, Manjavacas A, Calzolari A, Corni S, Molinari E, Carter EA, Garcia de Abajo FJ, Zhang H, Nordlander P. How to identify plasmons from the optical response of nanostructures. ACS Nano. 2017;**11**(7): 7321-7335

[15] Solís DM, Taboada JM, Obelleiro F, Liz-Marzan LM, Garcia de Abajo FJ. Toward ultimate nanoplasmonics modeling. ACS Nano. 2014;**8**(8):7559-7570

[16] Jiang N, Zhuo X, Wang J. Active plasmonics: Principles, structures, and applications. Chemical Reviews. 2018;**118**(6):3054-3099

[17] Liu K, Zhao N, Kumacheva E. Self-assembly of inorganic nanorods. Chemical Society Reviews. 2011;**40**(2):656-671

[18] Grzelczak M, Liz-Marzan LM. Colloidal nanoplasmonics: From building blocks to sensing devices. Langmuir. 2013;**29**(15):4652-4663

[19] Sharma B, Fernanda Cardinal M, Kleinman SL, Greeneltch NG, Frontiera RR, Blaber MG, Schatz GC, Van Duyne RP. High-performance SERS substrates: Advances and challenges. MRS Bulletin. 2013;**38**(8):615-624

[20] Kuttner C, Chanana M, Karg M, Fery A. Macromolecular decoration of nanoparticles for guiding self-assembly in 2D and 3D. In: Billon L, Borisov OV, editors. Macromolecular Self-Assembly. Hoboken, New Jersey: John Wiley & Sons, Inc; 2016:159-192 ISBN: 978-1118887127

[21] Kraus T, Brodoceanu D, Pazos-Perez N, Fery A. Colloidal surface assemblies: Nanotechnology meets bioinspiration. Advanced Functional Materials. 2013;**23**(36):4529-4541

[22] Hiltl S, Schuerings M-P, Balaceanu A, Mayorga V, Liedel C, Pich A, Boeker A. Guided self-assembly of microgels: From particle arrays to anisotropic nanostructures. Soft Matter. 2011;**7**(18):8231-8238

[23] Alvarez-Puebla R, Liz-Marzan LM, Garcia de Abajo FJ. Light concentration at the nanometer scale. Journal of Physical Chemistry Letters. 2010;**1**(16):2428-2434

[24] Halas NJ, Lal S, Chang W-S, Link S, Nordlander P. Plasmons in strongly coupled metallic nanostructures. Chemical Reviews. 2011;**111**(6):3913-3961

[25] Nordlander P, Oubre C, Prodan E, Li K, Stockman MI. Plasmon hybridization in nanoparticle dimers. Nano Letters. 2004;**4**(5):899-903

[26] Willets KA, Van Duyne RP. Localized surface plasmon resonance spectroscopy and sensing. Annual Review of Physical Chemistry. 2007;**58**(1):267-297

[27] Le Ru EC, Etchegoin PG. Quantifying SERS enhancements. MRS Bulletin. 2013;**38**(08):631-640

[28] Schlücker S. Surface-enhanced Raman spectroscopy: Concepts and chemical applications. Angewandte Chemie, International Edition. 2014;**53**(19):4756-4795

[29] Cardinal MF, Vander Ende E, Hackler RA, McAnally MO, Stair PC, Schatz GC, Van Duyne RP. Expanding applications of SERS through versatile nanomaterials engineering. Chemical Society Reviews. 2017;**46**:3886-3903

[30] Barnes WL, Dereux A, Ebbesen TW. Surface plasmon subwavelength optics. Nature. 2003;**424**(6950):824-830

[31] Oates TWH, Wormeester H, Arwin H. Characterization of plasmonic effects in thin films and metamaterials using spectroscopic ellipsometry. Progress in Surface Science. 2011;**86**(11-12):328-376

[32] Guo X. Surface plasmon resonance based biosensor technique: a review. Journal of Biophotonics. 2012;**5**(7):483-501

[33] Yanase Y, Hiragun T, Ishii K, Kawaguchi T, Yanase T, Kawai M, Sakamoto K, Hide M. Surface plasmon resonance for cell-based clinical diagnosis. Sensors. 2014;**14**(3):4948-4959

[34] Roh S, Chung T, Lee B. Overview of the characteristics of micro- and nano-structured surface plasmon resonance sensors. Sensors. 2011;**11**(12):1565-1588

[35] Dhawan A, Canva M, Vo-Dinh T. Narrow groove plasmonic nano-gratings for surface plasmon resonance sensing. Optics Express. 2011;**19**(2):787-813

[36] Szunerits S, Boukherroub R. Sensing using localised surface plasmon resonance sensors. Chemical Communications. 2012;**48**(72):8999

[37] Chung T, Lee S-Y, Song EY, Chun H, Lee B. Plasmonic nanostructures for nano-scale bio-sensing. Sensors. 2011;**11**(12):10907-10929

[38] Miller MM, Lazarides AA. Sensitivity of metal nanoparticle surface plasmon resonance to the dielectric environment. The Journal of Physical Chemistry. B. 2005;**109**(46):21556-21565

[39] Jatschka J, Dathe A, Csáki A, Fritzsche W, Stranik O. Propagating and localized surface plasmon resonance sensing — a critical comparison based on measurements and theory. Sensing and Bio-Sensing Research. 2016;**7**:62-70

[40] Kreibig U. Hundert Jahre Mie-Theorie. Physik in Unserer Zeit. 2008;**39**(6):281

[41] Eustis S, El-Sayed MA. Why gold nanoparticles are more precious than pretty gold: noble metal surface plasmon resonance and its enhancement of the radiative and non-radiative properties of nanocrystals of different shapes. Chemical Society Reviews. 2006;**35**(3):209-217

[42] Atwater HA, Polman A. Plasmonics for improved photovoltaic devices. Nature Materials. 2010;**9**(3):205-213

[43] Yeh C-H, Zhao Z-Q, Shen P-L, Lin Y-C. Optimization of an optical inspection system based on the Taguchi method for quantitative analysis of point-of-care testing. Sensors. 2014;**14**(9):16148-16158

[44] McFarland AD, Van Duyne RP. Single silver nanoparticles as real-time optical sensors with zeptomole sensitivity. Nano Letters. 2003;**3**(8):1057-1062

[45] Rodríguez-Lorenzo L, la Rica de R, Alvarez-Puebla RA, Liz-Marzan LM, Stevens MM. Plasmonic nanosensors with inverse sensitivity by means of enzyme-guided crystal growth. Nature Materials. 2012;**11**(7):604-607

[46] Díez-Buitrago B, Briz N, Liz-Marzan LM, Pavlov V. Biosensing strategies based on enzymatic reactions and nanoparticles. Analyst. 2018;**143**(8):1727-1734

[47] Song JE, Cho EC. Dual-responsive and multi- functional plasmonic hydrogel valves and biomimetic architectures formed with hydrogel and gold nanocolloids. Scientific Reports. 2016;**6**:34622

[48] Laromaine A, Koh L, Murugesan M, Ulijn RV, Stevens MM. Protease-triggered dispersion of nanoparticle assemblies. Journal of the American Chemical Society. 2007;**129**(14): 4156-4157

[49] Pletsch H, Tebbe M, Dulle M, Förster B, Fery A, Förster S, Greiner A, Agarwal S. Reversible gold nanorod alignment in mechano-responsive elastomers. Polymer. 2015;**66**:167-172

[50] Schnepf MJ, Mayer M, Kuttner C, Tebbe M, Wolf D, Dulle M, Altantzis T, Formanek P, Förster S, Bals S, König TAF, Fery A. Nanorattles with tailored electric field enhancement. Nanoscale. 2017;**9**(27):9376-9385

[51] Müller MB, Kuttner C, König TAF, Tsukruk VV, Förster S, Karg M, Fery A. Plasmonic library based on substrate-supported gradiential plasmonic arrays. ACS Nano. 2014;**8**(9): 9410-9421

[52] Prasad J, Zins I, Branscheid R, Becker J, Koch AHR, Fytas G, Kolb U, Sönnichsen C. Plasmonic core–satellite assemblies as highly sensitive refractive index sensors. Journal of Physical Chemistry C. 2015;**119**(10):5577-5582

[53] Ross BM, Waldeisen JR, Wang T, Lee LP. Strategies for nanoplasmonic core-satellite biomolecular sensors: Theory-based design. Applied Physics Letters. 2009;**95**(19):193112

[54] Waldeisen JR, Wang T, Ross BM, Lee LP. Disassembly of a core–satellite nanoassembled substrate for colorimetric biomolecular detection. ACS Nano. 2011;**5**(7):5383-5389

[55] Maurer T, Marae-Djouda J, Cataldi U, Gontier A, Montay G, Madi Y, Panicaud B, Macias D, Adam P-M, Lévêque G, Bürgi T, Caputo R. The beginnings of plasmomechanics: towards plasmonic strain sensors. Frontiers of Materials Science. 2015;**9**(2):170-177

[56] Han X, Liu Y, Yin Y. Colorimetric stress memory sensor based on disassembly of gold nanoparticle chains. Nano Letters. 2014;**14**(5):2466-2470

[57] Liu Y, Han X, He L, Yin Y. Thermoresponsive assembly of charged gold nanoparticles and their reversible tuning of plasmon coupling. Angewandte Chemie, International Edition. 2012;**51**(26):6373-6377

[58] Cataldi U, Caputo R, Kurylyak Y, Klein G, Chekini M, Umeton C, Bürgi T. Growing gold nanoparticles on a flexible substrate to enable simple mechanical control of their plasmonic coupling. Journal of Materials Chemistry C. 2014;**2**:7927-7933

[59] Burel CAS, Alsayed A, Malassis L, Murray CB, Donnio B, Dreyfus R. Plasmonic-based mechanochromic microcapsules as strain sensors. Small. 2017;**13**(39):1701925

[60] Willingham B, Link S. Energy transport in metal nanoparticle chains via sub-radiant plasmon modes. Optics Express. 2011;**19**(7):6450-6461

[61] Hanske C, Tebbe M, Kuttner C, Bieber V, Tsukruk VV, Chanana M, König TAF, Fery A. Strongly coupled plasmonic modes on macroscopic areas via template-assisted colloidal self-assembly. Nano Letters. 2014;**14**:6863-6871

[62] Steiner AM, Mayer M, Seuss M, Nikolov S, Harris KD, Alexeev A, Kuttner C, König TAF, Fery A. Macroscopic strain-induced transition from quasi-infinite gold nanoparticle chains to defined plasmonic oligomers. ACS Nano. 2017;**11**(9):8871-8880

[63] Minati L, Chiappini A, Armellini C, Carpentiero A, Maniglio D, Vaccari A, Zur L, Lukowiak A, Ferrari M, Speranza G. Gold nanoparticles 1D array as mechanochromic strain sensor. Materials Chemistry and Physics. 2017;**192**:94-99

[64] Fleischmann M, Hendra PJ, McQuillan AJ. Raman spectra of pyridine adsorbed at a silver electrode. Chemical Physics Letters. 1974;**26**(2):163-166

[65] McQuillan AJ. The discovery of surface-enhanced Raman scattering. Notes and Records of the Royal Society of London. 2009;**63**(1):105-109

[66] Albrecht MG, Creighton JA. Anomalously intense Raman spectra of pyridine at a silver electrode. Journal of the American Chemical Society. 1977;**99**(15):5215-5217

[67] Jeanmaire DL, Van Duyne RP. Surface Raman spectroelectrochemistry. Journal of Electro analytical Chemistry and Interfacial Electrochemistry. 1977;**84**(1):1-20

[68] Etchegoin PG, Le Ru EC. Basic electromagnetic theory of SERS. In: Schlücker SS, editor. Surface enhanced Raman spectroscopy: Analytical, biophysical and life science applications. Weinheim: Wiley-VCH Verlag GmbH & Co. KGaA; 2011:1-37. ISBN: 978-3527325672

[69] Le Ru EC, Blackie E, Meyer M, Etchegoin PG. Surface enhanced Raman scattering enhancement factors: a comprehensive study. Journal of Physical Chemistry C. 2007; **111**(37):13794-13803

[70] Raman CV. A new radiation. Indian Journal of Physics. 1928;**2**:387-398

[71] Smekal A. Zur Quantentheorie der Dispersion. Naturwissenschaften. 1923;**11**(43):873-875

[72] Schmidt MK, Esteban R, González-Tudela A, Giedke G, Aizpurua J. Quantum mechanical description of Raman scattering from molecules in plasmonic cavities. ACS Nano. 2016;**10**(6):6291-6298

[73] Yamamoto YS, Itoh T. Why and how do the shapes of surface-enhanced Raman scattering spectra change? Recent progress from mechanistic studies. Journal of Raman Spectroscopy. 2016;**47**(1):78-88

[74] Graham D, Goodacre R, Arnolds H, Masson J-F, Schatz G, Baumberg J, Kim D-H, Aizpurua J, Lum W, Silvestri A, de Nijs B, Xu Y, Di Martino G, Natan M, Schlücker SS, Wuytens P, Bruzas I, Kuttner C, Hardy M, Chikkaraddy R, Sabanes NM, Delfino I, Dawson P, Gawinkowski S, Bontempi N, Mahajan S, Reich S, Hourahine B, Bell S, likowska AK, Porter M, Keeler A, Kamp M, Fountain A, Fasolato C, Giorgis F, Otero JC, Matricardi C, Van Duyne R, Lombardi J, Deckert V, Velleman L. Theory of SERS enhancement: general discussion. Faraday Discussions. 2017;**205**:173-211

[75] Etchegoin PG, Le Ru EC. Resolving single molecules in surface-enhanced Raman scattering within the inhomogeneous broadening of Raman peaks. Analytical Chemistry. 2010;**82**(7):2888-2892

[76] Lee PC, Meisel D. Adsorption and surface-enhanced Raman of dyes on silver and gold sols. The Journal of Physical Chemistry. 1982;**86**(17):3391-3395

[77] Höller RPM, Dulle M, Thomä S, Mayer M, Steiner AM, Förster S, Fery A, Kuttner C, Chanana M. Protein-assisted assembly of modular 3D plasmonic raspberry-like core/satellite nanoclusters: Correlation of structure and optical properties. ACS Nano. 2016;**10**(6):5740-5750

[78] Chen S, Meng L-Y, Shan H-Y, Li J-F, Qian L, Williams CT, Yang Z-L, Tian Z-Q. How to light special hot spots in multiparticle-film configurations. ACS Nano. 2016;**10**(1):581-587

[79] Itoh T, Yoshida K, Biju V, Kikkawa Y, Ishikawa M, Ozaki Y. Second enhancement in surface-enhanced resonance Raman scattering revealed by an analysis of anti-Stokes and Stokes Raman spectra. Physical Review B. 2007;**76**(8):085405

[80] Sivapalan ST, Devetter BM, Yang TK, van Dijk T, Schulmerich MV, Carney PS, Bhargava R, Murphy CJ. Off-resonance surface-enhanced Raman spectroscopy from gold nanorod suspensions as a function of aspect ratio: Not what we thought. ACS Nano. 2013;**7**(3):2099-2105

[81] Kuttner C, Mayer M, Dulle M, Moscoso A, López-Romero JM, Förster S, Fery A, Pérez-Juste J, Contreras-Cáceres R. Seeded growth synthesis of gold nanotriangles: Size control, SAXS analysis, and SERS performance. ACS Applied Materials & Interfaces. 2018;**10**(13):11152-11163

[82] Lee S, Anderson LJE, Payne CM, Hafner JH. Structural transition in the surfactant layer that surrounds gold nanorods as observed by analytical surface-enhanced Raman spectroscopy. Langmuir. 2011;**27**(24):14748-14756

[83] Tebbe M, Kuttner C, Männel M, Fery A, Chanana M. Colloidally stable and surfactant-free protein-coated gold nanorods in biological media. ACS Applied Materials & Interfaces. 2015;**7**(10):5984-5991

[84] Tebbe M, Kuttner C, Mayer M, Maennel M, Pazos-Perez N, König TAF, Fery A. Silver-overgrowth-induced changes in intrinsic optical properties of gold nanorods: From non invasive monitoring of growth kinetics to tailoring internal mirror charges. Journal of Physical Chemistry C. 2015;**119**(17):9513-9523

[85] Xie W, Schlücker S. Hot electron-induced reduction of small molecules on photorecycling metal surfaces. Nature Communications. 2015;**6**(1):467

[86] Tian X-D, Liu B-J, Li J-F, Yang Z-L, Ren B, Tian Z-Q. SHINERS and plasmonic properties of Au Core $SiO_2$ shell nanoparticles with optimal core size and shell thickness. Journal of Raman Spectroscopy. 2013;**44**(7):994-998

[87] Li J-F, Huang YF, Ding Y, Yang Z-L, Li S-B, Zhou XS, Fan FR, Zhang W, Zhou ZY, De Yin W, Ren B, Wang ZL, Tian Z-Q. Shell-isolated nanoparticle-enhanced Raman spectroscopy. Nature. 2010;**464**(7287):392-395

[88] Gellner M, Steinigeweg D, Ichilmann S, Salehi M, Schütz M, Kömpe K, Haase M, Schlücker S. 3D Self-assembled plasmonic superstructures of gold nanospheres: Synthesis and characterization at the single-particle level. Small. 2011;**7**(24):3445-3451

[89] Hanske C, Sanz-Ortiz MN, Liz-Marzan LM. Silica-coated plasmonic metal nanoparticles in action. Advanced Materials. 2018;**6**:1707003 DOI: 10.1002/adma.201707003

[90] Mir-Simon B, Reche-Perez I, Guerrini L, Pazos-Perez N, Alvarez-Puebla RA. Universal one-pot and scalable synthesis of SERS encoded nanoparticles. Chemistry of Materials. 2015;**27**(3):950-958

[91] Contreras-Cáceres R, Pastoriza-Santos I, Alvarez-Puebla RA, Pérez-Juste J, Fernández-Barbero A, Liz-Marzan LM. Growing Au/Ag nanoparticles within microgel colloids for improved surface-enhanced Raman scattering detection. Chemistry - A European Journal. 2010;**16**(31):9462-9467

[92] Casado-Rodriguez MA, Sanchez-Molina M, Lucena-Serrano A, Lucena-Serrano C, Rodriguez-Gonzalez B, Algarra M, Diaz A, Valpuesta M, Lopez-Romero JM, Pérez-Juste J, Contreras-Caceres R. Synthesis of vinyl-terminated Au nanoprisms and nanooctahedra mediated by 3-butenoic acid: Direct Au@pNIPAM fabrication with improved SERS capabilities. Nanoscale. 2016;**8**(8):4557-4564

[93] Alvarez-Puebla RA, Contreras-Cáceres R, Pastoriza-Santos I, Pérez-Juste J, Liz-Marzan LM. Au@pNIPAM colloids as molecular traps for surface-enhanced, spectroscopic, ultra-sensitive analysis. Angewandte Chemie, International Edition. 2008;**48**(1):138-143

[94] Sanz-Ortiz MN, Sentosun K, Bals S, Liz-Marzan LM. Templated growth of surface enhanced Raman scattering-active branched gold nanoparticles within radial mesoporous silica shells. ACS Nano. 2015;**9**(10):10489-10497

[95] Lim D-K, Jeon K-S, Hwang J-H, Kim H, Kwon S, Suh YD, Nam J-M. Highly uniform and reproducible surface-enhanced Raman scattering from DNA-tailorable nanoparticles with 1-nm interior gap. Nature Nanotechnology. 2011;**6**(7):452-460

[96] Zhang W, Rahmani M, Niu W, Ravaine S, Hong M, Lu X. Tuning interior nanogaps of double-shelled Au/Ag nanoboxes for surface-enhanced Raman scattering. Scientific Reports. 2015;**5**:8382

[97] Shang Y, Shi J, Liu H, Liu X, Wang Z-G, Ding B. A bumpy gold nanostructure exhibiting DNA-engineered stimuli-responsive SERS signals. Nanoscale. 2018;**10**(20):9455-9459

[98] Liebig F, Sarhan RM, Prietzel C, Thünemann AF, Bargheer M, Koetz J. Undulated gold nanoplatelet superstructures: in situ growth of hemispherical gold nanoparticles onto the surface of gold nanotriangles. Langmuir. 2018;**34**(15):4584-4594

[99] Mayer M, Steiner AM, Röder F, Formanek P, König TAF, Fery A. Aqueous gold overgrowth of silver nanoparticles: merging the plasmonic properties of silver with the functionality of gold. Angewandte Chemie, International Edition. 2017;**56**(50):15866-15870

[100] Fazio B, D'Andrea C, Foti A, Messina E, Irrera A, Donato MG, Villari V, Micali N, Maragò OM, Gucciardi PG. SERS detection of biomolecules at physiological pH via aggregation of gold nanorods mediated by optical forces and plasmonic heating. Scientific Reports. 2016;**6**:26952

[101] Langer J, García I, Liz-Marzan LM. Real-time dynamic SERS detection of galectin using glycan-decorated gold nanoparticles. Faraday Discussions. 2017;**205**:363-375

[102] Taylor RW, Lee T-C, Scherman OA, Esteban R, Aizpurua J, Huang FM, Baumberg JJ, Mahajan S. Precise subnanometer plasmonic junctions for SERS within gold nanoparticle assemblies using cucurbit[n]uril "glue". ACS Nano. 2011;**5**(5):3878-3887

[103] Kim NH, Hwang W, Baek K, Rohman MR, Kim J, Kim HW, Mun J, Lee SY, Yun G, Murray J, Ha JW, Rho J, Moskovits M, Kim K. Smart SERS hot spots: single molecules can be positioned in a plasmonic nanojunction using host–guest chemistry. Journal of the American Chemical Society. 2018;**140**(13):4705-4711

[104] Hidi IJ, Jahn M, Pletz MW, Weber K, Cialla-May D, Popp J. Toward levofloxacin monitoring in human urine samples by employing the LoC-SERS technique. Journal of Physical Chemistry C. 2016;**120**(37):20613-20623

[105] Hidi IJ, Jahn M, Weber K, Cialla-May D, Popp J. Droplet based microfluidics: spectroscopic characterization of levofloxacin and its SERS detection. Physical Chemistry Chemical Physics. 2015;**17**(33):21236-21242

[106] Hidi IJ, Mühlig A, Jahn M, Liebold F, Cialla D, Weber K, Popp J. LOC-SERS: towards point-of-care diagnostic of methotrexate. Analytical Methods. 2014;**6**(12):3943

[107] Hidi IJ, Jahn M, Weber K, Bocklitz T, Pletz MW, Cialla-May D, Popp J. Lab-on-a-chip-surface enhanced Raman scattering combined with the standard addition method:

Toward the quantification of nitroxoline in spiked human urine samples. Analytical Chemistry. 2016;**88**(18):9173-9180

[108] Jahn IJ, Žukovskaja O, Zheng XS, Weber K, Bocklitz TW, Cialla-May D, Popp J. Surface-enhanced Raman spectroscopy and microfluidic platforms: Challenges, solutions and potential applications. Analyst. 2017;**142**(7):1022-1047

[109] Pazos-Perez N, Wagner CS, Romo-Herrera JM, Liz-Marzan LM, Garcia de Abajo FJ, Wittemann A, Fery A, Alvarez-Puebla RA. Organized plasmonic clusters with high coordination number and extraordinary enhancement in surface-enhanced Raman scattering (SERS). Angewandte Chemie, International Edition. 2012;**51**(51):12688-12693

[110] Zheng Y, Thai T, Reineck P, Qiu L, Guo Y, Bach U. DNA-directed self-assembly of core-satellite plasmonic nanostructures: A highly sensitive and reproducible near-IR SERS sensor. Advanced Functional Materials. 2012;**23**(12):1519-1526

[111] Dregely D, Hentschel M, Giessen H. Excitation and tuning of higher-order Fano resonances in plasmonic oligomer clusters. ACS Nano. 2011;**5**(10):8202-8211

[112] Yorulmaz M, Hoggard A, Zhao H, Wen F, Chang W-S, Halas NJ, Nordlander P, Link S. absorption spectroscopy of an individual Fano cluster. Nano Letters. 2016;**16**(10): 6497-6503

[113] Chang W-S, Lassiter JB, Swanglap P, Sobhani H, Khatua S, Nordlander P, Halas NJ, Link S. A plasmonic Fano switch. Nano Letters. 2012;**12**(9):4977-4982

[114] Xiong W, Sikdar D, Yap LW, Premaratne M, Li X, Cheng W. Multilayered core–satellite nanoassemblies with fine-tunable broadband plasmon resonances. Nanoscale. 2015;**7**(8):3445-3452

[115] Liu K-K, Tadepalli S, Tian L, Singamaneni S. Size-dependent surface enhanced Raman scattering activity of plasmonic nanorattles. Chemistry of Materials. 2015;**27**(15):5261-5270

[116] Jaiswal A, Tian L, Tadepalli S, Liu K-K, Fei M, Farrell ME, Pellegrino PM, Singamaneni S. Plasmonic nanorattles with intrinsic electromagnetic hot-spots for surface enhanced Raman scattering. Small. 2014;**267**(10):4287-4292

[117] Brown LV, Sobhani H, Lassiter JB, Nordlander P, Halas NJ. Heterodimers: Plasmonic properties of mismatched nanoparticle pairs. ACS Nano. 2010;**4**(2):819-832

[118] Liebig F, Sarhan RM, Sander M, Koopman W, Schuetz R, Bargheer M, Koetz J. Deposition of gold nanotriangles in large scale close-packed monolayers for X-ray-based temperature calibration and SERS monitoring of plasmon-driven catalytic reactions. ACS Applied Materials & Interfaces. 2017;**9**(23):20247-20253

[119] Radziuk D, Möhwald H. Surpassingly competitive electromagnetic field enhancement at the silica/silver interface for selective intracellular surface enhanced Raman scattering detection. ACS Nano. 2015;**9**(3):2820-2835

[120] Radziuk D, Schuetz R, Masic A, Moehwald H. Chemical imaging of live fibroblasts by SERS effective nanofilm. Physical Chemistry Chemical Physics. 2014;**16**:24621-24634

[121] Pazos-Perez N, Garcia de Abajo FJ, Fery A, Alvarez-Puebla RA. From nano to micro: Synthesis and optical properties of homogeneous spheroidal gold particles and their superlattices. Langmuir. 2012;**28**(24):8909-8914

[122] Tebbe M, Lentz S, Guerrini L, Fery A, Alvarez-Puebla RA, Pazos-Perez N. Fabrication and optical enhancing properties of discrete supercrystals. Nanoscale. 2016;**8**(25):12702-12709

[123] Tebbe M, Maennel M, Fery A, Pazos-Perez N, Alvarez-Puebla RA. Organized solid thin films of gold nanorods with different sizes for surface-enhanced Raman scattering applications. Journal of Physical Chemistry C. 2014;**118**(48):28095-28100

[124] Thai T, Zheng Y, Ng SH, Mudie S, Altissimo M, Bach U. Self-assembly of vertically aligned gold nanorod arrays on patterned substrates. Angewandte Chemie, International Edition. 2012;**51**(35):8732-8735

[125] Alba M, Pazos-Perez N, Vaz B, Formentin P, Tebbe M, Correa-Duarte MA, Granero P, Ferré-Borrull J, Alvarez R, Pallares J, Fery A, de Lera AR, Marsal LF, Alvarez-Puebla RA. Macroscale plasmonic substrates for highly sensitive surface-enhanced Raman scattering. Angewandte Chemie, International Edition. 2013;**52**(25):6459-6463

[126] Hanske C, González-Rubio G, Hamon C, Formentin P, Modin E, Chuvilin A, Guerrero-Martínez A, Marsal LF, Liz-Marzan LM. Large-scale plasmonic pyramidal supercrystals via templated self-assembly of monodisperse gold nanospheres. Journal of Physical Chemistry C. 2017;**121**(20):10899-10906

[127] Slaughter LS, Willingham BA, Chang W-S, Chester MH, Ogden N, Link S. Toward plasmonic polymers. Nano Letters. 2012;**12**(8):3967-3972

[128] Pazos-Perez N, Ni W, Schweikart A, Alvarez-Puebla RA, Fery A, Liz-Marzan LM. Highly uniform SERS substrates formed by wrinkle-confined drying of gold colloids. Chemical Science. 2010;**1**(2):174-178

[129] Mueller M, Tebbe M, Andreeva DV, Karg M, Alvarez-Puebla RA, Pazos-Perez N, Fery A. Large-area organization of pNIPAM-coated nanostars as SERS platforms for polycyclic aromatic hydrocarbons sensing in gas phase. Langmuir. 2012;**28**(24):9168-9173

[130] Tebbe M, Mayer M, Glatz BA, Hanske C, Probst PT, Mueller MB, Karg M, Chanana M, König TAF, Kuttner C, Fery A. Optically anisotropic substrates via wrinkle-assisted convective assembly of gold nanorods on macroscopic areas. Faraday Discussions. 2015;**181**:243-260

[131] Kuttner C. Macromolecular interphases and interfaces in composite materials. Dr. Hut Verlag München. 2014:1-359. ISBN: 978-3-8439-1845-9

# Plasmonics on Optical Fiber Platforms

Hyuntai Kim

Additional information is available at the end of the chapter

http://dx.doi.org/10.5772/intechopen.79146

**Abstract**

Optical fiber platforms are promising for plasmonics research and applications, thanks to their compactness, flexibility, and cost-effectiveness, which are further leveraged by easy accessibility to numerous fiberized sources and devices. In this chapter, the author particularly pays attention to novel surface plasmon polariton (SPP) devices implemented onto optical fiber platforms. First, the author investigates novel circular metallic nanoslit-based optical fiber facets for the generation of axially symmetric SPPs with significantly enhanced noise characteristics. Second, the author investigates novel metallic Fresnel-zone-plate optical fiber facets for super-variable focusing with incident wavelength and for selective focusing with incident polarization. Third, the author investigates novel metal-coated angled optical fiber facets for versatile SPP coupling and its application to wavelength-dependent off-axis beaming, which offer high efficiency, unidirectionality, and perfect compatibility with fiberized light sources. The author expects that these investigations will broaden both fiber optics and plasmonics research fields, and also be useful for various novel applications, including micro-/nanomachining, optical trapping, and biomedical sensing, for example.

**Keywords:** fiber optics, plasmonic hotspot, optical focusing, surface plasmon coupling, plasmonic lens

## 1. Introduction

Optical fiber is a strand of transparent dielectric waveguide, which can guide and transmit optical signals with extremely low loss [1, 2]. It has a lot of merits in being used as a platform for the excitation of surface plasmon polariton (SPP), which is the collective oscillation of electrons at a dielectric-metal interface, and for its applications from the perspectives of compactness, flexibility, and cost-effectiveness [1, 3]. Moreover, such merits are further leveraged

IntechOpen

© 2018 The Author(s). Licensee IntechOpen. This chapter is distributed under the terms of the Creative Commons Attribution License (http://creativecommons.org/licenses/by/3.0), which permits unrestricted use, distribution, and reproduction in any medium, provided the original work is properly cited. cc BY

by the full accessibility to premium grade fiberized devices already combined with light sources, detectors, and various other components of optical functionalities. Once optical fiber platforms are considered for SPP research and applications, one most apparent effect obtained from them is the fact that the use of free-space optics can be eliminated or minimized as illustrated in **Figure 1**.

In fact, a variety of plasmonic nanostructures implemented onto optical fiber platforms have been investigated to date: Most of them were based on metallic nanostructures constructed on the facet, tip, and polished or tapered side of optical fiber [4–7]. Among them, the author focuses on the optical fiber facet structures in that they inherently provide an easy and efficient access to light that the core of the optical fiber guides. Thus, in this chapter, the author investigates and discusses various optical fiber facet structures for an efficient platform for plasmonics research and applications: First, the author investigates trench-assisted circular metallic nanoslits on flat-cleaved optical fiber facets for the generation of axially symmetric SPP hotspots with significantly enhanced noise characteristics [8]. Second, the author investigates fiberized plasmonic Fresnel zone plates for super-variable focusing with incident wavelength and for selective focusing with incident polarization [9]. Third, the author investigates novel metal-coated angled optical fiber facets for a versatile optical-to-SPP mode converter, which provide high efficiency, unidirectionality, and perfect compatibility with fiberized light sources [10]. The detailed investigation and discussion with numerical and experimental demonstrations are given in the following sections. In addition, it is noteworthy that all the numerical simulations were done based on the finite element method (FEM: COMSOL Multiphysics®), and that all the metallic nanostructures were fabricated based on the electron-beam evaporation method and the focused ion beam (FIB) milling method, unless stated otherwise.

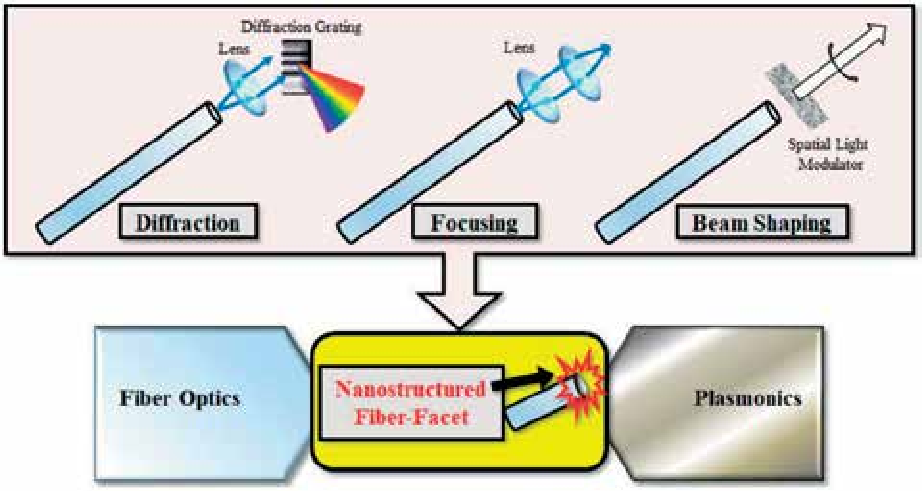

**Figure 1.** Schematic illustrations of various nanostructured optical fiber facets for plasmonic applications.

## 2. Trench-assisted circular metallic nanoslits for low-noise plasmonic hotspot generation

Plasmonic focusing is beneficial to diverse novel applications, such as lithography [11], high harmonic generation [12], and sensing [13], etc. To date, various configurations have been suggested for plasmonic focusing, such as nanoparticles [14], circular nanoslits [15], bowtie structures [16], metal tips [17], etc. Among them, circular metallic nanoslits (CMNSs) engraved on a thin metal film are of great interest because of their capability of generating focused cylindrical SPPs (C-SPPs), that is, plasmonic hotspots, via modest fabrication procedures [8]. While various structures and schemes were extensively investigated to intensify the plasmonic hotspots, the effect of nonconfined diffracted light (NCDL) that accompanies C-SPPs has not been investigated rigorously [18]. In most cases of CMNSs, it is hard to avoid the disturbance of NCDL, so that its consequence increases the background noise, thereby degrading the signal-to-noise ratio (SNR) and sharpness of the C-SPP hotspot.

Recently, exploiting the multipole cancelation mechanism (MPCM) proposed for effective noise-canceling [19], the author has investigated novel trench-assisted circular metal nanoslits (TA-CMNSs) implemented onto optical fiber facets [20], where the use of the optical fiber platform leads to considerably simplified procedures to excite C-SPPs with low noise [21].

In this section, the author discusses the characteristics of TA-CMNS structures implemented on a metal-coated optical fiber facet and shows that they can have substantially improved SNR characteristics based on the MPCM. In particular, these structures are useful for plasmonic devices that particularly require high SNR characteristics, such as bio-sensing, imaging, surface-enhanced Raman spectroscopy, etc.

### 2.1. Fiberized circular metallic nanoslits

Different from one-dimensional nanoslits, a CMNS generates a plasmonic hotspot at its center by two-dimensionally focusing the inward-propagating C-SPP, so that the hotpot can be intensified to a substantial level. Moreover, its efficiency can also be enhanced if radially polarized light is utilized [22]. Indeed, the use of the optical fiber platform for CMNS applications can bring in a considerable advantage, because radially polarized fiber-optic modes (e.g., $TM_{01}$ mode) are readily accessible.

A full-vectorial simulation of a CMNS constructed on top of an optical fiber facet is considered in the following, which was initially proposed and analyzed in [8]. It was assumed that the optical fiber had a step-index core with a diameter of 8 μm and a numerical aperture (NA) of 0.1, and that the metal was made of gold, the material parameters of which, that is, the refractive index and extinction coefficient, were given by $n$ = 0.16918 and $k$ = 3.8816, respectively. The wavelength of incident light was set as $\lambda$ = 700 nm. The width of the slit and the thickness of the metal layer were set to 87.5 nm and 500 nm, respectively. The annular slit was concentric with the fiber core. In particular, the radius of the annular slit was matched with the intensity distribution of the $TM_{01}$ mode of the optical fiber in order to maximize the modefield overlap with the opening of the annular slit.

First of all, a simple CMNS without having any trench structure was numerically analyzed [8]. The C-SPP (graded red/yellow) and NCDL (graded blue) field intensity patterns are illustrated in **Figure 2**. It is shown that while a plasmonic hotspot was formed at the center of the metal surface, the NCDL was also focused at the same position of the hotspot. In particular, the NCDL component at the center was hardly distinguishable with the C-SPP signal, so that the SNR (defined as the ratio of the C-SPP intensity to the NCDL intensity) of the device was inevitably degraded. The peak and mean SNRs within the central main lobe of the C-SPP hotspot were given by 22.74 and 14.70 dB, respectively.

### 2.2. Noise cancelation in trench-assisted CMNSs

As discussed in the preceding section, NCDL tends to be overlapped with the C-SPP hotspot. In particular, the NCDL propagating in the direction parallel to the metal surface can considerably degrade the SNR of the C-SPP hotspot. Thus, to improve the SNR, NCDL should be suppressed. As proposed in [8], a trench-assisted (TA) structure along with the conventional CMNS can be considered in order for minimizing the disturbance incurred by the unwanted NCDL. The proposed TA-CMNS structure and its operation principle are illustrated in **Figure 3**. The main strategy of exploiting the TA structure is such that a considerable portion of the primary NCDL (depicted in blue) from the slit is canceled out by the secondary NCDL (depicted in red) excited by the TA structure alongside the slit. The TA-CMNS was in fact designed in a way that the secondary NCDL destructively interferes with the primary NCDL, as shown in **Figure 3**. It should be further noted that the trench structure having a sharp edge at $P_2$ is

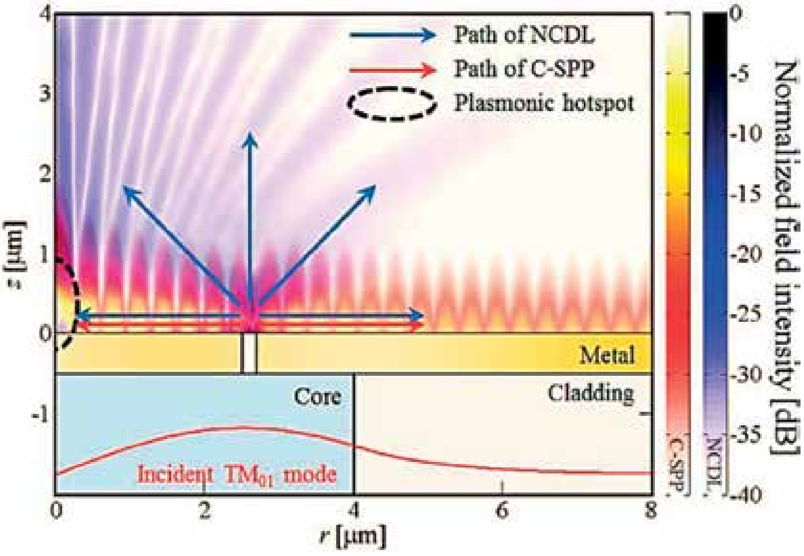

**Figure 2.** Relative field intensity patterns in dB calculated for a simple CMNS with $TM_{01}$ optical fiber mode incidence [8].

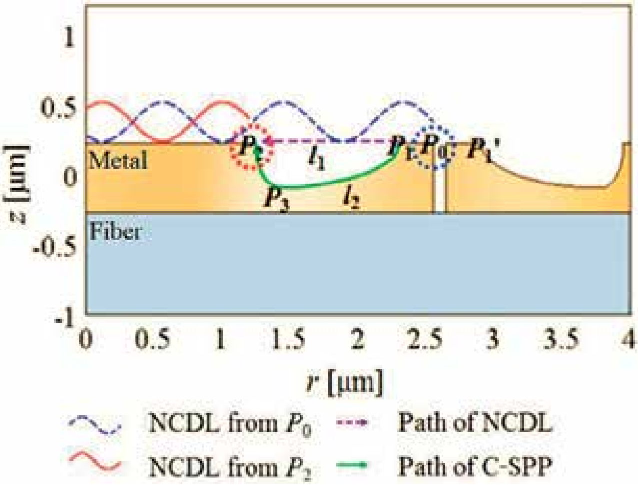

**Figure 3.** Schematic of a TA-CMNS and its operation principle [8].

preferred, because $P_2$ is the location where charges are predominantly induced [14], so that it can be regarded as a "quasi-pole source" that generates secondary NCDL [8].

In order to make the primary NCDL and the secondary NCDL out of phase completely, the phase difference between the primary NCDL (path $l_1$) and the C-SPP (path $l_2$) should be an odd integral multiple of $\lambda$, because the phase of the secondary NCDL is mostly determined by the phase of the C-SPP, such that [8].

$$\mathrm{Re}(k_{C-SPP})l_2 - kl_1 = (2m-1)\pi, \tag{1}$$

where $k$ and $k_{C-SPP}$ denote the wavenumbers of the NCDL and the C-SPP, respectively, Re the real part of the argument, and $m$ an integer number. In addition, the location $P_1$ should also be determined carefully in order that the cavity formed between the two inner edges of the trench $P_1$ and $P_1'$ satisfies the resonance condition maximizing the C-SPP transmission out of it, such that [8].

$$\mathrm{Re}\left(k_{csp}\right)d - \varphi_{Trench} = 2m'\pi, \tag{2}$$

where $d$ dentoes the distance between $P_1$ and $P_1'$, $\varphi_{Trench}$ the phase shift caused by the reflection at the trench wall, and $m'$ an integer number.

Here, two different types of TA-CMNSs are under consideration [8]: One is a rectangular trench (RT) and the other is an asymmetric parabolic trench (APT). While the RT-CMNS has a merit in terms of ease of fabrication, one can improve the SNR performance more significantly with the APT-CMNS because it facilitates increasing the charge concentration at $P_2$ relative to $P_1$ [8, 20]. All the detailed parameters can be optimized via iterative numerical procedures as discussed in [8].

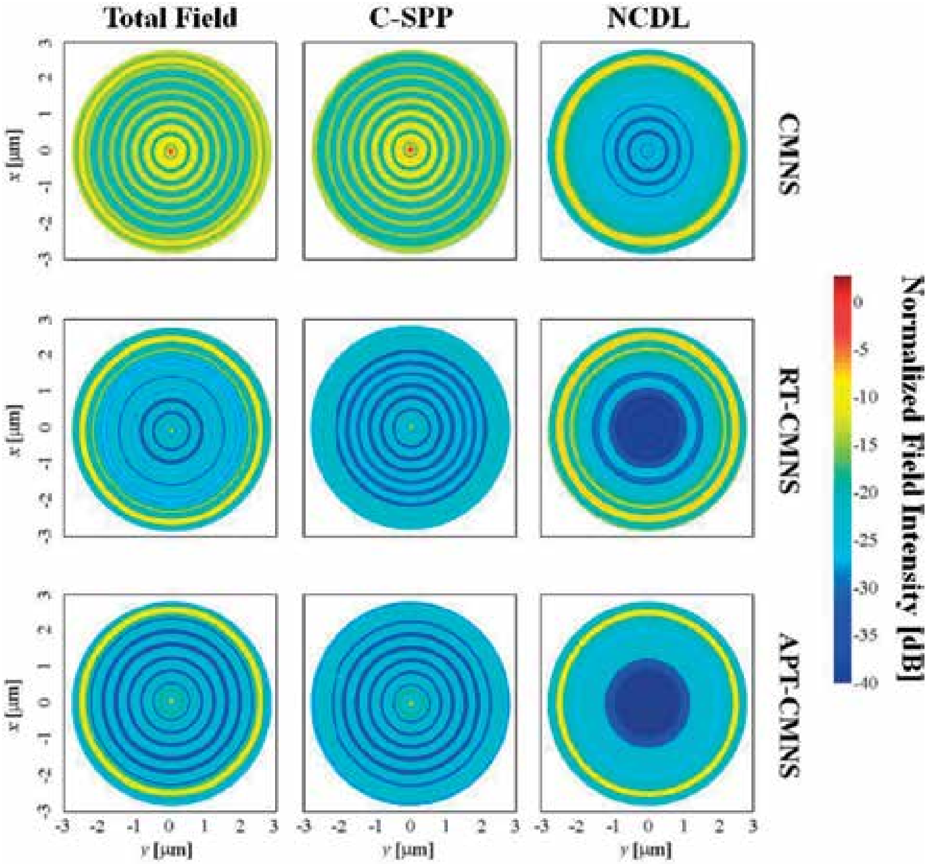

**Figure 4.** Top views of the total, plasmonic, and NCDL field intensity distributions [8].

**Figure 4** illustrates the field intensity distributions of the total field, the C-SPP, and the NCDL for the CMNSs with no trench structure and the optimized RT and APT structures, respectively [8]. From the figure, one can observe that there are clear differences among the simple CMNS and the TA-CMNSs in terms of the NCDL suppression characteristics. With the TA structures, the NCDL noises were substantially canceled out at the center of the device. In particular, the peak and mean SNRs could reach 50.71 and 36.03 dB, respectively, for the APT-CMNS, which were more than one order of magnitude higher than those of the simple CMNS. The peak and mean SNRs of all the three devices are summarized in **Table 1**.

| | CMNS (dB) | RT-CMNS (dB) | APT-CMNS (dB) |
|---|---|---|---|
| Peak SNR | 34.27 | 38.58 | 50.71 |
| Mean SNR | 24.14 | 31.11 | 36.03 |

**Table 1.** Summary of the SNR values estimated within the main lobe of the C-SPP hotspots [8].

## 3. Fiberized plasmonic Fresnel zone plates

Focusing light is invariably an important issue for numerous applications, including micromachining [23], optical tweezing [24, 25], bio-sensing [26, 27], etc. In particular, easy and accurate control of the focal point is one of the greatest factors to be considered for focusing apparatus from the perspective of practical implementation. A traditional method for shifting the focal point is to move either the focusing lens or the target object. Such mechanical adjustments tend to result in relatively large inaccuracies, which are undesirable by any means.

Recently, the author has proposed and demonstrated a simple and compact micro/nanophotonic structure combining fiber-optic and metal-optic technologies in order for super-variable focusing of light [9], where the relatively high chromatic aberration properties of flat-metal-optical lenses were exploited for an alternative measure of varying its focal point in a wide range.

In this section, the author discusses the characteristics of metallic Fresnel zone plate (FZP/MFZP) structures implemented on a metal-coated optical fiber facet, that is, metallic Fresnel-zone-plated optical fiber facets (MFZP-OFFs), and shows that they can have novel super-variable focusing functionality [9]. Moreover, the author discusses another SPP-based MFZP-OFF scheme that can selectively focus light, depending on its polarization state [9, 28]. In particular, this novel SPP-based lens can be useful for some specific applications that inevitably require centrosymmetric optical force, such as optical trapping [29] and micro-machining [30].

### 3.1. MFZP-OFFs for super-variable focusing of light

The focal position of a conventional lens, such as spherical lens, varies mainly by the chromatic dispersion of the lens material. For example, the focal length of a bi-convex lens is given by [31].

$$f = \frac{R_1 R_2}{R_2 - R_1} \frac{1}{n_{lens} - 1}, \tag{3}$$

where $f$ denotes the focal length, $R_1$ and $R_2$ the radii of the curvatures of both lens facets, and $n_{lens}$ the optical refractive index of the lens material. In general, the chromatic dispersion of $n_{lens}$ is given by a value in the order of $\sim 10^{-5}$/nm for fused silica [32], so that it results in a very limited focal length change with respect to incident wavelength. In contrast, a flat-metal-optical lens based on an FZP exhibits a drastically different aspect because the focusing of light is obtained from the constructive interference of light at a location where all the possible optical paths from the annular openings of the FZP become in phase, so that detuning of the condition is caused not by the material dispersion but by the direct change of the wavelength of incident light [31, 33].

In general, the product of the focal length and the incident wavelength is approximately invariant regardless of the given FZP geometry [9, 33], so that the general expression for the focal length $f_\lambda$ as a function of the incident wavelength $\lambda$ can be given by

$$f_\lambda \approx \frac{\lambda_0 f_0}{\lambda}, \tag{4}$$

where $\lambda_0$ and $f_0$ denote the reference wavelength and focal length, respectively. It shows that an FZP has a focal length that is inversely proportional to the incident optical wavelength. In addition, one can also notice that the beam radius at the focal point of an FZP, that is, $r_r^2$ tends to remain nearly consistent regardless of the incident wavelength, considering the optical diffraction principle [9, 31] such as

$$r_{e^2} \propto \frac{1}{kNA} \approx \frac{\lambda f_\lambda}{2\pi R}, \tag{5}$$

where $k$, $NA$, and $R$ denote the wavenumber of the incident light, the effective numerical aperture of the lens, and the radius of the lens, respectively. Since the product of the wavelength and the focal length remains invariant from Eq. (4), Eq. (5) indicates that the beam radius at the focal point of an FZP is approximately preserved regardless of the wavelength of the incident light.

On the other hand, MFZP-OFFs can readily be fabricated using electron-beam and evaporation and FIB milling techniques [34, 35]. **Figure 5** illustrates an MFZP-OFF fabricated in house based on the techniques and its focusing characteristics. Silver was initially deposited via an electron-beam evaporation system to form a 100-nm layer on the flat-cleaved multimode optical fiber facet. The multimode optical fiber had a 50-μm diameter step-index core with 0.22 NA. The silver layer was processed by FIB milling to have the FZP structure consisting of 6 rings [9]. It should be noted that this FZP was designed to produce a focal spot at 20 μm from the fiber facet when the wavelength of incident light was tuned at 550 nm.

To characterize the MFZP-OFF, visible light of three different colors (RGB) was launched into the other end of the optical fiber. The center wavelengths of them were given by 612 (R), 527 (G), 473 (B) nm, respectively. The focal length of the MFZP-OFF was measured by an optical

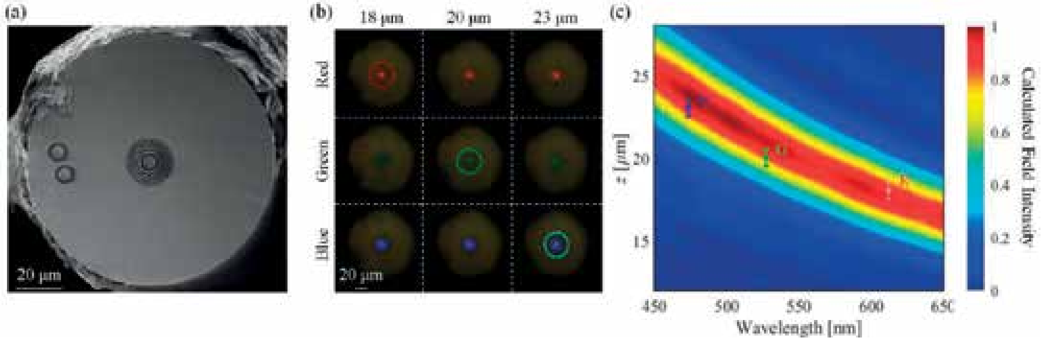

**Figure 5.** Experimental results of the fabricated MFZP-OFF [9]: (a) Scanning electron microscope (SEM) image of the fabricated MFZP-OFF. (b) Optical microscope images of the transmitted light at various incidence and distance conditions. (c) Numerical results on the normalized field intensity distributions along the z-axis with respect to the wavelength of incident light.

microscope system, and the measured focal points for RGB colors were at $z = 18$ (R), 20 (G), and 23 (B) μm, respectively. Numerical simulations were also performed to verify the experimental results, which are shown in **Figure 5(c)**. The numerically calculated focal points for RGB colors were given by $z = 17.6$ (R), 21.0 (G), and 23.8 (B) μm, respectively, which were actually in good agreement with the experimental results. In fact, the focal length of the MFZP-OFF varied from 28.6 to 14.9 μm for the wavelength range from 400 to 700 nm, which means the relative focal-length change per unit wavelength was as large as 45.5. It is highlighted that this relative change rate is over 20 times higher than the rate that can be obtained with a conventional silica-based lens [9, 31], as the latter can only be detuned from 20.2 to 19.6 μm for the same spectral detuning range. In addition, the mean beam radius averaged out over the whole visible range was calculated to be 768 nm with a standard deviation of 14.2 nm, which indicates that the relative change was only 1.84% over the whole visible range as expected from Eq. (5). Nevertheless, it should be noted that even though the super-variable focusing capability along with a nearly constant beam spot size at the focal point over the very wide spectral range was verified both numerically and experimentally, the depth of focus of the focal spot along the optical axis should still be inversely proportional to the wavelength of incident light [28, 33].

### 3.2. All-sub-wavelength-scaled MFZP

If all the openings of the standard MFZP discussed in the preceding section are reduced down into the sub-wavelength scale [9, 28], its transmission starts to be dominated by the SPP-mediated radiation, that is, the extraordinary optical transmission (EOT) via SPPs. Subsequently, such an MFZP (hereinafter SPP-MFZP) will bring in polarization-dependent characteristics because SPPs are normally excited in the direction perpendicular to the slit walls, so that only the radially polarized mode can lead to a hotspot. Thus, this SPP-MFZP can be utilized for focusing of radially polarized light, which has considerable advantages over the linearly polarized or un-polarized counterparts in various applications, thanks to its axially symmetric optical characteristics [30, 36]. The author has investigated the polarization-selective characteristics of the sub-wavelength-scale annular slit in [9], verifying that the transmission of azimuthally polarized (i.e., parallel-polarized) light was suppressed drastically if the relative slit width with respect to wavelength, that is, $s/\lambda$, was given by $< \sim 0.3$, while the transmission of radially polarized (i.e., perpendicular-polarized) light remained nearly unchanged.

Thus, building upon the principle, an SPP-MFZP was fabricated and characterized experimentally. A 195-nm-thickness gold layer was deposited on a fused-silica substrate, using the electron-beam evaporation method. A standard 6-ring FZP was designed for the reference wavelength of 660 nm and the reference focal length of 20-μm, and all the rings was filled with sub-wavelength-slits of a 120-nm width with a 50% duty ratio. **Figure 6(a)** illustrates the SEM image of the fabricated SPP-MFZP. To characterize its polarization-dependent functionality, linearly polarized light was illuminated on it. Rotating the axis of the incident polarization, its transmission through the SPP-MFZP was measured by the optical microscope. Considering that the linearly polarized light can be decomposed into a radial component and an azimuthal component with a different ratio depending on the location on the SPP-MFZP plane, the transmitted light pattern should be like a “figure of eight.” **Figure 6(b)** illustrates the optical

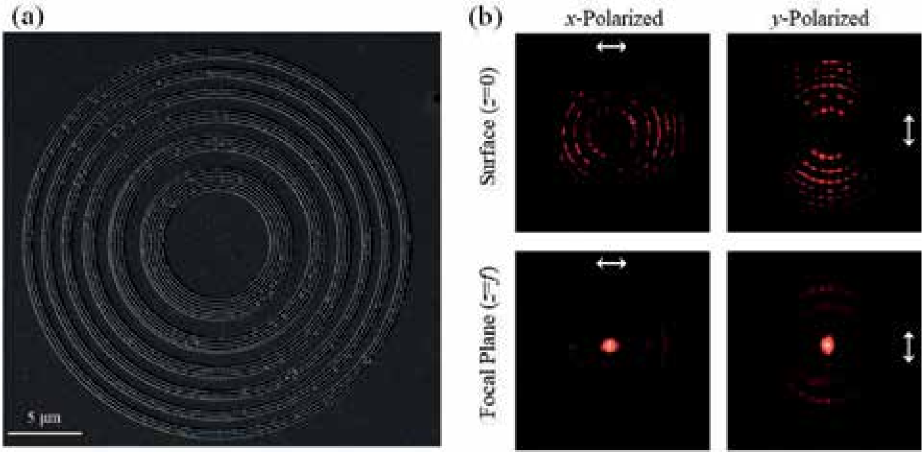

**Figure 6.** Experimental results of the fabricated SPP-MFZP [9]: (a) SEM image of the SPP-MFZP fabricated on a gold-coated fused-silica substrate. (b) Dark-field optical microscope images of the transmitted light at different image planes and for different incident polarization states.

microscope images of the transmitted light patterns at the top surface of the SPP-MFZP and at the focal plane for two different linear polarization states. The results suggest that the SPP-MFZP functioned as expected, such that only the radial-polarization mode could efficiently pass through the SPP-MFZP, being selectively focused down at the focal plane. It is noteworthy that the SPP-MFZP can readily be implemented onto a fiber facet in a way similar to the MFZP-OFF discussed in the preceding section.

## 4. Metal-coated angled optical fiber facets

Efficient excitation of SPPs is invariably important because SPPs cannot be excited naturally, which means it requires some specific apparatus leading to the special boundary condition at the dielectric-metal interface [37]. The prism coupling technique based on the Kretschmann configuration is one of the most frequently used methods for this purpose [37]. This technique utilizes an oblique incidence toward a dielectric-metal interface, in which the real part of the dielectric material should be higher than that of the metal. In optical fiber platforms, the technique was not fully exploited, such that SPPs were normally excited via using tip structures, nanoslits or apertures, the polished or tapered side of the optical fiber, etc. [4–7].

Recently, the author has introduced a novel SPP coupling scheme in the optical fiber platform that is based on a metal-coated angled fiber facet (MCAFF) different from the aforementioned conventional schemes [10]. In fact, this scheme exploited the so-called Kretschmann configuration on the optical fiber platform, because the angle fiber facet can play exactly the same role as a prism to the optical mode guided in the core of the fiber [10, 37].

In this section, the author discusses the MCAFF configuration with corresponding numerical and experimental results, and also shows how it can be utilized for further applications, including a corrugation-assisted MCAFF for wavelength-dependent off-axis directional beaming. Unlike the conventional SPP-coupling techniques having trade-offs and limitations from various perspectives, such as efficiency, compactness, unidirectional coupling, alignment, etc., the MCAFF configuration can readily resolve the aforementioned issues, so that it can be an efficient alternative to the existing techniques.

### 4.1. SPP coupling scheme based on a metal-coated angled fiber facet

In general, optical-fiber-based SPP generation has mostly been done based on nanoslit structures [4, 6, 9, 38]. However, its coupling efficiency tends to be considerably low by the following factors: the generation of NCDL, the excitation of multidirectional SPPs, and the reflection of the incident light by aperture [10] as illustrated in **Figure 7(a)**. In fact, such issues can be overcome if the Kretschmann configuration [37] is directly exploited on an angled optical fiber facet as illustrated in **Figure 7(b)**.

In fact, the Kretschmann's prism coupling configuration should still be valid for an angled fiber facet, because it can be regarded as a prism to the optical mode guided in the core of the fiber [10, 37]. Subsequently, an MCAFF can excite SPPs along the dielectric-metal interface as long as the following phase-matching condition is satisfied [10]:

$$k_{SP0} = n_{eff} k_0 sin\theta = k_0\sqrt{\frac{\varepsilon_d\varepsilon_m}{\varepsilon_d + \varepsilon_m}}, \tag{6}$$

where $k_0$ denotes the wavenumber of the optical radiation in free space, $k_{SP0}$ the wavenumber of the SPP, $\varepsilon_d$ and $\varepsilon_m$ the electric permittivities of the dielectric and the metal, respectively, $n_{eff}$ the effective refractive index of the optical fiber mode, and $\theta$ the incidence angle of the optical

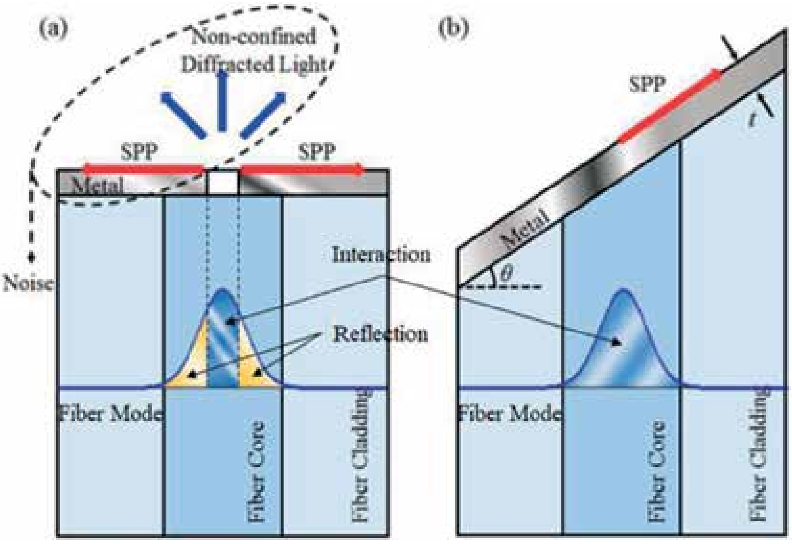

**Figure 7.** Fiber-SPP-mode coupling schemes [10]: (a) Nanoslit coupling scheme and (b) MCAFF scheme.

fiber mode relative to the fiber-metal interface or simply the angle of the optical fiber facet relative to the optical fiber axis as illustrated in **Figure 7(b)**.

In this scheme, two kinds of SPPs can be generated. One is the propagating SPP (P-SPP) mode that is the eigen mode of the given interface geometry, and the other is the localized SPP (L-SPP) mode directly induced by the incident wave [2, 10, 26, 37]. In order to verify the functional characteristics of the MCAPP, one can first perform numerical calculations of an example structure, assuming that the optical fiber is a step-index fiber with a core diameter of 3 μm and an NA of 0.1, and that the metal coating material is silver.

**Figure 8(a)** illustrates the field pattern of the MCAFF when the incident light was launched from the other end of the optical fiber, in which the metal thickness, the fiber-facet angle, and the incident wavelength were given by 20 nm, 45°, and 600 nm, respectively [38]. It should be noted that the incident optical fiber mode was assumed to be an $x$-polarized $LP_{01}$ mode. From the figure, one can see that an SPP mode was dominantly generated at the top surface of the metal layer, and a fraction of the incident light was immediately reflected by the dielectric-metal interface, and some of the SPP mode was decoupled back into the dielectric region after some propagation length. In fact, the decoupled component can also give rise to loss to the P-SPP, which can be observed at the right-top-corner indicated by a round-rectangle in a dashed-line. This is different from the direct reflection of the optical mode around the core region, and it can be avoided if the metal thickness increases considerably [10]. With the metal thickness of 20 nm, the spectral SPP coupling efficiency in terms of the fiber-facet angle is illustrated in **Figure 8(b)**. The calculated efficiency reached close to 70% in the phase-matched condition. In addition, the given MCAFF structure showed a sufficiently broad spectral bandwidth covering the whole visible range with the given metal thickness of 20 nm. In fact, deciding the thickness of the metal layer is really dependent on the type of the application of the MCAFF. If the excitation of SPP is important only nearby the core region, one may choose a thin metal layer (~ 20 nm) to intensify the direct coupling. In contrast, if it requires a relatively long propagation length, one may go for a considerably thick metal layer (> 30 nm) in order to

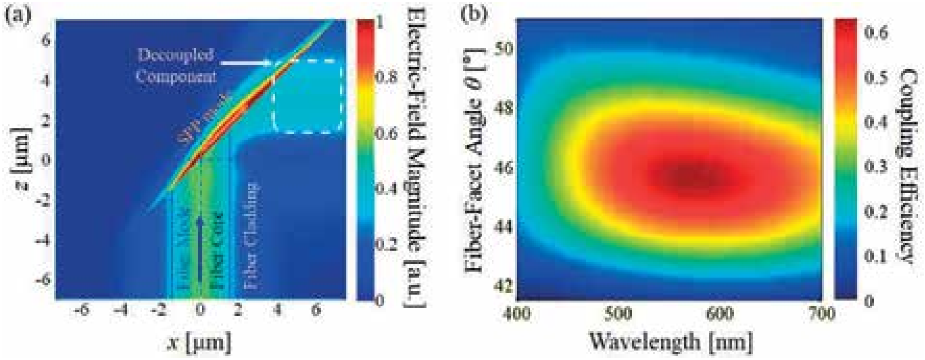

**Figure 8.** SPP coupling scheme based on the MCAFF [10]: (a) Field pattern of a specific MCAFF configuration. (b) Spectrum of the SPP coupling efficiency in terms of the fiber-facet angle and incident wavelength.

suppress the decoupling of the SPP. In the latter case one may also alternatively consider choosing a thin layer nearby the core region and gradually increasing the thickness of the metal layer outside the core region.

**Figure 9(a)** illustrates an experimental setup to characterize the MCAFF [39]. An angle-cleaved optical fiber end supported in the substrate was metal (silver)-coated based on the electron-beam evaporation method. The optical fiber had a step-index core of a 5.3 μm diameter and of an NA of 0.14. The facet angle and the wavelength of incident light were given by $\theta = 46^\circ$ and 650 nm, respectively. Two samples with different metal thicknesses of 20 and 30 nm were fabricated. In order to decouple the SPP excited on the MCAFF surface out to free space, the surface was roughly ground to have some randomized texture. In addition, the incident polarization state was controlled by the rotation of the input polarizer, and the transmitted light was monitored and imaged by an optical microscope with a complementary metal-oxide-semiconductor (CMOS) camera. It should be noted that the SPP mode can only be excited by a transverse-magnetic (TM) mode. Thus, one can expect that the out-coupled light could only be observed if a TM optical mode were incident onto the MCAFF. In contrast, a transverse-electric (TE) mode would undergo substantial attenuation, so that it would be hard to observe its transmission. The facet images detected by the CMOS camera are shown in **Figure 9(b)** for the two MCAFF samples in the TM and TE incidence conditions. One can clearly see that significantly brighter transmission was detected when TM-polarized light was launched than when TE-polarized light was launched. Moreover, significantly brighter transmission was detected from the 30-nm-thickness MCAFF than the 20-nm-thickness MCAFF, which was due to the fact that the thinner (~ 20 nm) metal layer caused relatively larger decoupling loss than the thicker (~ 30 nm) metal layer, because the SPP was allowed to propagate a relatively long distance in this case, as already discussed.

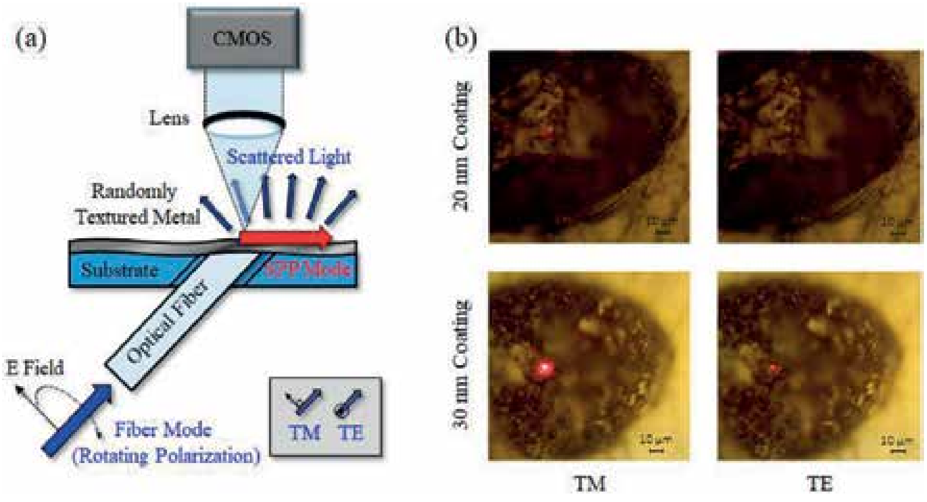

**Figure 9.** Experimental results of fabricated MCAFFs [39]: (a) Experimental arrangement for characterizing the fabricated MCAFFs. (b) Decoupled light from the MCAFFSs for incident light at 650 nm with different polarization modes.

### 4.2. Application of the MCAFF scheme: corrugation-assisted MCAFF for wavelength-dependent off-axis beaming

In this section, the author discusses a corrugation-assisted MCAFF (CA-MCAFF) structure, which has wavelength-dependent off-axis directional beaming (WODB) functionality [40–42]. The schematic of the CA-MCAFF is shown in **Figure 10**. It is noteworthy that the incident optical fiber mode can be coupled into both P-SPP and L-SPP at the top surface of the metal layer, which can be decoupled into free-space mode through the periodic corrugation structure depending on the phase-matching condition given by [10, 42]:

$$k_{SPP} \pm m k_c + k_0 \sin\phi = 0, \tag{7}$$

where $k_{SPP}$ denotes the wavenumber of the SPP (either P-SPP or L-SPP), $k_0$ the wavenumber of the optical radiation in free space, $k_c$ the reciprocal lattice vector (i.e., $k_c = 2\pi/\Lambda$) of the corrugation having a period of $\Lambda$ and $\phi$ the azimuthal angle of the out-coupled optical radiation in free space relative to the surface-normal vector of the MCAFF as shown in **Figure 10(a)**. If the period of the corrugation $\Lambda$ is fixed, the angle of the out-coupling $\phi$ will subsequently vary with wavelength [10, 42]. It is noteworthy that the L-SPP is excited owing to the localized plasmonic oscillation in the trough segment of the corrugation whereas the P-SPP is excited owing to the nonlocalized, normal SPP oscillation spread out along the whole metal-air interface of the periodical corrugation. Therefore, in the given condition, one can expect that the L-SPP will become the dominant mode rather than the P-SPP, because the latter will undergo significantly higher attenuation by ohmic loss in the metal than the former [37].

It is noteworthy that the CA-MCAFF requires high coupling efficiency nearby the core region, so that a thin metal layer of 20 nm should be a relevant choice. In addition, the initial fiber-facet angle $\theta$ and the duty ratio of the unit corrugation should also be determined carefully,

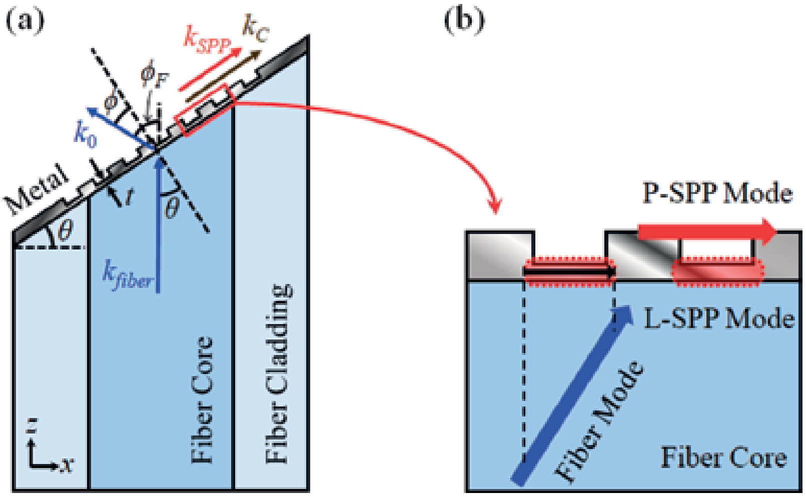

**Figure 10.** CA-MCAFF and its corresponding SPP modes [10]: (a) Schematic of the CA-MCAFF. (b) Two different types of SPP modes excited at the periodically corrugated metal surface.

depending on what characteristic of the CA-MCAFF is most desired, for example, the overall out-coupling efficiency, spectral bandwidth, etc. [10]. **Figure 11** illustrates the calculated far-field magnitude distribution through the CA-MCAFF, in which the thickness of the metal layer and the fiber-facet angle were set to 20 nm and 50°, respectively, and the period, modulation depth, and duty ratio of the corrugation were set to 380 nm, 40 nm, and 47%, respectively. These parameters were determined after going through iterative calculations from the perspective of maximizing the overall out-coupling efficiency [10]. In the figure, there are a few virtual lines drawn: The solid white line and dashed black line denote the theoretically calculated output beaming angles when phase-matched with the L-SPP and the P-SPP, respectively. As already explained that the L-SPP mode should be the dominant SPP mode in the given structure, one can see that the actual beaming angle was better fitted with the beaming angle trace by the L-SPP mode than with the trace by the P-SPP mode. In particular, higher out-coupling took places where both traces are matched or close to each other, which peaked at ~ 500 nm as depicted in **Figure 11**. This means that the wavenumber of L-SPP and P-SPP was close to each other in the given condition, which eventually enhanced the aggregate coupling efficiency of the SPPs. In addition, it is noteworthy that the beaming angle exhibited good linearity with wavelength, which in fact justifies that the CA-MCAFF can efficiently be used for WODB. On the other hand, the dash-dotted blue and red lines represent the case when the incident fiber optical mode was phase matched with unwanted backward-propagating SPP modes, such as the SPP modes excited at the metal-fiber interface and the air-metal interface, respectively, for $m = -2$ in Eq. (7). The second-order coupling should be possible because the periodic corrugation was formed in an asymmetrically layered structure in the transverse (or vertical) direction [10]. When the main beaming line passed across these two traces, the out-coupling efficiency dropped a bit, because the phase-matching conditions for the L-SPP and for the backward-propagating SPPs were satisfied at the same time. However, this unwanted consequence had already been minimized while optimizing the duty ratio of the corrugation [10].

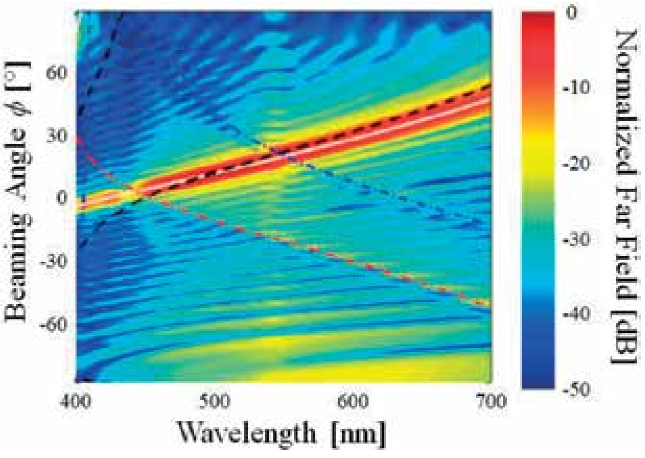

**Figure 11.** Numerical results of the far-field magnitude distribution and the analytical results of the primary beaming angle of the optical radiation from the CA-MCAFF with respect to the wavelength of incident light and the azimuthal angle $\phi$ [10].

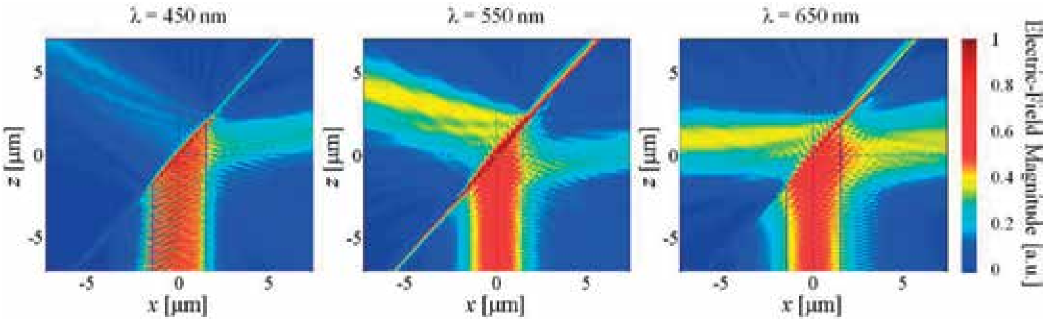

**Figure 12.** Field magnitude patterns of a specific CA-MCAFF for RGB incidence conditions [10].

**Figure 12** illustrates the resultant field pattern nearby the core region for different incident wavelengths, which justifies the spatial beaming characteristics of the out-coupled optical radiation from the CA-MCAFF. It is clearly shown that the L-SPP mode was dominantly generated above the core region, and a fraction of it propagates along the air-metal interface and another fraction was out-coupled into free space. They show different beaming angles with incident wavelength, confirming the WODB characteristics. In particular, for 550 nm, one can see that the incident light was also coupled to the counter-directionally propagating SPP, which has also been denoted by the dash-dotted blue line in **Figure 11**. The overall out-coupling efficiency for WODB was estimated to be as high as 30% [10] for the given CA-MCAFF.

## 5. Conclusion

Throughout this chapter, the author has discussed novel plasmonic structures implemented on various optical fiber platforms. These fiber-optic-based plasmonic devices demonstrated novel features of SPP-based functionality in a compact, flexible, and cost-effective form leveraged by optical fiber technology.

First, fiberized TA-CMNSs that can produce a low-noise C-SPP hotspot were introduced and discussed. The trench structures were designed based on the MPCM in order to suppress the co-existing NCDL at the hotspot location. Two types of novel TA-CMNSs were designed and investigated: an RT-CMNS was proposed for its simple fabrication procedure, and an APT-CMNS was proposed for maximally exploiting the multipole cancelation effect. Numerical analysis of them verified that the auxiliary trench structure can substantially improve the SNR performance of the CMNS, being capable of producing a low-noise plasmonic hotspot at the center of the whole structure. These schemes will be useful for designing various plasmonic devices that particularly require high SNR characteristics, such as bio-sensing, imaging, surface-enhanced Raman spectroscopy, etc.

Second, fiberized and fiberizable metal-optical lenses based on the FZP were introduced and discussed, which included an MFZP-OFF and an SPP-MFZP. The former exhibited super-variable focusing with respect to incident wavelength, and the latter had substantially high radial-polarization selectivity owing to the EOT effect from the auxiliary subwavelength annular slits inserted in the openings of the FZP structure. Numerical and experimental analyses verified their novel functionality. These schemes will be useful for various applications that require accurate, flexible, and centrosymmetric optical focusing with a broad focal-length tuning range, such as in micro/nanomachining and optical trapping. In addition, these schemes can also be exploited for mono-chromatic-multi-focal or multi-chromatic-mono-focal lenses [43, 44].

Third, a fiberized SPP coupling scheme and its application to a CA-MCAFF were introduced and discussed. The former realized the Kretschmann SPP coupling scheme in the optical fiber platform, and the latter exhibited novel WODB functionality. Numerical and experimental analyses verified that the MCAFF-based SPP coupling scheme worked efficiently and has great potential for being used as an excellent, alternative SPP generation method, which provides high efficiency, unidirectionality, and full compatibility with fiber-based optical sources. The CA-MCAFF scheme will also be very useful for various plasmonic and optical applications where WODB functionality is required, such as a nanophotonic wavelength-division-multiplexer, a compact spectrometer, etc.

Optical fibers are an excellent platform for plasmonics studies and applications. The novel plasmonic nanostructures realized on various optical fiber platforms successfully demonstrated fascinating characteristics of plasmonics in a compact, flexible, and cost-effective format. The author believes that the investigations and discussions given in this chapter will broaden the fiber-optic and plasmonics research fields, as well as expecting further advances and convergence of them to come.

## Acknowledgements

The author acknowledges the useful discussion with Prof. Y. Jeong.

## Author details

Hyuntai Kim

Address all correspondence to: H.Kim@soton.ac.uk

Optoelectronics Research Centre, University of Southampton, Southampton, United Kingdom

## References

[1] Ghatak A, Thyagarajan K. An Introduction to Fiber Optics. Cambridge: Cambridge University Press; 1998

[2] Agrawal G. Nonlinear fiber optics. San Diego, California: Academic Press; 1995

[3] Alwayn V. Optical Network Design and Implementation. Indianapolis: Cisco Press; 2004

[4] Guan C, Ding M, Shi J, Wang P, Hua P, Yuan L, Brambilla G. Compact all-fiber plasmonic Airy-like beam generator. Optics Letters. 2014;**39**(5):1113-1116

[5] Lin Y, Guo J, Lindquist RG. Demonstration of an ultra-wideband optical fiber inline polarizer with metal nano-grid on the fiber tip. Optics Express. 2009;**17**(20):17849-17854

[6] Kostovski G, Stoddart PR, Mitchell A. The optical fiber tip: An inherently light-coupled microscopic platform for micro-and nanotechnologies. Advanced Materials. 2014;**26**(23): 3798-3820

[7] Mullen KI, Carron KT. Surface-enhanced Raman spectroscopy with abrasively modified fiber optic probes. Analytical Chemistry. 1991;**63**(19):2196-2199

[8] Kim H, Lee S-Y, Koo S, Kim J, Park K, Lee D, Vazquez-Zuniga LA, Park N, Lee B, Jeong Y. Theoretical study on the generation of a low-noise plasmonic hotspot by means of a trench-assisted circular nano-slit. Optics Express. 2014;**22**(22):26844-26853

[9] Kim H, Kim J, An H, Lee Y, Lee G-y, Na J, Park K, Lee S, Lee S-Y, Lee B, Jeong Y. Metallic Fresnel zone plate implemented on an optical fiber facet for super-variable focusing of light. Optics Express. 2017;**25**(24):30290-30303

[10] Kim H, An H, Kim J, Lee S, Park K, Lee S, Hong S, Vazquez-Zuniga LA, Lee S-Y, Lee B, Jeong Y. Corrugation-assisted metal-coated angled fiber facet for wavelength-dependent off-axis directional beaming. Optics Express. 2017;**25**(7):8366-8385

[11] Srituravanich W, Pan L, Wang Y, Sun C, Bogy DB, Zhang X. Flying plasmonic lens in the near field for high-speed nanolithography. Nature Nanotechnology. 2008;**3**(12):733-737

[12] Kim S, Jin J, Kim Y-J, Park I-Y, Kim Y, Kim S-W. High-harmonic generation by resonant plasmon field enhancement. Nature. 2008;**453**(7196):757-760

[13] Moh K, Yuan X-C, Bu J, Zhu S, Gao BZ. Radial polarization induced surface plasmon virtual probe for two-photon fluorescence microscopy. Optics Letters. 2009; **34**(7):971-973

[14] Radko IP, Bozhevolnyi SI, Evlyukhin AB, Boltasseva A. Surface plasmon polariton beam focusing with parabolic nanoparticle chains. Optics Express. 2007;**15**(11):6576-6582

[15] Lerman GM, Yanai A, Levy U. Demonstration of nanofocusing by the use of plasmonic lens illuminated with radially polarized light. Nano Letters. 2009;**9**(5):2139-2143

[16] Kinkhabwala A, Yu Z, Fan S, Avlasevich Y, Müllen K, Moerner W. Large single-molecule fluorescence enhancements produced by a bowtie nanoantenna. Nature Photonics. 2009; **3**(11):654-657

[17] Ropers C, Neacsu C, Elsaesser T, Albrecht M, Raschke M, Lienau C. Grating-coupling of surface plasmons onto metallic tips: A nanoconfined light source. Nano Letters. 2007;**7**(9): 2784-2788

[18] Kihm H, Kang J, Kyoung J, Lee K, Seo M, Ahn K. Separation of surface plasmon polariton from nonconfined cylindrical wave launched from single slits. Applied Physics Letters. 2009;**94**(14):141102

[19] Johnson SG, Fan S, Mekis A, Joannopoulos J. Multipole-cancellation mechanism for high-Q cavities in the absence of a complete photonic band gap. Applied Physics Letters. 2001; **78**(22):3388-3390

[20] Kim H, Koo S, Park N, Kihm H-w, Kim D. Application of multi-pole cancellation theory for the enhancement of signal to noise ratio of nano-slit-excited surface plasmon waves. In: SPP5; 2011

[21] Kim H, Kwon Y, Vazquez-Zuniga LA, Jeong Y. Rigorous analysis on a U-shaped index fiber for generating cylindrical vector beams in an all-fiber format. In: Opto-Electronics and Communications Conference (OECC). IEEE; 2012

[22] Chen W, Abeysinghe DC, Nelson RL, Zhan Q. Plasmonic lens made of multiple concentric metallic rings under radially polarized illumination. Nano Letters. 2009;**9**(12):4320-4325

[23] Venkatakrishnan K, Tan B. Interconnect microvia drilling with a radially polarized laser beam. Journal of Micromechanics and Microengineering. 2006;**16**(12):2603

[24] Ribeiro RSR, Dahal P, Guerreiro A, Jorge PA, Viegas J. Fabrication of Fresnel plates on optical fibres by FIB milling for optical trapping, manipulation and detection of single cells. Scientific Reports. 2017;**7**(1):4485

[25] Neuman KC, Block SM. Optical trapping. The Review of Scientific Instruments. 2004; **75**(9):2787-2809

[26] Spillman W, Patriquin D, Crowne D. Fiber optic linear displacement sensor based on a variable period diffraction grating. Applied Optics. 1989;**28**(17):3550-3553

[27] Aydin K, Seliga T, Balaji V. Remote sensing of hail with a dual linear polarization radar. Journal of Climate and Applied Meteorology. 1986;**25**(10):1475-1484

[28] Kim H, Kim J, An H, Park K, Jeong Y. Subwavelength ring assisted Fresnel zone plate for radially polarized light focusing. In: Lasers and Electro-Optics Pacific Rim (CLEO-PR). IEEE; 2017

[29] Rohrbach A, Stelzer EH. Trapping forces, force constants, and potential depths for dielectric spheres in the presence of spherical aberrations. Applied Optics. 2002;**41**(13):2494-2507

[30] Dorn R, Quabis S, Leuchs G. Sharper focus for a radially polarized light beam. Physical Review Letters. 2003;**91**(23):233901

[31] Saleh B, Teich M. Fundamental of Photonics. New York: John Wiley & Sons; 1991

[32] Malitson I. Interspecimen comparison of the refractive index of fused silica. Journal of the Optical Society of America. 1965;**55**(10):1205-1209

[33] Young M. Zone plates and their aberrations. Journal of the Optical Society of America. 1972;**62**(8):972-976

[34] Tomiyasu B, Fukuju I, Komatsubara H, Owari M, Nihei Y. High spatial resolution 3D analysis of materials using gallium focused ion beam secondary ion mass spectrometry (FIB SIMS). Nuclear Instruments and Methods in Physics Research Section B: Beam Interactions with Materials and Atoms. 1998;**136**:1028-1033

[35] Vesseur EJR, De Waele R, Lezec H, Atwater H, De Abajo FG, Polman A. Surface plasmon polariton modes in a single-crystal Au nanoresonator fabricated using focused-ion-beam milling. Applied Physics Letters. 2008;**92**(8):083110

[36] Zhan Q. Trapping metallic Rayleigh particles with radial polarization: Reply to comment. Optics Express. 2012;**20**(6):6058-6059

[37] Maier SA. Plasmonics: Fundamentals and Applications. New York: Springer Science & Business Media; 2007

[38] Kim H, Lee S-Y, Lee S, Lee B, Jeong Y. Plasmonic Grating-Assisted Nano-Slit Implemented in an all-Fiberized Format for Wavelength-Dependent Beaming. In: Advanced Solid State Lasers. OSA; 2014

[39] Kim H, Lee Y, An H, Vazquez-Zuniga LA, Lee B, Jeong Y. Metal-coated angled fiber facet for surface plasmon generation. In: Asia-Pacific Laser Symposium (APLS). OSK; 2016

[40] Lakowicz JR, Malicka J, Gryczynski I, Gryczynski Z. Directional surface plasmon-coupled emission: A new method for high sensitivity detection. Biochemical and Biophysical Research Communications. 2003;**307**(3):435-439

[41] Kim S, Kim H, Lim Y, Lee B. Off-axis directional beaming of optical field diffracted by a single subwavelength metal slit with asymmetric dielectric surface gratings. Applied Physics Letters. 2007;**90**(5):051113

[42] Yu L-B, Lin D-Z, Chen Y-C, Chang Y-C, Huang K-T, Liaw J-W, Yeh J-T, Liu J-M, Yeh C-S, Lee C-K. Physical origin of directional beaming emitted from a subwavelength slit. Physical Review B. 2005;**71**(4):041405

[43] Kim J, Kim J, Na J, Jeong Y. Numerical study of a novel bi-focal metallic Fresnel zone plate having shallow depth-of-field characteristics. Current Optics and Photonics. 2018;**2**(2): 147-152

[44] Kim J, Kim H, Lee G-Y, Kim J, Lee B, Jeong Y. Numerical and experimental study on multi-focal metallic Fresnel zone plates designed by the phase selection rule via virtual point sources. Applied Sciences. 2018;**8**(3):449

# Ultrathin Oxide Wrapping of Plasmonic Nanoparticles via Colloidal Electrostatic Self-Assembly and their Enhanced Performances

Haoming Bao, Hongwen Zhang,
Guangqiang Liu and Weiping Cai

Additional information is available at the end of the chapter

http://dx.doi.org/10.5772/intechopen.79573

## Abstract

Ultrathin and uniform oxide layer-wrapped plasmonic nanoparticles (NPs) have been expected in the fields of light energy conversion and optical sensing fields. In this chapter, we proposed a universal strategy to prepare such core-shell plasmonic NPs based on colloidal electrostatic attraction and self-assembly procedures. Based on the self-assembly strategy, laser ablation of metal targets in liquid medium was conducted at room temperature to one-pot fabricate the oxide-wrapped plasmonic NPs. It demonstrates that a series of core-shell nanostructured NPs such as Au@$Fe_2O_3$, Au@$Al_2O_3$, Au@CuO, Au@ZnO, Pt@$TiO_2$, and Pd@$TiO_2$, have been readily obtained free of contaminations. Technical analyses illustrate that those composite NPs possess uniform and symmetrical oxides layers with several nanometers in thickness. Furthermore, both the thickness and crystallinity of the oxides layer could be precisely tailored simply by controlling hydrolysis of precursors and irradiation durations. Finally, due to ultrathin wrapping of oxides, the as-obtained core-shell plasmonic NPs show excellent surface-enhanced Raman scattering (SERS) and gas-sensing performances compared with bare metal or oxides NPs.

**Keywords:** plasmonic nanoparticles, ultrathin oxide wrapping, colloidal electrostatic self-assembly, enhanced performances

## 1. Introduction

Microstructured/nanostructured plasmonic materials (Au, Ag, Cu, etc.) have great applications in optical sensing [1, 2] and energy conversion [3, 4] due to their surface plasmon-enhanced

IntechOpen

© 2018 The Author(s). Licensee IntechOpen. This chapter is distributed under the terms of the Creative Commons Attribution License (http://creativecommons.org/licenses/by/3.0), which permits unrestricted use, distribution, and reproduction in any medium, provided the original work is properly cited.

interaction with incident light. However, in many specific applications, the surfaces of these plasmonic materials need to be modified or coated by organic or inorganic species to achieve core-shell structured nanomaterials with functional properties [5, 6]. Among them, stable semiconducting oxide-coated plasmonic NPs, which couple strong bandgap absorption and plasmon absorption of the light, possess a relatively sensitive surface and have been extremely applied in photo/electro catalysis [7–9], chemical analysis [10, 11], and solar cells [12, 13]. In those applications, the thickness of the shell has been accepted as a fundamental and an important parameter. In particular, the shell is commonly required to be thin enough for maximizing the short-range local surface plasmon resonance (LSPR) effect of the plasmonic metal core. Typically, the wrapping shell thickness is often expected to not exceed 10 nm to ensure strong LSPR effect in the sensitive surface-enhanced Raman scattering (SERS) detection of target analytes [14, 15]. As a result, facile approaches to obtain ultrathin oxides wrapped plasmonic metal NPs are in urgent demands for high performance SERS-based detection application.

In the literature, conventional methods including Stöber method [16], hydrothermal method [17], and sol-gel method [18] have been extremely applied to prepare oxide layers coated plasmonic NPs. For example, Yoshio et al. prepared core-shell structured Ag@$SiO_2$ NPs through borohydride reduction method [16]. Kim et al. deposited 60 nm of $TiO_2$ shell layer on gold NPs via microwave-assisted hydrothermal method [17]. In general, these wet chemical fabrications are usually relied on two steps: the formation of the core and subsequent wrapping of the shell, in which an organic substance with multifunctional groups is commonly utilized as a bridge to connect the metal core and the oxide shell. The as-obtained products are often encapsulated with surfactants or the media molecules that cause severe interfering signals in SERS detection and deteriorate the performances in practical applications. What's more, most of these mentioned methods are difficult to achieve ultrathin wrapping layer due to the difficulty in controlling the nucleation and growth stages of the shell. The present reports in literature illustrate that the thickness of the shell is generally thicker than 10 nm, which is beyond or close to the working distance limit of LSPR. And a very few reports regarding one-pot synthesis method could be found for the ultrathin oxides wrapped plasmonic metal NPs [9, 19, 20]. In addition to the wet chemical methods, atomic layer deposition (ALD) has been widely reported to realize homogenous oxide shell thin to monoatomic layers [21–23]. For example, Qian et al. fabricated Au@$TiO_2$ core-shell structured NPs by using an electrochemistry controlled atomic layer deposition [22]. However, despite of its ultrathin and uniform oxide shell characters, it is time-consuming and tedious in operation and commonly restricted to deposit $Al_2O_3$ or $SiO_2$ layers. In total, controllable and flexible methods to facilely and one-pot prepare the ultrathin and uniform oxide-coated plasmonic metal NPs free of contaminations are still expected.

Recently, some important progresses have been made in fabrication of ultrathin and uniform oxide-wrapped plasmonic NPs [24, 25]. In this chapter, we introduce a universal strategy for wrapping NPs based on colloidal electrostatic attraction and self-assembly on the plasmonic NPs. Using this strategy and via one-step laser ablation of noble metal targets in the hydrolysis-induced hydroxide sol solutions at room temperature, the oxide shell-wrapped plasmonic NPs with several tens of nanometers in size could be obtained, such as Au@oxides ($Fe_2O_3$, $Al_2O_3$, $In_2O_3$, CuO, and ZnO) as well as Pt@$TiO_2$ and Pd@$TiO_2$.

The oxide shell layers were very uniform and symmetrical and could be controlled from several nanometers down to <1 nm in thickness. The shell thickness shows independence on the plasmonic NPs' size. Finally, the enhanced performances for such oxide layer-wrapped plasmonic NPs were also demonstrated compared with the pure component NPs, mainly including the much stronger SERS performances and the significantly better gas-sensing performance to some toxic molecules.

## 2. Electrostatic Self-Assembly and Laser Ablation in Liquid (LAL) Method

Laser ablation of metal target in colloidal medium will one step produce the nano-sized metal NPs and wrapping of the oxides layer. The physical and chemical properties of oxides shell depend on diverse parameters, including the metal, colloidal type, temperature and pH of the colloidal medium.

### 2.1. Charged properties of colloids

We propose that the surface charge status of both colloids and metal NPs are crucial to the self-assembly formation of oxides shells. Since the surface of the colloids attracts the anions and cations, these ions are distributed in a diffusive state at the two-phase interface to form a diffusion double layer [26–28]. The electric double layer can be divided into two parts by the Stern plane as Stern layer and the diffusion layer. The double layer theory suggests some possible behaviors of the colloids in solution, such as repelling each other and staying stable or attracting each other and coagulating. A parameter quantitatively describes charged properties of the colloids is Zeta potential [27, 28], which refers to the potential of the Shear plane relative to the solution at infinity. The Zeta potential can be positive or negative, which suggests different charged properties of the colloids. The larger the absolute value of Zeta potential usually indicates the more charges on colloids and better stability. If two kinds of colloids charged differently close to each other, a strong electrostatic attraction between them will occur.

### 2.2. Colloidal electrostatic self-assembly

A key issue in the preparation of core-shell-structured NPs is how to efficiently attach the shell materials or its precursors to the preformed core particles. Considering the charging characteristics of colloidal NPs, if two colloidal NPs with different charge properties are brought close to each other, a strong Coulomb attraction will attract them together. When the sizes of the two colloidal NPs differ greatly, the small colloids should be adsorbed onto the surface of the big one to complete the electrostatic assembly process. And such method has been reported for the preparation of Au-wrapped magnetic $Fe_3O_4$ NPs [29], and Au-wrapped silica NPs [30]. However, the oxides wrapped plasmonic metal NPs are rarely reported.

In order to achieve the ultrathin oxide wrapping layer, the oxides or its precursor colloids used in the colloidal electrostatic self-assembly should be small enough. Generally, the artificially assisted methods usually results in bigger oxides or its precursor colloids (most of them are no less than 5 nm). Generally, metal cations ($Fe^{3+}$, $Al^{3+}$, $Cu^{2+}$, $Ti^{4+}$, $Sn^{4+}$, etc.) are hydrolyzed in solution to form corresponding hydroxide colloids. The size of these hydroxide colloids is generally at several nanometers [31, 32], which is suitable for such a colloidal electrostatic self-assembly. And most of them are positively charged. On the other hand, many plasmonic metal NPs tend to adsorb anions on the surface and carry negative charges [33, 34]. Strong electrostatic attraction between the two kinds of colloids will occur when they are close enough to each other. The small hydroxide colloids will be attached on the surface of the plasmonic metal NPs and a monolayer hydroxide wrapping layer would be formed on the metal NPs due to the colloidal self-assembly, as schematically shown in **Figure 1a** and **b**. After dehydration treatment by annealing or heating, the hydroxides shell will be transformed to corresponding oxides (**Figure 1c**).

Obviously, such a self-assembly process should be a flexible and universal, which is suitable to fabricate a series of core-shell NPs. And the thickness of the shell is highly relied on the size of the colloids produced by the hydrolysis, which could be simply controlled by the pH value and temperature of the colloidal precursor. This has been confirmed by a one-step laser ablation of plasmonic metal target in hydrolyses induced hydroxides sol solutions.

### 2.3. Laser ablation in hydroxides sol solutions

In order to avoid and remove interferences from other substances (such as surfactants), the laser ablation in liquid method, typically been accepted as a chemical green approach, has been adopted to verify the colloidal electrostatic self-assembly strategy.

In the laser-based synthesis procedure, metal foils are usually utilized as the ablation target while metal salt solutions are used as the liquid medium, as shown in **Figure 2**. When a pulsed laser is focused onto the surface of metal target, a localized high-temperature and high-pressure plasma involving atoms, ions, electrons, and clusters is generated. From the moment on formation, the

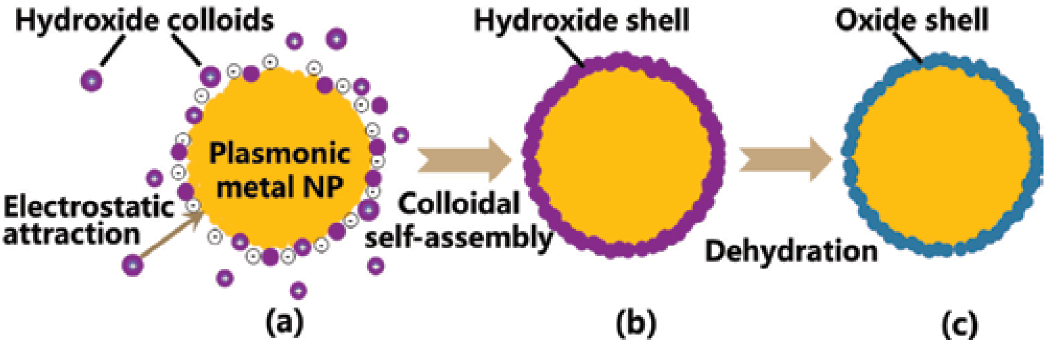

**Figure 1.** Schematic illustration for the fabrication strategy of ultrathin oxide layer-wrapped metal NPs based on the electrostatic colloidal attraction and self-assembly. (a) Adsorption or attachment of hydroxide colloids on a metal NP due to the electrostatic attraction. (b) Formation of monolayer hydroxide colloidal shell by colloidal self-assembly on the metal NP. (c) Formation of ultrathin oxide shell layer on the metal NP by dehydration [24].

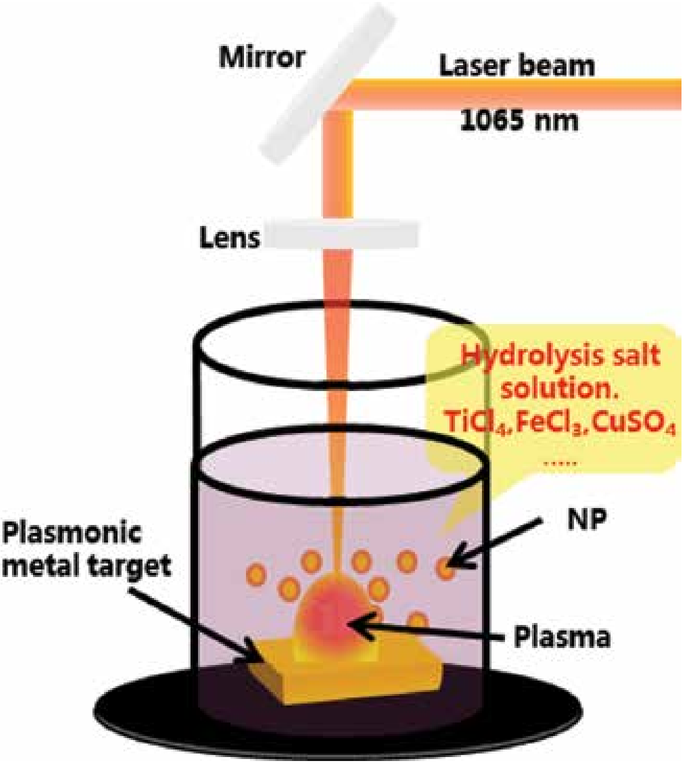

**Figure 2.** Schematic illustration of the laser ablation for ultrathin oxide layer-wrapped plasmonic metal NPs via the colloidal electrostatic self-assembly strategy.

plasma adiabatically expands at supersonic speeds and transfer heat to the surrounding liquid medium. The quenched plasma nucleates and gradually grows up to form plasmonic NPs [35, 36]. Commonly, the newly formed metal NPs are negatively charged and, when they are dispersed into the colloidal solution, they rapidly absorb the cations in the solution. The small hydroxide colloids, which are formed through hydrolysis of the metal cations, in the solution are positively charged. As a result, the metal NPs will electrostatically attract with the positively charged hydroxide colloids. The hydroxide colloids will form a nano-sized layer around the metal core, forming a core-shell structured NP. With the ongoing laser ablation, the hydroxide-based core-shell NPs will absorb the latter arrived laser and slowly dehydrated to oxide shell due to the laser-induced heating.

## 3. LAL-induced oxides wrapped metal NPS

Based on the aforementioned formation process, pulsed laser ablation in colloidal solution will one-pot fabricate the oxides wrapped metal NPs.

### 3.1. Typical morphology and structure of the NPs

First, let us take the $TiO_2$-wrapped Au NPs as an example. The $Ti(OH)_4$ sol solution shows obvious Tyndall effect, as shown in the (1–2) of the inset in the **Figure 3a**. The Zeta potential is about +28.9 mV, indicating they are positively charged. And after ablation of a gold target in the sol solution for 15 min, the Zeta potential drops to +26.2 mV, and the pH value was slightly decreased from 1.77 to about 1.65. The Zeta potential of the Au colloidal solution obtained by ablation in pure water was −24.2 mV. After centrifugation for three times of cleaning, the products were redispersed in water to form an aqueous colloidal solution, as shown in inset (3) of **Figure 3a**, and the Zeta potential was almost unchanged and nearly the same as curve (II) in **Figure 3a**. Optical absorption measurement shows that the well-known absorption peak of the Au NPs has an obvious red shift of about 23 nm, which means that the change of the dielectric environment around the Au NPs' surface [7, 37].

**Figure 4** shows the typical microstructure and morphology of the electrostatically assembled core-shell Au@$TiO_2$ NPs. The field emission scanning electron microscope (FESEM) micrographs reveal that the products consist of nearly spherical particles with diameters ranging from 10 to 60 nm with a mean size of 35 nm, as shown in **Figure 4a**. The energy dispersion spectrum (EDS) shows that the product contains the elements of Au, O, Ti, C, and Si, in which Si and C are from the silicon substrate and cleaning reagent, respectively. The inset of **Figure 4b** shows the EDS mapping from a transmission electron microscopy (TEM) of an isolated NP, which reveals that the elements of Ti and O are preferentially distributed on the surface of the spherical Au NP. Corresponding microstructural examination was carried on a TEM (**Figure 4c**), which shows that the surface of these NPs is obviously wrapped with ultrathin (few nanometers) shell layer. The well-defined core-shell structure can be vividly

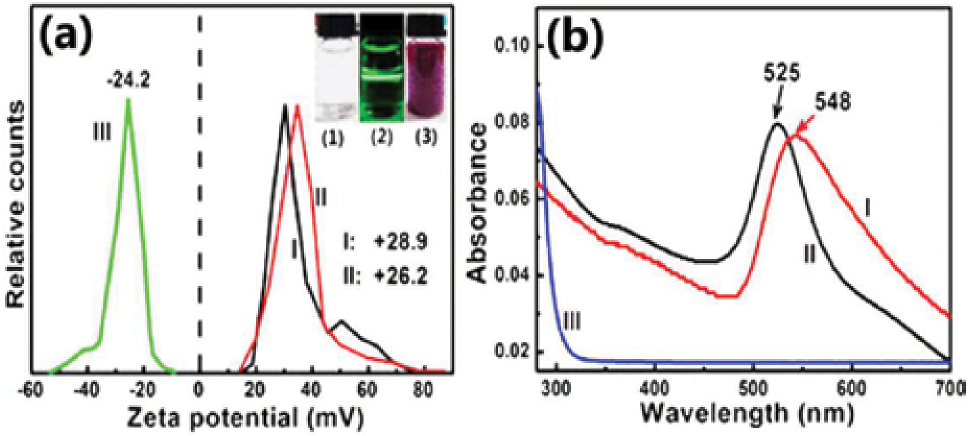

**Figure 3.** (a) Zeta potentials of different colloidal solutions. Curve (I): $TiCl_4$ aqueous solution (or $Ti(OH)_4$ colloidal solution); Curve (II): the colloidal solution obtained by laser ablation of Au target in the $TiCl_4$ aqueous solution without or with centrifugation for cleaning; curve (III): the pure Au colloidal solution induced by laser ablation of Au target in water. The insets (1) and (2) are the photos of the $Ti(OH)_4$ colloidal solution without and with an incident laser beam (532 nm), respectively; (3) is the photo of the colloidal solution of curve (II) in (a). (b) Optical absorbance spectra of the different colloidal solutions. Curves (I), (II), and (III) correspond to the samples (II), (III), and (I) in (a), respectively [24].

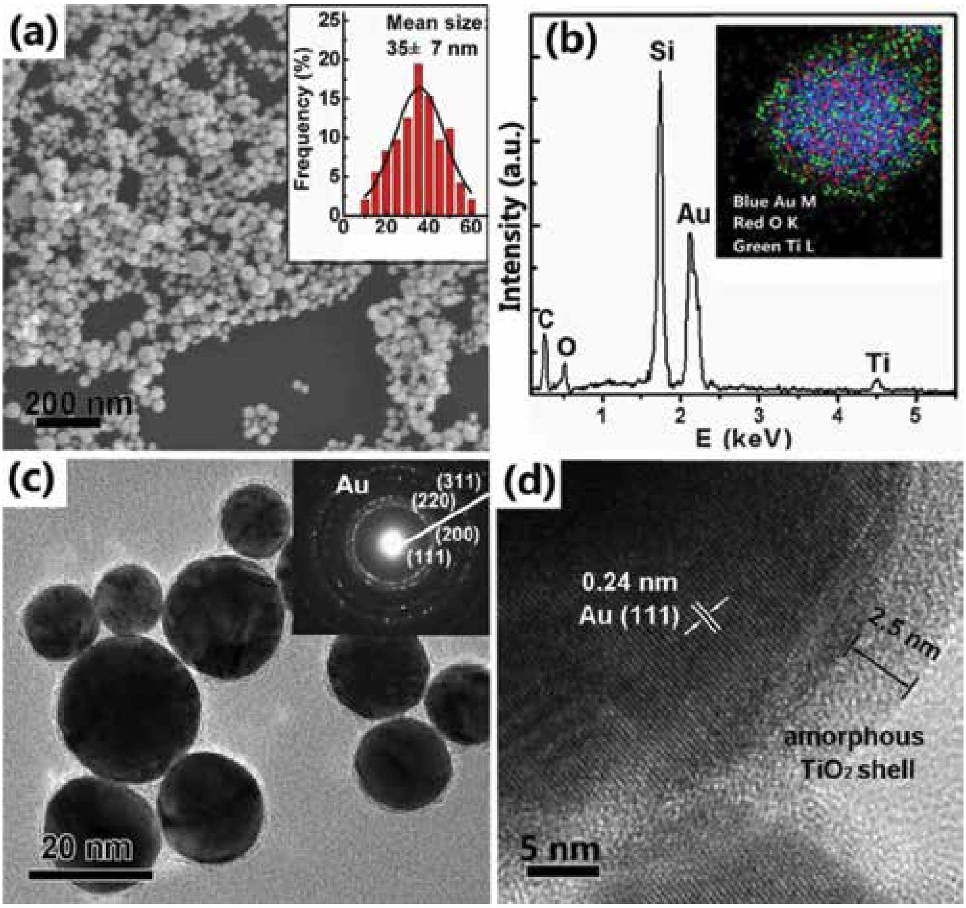

**Figure 4.** Morphological and microstructural observations of the as-prepared products. (a) FESEM image. The inset is the size contribution of the particles. (b) EDS spectrum. The inset is the EDS mapping of a single particle. (c) TEM image. The inset is the corresponding SAED pattern. (d) HRTEM image of a partial particle [24].

observed. However, the corresponding selected area electron diffraction (SAED) pattern only shows the rings of polycrystalline gold, without diffraction pattern belonging to other crystalline substances. High-resolution TEM (HRTEM) photograph (**Figure 4d**) shows clean lattice fringes with an interplanar spacing of 0.24 nm in the core part, which corresponds to the (111) of Au. The shell was measured to be about 2.5 nm in thickness and reveals amorphous nature. Considering the $Ti(OH)_4$ precursors in ablation process and existence of Ti and O elements in the wrapping layer, we proposed that the shell might be amorphous $TiO_2$.

In order to further confirm the components of the shell, X-ray diffraction (XRD) measurement was carried out for the products after dropping it on a cleaned amorphous silicon wafer and the subsequent natural drying. There are only three diffraction peaks at $2\theta = 38.2$, 44.4, and 64.6, corresponding to crystal planes {111}, {200}, and {220} of the Au crystal with the face-centered cubic structure (PDF, No. 00-001-1172), respectively. No other phase was detected, as illustrated in **Figure 5a**. This confirms the amorphous properties of the shell. The X-ray

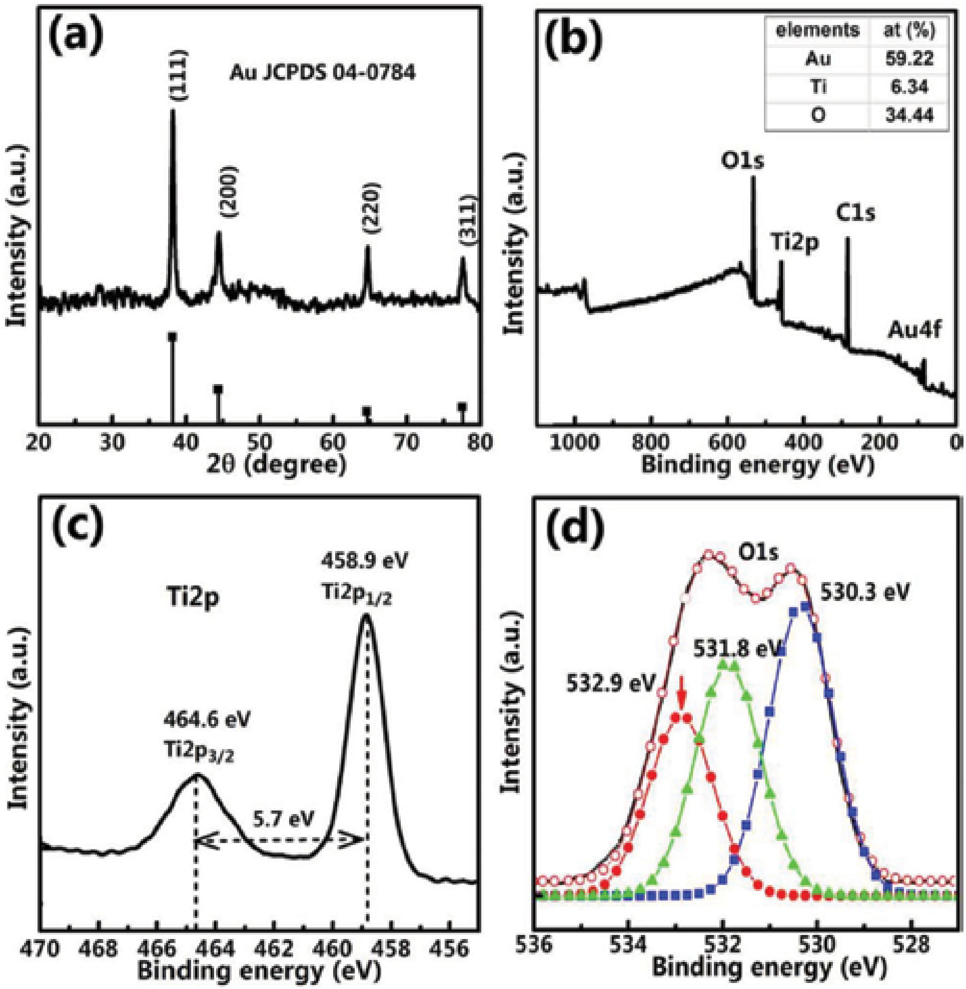

**Figure 5.** (a) XRD pattern of the obtained products. The line spectrum corresponds to the standard pattern of Au powders (JCPDS No. 00-001-1172). XPS spectra of the as-prepared Au@$TiO_2$ NPs. (b) the full spectrum. (c) Binding energy spectrum of Ti 2p. (d) Binding energy spectrum of O 1 s [24].

photoelectron spectrum (XPS) full spectrum presented in **Figure 5b** was also conducted to analyze the surface composition and chemical bonds of the core-shell structured NPs. It shows that the existence of elements Ti, O, and Au. And the atomic ratio of Ti to O is determined to be about 6.34:34.44. The Ti 2p spectrum presented in **Figure 5c** shows two peaks at 464.6 and 458.9 eV correspond to Ti $2p_{3/2}$ and $2p_{1/2}$, respectively. The splitting with 5.7 eV is in good agreement with the standard value for Ti in $TiO_2$ [38]. **Figure 5d** presents the spectrum of O 1 s, in which strongly overlapping peaks could be found. By a peak differentiation imitating analysis, three peaks at 530.3, 531.8, and 532.9 eV can be parsed out. The peak at 530.3 eV corresponds to the oxygen in $TiO_2$, and the peaks at 531.8 and 532.9 eV originate from hydroxyl groups (OH) and adsorbed $H_2O$, respectively [38, 39]. Furthermore, the integral area of the peak at 530.3 eV takes 39% of the whole integral area under O 1 s spectrum. So the atomic ratio of Ti to O in the lattice of wrapping layer should be about 6.34: (34.44 × 39%), or 1:2.1, which is in good agreement with the stoichiometric ratio of $TiO_2$. From the results mentioned previously, the wrapping layer could be confirmed as the amorphous titanium oxide. As an example, it demonstrates that the LAL approach can facilely obtain ultrathin oxides wrapped metal NPs.

### 3.2. The universality of LAL fabrication

Furthermore, such LAL synthesis route based on colloidal electrostatic self-assembly has been confirmed as a universal approach, and it is suitable for fabricating many other ultrathin oxide layer-wrapped plasmonic metal NPs, such as $Au@SnO_2$, Au@ ZnO, Au@CuO, $Au@Al_2O_3$, $Au@In_2O_3$, and $Au@Fe_2O_3$ NPs. All the products consist of spherical particles, with about 10–50 nm in mean size. The wrapping layer of these NPs is measured in 2–3 nm [24].

Besides the oxides wrapped Au NPs, the $Pt@TiO_2$ and $Pd@TiO_2$ NPs can also be prepared via laser ablation in $Ti(OH)_4$ sol solution but using the Pt and Pd as ablation targets, respectively. All the core-shell NPs are wrapped with *ca.* 1–3 nm shell layers [24].

It should be pointed out that the method of electrostatic assembly should be suitable for all colloidal systems, only requiring two kinds of colloids with opposite electrical properties and big size gap. Therefore, the plasmonic metal NPs prepared by the traditional wet chemical method can also be wrapped by oxide layers via this strategy.

### 3.3. Confirmation of the electrostatic self-assembly mechanism

The electrostatic self-assembly of colloids has been confirmed by further experiments. First, laser-induced Au NPs from the pure water are slowly (1 mL per min) added into the stirred $SnCl_4$ aqueous solution. According to the proposed electrostatic self-assembly mechanism, it should also obtain the ultrathin $SnO_2$ layer-wrapped Au NPs, which is confirmed in **Figure 6a**. Similarly, by using the same two-step fabrication, we could also obtain the ultrathin $TiO_2$ shell-wrapped Au NPs, as illustrated in **Figure 6b**. The only thing that deserves a bit of attention is that the laser ablation-formed Au NPs should be slowly added into the corresponding hydroxides sol solutions to avoid a possible colloidal coagulation process.

To confirm the opposite charge-induced electrostatic self-assembly mechanism, we ablated Au target in $Na_2WO_4$ solution, which induces both negatively charged Au NPs and $H_2WO_4$ colloids. For this case, no obvious shell can be observed around the Au NPs.

### 3.4. The dependence of the shell thickness

The thickness of the wrapping oxide layer was measured as a function of the Au core's size, as illustrated in **Figure 7**. For the $Au@TiO_2$ NPs, the $TiO_2$ shell is estimated approximately 2.5 nm in thickness for all NPs regardless of the Au core size. Similarly, the $SnO_2$ shell also shows a similar tendency, indicating that the shell is around 2.5 nm for all Au NPs. The shell layer could be the oxides colloidal monolayer formed on Au NPs.

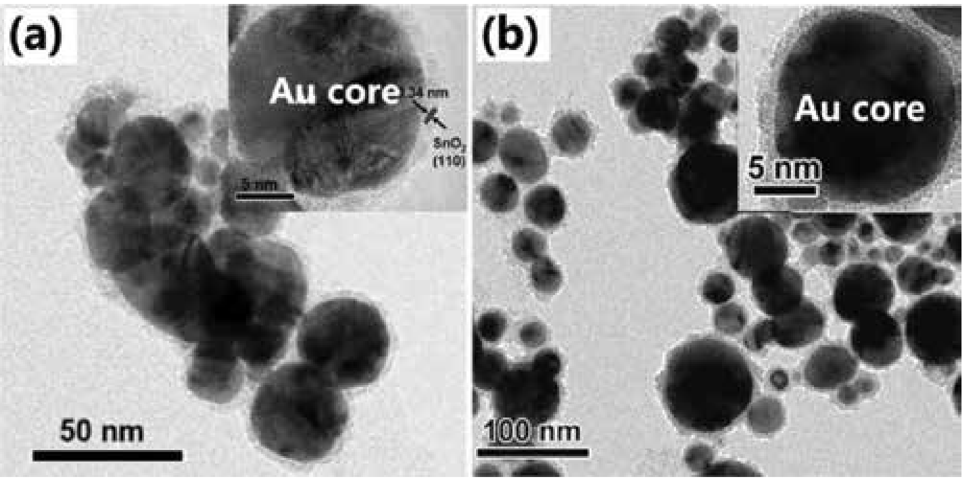

**Figure 6.** TEM image of the products obtained by adding the laser-induced gold colloidal solution into (a) $Sn(OH)_4$ and (b) $Ti(OH)_4$ sol solution. The inset is the magnified image of a single particle.

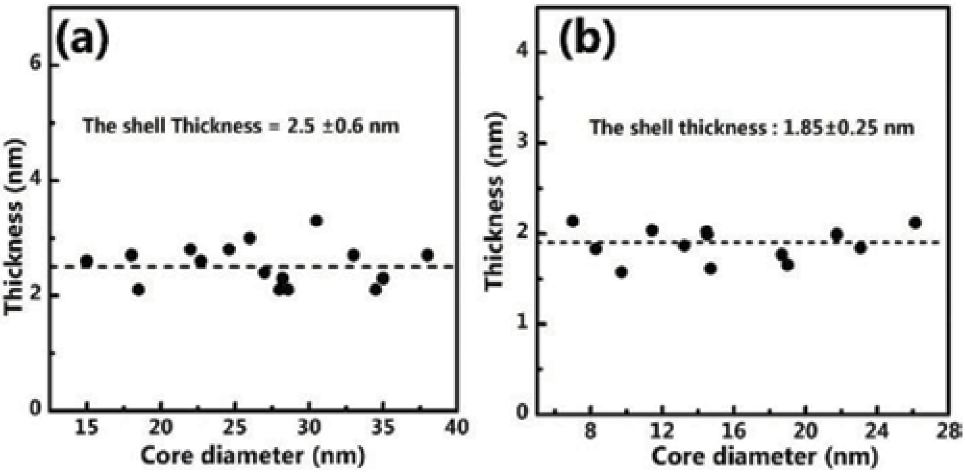

**Figure 7.** Shell thickness versus the core sizes of (a) Au@$TiO_2$ and (b) Au@$SnO_2$ NPs.

## 3.5. The controllability

The laser-based colloidal electrostatic self-assembly strategy shows good flexibility in the fabrication. Here, the controllability in the shell's crystallinity and thickness as well as core's uniformity will be discussed.

### *3.5.1. Homogenizing the NPs size with secondary irradiation*

It is well known that a narrow size distribution is critical to the stable performance of NPs in applications. However, plenty of reports have demonstrated that the laser ablation commonly lead to formation of NPs with large size distribution. Furthermore, a secondary irradiation technique was proposed as an efficient way to fabricate more uniform NPs. Generally, the gold NPs turn more round and bigger after secondary irradiation treatment [40]. For our Au@$SnO_2$ NPs, secondary irradiation with wavelength of 532 nm and frequency of 10 Hz for 10 min (yttrium aluminum garnet, and pulse width of 10 ns, 40 mJ per pulse) was also conducted. It has been found that both products show the typical ultrathin wrapped core-shell structure. However, the number of the small NPs is obviously decreased after the secondary irradiation. And this is confirmed by their size distributions. After the secondary irradiation, the distribution becomes narrower and the relative standard deviation (RSD) decreased from 46 to 21%. Additionally, the mean size increased from 12 to 16 nm.

### 3.5.2. *The shell crystalline*

For some oxides that are easier to crystallize, such as tin oxide, the crystalline shell layer can be usually achieved by a simple drying process. **Figure 8a** and **b** shows TEM and corresponding SAED pattern of the initially prepared Au@$SnO_2$ NPs. Besides the diffraction rings of Au crystal, some rings of the crystalline $SnO_2$ also can be observed. The HRTEM image shows the well-defined interplanar spacing of 0.24 and 0.34 nm in the core and shell, corresponding to the (111) and (110) of Au and $SnO_2$, respectively. However, for Au@$TiO_2$ NPs (**Figure 8c** and **d**), most oxides layer is amorphous. Such an amorphous layer may influence or even decrease their performances in optical and electrical applications. Here, we found that the crystallinity of the shell layer could be significantly improved just by prolonging the ablation time. TEM examination has shown that only few areas in the shell layers were crystallized for the sample with 1-h ablation (**Figure 8c**), and for the sample obtained after ablation for 2 h (**Figure 8d**), the shell layers were almost completely crystallized. The lattice fringes with about 0.35 nm in spacing correspond to (101) planes of anatase $TiO_2$ (PDF, No. 001-0562). Such crystallization

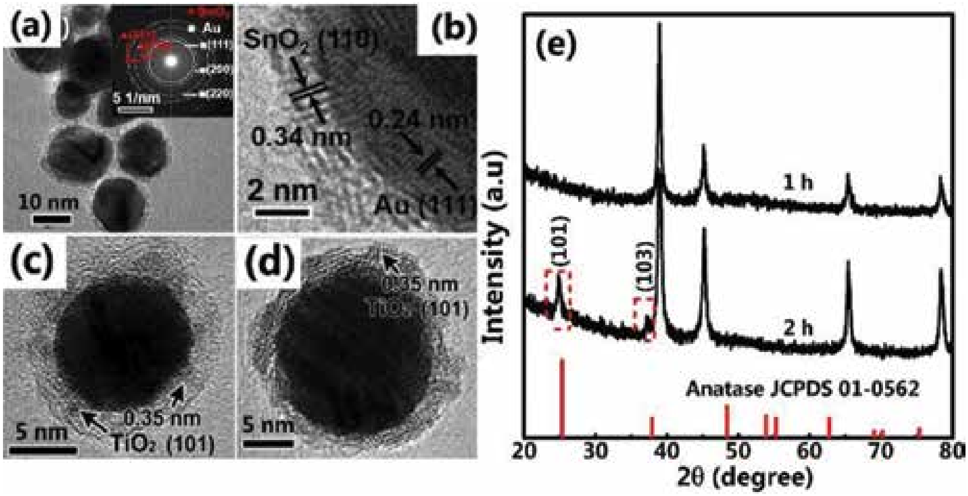

**Figure 8.** (a–d) the TEM observations of the Au@oxides NPs. (a, b) Au NPs wrapped with crystalline $SnO_2$ shell. (c, d) the Au@$TiO_2$ NPs prepared by prolonging the laser duration to 1 h (a) and 2 h (b). And (e), the XRD spectra of the Au@$TiO_2$ NPs corresponding to (c) and (d).

should be attributed to laser-induced thermal effect. The XRD measurements reveal that for products with 1-h ablation, only Au diffraction peaks were detected, while with the ablation duration reached 2-h, additional peaks at 25 and 37° were observed, which correspond to crystal planes (101) and (103) of anatase $TiO_2$ (**Figure 8e**).

### 3.5.3. The thickness of the shell

Regulation of the wrapping layer thickness for core-shell NPs is a key issue in gas sensing, SERS detection, and catalysis applications. Accordingly, it is critical to realize the flexible regulation of shell thickness. In present colloidal electrostatic self-assembly strategy, we demonstrate that the shell thickness depend only on the size of the hydrolysis-induced hydroxide colloids. As a result, to modulate the wrapping thickness, the hydroxide colloidal size should be precisely controlled by changing experimental parameters such as the concentration, temperature, and pH value of the colloidal solution [41]. Thus, the shell thickness would be simply tuned by changing the related conditions during laser ablation process.

#### 3.5.3.1. The concentrations

If the content of metal ions is too low, most of the Au NPs could not be wrapped with the oxides shell due to insufficient oxide source in the solution. However, if the content of metal ions is too high, the wrapped Au NPs are not obviously increased and even decreased. For example, as illustrated in **Figure 9**, most of the Au@$SnO_2$ NPs fabricated by ablating Au target in 0.5 M $Sn^{4+}$ solution shows that the NPs are fused together. Meanwhile, the wrapping layer thickness is much thinner (approximately 1 nm) than those shown in **Figure 8a** and **b**, and even some NPs are not completely wrapped. In this case, only when the $Sn^{4+}$ concentration ranges from 0.01 to 0.1 M, the shell layer of the NPs can be uniform and the Au cores are spherical with nearly same dimensions, as shown in **Figures 8a**, **b** and **9b**. Although the concentration is difficult to accurately modulate the thickness of the shell, it does obviously affect the thickness of the shell to a certain extent.

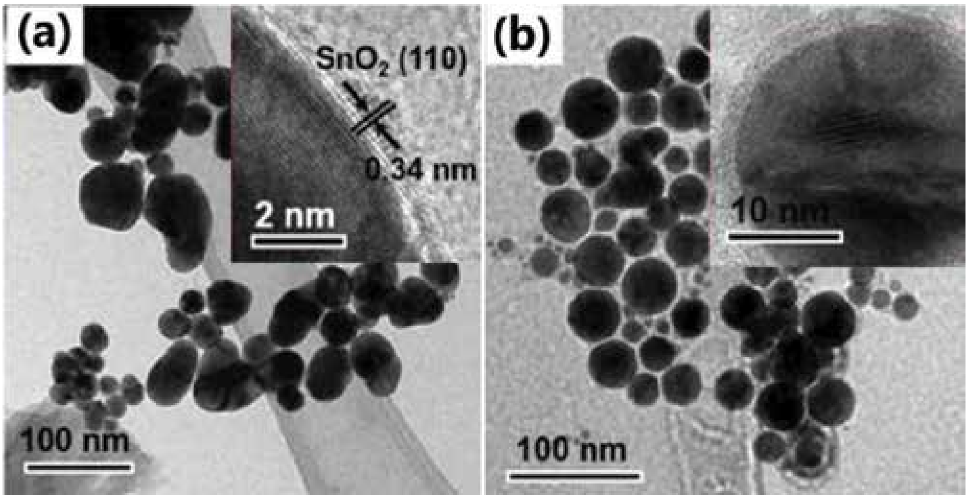

**Figure 9.** TEM observations of the Au@$SnO_2$ NPs prepared by using 0.5 M (a) and 0.01 M (b) $SnCl_4$ solutions.

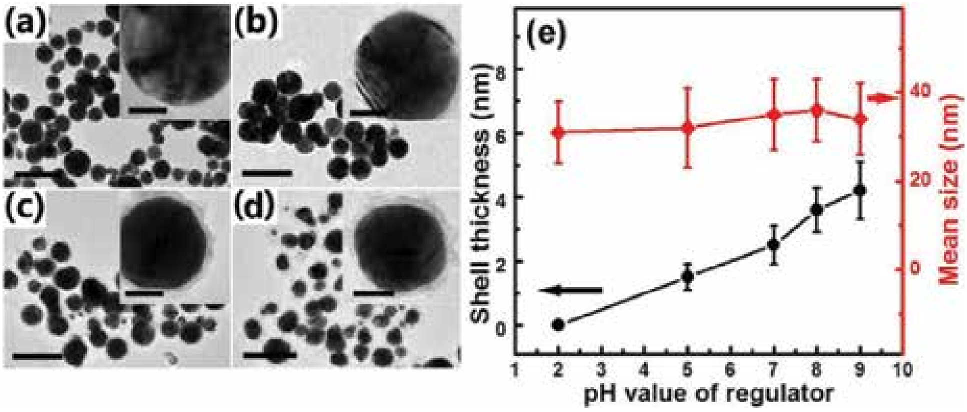

**Figure 10.** The evolution of the shell thickness and size of NPs with the treatment of different pH regulator. (a–d) TEM observations of the NPs obtained with the pH values of 2, 5, 8, and 9, respectively. The scale bars are 50, and 10 nm in the insets. (e) The statistical plots of the shell thickness and mean size versus the pH value of the regulator.

#### 3.5.3.2. The temperature

The shell thickness would increase with the temperature increasing of the colloidal solution during laser ablation. Typically, when the temperature of $Ti(OH)_4$ sol solution was increased to 50°C, the mean thickness was about 3.8 nm. If the temperature was increased up to 95°C, the shell was about 5.5 nm in thickness.

#### 3.5.3.3. The pH value

Furthermore, the pH value of precursor solution also dramatically influences the shell thickness. By simply dropping regulator solution (NaOH or HCl solution) in the laser ablation process with a dropping rate of 10 μL per min, Au@$TiO_2$ NPs with diverse shell thicknesses are achieved. **Figure 10a–d** shows typical TEM photographs of isolated nanoparticles obtained under different pH regulators. It is worth noting that when the pH of the regulator is too low (pH = 2), the oxide shell disappears (**Figure 10a**). And with the pH increase, the shell thickness increases obviously. However, the sizes of Au NPs have no obvious changes (30–35 nm, red line in **Figure 10e**).

## 4. Enhanced performance

### 4.1. High performance SERS detection

As mentioned previously, ultrathin oxide layer–wrapped plasmonic metal NPs have potential applications in many fields. Among them, SERS substrate, which consisted of the core-shell NPs, has huge applications in the detection of some special target molecules that are difficult to be efficiently detected by pure plasmonic metal substrate due to their weak interaction.

### 4.1.1. SERS effect of the oxide-wrapped plasmonic metal NPs

Due to the strong LSPR effect of gold cores, strong local electromagnetic field thus can be formed near the surface of the NPs with the incident light irradiating. It is reasonable that such core-shell NPs illustrate SERS effect to specific target molecules. However, considering that the SERS is a short-range effect, the distance it can effectively act on is generally considered not to exceed 10 nm on the plasmonic particle surface. As previously reported [15], the enhancement effect of SERS decreases exponentially with the shell thickness increasing. So, the SERS activity of the coated Au NPs should be much lower than that of pure Au NPs due to the existence of the wrapping layer.

### 4.1.2. Enhanced interaction between analytes and SERS substrate

Improvement of the interaction between the analytes and the SERS substrates is important in SERS-based detection. For the analytes which weakly interact with plasmonic metal NPs but can strongly be adsorbed on oxides, the ultrathin oxide layer-wrapped plasmonic metal NPs could be the better SERS substrate than the pure noble metal NPs.

For example, the explosive raw material $KNO_3$, which weakly interacts with the Au NPs, was utilized as the analyte. Because of the positively charged Au@$TiO_2$ NPs in $KNO_3$ solution, the surface of NPs could enrich more nitrate anions than the pure negatively charged Au NPs. Thus, the Au@$TiO_2$ NPs-built film as the SERS substrate can absorb the molecules well for further SERS detection. **Figure 11a** presents the Raman spectra for the Au@$TiO_2$ NPs and the pure Au NPs substrates after soaking in the $KNO_3$ solution with 1000 ppm and drying. For the Au@$TiO_2$ NPs substrate, there exists a strong main peak at 1048 $cm^{-1}$ together with a relatively weak peak at 712 $cm^{-1}$ and a very weak peak at 1345 $cm^{-1}$. Such a spectral pattern is in good agreement with that of pure solid $KNO_3$, and

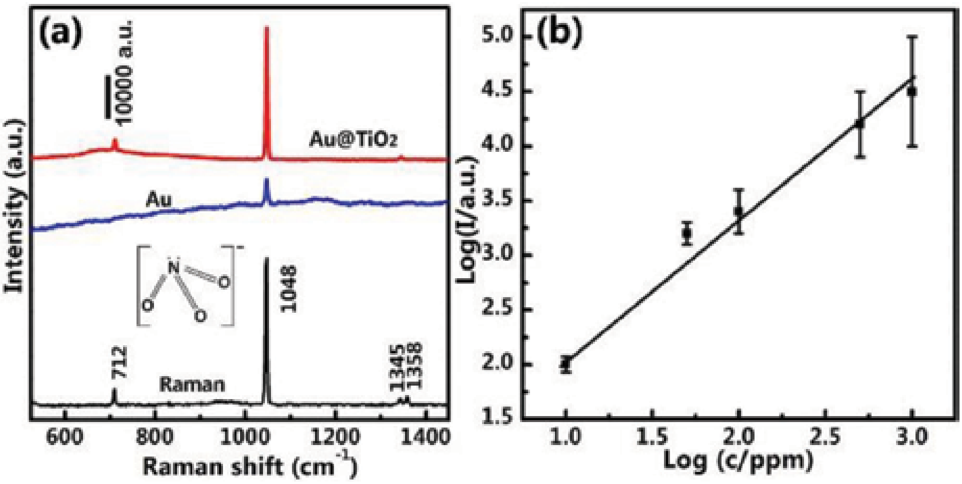

**Figure 11.** (a) Raman spectra of $KNO_3$ on different substrates of Au@$TiO_2$ NPs and pure Au NPs, respectively, after soaking in the $KNO_3$ solution with 1000 ppm. And the Raman spectrum of pure solid $KNO_3$. (b) Plot of the peak intensity $I$ at 1048 $cm^{-1}$ versus the $KNO_3$ concentration $C$ for the soaked Au@TiO2 substrate [24].

all the peaks should originate from nitrate $NO^{3-}$ [42]. In contrast, the signal from the Au NP-built substrate was much lower. The intensity of the main peak at 1048 $cm^{-1}$ is five times higher for the Au@ $TiO_2$ substrate than that from the Au NPs′ substrate. Furthermore, the Raman spectral dependence on the $NO^{3-}$ concentration was measured for the Au@$TiO_2$ substrate, as demonstrated in **Figure 11b**. It shows the plot of the peak intensity at 1048 $cm^{-1}$ versus the $NO_3^-$ concentration, which exhibits a good linear double logarithmic relation between them. The SERS detection limit is less than 1 ppm.

### *4.1.3. Reusability of SERS substrate*

Most SERS substrates are often disposable. As a result, the reusability of them is significantly important from the view of economics and complexity in the repeated fabrication of substrate. As we known, the oxides have shown excellent photocatalyst properties in many previous works. The oxide wrapping layer is thus expected to photocatalyze the target molecules after a SERS detection. Indeed, the reusability of the Au@$TiO_2$ NP substrate has been confirmed, as previously reported [24]. Typically, the 4-Nitrophenol (4-NP), which can be photocatalyzed by $TiO_2$, [43] was used as the target molecules for SERS detection. The Raman spectrum of the Au@$TiO_2$ NP-built film after soaking in the 4-NP solution with 20 ppm is well shown. All Raman peaks are from 4-NP molecules [44]. If the soaked film was subsequently irradiated for 5 min by a xenon lamp before Raman spectral measurement, the Raman signals are significantly decreased. A 10-min irradiation led to complete disappearance of the Raman peaks. After resoaking the substrate in the 4-NP solution before Raman measurement, we can obtain the Raman spectrum with the similar peak intensities to those of the initial one, showing good reusability of Au@$TiO_2$ NPs for the SERS-based detection of such molecules.

## 4.2. Enhanced gas sensing

It is well known that metal oxides are typical gas-sensing materials and are sensitive to many gas molecules such as $NO_2$, $NH_3$, $H_2S$, etc., exhibiting huge application prospect in this field. Here, the colloidal electrostatic self-assembly formed oxides wrapped gold NPs also has shown excellent performance in the gas sensing.

### *4.2.1. Fast response at room temperature*

Usually, the significant responses to the gas molecules generally occur at a high temperature (200–450°C). Thus, the response to gas molecules at room temperature is very important due to low power consumption and safety purpose (especially for some inflammable gases). It has been found that such colloidal electrostatic self-assembly formed Au@$SnO_2$ NPs are much better in the gas sensing to $H_2S$ gas at room temperature than the pure $SnO_2$ NPs′ film [45].

Typically, the responses to $H_2S$ gas (1–3 ppm) at room temperature for these two NPs build films are illustrated in **Figure 12a**. For the pure $SnO_2$ NPs′ film, the response to $H_2S$ at room temperature was not recoverable [25]. As a result, the pure $SnO_2$ NPs′ film cannot be used at room temperature for detection of $H_2S$ gas. While for Au@$SnO_2$ sensor, the response was quickly recovered to the baseline upon gas off. Besides, Au@$SnO_2$ exhibits much faster

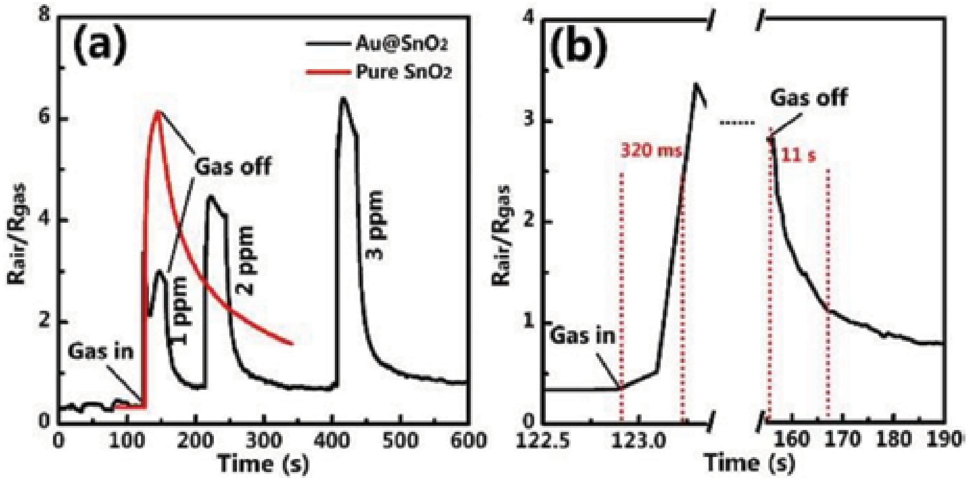

**Figure 12.** (a) Responses to $H_2S$ gas at room temperature for the Au@$SnO_2$ NPs' film and the pure $SnO_2$ NPs' film. (b) The response and recover part of the plot of Au@$SnO_2$ NPs' film to 1 ppm $H_2S$ gas.

response (320 ms) and recovery (11 s) compared with pure $SnO_2$ counterpart (**Figure 12b**). This could be associated with both electronic sensitization of Au metal and the ultrathin wrapping layer in such a core/shell structure. Further work is needed to understand and reveal the origin of this phenomenon.

### *4.2.2. Quantifiable sensing and selectivity*

Quantitative detection makes sensing more reliable and scientific. The response of Au@$SnO_2$ NPs to $H_2S$ here shows obvious concentration dependence. With the concentration increasing from 1 to 10 ppm, the sensitivity increases linearly, as shown in **Figure 13a**. This provides an

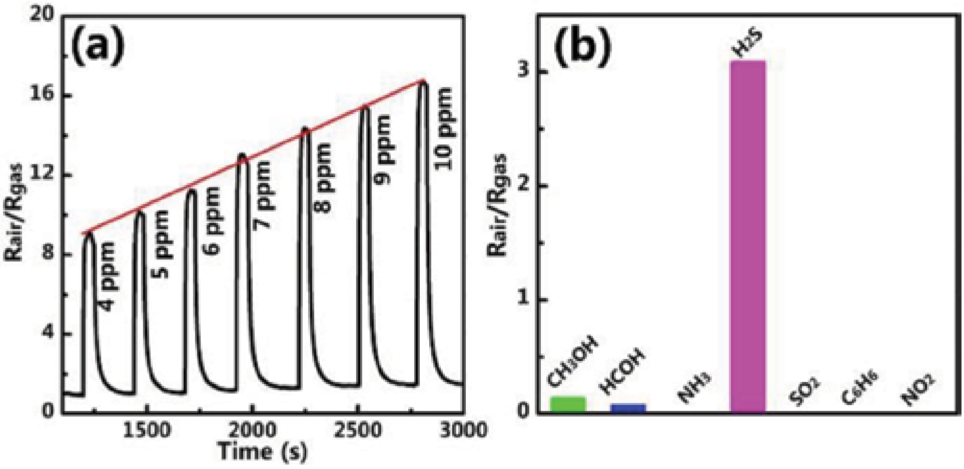

**Figure 13.** (a) The responses of the Au@$SnO_2$ NPs' film to different concentrations of $H_2S$ gas. (b) The selectivity of the substrates to a variety of gases.

opportunity for the quantitative gas detection of $H_2S$ at room temperature. In addition, such core-shell materials also show good selectivity to the $H_2S$ gas. Under the same test conditions and gas concentration, it shows no responses to a variety of gases, such as ammonia and benzene vapor, and only shows weak responses to alcohol and formaldehyde vapors. And the corresponding sensitivity was 24 and 38 times lower than that of substrate to $H_2S$ gas, as shown in **Figure 13b**.

In short, since many metal oxides can be used as the gas-sensing materials, the colloidal electrostatic self-assembly fabrication can provide a general method to achieve the ultrathin metal layer-wrapped plasmonic NPs, which are a class of new gas-sensing materials.

## 5. A brief summary

We have introduced a facile strategy for fabrication of ultrathin oxide layer-wrapped plasmonic metal NPs based on colloidal electrostatic attraction and self-assembly. In this approach, hydrolysis-induced small positively charged hydroxide colloids are wrapped on negatively charged plasmonic metal NPs via the electrostatic self-assembly. After dehydration process by annealing, the shell will be transformed to oxide, resulting in oxides wrapped metal NPs. Based on this strategy, one-step laser ablation of metal targets in the hydrolysis-induced hydroxide sol solutions have been conducted to fabricate the Au@oxides ($Fe_2O_3$, $Al_2O_3$, $Al_2O_3$, CuO, and ZnO) as well as Pt@$TiO_2$ and Pd@$TiO_2$ NPs. Furthermore, the thickness of these oxide layers are as thin as 1∼3 nm and homogenous. And it also shows independence on the plasmonic metal NPs' size. Additionally, such a strategy shows excellent controllability to the shell in the fabrication. Typically, a secondary irradiation can homogenize the NPs' size. Prolonging the ablation duration can improve the shell's crystallinity hugely. And the shell thickness also could be tuned by the temperature, concentration, and pH value, simply by adjusting the hydrolysis of the metal ion. Finally, enhanced SERS and gas-sensing performances of such oxide layer-wrapped plasmonic metal NPs also have been demonstrated. It demonstrates that ultrathin $TiO_2$-wrapped Au NPs can achieve a much stronger SERS performances in the detection of nitrates due to its positively charged composite NPs. In addition, such a SERS substrate can be recycled by irradiating the used substrate to photodegradate the target organic molecules. Also, significantly better gas-sensing performance of Au@$SnO_2$ NPs has been studied, which demonstrates quickly and linearly respond to $H_2S$ gas at room temperature with excellent selectivity.

## Acknowledgements

This work is financially supported by the National Key Research and Development Program of China (Grant No. 2017YFA0207101), Natural Science Foundation of China (Grant Nos. 51771182, 51531006, and 11574313), and the CAS/SAF International Partner-ship Program for Creative Research Teams.

## Author details

Haoming Bao[1,2], Hongwen Zhang[1]*, Guangqiang Liu[1] and Weiping Cai[1,2]*

*Address all correspondence to: hwzhang@issp.ac.cn; wpcai@issp.ac.cn

1 Key Laboratory of Materials Physics, Anhui Key Laboratory of Nanomaterials and Nanotechnology, Institute of Solid State Physics, Chinese Academy of Sciences, Hefei, PR China

2 University of Science and Technology of China, Hefei, PR China

## References

[1] Homola J, Yee SS, Gauglitz G. Surface plasmon resonance sensors: Review. Sensors and Actuators B. 1999;**54**(1–2):3-15

[2] Homola J. Surface plasmon resonance based sensors. Analytical and Bioanalytical Chemistry. 2006;**377**(3):528-539

[3] Devi BP, Wu KC, Pei Z. Gold nanomesh induced surface plasmon for photocurrent enhancement in a polymer solar cell. Solar Energy Materials & Solar Cells. 2011;**95**(8): 2102-2106

[4] Barazzouk S, Hotchandani S. Enhanced charge separation in chlorophyll a solar cell by gold nanoparticles. Journal of Applied Physics. 2004;**96**(12):7744-7746

[5] Liu B et al. Influence of dimensionality and crystallization on visible-light hydrogen production of Au@$TiO_2$ core–shell photocatalysts based on localized surface plasmon resonance. Catalysis Science & Technology. 2018;**8**(4):1094-1103

[6] Kim M et al. Efficient visible light-induced $H_2$ production by Au@CdS/$TiO_2$ nanofibers: Synergistic effect of core–shell structured Au@CdS and densely packed $TiO_2$ nanoparticles. Applied Catalysis B: Environmental. 2015;**s166–167**(10):423-431

[7] Sun Y et al. Complete Au@ZnO core-shell nanoparticles with enhanced plasmonic absorption enabling significantly improved photocatalysis. Nanoscale. 2016;**8**(20):10774-10782

[8] Kuo CH et al. Facet-dependent and Au nanocrystal-enhanced electrical and photocatalytic properties of Au−$Cu_2O$ core−shell heterostructures. Journal of the American Chemical Society. 2011;**133**(4):1052-1057

[9] Han L et al. One-pot synthesis of a Au@$TiO_2$ core-shell nanocomposite and its catalytic property. RSC Advances. 2013;**3**(31):12568-12570

[10] Lin XD et al. Synthesis of ultrathin and compact Au@MnO. Journal of Raman Spectroscopy. 2012;**43**:40-45

[11] Chen L et al. SERS study of surface plasmon resonance induced carrier movement in Au@$Cu_2O$ core-shell nanoparticles. Spectrochimica Acta Part A: Molecular and Biomolecular Spectroscopy. 2018;**189**:608-612

[12] Liu WL et al. The influence of shell thickness of Au@$TiO_2$ core-shell nanoparticles on the plasmonic enhancement effect in dye-sensitized solar cells. Nanoscale. 2013;**5**(17):7953

[13] Fan R et al. Tailored Au@$TiO_2$ nanostructures for plasmonic effect in planar perovskite solar cells. Journal of Materials Chemistry A. 2017;**5**(24):12034-12042

[14] Moskovits M. Surface-enhanced spectroscopy. Reviews of Modern Physics. 1985;**57**(3): 783-826

[15] Li JF et al. Shell-isolated nanoparticle-enhanced Raman spectroscopy. Nature. 2010; **1267**(1):392-395

[16] Kobayashi Y et al. Silica coating of silver nanoparticles using a modified Stöber method. Journal of Colloid and Interface Science. 2005;**283**(2):392-396

[17] Kim YS, Rai P, Yu YT. Microwave assisted hydrothermal synthesis of Au@$TiO_2$ core–shell nanoparticles for high temperature CO sensing applications. Sensors and Actuators B: Chemical. 2013;**186**(6):633-639

[18] Chung FC, Wu RJ, Cheng FC. Fabrication of a Au@$SnO_2$ core–shell structure for gaseous formaldehyde sensing at room temperature. Sensors and Actuators B: Chemical. 2014;**190** (Complete):1-7

[19] Solovyeva VA et al. One-pot synthesis of Au@$SiO_2$ catalysts: A click chemistry approach. ACS Combinatorial Science. 2014;**16**(10):513

[20] Pastorizasantos I et al. One-pot synthesis of Ag@$TiO_2$ core−shell nanoparticles and their layer-by-layer assembly. Langmuir. 2000;**16**(6):2731-2735

[21] Kikuchi K et al. Room temperature atomic layer deposition of $TiO_2$ on gold nanoparticles. Journal of Vacuum Science & Technology A. 2017;**35**(1):01B121-(1-5)

[22] Qian L et al. Widely tuning optical properties of nanoporous gold-titania core-shells. Journal of Chemical Physics. 2011;**134**(1):014707

[23] Bai Y et al. Core-shell Si@$TiO_2$ nanosphere anode by atomic layer deposition for Li-ion batteries. Journal of Power Sources. 2016;**308**:75-82

[24] Bao H et al. Ultrathin oxide layer-wrapped noble metal nanoparticles via colloidal electrostatic self-assembly for efficient and reusable SERS substrates. Langmuir. 2017;**33**: 12934-12942

[25] Bao H et al. Ultrathin tin oxide layer-wrapped gold nanoparticles induced by laser ablation in solutions and their enhanced performances. Journal of Colloid and Interface Science. 2017;**489**:92-99

[26] Verwey E, Overbeek J, Nes KV, Theory of the Stability of Lyophobic Colloids: The Interaction of Sol Particles Having an Electric Double Layer. Amsterdam: Elsevier, 1948

[27] Hunter RJ, et al. Interaction Between Colloidal Particles—Zeta Potential in Colloid Science —Appendix 5. Zeta Potential in Colloid Science. San Diego: Academic Press; 1981, pp. 363-369

[28] Hunter RJ, Ottewill RH, Rowell RL. Zeta Potential in Colloid Science. San Diego: Academic Press; 1981, pp. 11-58

[29] Liu G et al. Electrostatic self-assembly of Au nanoparticles onto thermosensitive magnetic core-shell microgels for thermally tunable and magnetically recyclable catalysis. Small. 2015;**11**(23):2807-2816

[30] Sadtler B, Wei A. Spherical ensembles of gold nanoparticles on silica: Electrostatic and size effects. Chemical Communications. 2002;**15**(15):1604

[31] Liu Z et al. Adhesion of *Escherichia coli* and *Bacillus subtilis* to amorphous Fe and Al hydroxides and their effects on the surface charges of the hydroxides. Journal of Soils and Sediments. 2015;**15**(11):2293-2303

[32] Brodskii VA et al. Electro-surface properties of metal oxides and hydroxides in water solutions. Glass and Ceramics. 2015;**72**(5–6):220-224

[33] Perito B et al. Antibacterial activity of silver nanoparticles obtained by pulsed laser ablation in pure water and in chloride solution. Beilstein Journal of Nanotechnology. 2016;**7**(1): 465-473

[34] Nikov RG et al. Stability of contamination-free gold and silver nanoparticles produced by nanosecond laser ablation of solid targets in water. Applied Surface Science. 2012;**258**(23): 9318-9322

[35] Simakin AV et al. Nanoparticles produced by laser ablation of solids in liquid environment. Applied Physics A. 2004;**79**(4–6):1127-1132

[36] Patil PP et al. Pulsed-laser-induced reactive quenching at liquid-solid interface: Aqueous oxidation of iron. Physical Review Letters. 1987;**58**(3):238

[37] Zhang L et al. Geometry control and optical tunability of metal-cuprous oxide core-shell nanoparticles. ACS Nano. 2012;**6**(4):3514-3527

[38] Zhang H et al. Defect-mediated formation of Ag cluster-doped $TiO_2$ nanoparticles for efficient photodegradation of pentachlorophenol. Langmuir. 2012;**28**(8):3938-3944

[39] Gole A et al. Pepsin−gold colloid conjugates: Preparation, characterization, and enzymatic activity. Langmuir. 2001;**17**(5):1674-1679

[40] Wang H et al. Selective pulsed heating for the synthesis of semiconductor and metal submicrometer spheres. Angewandte Chemie International Edition. 2010;**49**(36):6361-6364

[41] Surender GD, et al. Synthesis of ultrafine rutile phase titanium dioxide particles. US. 2008. Patent No. 7,413,726. Washington, DC: U.S

[42] Shi YE, Wang W, Zhan J. A positively charged silver nanowire membrane for rapid on-site swabbing extraction and detection of trace inorganic explosives using a portable Raman spectrometer. Nano Research. 2016;**9**(8):2487-2497

[43] Marcì G et al. Influence of tungsten oxide on structural and surface properties of sol–gel prepared $TiO_2$ employed for 4-nitrophenol photodegradation. Journal of the Chemical Society, Faraday Transactions. 1996;**92**(5):819-829

[44] Muniz-Miranda M. SERS monitoring of the catalytic reduction of 4-nitrophenol on Ag-doped titania nanoparticles. Applied Catalysis B: Environmental. 2014;**146**(3):147-150

[45] Tans SJ, Verschueren ARM, Dekker C. Room-temperature transistor based on single carbon nanotube. Nature. 1997;**393**:49-52

Chapter 12

# Plasmonic Effect in Photoelectrochemical Cells

Abdul Kariem Bin Mohd Arof and
Mohd Hamdi Bin Ali Buraidah

Additional information is available at the end of the chapter

http://dx.doi.org/10.5772/intechopen.79580

### Abstract

Two types of third-generation photovoltaic (PV) cells are sensitized by dyes and quantum dots (QDs), the former being dye-sensitized solar cell abbreviated as DSSC. The second is the quantum dot-sensitized solar cell or QDSSC. There are three main components in DSSC and QDSSC. The photoanode is the component where the light is being absorbed either by molecules of the dye or by the quantum dots (QDs). The sensitizers are attached on the semiconductor (normally $TiO_2$) surface. The conduction band (CB) of the semiconducting material should be at a level lower than the lowest unoccupied molecular orbital (LUMO) of the dye molecules or CB of QDs for fast electron transfer. Incorporation of plasmonic materials into the photoanode can increase light absorption efficiency by surface plasmon effect and thus improve the efficiency of the DSSCs and QDSSCs. Plasmonic materials that have been employed include gold (Au), silver (Ag) and aluminum (Al) nanoparticles (NPs). Different NPs exhibit different effects on the cell parameters. Covering the NPs with a thin wide bandgap semiconducting film is necessary to protect the plasmonic NP materials from the corrosive nature of the electrolyte.

**Keywords:** DSSC, QDSSC, plasmon surface

## 1. Introduction

One of the cleanest technologies that convert sunlight into electricity is the DSSC. The research on PVs has been conducted for over a century. The first commercial silicon solar cell was produced over six decades ago. Until now, 90% of the global photovoltaic market has been dominated by silicon-based solar cells. There are several solar cell technologies. Silicon wafer-based solar cell falls under the class of first-generation photovoltaic cells, which are expensive although the price has decreased. The second-generation solar cell comes with the purpose to further reduce the production cost. The third-generation photovoltaic (PV) cells are expected to

IntechOpen

© 2018 The Author(s). Licensee IntechOpen. This chapter is distributed under the terms of the Creative Commons Attribution License (http://creativecommons.org/licenses/by/3.0), which permits unrestricted use, distribution, and reproduction in any medium, provided the original work is properly cited.

be even cheaper. The third generation is based on thin films similar to second-generation solar cells. QDSSC, DSSC, perovskite, and organic PVs are third-generation solar cells. The drawback of thin-film cells is that if the thin layer photoactive semiconductor is impinged by photons of energy similar to that of the semiconductor energy gap, the photons are only partially absorbed. One of the promising methods to improve photon absorption is by employing plasmonic materials. Plasmonic materials are metals having negative dielectric constant. Plasmonic materials in solar cells can amplify electromagnetic field, trap, and scatter light strongly to the sensitizer. In this chapter, the effect of plasmonic materials on solar cell performance will be discussed.

## 2. Enhancement mechanism of plasmonic materials

A plasmon is a quasi-particle that can be described by oscillations of a collection of free charges (electrons). Plasmons at the boundary of a metal and a dielectric are called surface plasmons. When the oscillation frequency of conducting electrons equals that of the incoming light, surface plasmon resonance (SPR) occurs, and a strong electromagnetic field with energy greater than that of the incident photons is generated near the nanoparticles (NPs) and is referred to as the 'near electric field'. The non-propagating excited surface plasmon in plasmonic materials is referred to as the localized surface plasmon resonance (LSPR). Size and geometry of the plasmonic NPs influence LSPR. For example, the LSPR is red-shifted if the NP size is increased. This will lead to the increase in electric field wavelength. The dielectric materials surrounding plasmonic NPs also affect the frequency of LSPR ($\omega_{LSPR}$) [1] as can be described by Eq. (1):

$$\omega_{LSPR} = \omega_p \left( \frac{1}{1 + 2\varepsilon_m} - \frac{1}{\omega_p^2 \tau^2} \right)^{1/2} \tag{1}$$

The free electrons in the metallic NPs have a plasma frequency of $\omega_p$. $\tau$ is electron relaxation time and $\varepsilon_m$ is dielectric constant of the semiconducting materials. The LSPR frequency is red shifted when $\varepsilon_m$ increases. Surface plasmon polaritons (SPPs) are created when the electromagnetic field of incident light is combined or coupled with the plasmon. The SPPs propagate along the metal/dielectric interface. In addition, incident photons are efficiently scattered by plasmonic or metal NPs depending on their geometry and size. In general, there are three ways in which plasmonic materials can affect the performance of DSSCs and QDSSCs:

**i.** By LSPR where the metal NPs act as subwavelength antennas through an oscillation of strong conducting electrons

**ii.** By SPP where the incoming light is trapped and promotes more light to be absorbed in the photoactive semiconductor

**iii.** By increasing light scattering and number of optical pathways

## 3. Structure and mechanism of DSSC and QDSSC

The main components of a DSSC are as shown in **Figure 1**. The photoanode which absorbs incident light and separates the charge is made up of a substrate (either glass or plastic). The substrate is coated on one side by a conducting oxide that is transparent. Hence, the substrate is referred to as transparent conducting oxide (TCO) substrate. The conducting oxide can be either fluorine doped tin oxide (FTO) or indium tin oxide (ITO). The TCO is coated with a semiconducting oxide layer (typically titanium dioxide ($TiO_2$)) and a sensitizing dye. The counter electrode (CE) is where charges (electrons released by the sensitizer) are collected from the photoanode. CE comprises TCO coated with catalyst materials. The catalyst material can be platinum (Pt), carbon, conducting polymer, metal oxide or metal carbide. The electrolyte contains a redox couple. The iodide/triiodide $\left(I^-/I_3^-\right)$ couple is an example. For solid or gel electrolytes, the ion-conducting medium is placed between the photoanode and CE. Details of the DSSC working principle are as follows:

When the DSSC is illuminated, the sensitizing dye molecules $D$, on the $TiO_2$ surface are excited $D^*$ upon absorbing photons (Eq. 2) The excited molecules are immediately oxidized, $D^+$. The released electrons are driven into the CB of $TiO_2$ (Eq. 3). This can occur only if LUMO of the dye is at a higher position than the $TiO_2$ Fermi level.

$$D + hv \rightarrow D^* \tag{2}$$

$$D^* \rightarrow e^-{}_{(TiO_2)} + D^+ \tag{3}$$

The electrons that have entered the CB of $TiO_2$ exit the cell via the TCO substrate, travel through the external circuit and reach the Pt CE. Electron transfer occurs at the Pt CE/electrolyte boundary when the $I_3^-$ ions each receive two electrons from the CE and become $I^-$ ions

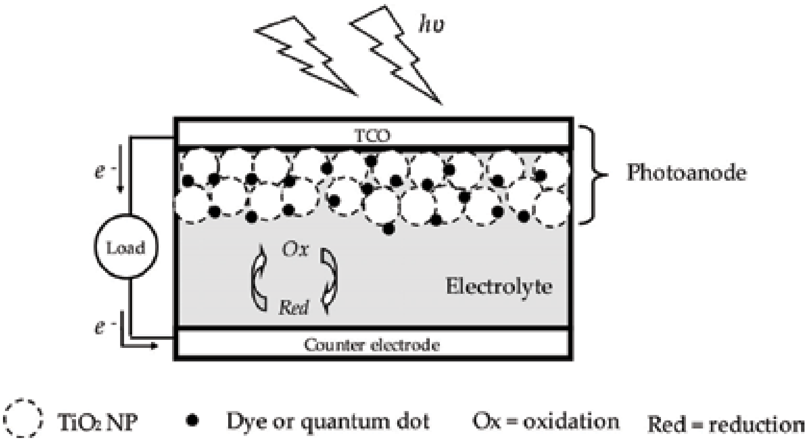

**Figure 1.** Schematic diagram of DSSC or QDSSC.

(Eq. 4). The $I^-$ ions diffuse back to the photoanode getting oxidized again into $I_3^-$ to complete the circuit. The iodide ions neutralize the ionized dye molecules as shown in Eq. (5):

$$I_3^- + 2e^-{}_{(C.E.)} \rightarrow 3I^- \tag{4}$$

$$2D^+ + 3I^- \rightarrow 2D + I_3^- \tag{5}$$

QDSSC has a similar structure with DSSC except that the sensitizers used are quantum dots (QDs) such as lead sulphide (PbS) [2, 3], cadmium sulphide (CdS) [4, 5], lead selenide (PbSe) [6, 7] and cadmium selenide (CdSe) [8, 9]. Since the $I^-/I_3^-$ couple is corrosive towards QD, it has been replaced with $S^{2-}/S_x{}^{2-}$ couple as the redox mediator in QDSSC. The working principle of QDSSC is the same as DSSC. Electron–hole (*e-h*) pairs are created upon photon absorption by QD (see Eq. 6). Electrons in the CB of the QD are driven into the $TiO_2$ CB (Eq. 7), and the QD reverts back to its original state when the holes in the QD valence band receive electrons from $S^{2-}$ ions in the electrolyte. An example for a Cd chalcogenide is illustrated in Eq. (8):

$$QD + photons \rightarrow QD\,(e - h) \tag{6}$$

$$QD\,(e + h) + TiO_2 \rightarrow QD(h) + TiO_2(e) \tag{7}$$

$$CdX(h) + S^{2-} \rightarrow CdX + S \tag{8}$$

As in DSSCs, the injected electrons will end up at the CE. $S_x^{2-}$ ion in the electrolyte is then reduced (when it receives 2*e*) to $S^{2-}$ ions. The $S^{2-}$ ions will diffuse back to the photoanode to complete the circuit as shown in Eqs. (9) and (10):

$$S_x{}^{2-} + 2e \rightarrow S_{x-1}{}^{2-} + S^{2-} \tag{9}$$

$$S + S_{x-1}{}^{2-} \rightarrow S_x{}^{2-} \tag{10}$$

The plasmonic NPs can be either deposited on the FTO or ITO surface of the TCO substrate or incorporated in the $TiO_2$ semiconducting layer of the DSSC and QDSSC (**Figure 2**). However, the studies of plasmonic effect at the CE on the cell performance have also been investigated by some researchers. If the plasmonic NP is embedded in the photoanode, the electrolyte can be either in the solid, gel or liquid state. However, for SPR to occur at the CE and improve

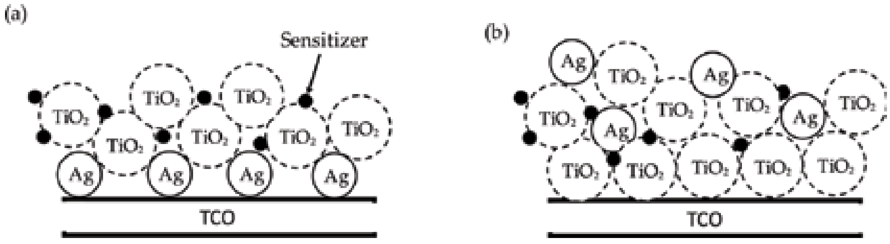

**Figure 2.** Incorporation of plasmonic NP in photoanode (a) on the surface of TCO and (b) in the semiconductor active layer.

absorption of the sensitizer at the photoanode, the electrolyte must be very thin. Liquid electrolyte is usually used when the NP is deposited at the CE.

## 4. Performance of DSSC and QDSSC with plasmonic materials incorporated

**Table 1** summarizes the performance of DSSC and QDSSC incorporated with plasmonic materials. Gold (Au) and silver (Au) NPs are two most popular plasmonic materials that have been widely used for studying the plasmonic effect on the performance of DSSC and QDSSC.

The most popular method to study the influence of NP on the PV cell characteristics is by introducing the NP in the semiconductor network. An improvement on the efficiency of DSSC from 2.7 to 3.3% was observed by Nahm et al. [10] when 100 nm Au NPs were incorporated into the $TiO_2$ layer and sensitized with N719 dye. They found that the absorption was stronger in the cell with Au/$TiO_2$ NP layer than in the cell without Au NPs. This showed that the Au NP plasmonic material helped to increase light absorption, which increased the number of electrons entering the $TiO_2$ and increased the $J_{sc}$ that led to efficiency improvement. Jun et al. [11] showed that with 5 nm Au NPs, the $J_{sc}$ increased by 65% and efficiency increased from 2.09 to 3.12%. Saravanan et al. [30] studied the plasmonic effect Ag NPs produced from $Ag^+$ ions treated with *Peltophorum pterocarpum* flower. An efficiency of 3.62% was noted when 2 wt.% of Ag NPs was doped into $TiO_2$. Efficiency was only 2.83% for the undoped $TiO_2$. Efficiency increased because of enhancement in light absorption via LSPR, SPP or increased optical pathways. Plasmonic effect on DSSC using phthaloyl chitosan and polyethylene oxide-based gel polymer electrolyte has been studied by Shah et al. [29]. Efficiency enhanced by 13% when Ag NPs were included.

Although efficiency can be enhanced by plasmonic effect, the long-term stability is a major concern, especially when $I^-/I_3^-$ redox mediator was used. This is because the iodide/triiodide couple can corrode the NPs. The presence of NPs in the semiconductor network can also increase recombination process that leads to shorter electron lifetime and lowering of $V_{oc}$ [31]. Due to the high electrical conductivity and the lower work function of the NPs than the CB of $TiO_2$, the NPs can act as electron recombination centres where electrons that have been driven into $TiO_2$ re-associated with the holes in the dye molecules or $I_3^-$ ions in the electrolyte. Several efforts have been undertaken to prevent the metal NPs from being corroded. The efforts include utilizing sandwich structure and applying a coating or insulating layer or shell on the surface of the NPs as a protective layer (**Figure 3**).

Sandwich structure ($TiO_2$/Ag NPs/$TiO_2$) has been developed by Lin et al. [38] to protect Ag NPs from $I^-/I_3^-$ redox couple. For this sandwich structure, although they have achieved 23% enhancement in Jsc, the Ag NPs are still corroded during the illumination period. Hence, the authors have concluded that applying protective layer on Ag NPs is a necessity. The choice of materials (usually wide bandgap materials) and thickness of the protective layer also influence the performance of DSSC. Brown et al. [15] have incorporated Au NPs coated with silica ($SiO_2$)

| Plasmonic | Semiconductor | Sensitizer | Electrolyte | Performance | | | | Ref. |
|---|---|---|---|---|---|---|---|---|
| | | | | $J_{sc}$ (mA/cm$^2$) | $V_{oc}$ (V) | Efficiency (%) | Efficiency enhancement | |
| Au NP in active layer | $TiO_2$ | N719 dye | — | 5*–6 | ~ 0.78 | 2.7*–3.3 | 22.2% | [10] |
| Au NP in active layer | $TiO_2$ | N749 dye | Liquid ($I^-/I_3^-$) | 3.89*–6.42 | 0.71–0.75* | 2.09*–3.12 | 49.3% | [11] |
| Au NP in active layer | $TiO_2$ | CdS/ZnS QD | Liquid polysulphide | 9.85*–9.48 | 0.58* – 0.61 | 2.63*–2.96 | 12.5% | [12] |
| Au NP in active layer | $TiO_2$ | N719 dye | Liquid ($I^-/I_3^-$) | 18.67*–20.11 | 0.74* – 0.79 | 9.59–10.8 | 12.6% | [13] |
| Au NP in active layer | $TiO_2$ nanotube | N719 dye | Liquid ($I^-/I_3^-$) | 8.59*–10.25 | 0.70 | 3.89*–4.59 | 18% | [14] |
| | $TiO_2$ nanotube/ nanotube photonic crystal | N719 dye | Liquid ($I^-/I_3^-$) | 8.59*–11.71 | ~ 0.70 | 3.89*–5.63 | 44.7% | |
| Au@$SiO_2$ NP in active layer | $TiO_2$ | N719 dye | Liquid ($I^-/I_3^-$) | 2.14*–3.37 | ~ 0.74 | 1.05*–1.95 | 86% | [15] |
| | | Z907 dye | Hole conductor (spiro-OMeTAD) | 3–5* | ~ 0.72 | 1.2*–2.2 | 83% | |
| Au@$TiO_2$ NP in active layer | $TiO_2$ | N719 dye | Liquid ($I^-/I_3^-$) | 11.55*–14.73 | ~ 0.73 | 6.00*–7.38 | 23% | [16] |
| Au@$TiO_2$ NP in active layer | $TiO_2$ | N719 dye | Liquid ($I^-/I_3^-$) | 18.28 | 0.73* – 0.79 | 9.29*–9.78 | 5.3% | [17] |
| Au@$TiO_2$ NP in active layer | $TiO_2$ hollow sphere | N719 dye | Liquid ($I^-/I_3^-$) | 13.6*–22.1 | 0.72* – 0.63 | 6.25*–8.13 | 30% | [18] |
| Au@$SiO_2$ NP in active layer | $TiO_2$ | N719 dye | Liquid ($I^-/I_3^-$) | 18.28*–20.31 | 0.73 | 9.29*–10.21 | 9.9% | [17] |
| Au@$SiO_2$ NP in active layer | $TiO_2$ | N3 dye | Liquid ($I^-/I_3^-$) | 8.25*–10.31 | ~ 0.70 | 3.88*–4.63 | 19.3% | [19] |
| | | N719 dye | Liquid ($I^-/I_3^-$) | 7.70*–9.80 | ~ 0.70 | 3.52*–4.81 | 36.6% | |
| | | N749 dye | Liquid ($I^-/I_3^-$) | 5.58*–6.29 | 0.65 | 2.41*–2.74 | 13.7% | |
| Au nanorod in active layer | $TiO_2$ | N3 dye | — | 14.12*–16.19 | 0.63* – 0.65 | 6.21*–7.29 | 17.4% | [20] |
| Au nanorod in active layer | $TiO_2$ | Y123 dye | Liquid ($I^-/I_3^-$) | 12.45*–15.74 | 0.71* – 0.80 | 5.31*–8.86 | 66.9% | [21] |

| Plasmonic | Semiconductor | Sensitizer | Electrolyte | Performance | | | | Ref. |
|---|---|---|---|---|---|---|---|---|
| | | | | $J_{sc}$ (mA/cm$^2$) | $V_{oc}$ (V) | Efficiency (%) | Efficiency enhancement | |
| Au nanostar in active layer | $TiO_2$ | N719 | Liquid ($I^-/I_3^-$) | 15.1*–17.2 | 0.75* – 0.78 | 7.00*–8.45 | 20.7% | [22] |
| | | N749 | Liquid ($I^-/I_3^-$) | 8.66*–10.69 | 0.71* – 0.73 | 3.53*–5.13 | 45.3% | |
| Au@$SiO_2$ nanorod in active layer | $TiO_2$ | N719 | Liquid ($I^-/I_3^-$) | 13.15*–15.88 | 0.69* – 0.73 | 5.86*–7.21 | 23% | [23] |
| Au@$SiO_2$@Ag@$SiO_2$ in active layer | $TiO_2$ | N719 | Liquid ($I^-/I_3^-$) | 13.9*–17.58 | ~ 0.75 | 7.34*–9.22 | 25.6% | [24] |
| Au@Ag@$SiO_2$ in active layer | $TiO_2$ | N719 | Liquid ($I^-/I_3^-$) | 13.89*–16.67 | 0.68 | 6.55*–7.72 | 17.9% | [25] |
| Au NP on FTO | $TiO_2$ | N719 dye | Liquid ($I^-/I_3^-$) | 11.90*–12.84 | ~ 0.78 | 5.84*–6.69 | 14.6% | [26] |
| Au NP on FTO | $TiO_2$ | N719 dye | Liquid ($I^-/I_3^-$) | 12.83*–12.34 | ~ 0.82 | 6.5*–6.3 | Efficiency decreases due to high Schottky barrier | [27] |
| Au NP on FTO | $TiO_2$ | CdS QD | Liquid polysulphide | 5.72*–7.11 | 0.47* – 0.56 | 0.86*–1.62 | 88.4% | [28] |
| Ag NP in active layer | $TiO_2$ | N3 | GPE ($I^-/I_3^-$) | 13.04*–14.74 | ~0.59 | 4.61*–5.21 | 13% | [29] |
| Ag NP in active layer | $TiO_2$ | Ruthenium N7 dye | Liquid ($I^-/I_3^-$) | 7.52*–8.28 | 0.63* – 0.71 | 2.83*–3.62 | 27.9% | [30] |
| Ag NP in active layer | $TiO_2$ nanofiber | N719 dye | Liquid ($I^-/I_3^-$) | 7.57*–9.51 | 0.8* - 0.78 | 3.3*–4.13 | 25% | [31] |
| Ag NP in active layer | $TiO_2$ | N719 dye | Liquid ($I^-/I_3^-$) | 12.4*–16.20 | 0.76 | 7.10*–8.90 | 25% | [32] |
| Ag NP in active layer | $TiO_2$ and ZnO nanorod | CdS and CdSe QDs | Liquid polysulphide | 13.27*–15.67 | 0.70* – 0.74 | 4.80*–5.92 | 23.3% | [33] |
| Ag NP in active layer | ZnO nanorod | CdS QD | Liquid polysulphide | 2.18*–3.25 | 0.59* - 0.63 | 0.28*–0.60 | > 100% | [34] |
| Ag NP in active layer | $TiO_2$ | N719 dye | Liquid ($I^-/I_3^-$) | 11.97*–15.12 | ~ 0.73 | 6.34*–8.05 | 27% | [35] |
| Ag NP in active layer | $TiO_2$ nanorod | N719 dye | — | 5.81*–7.11 | 0.72* – 0.76 | 1.87*–2.83 | 51.3% | [36] |
| Ag NP in electrolyte | $TiO_2$ | N719 dye | Liquid ($I^-/I_3^-$) | 11.97*–12.89 | 0.73* – 0.76 | 6.34*–7.11 | 12% | [35] |

| Plasmonic | Semiconductor | Sensitizer | Electrolyte | Performance | | | | Ref. |
|---|---|---|---|---|---|---|---|---|
| | | | | $J_{sc}$ (mA/ $cm^2$) | $V_{oc}$ (V) | Efficiency (%) | Efficiency enhancement | |
| Polyacrylate modified Ag NP | $TiO_2$ | (Ru (bipy)$_2$(SCN)$_2$ dye | Liquid ($I^-/I_3^-$) | 2.7*–4.40 | 0.78* - 0.81 | 1.5*–2.50 | 66.6% | [37] |
| Ag NP in active layer—sandwiched structure $TiO_2$/Ag/ $TiO_2$ | $TiO_2$ | N3 dye | Liquid ($I^-/I_3^-$) | ~ 2.7*–6.18 | ~ 0.83 | 1.43*–3.01 | > 100% | [38] |
| Ag-ion implantation in active layer | $TiO_2$ tri-layer | N719 dye | Liquid ($I^-/I_3^-$) | 9.59*–13.04 | ~ 0.72 | 4.36*–5.85 | 34% | [39] |
| Ag@$TiO_2$ NP in active layer | $TiO_2$ | N719 dye | Liquid ($I^-/I_3^-$) | 5.12*–6.67 | 0.66* - 0.69 | 1.42*–1.83 | 28.9% | [40] |
| Ag@$TiO_2$ NP in active layer | $TiO_2$ | N3 dye | | 6.07*–8.31 | ~ 0.8 | 3.1*–4.4 | 42% | [41] |
| Ag@$TiO_2$ NP in active layer | $TiO_2$ | N719 dye | Liquid ($I^-/I_3^-$) | 7.86*–10.19 | 0.65* - 0.70 | 3.95*–5.33 | 34.9% | [42] |
| Ag@$SiO_2$ NP | $TiO_2$ | N719 dye | Liquid ($I^-/I_3^-$) | 10.2*–13.85 | 0.63* - 0.66 | 4.30*–6.16 | 43% | [43] |
| Ag NP in active layer | Nb-doped $TiO_2$ | N719 dye | Liquid ($I^-/I_3^-$) | 14.1*–16.1 | 0.73 | 6.8*–7.6 | 11.8% | [44] |
| | | | Solid ($I^-/I_3^-$) | 11.7*–14.8 | 0.85 | 5.4*–6.9 | 27.8 | |
| Biomass-coated Ag in active layer | $TiO_2$ | N719 dye | Liquid ($I^-/I_3^-$) | 7.48*–11.8 | 0.76* - 0.79 | 3.35*–5.12 | 52.8% | [45] |
| Ag nanowire in active layer | $TiO_2$ | Beet root | Liquid ($I^-/I_3^-$) | 2.16*–3.60 | 0.56 | 0.45*–0.76 | 68.9% | [46] |
| | | Metal orange | Liquid ($I^-/I_3^-$) | 4.21*–6.77 | ~ 0.53 | 1.57*–2.44 | 55.4% | |
| Ag nanowire in active layer | $TiO_2$ | N719 dye | Liquid ($I^-/I_3^-$) | 9.69*–11.83 | 0.71 | 5.45*–6.26 | 14.9% | [47] |
| Ag nanowire@$TiO_2$ | $TiO_2$ | N719 dye | Liquid ($I^-/I_3^-$) | 9.85*–12.01 | 0.76 | 4.68*–5.31 | 13.5% | [48] |
| Ag nanoplate in active layer | $TiO_2$ | N719 dye | Liquid ($I^-/I_3^-$) | 8.22*–12.47 | ~ 0.7 | 2.81*–3.84 | 36.7% | [49] |
| Ag@$TiO_2$ nanocube in active layer | $TiO_2$ | N719 dye | Liquid ($I^-/I_3^-$) | 6.51*–9.54 | 0.65* – 0.70 | 2.85*–4.26 | 49.5% | [50] |

| Plasmonic | Semiconductor | Sensitizer | Electrolyte | Performance | | | | Ref. |
|---|---|---|---|---|---|---|---|---|
| | | | | $J_{sc}$ (mA/ $cm^2$) | $V_{oc}$ (V) | Efficiency (%) | Efficiency enhancement | |
| Ag NP on FTO | $TiO_2$ | CdSe QD | Liquid polysulphide | 5.91*–8.04 | 0.53* - 0.57 | 1.05*–1.45 | 38% | [51] |
| Ag NP at CE | $TiO_2$ | N719 dye | Liquid ($I^-/I_3^-$) | 15.0*–16.7 | ∼ 0.75 | 7.60*–8.68 | 14.2% | [52] |
| Ag NP at CE | $TiO_2$ | C106 dye | Liquid ($I^-/I_3^-$) | 14.3*–16.5 | ∼ 0.75 | 6.95*–7.96 | 14.5% | [53] |

N719 = Di-tetrabutylammonium cis-bis(isothiocyanato) bis(2,2′-bipyridyl-4,4′-dicarboxylato) ruthenium(II); N749 = Triisothiocyanato-(2,2′,6′,6″-terpyridyl-4,4′,4″-tricarboxylato) ruthenium(II) tris(tetra-butylammonium); Z907 = Cis-diisothiocyanato-(2,2′-bipyridyl-4,4′-dicarboxylic acid)-(2,2′-bipyridyl-4,4′-dinonyl) ruthenium(II); N3 = Cis-diisothiocyanato-bis(2,2′-bipyridyl-4,4′-dicarboxylic acid) ruthenium(II); Y123 = 3-{6-{4-[bis(2′,4′-dihexyloxybiphenyl-4-yl)amino-]phenyl}-4,4-dihexyl-cyclopenta-[2,1-b,3,4-b′]dithiphene-2-yl}-2-cyanoacrylic acid; C106 = NaRu(4,40-bis(5-(hexylthio)thiophen-2-yl)-2,20-bipyridine)(4-carboxylic acid-40-carboxylate-2,20 -bipyridine)(NCS)2; GPE = Gel polymer electrolyte; $J_{sc}$ = Short-circuit current density; $V_{oc}$ = Open-circuit voltage.

*is the value without metal NPs.

**Table 1.** Plasmonic DSSC and QDSSC performance.

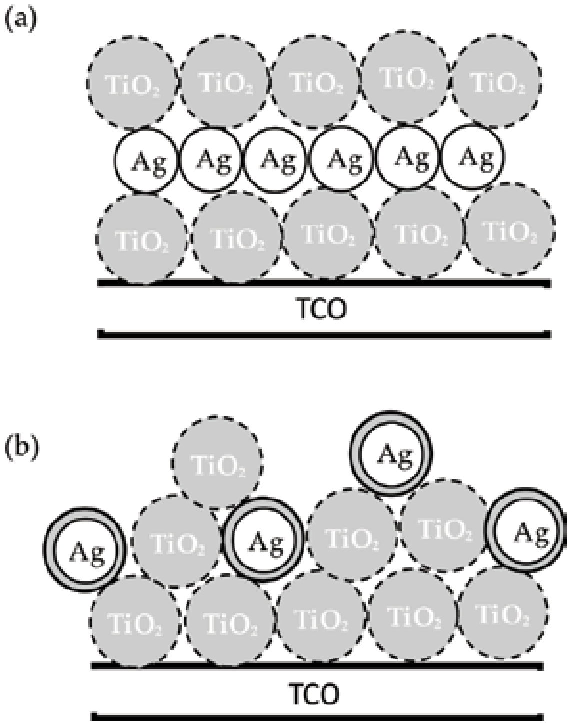

**Figure 3.** Active layer arrangement to protect metal NPs: (a) $TiO_2$/Ag sandwich structure and (b) metal core-shell.

layer, metal core-shell nanostructure, into the DSSC. $SiO_2$ is corrosion resistant towards $I^-/I_3^-$ couple and stable during the sintering process. The authors have employed both $I^-/I_3^-$ redox couple containing liquid electrolyte and spiro-OMeTAD as a medium for charge transportation from cathode to photoanode. Incorporating bare Au NPs in DSSC resulted in lower fill factor, photovoltage and photocurrent due to the metal NPs acting as recombination centres. An increment of about 67% was obtained for photocurrent when the $TiO_2$ mesoporous layer was incorporated with core-shell Au@$SiO_2$ NPs and sensitized with Z907 dye. However, due to the insulating nature of $SiO_2$, the excited dye molecules on $SiO_2$ have a difficulty in injecting electrons into the $SiO_2$ coating layer [41]. According to Choi et al. [17], the fact that DSSC with core-shell Au@$SiO_2$ NPs exhibited higher Jsc is due to surface plasmon effect, while the higher Voc obtained in Au@$TiO_2$ NPs is attributed to charging effect. In DSSC incorporating core-shell Au@$TiO_2$, the electrons are more easily injected from dye molecules into $TiO_2$ compared to $SiO_2$ and stored in the Au core leading to upward shifting of the $TiO_2$ Fermi level and increase $V_{oc}$. The effectiveness of Au NP size on DSSC operation behaviour was studied by Wang et al. [13]. Three different Au NP sizes (5, 45 and 110 nm) were prepared and mixed into a $TiO_2$ paste before deposition on the FTO or ITO substrate and consequently sensitized with N719 dye. The Au NPs were then protected by additional thin layer of $TiO_2$. They have observed that smaller-size Au NPs exhibited higher efficiency attributed to the higher $V_{oc}$ which is due to the photocharging effect. Jeong et al. [32] have coated Ag NPs with $TiO_2$ layer by refluxing

$TiO_2$/Ag NP electrode in 1.0 M titanium(IV) isopropoxide solution for 25 min. Two layers of $TiO_2$ NPs with diameter of 18 and 400 nm, respectively, have been deposited by the doctor-blade method. 5 mM $AgNO_3$ in ethanol solution was used to deposit Ag NPs inside the porous $TiO_2$ by drop-casting technique. From optical studies, the authors inferred that the Ag NPs are elliptical in shape. An improvement of 25% in efficiency was obtained when Ag NPs are included in the photoanode.

The effect of plasmonics in nanostructure oxide semiconductor on QDSSC performance has been studied by Zhao et al. [33]. They have constructed ZnO nanorod electrode doped with Ag and $TiO_2$ NPs sensitized with CdS and CdSe as shown in **Figure 4**. ZnO nanorods were first grown on FTO glass followed by deposition of Ag and $TiO_2$ NPs. The complete cell was constructed with polysulphide electrolyte and $Cu_2S$ as cathode. The higher absorption intensity due to LSPR was observed for ZnO/Ag/$TiO_2$/CdS/CdSe electrode, whereas the absorption intensity for ZnO/$TiO_2$/CdS/CdSe electrode was lower. An efficiency enhancement of 22% from 4.80 (without Ag NP) to 5.92% (with Ag NP) was obtained. Li et al. [31] have developed $TiO_2$ nanofiber doped with Ag NPs by electrospinning. The thickness of nanofiber was 15 μm, controlled by the electrospinning time. The authors chose N719 dye to sensitize the $TiO_2$ nanofiber. The DSSC efficiency increased from 3.3% for undoped DSSC to 4.13% for Ag-doped DSSC. The increased efficiency was attributed to increased $J_{sc}$. Optical studies revealed that the N719 absorption in Ag-doped semiconductor oxide layer was higher than that of the undoped layer. This is attributed to the strong localized electromagnetic field around the Ag NPs and resulting in higher $J_{sc}$ and efficiency. The authors also found that the electron diffusion coefficient in photoanode increased with Ag-doped DSSC. Eskandari et al. [34] have varied the Ag NP concentration to study the effect on QDSSC performance. The electrolyte used was liquid polysulphide. Different concentrations of Ag NPs (1, 5 and 10%) have been doped into ZnO nanorod array and sensitized with CdS QD as photoanode. Chemical bath deposition (CBD) and successive ion layer absorption and reaction (SILAR) processes were employed for growing ZnO nanorods (NRs) and CdS QDs, respectively. The Ag NPs in their work have been coated with zinc sulphide (ZnS) shell by two-step dipping method. The first step is dipping in 0.05 M

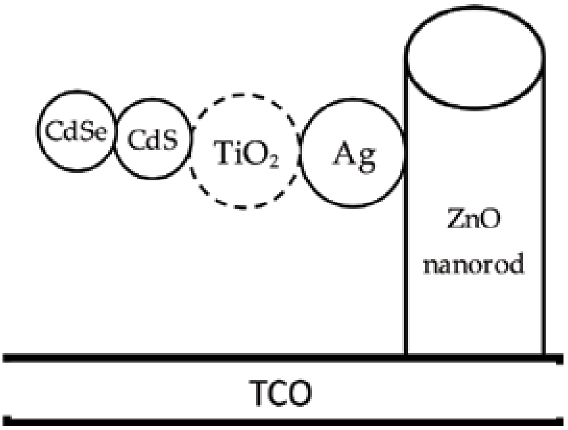

**Figure 4.** The arrangement of ZnO/Ag/$TiO_2$/CdS/CdSe electrode [33].

Zn $(CH_3COO)_2.2H_2O$, and the second dipping is in 0.05 M $Na_2S$ solution. Improvements in $J_{sc}$ and $V_{oc}$ were observed when 1 and 5% Ag NPs were embedded in the ZnO NR surface. This is due to LSPR and light scattering. The QDSSC performance dropped for 10% Ag NPs due to the NP corrosion. The authors attributed this to the imperfect coating of the ZnS shell. Guo et al. [42] have prepared several $TiO_2$ electrodes doped with various quantities (0.05, 0.10, 0.15 and 0.20 wt.%) of Ag@$TiO_2$ core-shells. The best $J_{sc}$ and $V_{oc}$ combination was obtained when the DSSC was incorporated with 0.15 wt.% Ag@$TiO_2$ core-shell NPs that subsequently lead to efficiency enhancement of 5.33% from 3.90% for DSSC without Ag@$TiO_2$ core-shell NPs.

Liu et al. [16] demonstrated the effect of different Au@$TiO_2$ core-shell NPs on DSSC performance. They found that thicker shell exhibited higher $V_{oc}$, while higher $J_{sc}$ was produced by thinner shells. Plasmonic DSSCs having Au@$TiO_2$ with 5 nm shell exhibited efficiency of 7.38% with percentage increment of 23%. Combining Au and Ag NPs have been proposed in order to obtain a broader absorption region. The absorption region between 400 and 550 nm has been noted by Wang et al. [24] for Au coated with Ag and $SiO_2$. The authors have constructed Au@$SiO_2$@Ag@$SiO_2$ NP structure with Au core-coated $SiO_2$@Ag@$SiO_2$ shell. The total NP size was about 100 nm. $SiO_2$ acted as interfacial layer between Au and Ag. It is capable of reducing charge recombination which can be determined by impedance spectroscopy. DSSC fabricated with Au@$SiO_2$@Ag@$SiO_2$ electrode exhibited the highest electron lifetime and reported the efficiency as high as 9.22%. Researchers from the same group have also examined how the thickness of Au@Ag@$SiO_2$ core-shell affects the DSSC operation [25]. The blue shift of absorption peak increased with increasing Ag shell thickness. This has been ascribed to the LSPR effect. The blue shift is due to the dielectric properties of Ag. Optimum efficiency of 7.72% was obtained for DSSC having Ag shell thickness of 15 nm.

The shape of nanoparticles influenced the optical properties. For example, Au with a spherical shape showed the absorption region between 400 and 500 nm, whereas Au nanostars exhibited a strong absorption up to near-infrared (NIR) region (500 nm to 1000 nm) [22]. Approximately 20% enhancement in efficiency from 7.1 (without Au) to 8.4% was obtained when the photoanode contained Au nanostars. Meen et al. [20] have studied the SPR effect of three different shapes of Au NPs (spherical, short and long nanorods) in the photoanode of DSSC. Spherical-shaped Au NPs with average diameter of 45 nm showed absorption peak at 540 nm, whereas the short Au NRs with length:width ratio of 2.5 displayed peaks at 510 and 670 nm. Peaks at 510 and 710 nm were observed for long Au NRs with aspect ratio of 4. The plasmonic bands of NRs are clearly dependent on the aspect ratio. The broader absorption wavelength for long Au nanorods resulted in higher efficiency of 7.29% followed by short Au nanorods and spherical Au with efficiencies of 7.08 and 6.77%, respectively. Without Au NPs, the efficiency of DSSC was only 6.21%. Similar results were obtained by Bai et al. [23] for Au nanorods with aspect ratio of 2.3. Two absorption peaks at 514 and 656 nm were observed. The absorption intensity of Au nanorods coated with $SiO_2$ is higher compared to that without coating. The efficiency was increased from 5.86% for the DSSC without Au to 7.21% for DSSC with 2.0 wt.% Au. Introduction of Ag@$TiO_2$ nanocube core-shells into reduced graphene oxide (RGO)-$TiO_2$ nanotube (NT) has been studied by Chandrasekhar et al. [50]. RGO can increase adsorption surface area and reduce charge recombination rate. Its presence has resulted in a 43% efficiency enhancement from 2.85 to 4.26%. The efficiency was further increased by 21.8% when 0.2 wt.% Ag@$TiO_2$ core-shell nanocubes were embodied in the photoanode. An increment in $J_{sc}$

by 22.1% from 9.69 mA/cm$^2$ and increment of efficiency by 14.9% from 5.45% were achieved when Ag@SiO$_2$ core-shell nanowire (NW) was applied to the DSSC with N719 dye [47]. Effectiveness of Ag nanowire on the DSSC operation behaviour that utilized natural dye has been investigated by Kazmi et al. [46]. The red shift in absorption spectra of TiO$_2$-Ag nanowire was observed and attributed to SPR effect. The efficiency of DSSC using Beet root dye is 0.45%, and it was increased to 0.76% in the presence of Ag nanowire.

The interface between TiO$_2$ and TCO can be modified by depositing metal NP in between TCO and TiO$_2$. Doosthosseini et al. [51] have deposited Ag NPs on top of FTO glass which acts as interfacial layer followed by a layer of anatase TiO$_2$ NPs (size = 20 nm) and a layer of rutile TiO$_2$ NPs (size = 400 nm) sensitized with CdSe QD. The number of SILAR cycles affects the size of the deposited QDs. Since the CB of TiO$_2$ is higher than the work function of Ag, electrons can be easily collected by the FTO substrate. The Jsc and efficiency of DSSC with Ag NPs as interfacial layer increased from 5.91 mA/cm$^2$ to 8.04 mA/cm$^2$ and from 1.05 to 1.45%, respectively. In a similar manner, Zhang et al. [26] have deposited FTO with different sizes of Au NP and by screen printing coating the assembly with TiO$_2$ NP. The TiO$_2$ was sensitized with N719 dye. The efficiency increased from 5.84% for without NP deposited FTO to 6.69% for FTO deposited with Au NP. Efficiency enhancement is due to increased Jsc from 11.90 to 12.84 mA/cm$^2$, and the fill factor increases by 4.9%. According to Ni et al. [54], the performance of DSSC by this arrangement (FTO/ NP/semiconductor) may be explained using the Schottky barrier height model. The Schottky barrier height, $\varphi_b$, is dependent on the metal–semiconductor contact. They have formulated the J-V relationship as shown in the following expression:

$$V = \frac{kTm}{q} \ln\left[\frac{(J_{sc} - J)L\cosh(d/L)}{qDn_0\sinh(d/L)} + 1\right] - \frac{kT}{q} \ln\left[1 + \frac{J}{A{*}T^2 \exp\left(-q\varphi_b/kT\right)}\right] \tag{11}$$

Here, $k$ is $1.38 \times 10^{-23}$ J K$^{-1}$, $T$ is temperature in kelvins (K), $q$ is $1.602 \times 10^{-19}$ C, $m$ = 2 is ideality factor, $D$ is electron diffusion coefficient and $n_0$ = $10^{16}$ cm$^{-3}$ is the dark electron concentration. Further, the electron diffusion length is represented by $L$, film thickness by $d$

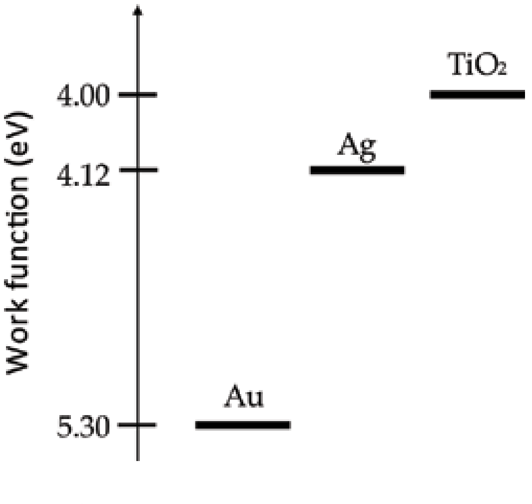

**Figure 5.** Work function of Au, Ag and TiO$_2$.

and $A^*$ is the Richardson constant for $TiO_2$ ($6.71 \times 10^6$ A $m^{-2}$ $K^{-2}$). Simulation results show that the fill factor and power output of DSSC are higher when $\phi_b$ is smaller. The smaller value of $\phi_b$ implies that the metal–semiconductor is ohmic. Hence, it will be easier for the electrons in CB of $TiO_2$ to be collected by FTO. Au NP deposited on FTO glass was also studied by Dao and Choi [27]. The $J_{sc}$ and efficiency slightly decreased from 12.82 mA/cm$^2$ and 6.54% for DSSC without Au NP to 12.34 mA/cm$^2$ and to 6.27% for FTO deposited with Au NP. However, an increment of $J_{sc}$ and efficiency was observed when the Ag NP was deposited on FTO glass. The efficiency increased to 7.49%. This is due to the higher $\varphi_b$ in FTO/Au/$TiO_2$ contact as compared to the FTO/Ag/$TiO_2$ contact. The work function of Au is 5.3 eV, Ag is 4.12 eV and $TiO_2$ is 4.0 eV as shown in **Figure 5**.

The effect of plasmonic NP also can be observed when the NP is deposited at CE. The plasmonic effect of Ag NP with three different shapes (prism, sphere and rod) incorporated in Pt CE has been investigated by Ganeshan et al. [52]. They found that the Ag nanorod embedded at Pt CE shows stronger LSPR effect and better scattering property. Hence, 14% enhancement in efficiency was obtained when the Ag/Pt CE is used. About 15% efficiency enhancement was observed by Dong et al. [53] when Au NP was incorporated into CE. This was attributed to the high surface area at CE and the plasmonic effect.

## 5. Summary

One of the methods to upgrade the optical properties of DSSC and QDSSC components is by incorporating DSSC and QDSSC NPs which lead to better efficiency. These materials can be incorporated in the photoanode and counter electrode of the cells. Both methods improved light absorption efficiency. Different types, shapes, concentrations and sizes of NPs contributed to the plasmonic effect.

## Acknowledgements

The authors would like to thank the University of Malaya and the Malaysian Ministry of Higher Education (MOHE) for the financial support (FG029-17AFR and FP053-2016).

## Author details

Abdul Kariem Bin Mohd Arof* and Mohd Hamdi Bin Ali Buraidah

*Address all correspondence to: akarof@um.edu.my

Centre for Ionics University of Malaya, Department of Physics, Faculty of Science, University of Malaya, Kuala Lumpur, Malaysia

## References

[1] Gangadharan DT, Xu Z, Liu Y, Izquierdo R, Ma D. Recent advancement in plasmon-enhanced promising third-generation solar cells. Nano. 2017;**6**:153-175

[2] Lee HJ, Chen P, Moon S-J, Sauvage F, Sivula K, Bessho T, Gamelin DR, Comte P, Zakeeruddin SM, Il SS, Grätzel M, Nazeeruddin MK. Regenerative PbS and CdS quantum dot sensitized solar cells with a cobalt complex as hole mediator. Langmuir. 2009;**25**:7602-7608

[3] Heo JH, Jang MH, Lee MH, Shin DH, Kim DH, Moon SH, Kim SW, Park BJ, Im SH. High-performance solid-state PbS quantum dot-sensitized solar cells prepared by introduction of hybrid Perovskite interlayer. ACS Applied Materials & Interfaces. 2017;**9**:41104-41110

[4] Lee Y-S, Gopi CVVM, Reddy AE, Nagaraju C, Kim H-J. High performance of $TiO_2$/CdS quantum dot sensitized solar cells with a Cu–ZnS passivation layer. New Journal of Chemistry. 2017;**41**:1914-1917

[5] Jun HK, Careem MA, Arof AK. Performances of some low-cost counter electrode materials in CdS and CdSe quantum dot-sensitized solar cells. Nanoscale Research Letters. 2014;**9**:69

[6] Zhang J, Gao J, Church CP, Miller EM, Luther JM, Klimov VI, Beard MC. PbSe quantum dot solar cells with more than 6% efficiency fabricated in ambient atmosphere. Nano Letters. 2014;**14**:6010-6015

[7] Kim S, Marshall AR, Kroupa DM, Miller EM, Luther JM, Jeong S, Beard MC. Air-stable and efficient PbSe quantum-dot solar cells based upon ZnSe to PbSe Cation-exchanged quantum dots. ACS Nano. 2015;**9**:8157-8164

[8] Huang F, Zhang L, Zhang Q, Hou J, Wang H, Wang H, Peng S, Liu J, Cao G. High efficiency CdS/CdSe quantum dot sensitized solar cells with two ZnSe layers. ACS Applied Materials & Interfaces. 2016;**8**:34482-34489

[9] Pandi DV, Muthukumarasamy N, Agilan S, Velauthapillai D. CdSe quantum dots sensitized ZnO nanorods for solar cell application. Materials Letters. 2018;**223**:227-230

[10] Nahm C, Choi H, Kim J, Jung D-R, Kim C, Moon J, Lee B, Park B. The effects of 100 nm-diameter Au nanoparticles on dye-sensitized solar cells. Applied Physics Letters. 2011;**99**: 253107

[11] Jun HK, Careem MA, Arof AK. Plasmonic effects of quantum size gold nanoparticles on dye-sensitized solar cell. Materials Today: Proceedings. 2016;**3S**:S73-S79

[12] Zarazúa I, Esparza D, López-Luke T, Ceja-Fdez A, Reyes-Gomez J, Mora-Seró I, de la Rosa E. Effect of the electrophoretic deposition of Au NPs in the performance CdS QDs sensitized solar cells. Electrochimica Acta. 2016;**188**:710-717

[13] Wang Q, Butburee T, Wu X, Chen H, Liu G, Wang L. Enhanced performance of dye-sensitized solar cells by doping Au nanoparticles into Photoanodes: A size effect study. Journal of Materials Chemistry A. 2013;**1**:13524-13531

[14] Guo M, Chen J, Zhang J, Su H, Liu L, Fu N, Xie K. Coupling plasmonic nanoparticles with $TiO_2$ nanotube photonic crystals for enhanced dye-sensitized solar cells performance. Electrochimica Acta. 2018;**263**:373-381

[15] Brown MD, Suteewong T, Kumar RSS, D'Innocenzo V, Petrozza A, Lee MM, Wiesner U, Snaith HJ. Plasmonic dye-sensitized solar cells using Core-Shell metal-insulator nanoparticles. Nano Letters. 2011;**11**:438-445

[16] Liu W-L, Lin F-C, Yang Y-C, Huang C-H, Gwo S, Huang MH, Huang J-S. The influence of shell thickness of Au@$TiO_2$ core–shell nanoparticles on the plasmonic enhancement effect in dye-sensitized solar cells. Nanoscale. 2013;**5**:7953-7962

[17] Choi H, Chen WT, Kamat PV. Know thy nano neighbor. Plasmonic versus Electron charging effects of metal nanoparticles in dye-sensitized solar cells. ACS Nano. 2012;**6**:4418-4427

[18] Du J, Qi J, Wang D, Tang Z. Facile synthesis of Au@$TiO_2$ core–shell hollow spheres for dye-sensitized solar cells with remarkably improved efficiency. Energy & Environmental Science. 2012;**5**:6914-6918

[19] Li H, Hong W, Cai F, Tang Q, Yan Y, Hu X, Zhao B, Zhang D, Xu Z. Au@$SiO_2$ nanoparticles coupling co-sensitizers for synergic efficiency enhancement of dye sensitized solar cells. Journal of Materials Chemistry. 2012;**22**:24734-24743

[20] Meen T-H, Tsai J-K, Chao S-M, Lin Y-C, Wu T-C, Chang T-Y, Ji L-W, Water W, Chen W-R, Tang I-T, Huang C-J. Surface plasma resonant effect of gold nanoparticles on the photoelectrodes of dye-sensitized solar cells. Nanoscale Research Letters. 2013;**8**:450

[21] Chandrasekhar PS, Parashar PK, Swami SK, Dutta V, Komarala VK. Enhancement of Y123 dye-sensitized solar cells performance using plasmonic gold nanorods. Physical Chemistry Chemical Physics. 2018;**20**:9651-9658

[22] Elbohy H, Kim MR, Dubey A, Reza KM, Ma D, Zai J, Qian X, Qiao Q. Incorporation of plasmonic Au nanostars into photoanodes for high efficiency dye sensitized solar cells. Journal of Materials Chemistry. 2016;**A4**:545-551

[23] Bai L, Li M, Guo K, Luoshan M, Mehnane HF, Pei L, Pan M, Liao L, Zhao X. Plasmonic enhancement of the performance of dye-sensitized solar cell by core-shell AuNRs@$SiO_2$ in composite photoanode. Journal of Power Sources. 2014;**272**:1100-1105

[24] Wang Y, Zhai J, Song Y, Lin J, Yin P, Guo L. Interfacial effect of novel Core–triple Shell structured Au@$SiO_2$@Ag@$SiO_2$ with ultrathin $SiO_2$ passivation layer between the metal interfaces on efficient dye-sensitized solar cells. Advanced Materials Interfaces. 2015;**2**: 1500383

[25] Wang Y, Zhai J, Song Y, He L. Ag Shell thickness effect of Au@Ag@$SiO_2$ Core-Shell nanoparticles on optoelectronic performance for dye sensitized solar cells. Chemical Communications. 2016;**52**:2390-2393

[26] Zhang D, Wang M, Brolo AG, Shen J, Li X, Huang S. Enhanced performance of dye-sensitized solar cells using gold nanoparticles modified fluorine tin oxide electrodes. Journal of Physics D: Applied Physics. 2013;**46**:024005

[27] Dao V-D, Choi H-S. Highly-efficient Plasmon-enhanced dye-sensitized solar cells created by means of dry plasma reduction. Nanomaterials. 2016;**6**:70. DOI: 10.3390/nano6040070

[28] Zhu G, Su F, Lv T, Pan L, Sun Z. Au nanoparticles as interfacial layer for CdS quantum dot-sensitized solar cells. Nanoscale Research Letters. 2010;**5**:1749-1754

[29] Shah S, Noor IM, Pitawala J, Albinson I, Bandara TMWJ, Mellander B-E, Arof AK. Plasmonic effects of quantum size metal nanoparticles on dye-sensitized solar cell. Optical Materials Express. 2017;**7**:2069-2083

[30] Saravanan S, Kato R, Balamurugan M, Kaushik S, Soga T. Efficiency improvement in dye sensitized solar cells by the plasmonic effect of green synthesized silver nanoparticles. Journal of Science: Advanced Materials and Devices. 2017;**2**:418-424

[31] Li J, Chen X, Ai N, Hao J, Chen Q, Strauf S, Shi Y. Silver nanoparticle doped $TiO_2$ nanofiber dye sensitized solar cells. Chemical Physics Letters. 2011;**514**:141-145

[32] Jeong NC, Prasittichai C, Hupp JT. Photocurrent enhancement by surface Plasmon resonance of silver nanoparticles in highly porous dye-sensitized solar cells. Langmuir. 2011; **27**:14609-14614

[33] Zhao H, Huang F, Hou J, Liu Z, Wu Q, H-b C, Jing Q, Peng S, Cao G. Efficiency enhancement of quantum dot sensitized $TiO_2$/ZnO nanorod arrays solar cells by plasmonic Ag nanoparticles. ACS Applied Materials & Interfaces. 2016;**8**:26675-26682

[34] Eskandari M, Ahmadi V, Yousefi rad M, Kohnehpoushi S. Plasmon enhanced CdS-quantum dot sensitized solar cell using ZnO nanorods array deposited with Ag nanoparticles as photoanode. Physica E: Low-dimensional Systems and Nanostructures. 2015;**68**:202-209

[35] Adhyaksa GWP, Baek S-W, Lee GI, Lee DK, Lee JY, Kang JK. Coupled near- and far-field scattering in silver nanoparticles for high-efficiency, stable, and thin Plasmonic dye-sensitized solar cells. ChemSusChem. 2014;**7**:2461-2468

[36] Hu H, Shen J, Cao X, Wang H, Lv H, Zhang Y, Zhang W, Zhao J, Cui C. Photo-assisted deposition of Ag nanoparticles on branched $TiO_2$ nanorod arrays for dye-sensitized solar cells with enhanced efficiency. Journal of Alloys and Compounds. 2017;**694**:653-661

[37] Ihara M, Kanno M, Inoue S. Photoabsorption-enhanced dye-sensitized solar cell by using localized surface plasmon of silver nanoparticles modified with polymer. Physica E: Low-dimensional Systems and Nanostructures. 2010;**42**:2867-2871

[38] Lin S-J, Lee K-C, Wu J-L, Wu J-Y. Enhanced performance of dye-sensitized solar cells via plasmonic sandwiched structure. Applied Physics Letters. 2011;**99**:043306

[39] Luo J, Zhou J, Guo H, Yang W, Liao B, Shi W, Chen Y. Effects of Ag-ion implantation on the performance of DSSCs with a tri-layer $TiO_2$ films. RSC Advances. 2014;**4**:56318-56322

[40] Zhang X, Liu J, Li S, Tan X, Yu M, Du J. Bioinspired synthesis of Ag@$TiO_2$ plasmonic nanocomposites to enhance the light harvesting of dye sensitized solar cells. RSC Advances. 2013;**3**:18587-18595

[41] Qi J, Dang X, Hammond PT, Belcher AM. Highly efficient Plasmon-enhanced dye-sensitized solar cells through metal@oxide CoreShell nanostructure. ACS Nano. 2011;**5**: 7108-7116

[42] Guo K, Li M, Fang X, Liu X, Sebo B, Zhu Y, Hu Z, Zhao X. Preparation and enhanced properties of dye-sensitized solar cells by surface plasmon resonance of Ag nanoparticles in nanocomposite photoanode. Journal of Power Sources. 2013;**230**:155e160

[43] Hossain MA, Park J, Yoo D, Baek Y, Kim Y, Kim SH, Lee D. Surface plasmonic effects on dye-sensitized solar cells by $SiO_2$-encapsulated Ag nanoparticles. Current Applied Physics. 2016;**16**:397-403

[44] Park JT, Chi WS, Jeon H, Kim JH. Improved electron transfer and plasmonic effect in dye-sensitized solar cells with bi-functional Nb doped $TiO_2$/Ag ternary nanostructures. Nanoscale. 2014;**6**:2718-2729

[45] Tian Z, Wang L, Jia L, Li Q, Song Q, Su S, Yang H. Photoanode for enhanced photocurrent in dye sensitized solar cells. RSC Advances. 2013;**3**:6369-6376

[46] Kazmi SA, Hameed S, Azam A. Synthesis and characterization of Ag nanowires: Improved performance in dye sensitized solar cells. Perspectives in Science. 2016;**8**:577-579

[47] Guo K, Li M, Fang X, Liu X, Zhu Y, Hu Z, Zhao X. Enhancement of properties of dye-sensitized solar cells by surface plasmon resonance of Ag nanowire core–shell structure in $TiO_2$ films. Journal of Materials Chemistry A. 2013;**1**:7229-7234

[48] Huang P-C, Chen T-Y, Wang Y-L, Wua C-Y, Lin T-L. Improving interfacial electron transfer and light harvesting in dye-sensitized solar cells by using Ag nanowire/$TiO_2$ nanoparticle composite films. RSC Advances. 2015;**5**:70172-70177

[49] Hwang H-J, Joo S-J, Patil SA, Kim H-S. Efficiency enhancement in dye-sensitized solar cells using the shape/size-dependent plasmonic nanocomposite photoanodes incorporating silver nanoplates. Nanoscale. 2017;**9**:7960-7969

[50] Chandrasekhar PS, Chander N, Anjaneyulu O, Komarala VK. Plasmonic effect of Ag@$TiO_2$ core–shell nanocubes on dye-sensitized solar cell performance based on reduced graphene oxide–$TiO_2$ nanotube composite. Thin Solid Films. 2015;**594**:45-55

[51] Doosthosseini F, Behjat A, Hashemizadeh S, Torabi N. Application of silver nanoparticles as an interfacial layer in cadmium sulfide quantum dot sensitized solar cells. Journal of Nanophotonics. 2015;**9**:093092

[52] Ganeshan D, Xie F, Sun Q, Li Y, Wei M. Plasmonic effects of silver nanoparticles embedded in the counter electrode on enhanced performance of dye-sensitized solar cells. Langmuir. 2018;**34**:5367-5373

[53] Dong H, Wu Z, Gao Y, El-Shafei A, Jiao B, Dai Y, Hou X. A nanostructure based counter electrode for dye-sensitized solar cells by assembly of silver nanoparticles. Organic Electronics. 2014;**15**:1641-1649

[54] Ni M, Leung MKH, Leung DYC, Sumathy K. Theoretical modeling of $TiO_2$/TCO interfacial effect on dye-sensitized solar cell performance. Solar Energy Materials & Solar Cells. 2006;**90**:2000-2009

*Edited by Tatjana Gric*

*Plasmonics* gives researchers in universities and industries and designers an overview of phenomena enabled by artificially designed metamaterials and their application for plasmonic devices. The purpose of this book is to provide a detailed introduction to the basic modeling approaches and an overview of enabled innovative phenomena. The main research agenda of this book is aimed at the study of modeling techniques and novel functionalities such as plasmonic enhancement of solar cell efficiency, plasmonics in sensing, etc. The topics addressed in this book cover the major strands: theory, modeling and design, applications in practical devices, fabrication, characterization, and measurement. It is worthwhile mentioning that the strategic objectives of developing new artificial functional materials require close cooperation of the research in each subarea.

Published in London, UK

© 2018 IntechOpen
© sakkmesterke / iStock

IntechOpen

ISBN 978-1-83881-738-1